Università degli Studi di Milano Bicocca

Facoltà di Scienze Matematiche, Fisiche e Naturali

Scuola di dottorato in Scienze

Corso di dottorato in Fisica e Astronomia

Development and implementation of quantitative methods for cardiac applications in Positron Emission Tomography

Relatore: Marco Paganoni
Correlatore: Valentino Bettinardi

Tesi di Dottorato di

Luca Presotto

Matricola 064046

Ciclo XXV Anno Accademico 2012/2013

Contents

Abstract

Il primo argomento affrontato nel lavoro di tesi è relativo alla caratterizzazione fisica di un nuovo tomografo integrato PET/CT (Discovery-690); strumento che è poi stato utilizzato per tutti gli studi (sperimentali e clinici) effettuati nell'ambito della tesi in oggetto.

Successivamente viene descritta la progettazione e l'uso di un fantoccio antropomorfo statico, rappresentativo della regione cardiaca, con il quale sono state analizzate le prestazioni di diversi algoritmi di ricostruzione, incorporanti diversi livelli di informazioni come: i) il tempo di volo (Time Of Flight-TOF) e ii)la funzione di risposta del tomografo PET (Point Spread Function–PSF).

Una problematica peculiare dell'elaborazione delle immagini cardiache in PET è lo sfocamento da movimento prodotto dal battito cardiaco stesso e dalla respirazione del paziente. Queste condizioni spontanee, e non governabili, comportano una degradazione della qualità delle immagini e dell'accuratezza quantitativa dei dati PET. Al fine di studiare l'incidenza di tali movimenti, sia qualitativamente che quantitativamente, è stato progettato e costruito un fantoccio semovente del ventricolo sinistro, capace di replicare entrambi i movimenti.

Dopo averlo utilizzato per questo scopo lo si è anche potuto sfruttare per valutare l'efficacia delle tecniche di gating (cardiaco e respiratorio) sia in modalità singola che doppio gating. In seguito le tecniche di doppio gating sono state applicate anche su studi di pazienti clinici. I risultati ottenuti con questa tecnica, hanno mostrato notevoli miglioramenti nella risoluzione spaziale delle immagini PET ma con livelli di rumore inaccettabili per un utilizzo diagnostico.

Per superare questo problema e mantenere i vantaggi in termini di risoluzione offerti dal doppio gating, sono state valutate e sperimentate due tecniche di registrazione delle immagini. La prima tecnica proposta consiste in una registrazione affine dei diversi gates respiratori a fase cardiaca fissata; la seconda coinvolge tutti i gates tramite una registrazione elastica. Per effettuare questa seconda si crea un modello della superficie miocardica, tramite un procedimento di segmentazione, che costituisce la base per la successiva deformazione non rigida. L'applicazione delle due tecniche di registrazione ha permesso in entrambi i casi di ridurre il livello di rumore presente nelle immagini. Inoltre, sia sui dati acquisiti con i fantocci che su studi clinici condotti su pazienti, ha mostrato promettenti miglioramenti nella qualità delle immagini.

Nella parte finale del lavoro di tesi è stato affrontato il problema della quantificazione assoluta della perfusione cardiaca mediante l'analisi con modelli cinetici di studi PET con $^{13}NH_3$. Sono state inizialmente analizzate le proprietà matematiche dei modelli cinetici proposti per questo tracciante; successivamente è stata analizzata l'influenza di diversi algoritmi di ricostruzione sui parametri stimati da un particolare modello cinetico. Sono state anche valutate le performance di due diversi software per l'analisi della perfusione cardiaca. I risultati, dagli studi sopra descritti, hanno consentito di definire e implementare un protocollo clinico PET con $^{13}NH_3$. Protocollo che è attualmente in uso.

Summary

The first topic addressed in this thesis was the characterization of a new hybrid PET/CT scanner (Discovery-690); that was later used for all of the studies (experimental and clinical) performed in this work.

Subsequently an antropomorphic static cardiac phantom is described. This was used to analyze the performances of different reconstruction algorithms, encompassing different levels of information such as: i) the Time Of Flight (TOF) of the photons and ii) the Point-Spread-Function (PSF) of the PET tomograph.

A problem, own of cardiac studies in PET, is the motion blur due to the cardiac beat and to the breath of the patient. To study the effects of this combined motion, both quantitatively and qualitatively, a moving mechanical phantom was built, that executed both movements in a separate and controlled way.

After this investigation this phantom was exploited to evaluate the efficacy of gating techniques (cardiac and respiratory), by using single and double gating. These techniques were also applied to patient data. Double gating revealed to be able to provide better spatial resolution but with noise levels too high for diagnostic purposes.

To overcome this problem while maintaining the full spatial resolution two registration techniques were proposed. The first one consists in an affine registration that can be applied to correct only for respiratory motion. The second technique aims at registering all of the gates using an elastic morphing technique. This is achieved by using a map of the myocardial surface to build a Thin-Plate-Spline deformation field, using a segmentation algorithm. Both techniques allowed the reduction of the noise. In both phantom and patient studies promising quality improvements were obtained.

The last chapter of the thesis involved the quantification of absolute cardiac perfusion analyzing $^{13}NH_3$ PET studies with kinetic models. Initially the mathematical proprieties of the models proposed to analyze this tracer were assessed. Following the effect of the image reconstruction algorithms on the parameters quantified with a specific model were assessed. Two different software programs that allow perfusion quantification were also compared. The results of the studies described allowed the definition of a clinical $^{13}NH_3$ PET protocol, currently in use.

I like to play with thing a while before annihilation

(Ming the Merciless on positron range)

Chapter 1

Positron Emission Tomography

Positron Emission Tomography (PET) is a technique which allows to measure in-vivo and 3-dimensionally the distribution of a molecule injected into the body, previously tagged with a β^+ decaying nuclide. An image of radioactivity distribution can be correlated to the organ function, depending on the biochemical proprieties of the involved tracer inside that organ. Differently from other nuclear medicine techniques, like Single Photon Emission Tomography (SPET/SPECT), the use of β^+ decaying nuclides results in the emission of two back-to-back mid-energy photons ($E = 511\,keV$), as shown in figure 1.1. The analysis of coincidence events allow the identification of a direction along which the decay has happened (the so called Line-Of-Response, LOR) without the need of collimators. Comparing to SPECT this allows to have a significantly higher sensitivity at an increased spatial resolution [1].

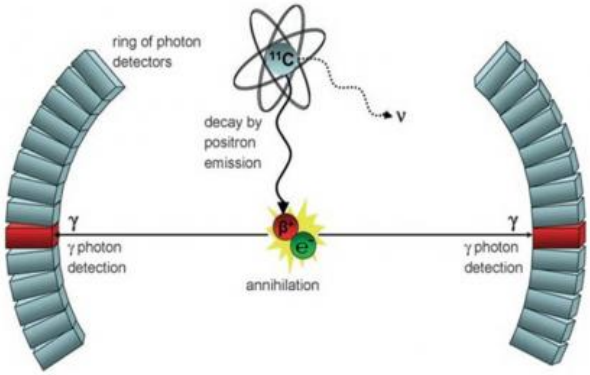

Figure 1.1: Principle of a PET scan, with the two γ being detected and defining a *Line Of Response* (LOR)

PET is a quantitative imaging tool. Thus it is possible to calibrate the output image in terms of absolute units of radioactivity concentration achieving good accuracy and precision. The capability to perform dynamic measurements of the regional tracer concentration with good temporal resolution allow the quantitative measurement of several physiologic parameters, exploiting specific kinetic models. This gives the possibility to visualize and quantify a number of molecular processes in-vivo.

1.1 PET physical principles

Positron emission tomography relies on the detection of two coincident $511 - keV$ photons to construct lines of response. Neutron deficient nuclei are usually prone to undergo a weak decay to restore a better balance of neutron and protons. There are two possible reaction, referred to as β^+ decay and electronic capture:

$$\begin{cases} p \to n + e^+ + \nu_e & \beta^+ \\ p + e^- \to n + \nu_e & E.C. \end{cases}$$

The β^+ decay is possible, for kinematic reasons, only if $M(^A_{Z+1}Y) - M(^A_Z X) > 2m_e$. The more the free energy of the decay the higher the probability of the β^+ decay. As every decay process this kind of events is regulated by a probabilistic law. This decay are described by a Poisson probability law

$$N(t) = N_0 e^{-\frac{t}{\tau}} = N_0 2^{-\frac{t}{t_{1/2}}}$$

where τ is called mean lifetime and $t_{1/2}$ half-life of the emitter. A nuclide, to be suitable for clinical use, must have an half-life which is neither too short (to allow its handling and to maintain a sufficient level of activity while the scan is performed) and neither too long (for dosimetric reasons). The most commonly used PET radioisotopes are listed in table 1.1 . Despite the conspicuous number of isotopes listed and their seemingly affinity to

	^{15}O	^{13}N	^{11}C	^{18}F	^{82}Rb	^{68}Ga	^{62}Cu
Half life	2 min	10 min	20 min	110 min	75 s	68 min	9.7 min
Availability	On-site cyclotron	On-site cyclotron	On-site cyclotron	Cyclotron, regional distribution	Generator $^{82}Sr/^{82}Rb$	Generator $^{68}Ge/^{68}Ga$	Generator $^{62}Zn/^{62}Cu$

Table 1.1: List of β^+ isotopes of potential interest in PET imaging

most common elements in biology only a limited number of nuclides and compounds have come in widespread routine clinical use. The most commonly used is ^{18}F, particularly when chemically synthesized as $Fluoro-desoxyglucose$. With almost $2\,h$ half life for many centers it is possible to perform a single production in the morning for all the patients of the day or to buy from an external producer a batch with enough activity to be used for a whole day. This half life is indeed long enough to allow the production in remote facilities (i.e. about 2 hours driving distances) and consequent shipping to centers that do not possess their own cyclotron and chemistry lab. ^{82}Rb has a very widespread use in the U.S.A. for cardiac imaging, as it is sold in easy-to-handle generators with long shelf life. Concerning ^{11}C there are a large number of compounds that have been synthesized to image many biological processes, especially in the field of brain receptor studies. Nonetheless only few reached application in clinical routine (as an example $^{11}C - Choline$ has been approved for diagnostic use by FDA recently, in September 2012). ^{13}N and ^{15}O, given their very short half life, cannot undergo chemical synthesis but both have found their niche, especially in perfusion studies. With its 2 minutes half-life sites that use ^{15}O have a direct connection

between cyclotron and the scanner room as the administration must be performed in the shortest possible time. The other nuclides are currently limited to research settings.

After a positron has been emitted it travels trough the medium until it is slowed enough to pick an electron from the matter. In this way the compound called "positronium" is formed. After its formation the compound then decays because of the annihilation between the e^+ and the e^-. Virtually all of the decays happen in a two-photon configuration. Kinematically in a two-body decay the only possibility is that the two outgoing photons have the same energy (equal to m_e) and are directed back-to-back. The emission process is isotropic over all the 4π.

1.1.1 Photon detection

After a decay has happened and the γ been emitted the following step is the detection of the two photons in coincidence. The current standard is to use crystalline inorganic scintillators. To reveal coincidences it is important that the material has an high stopping power (as the efficiency for coincidence detection goes with the square of single photon detection efficiency) and a fast light output (to achieve high count rates in dynamic studies and to use small time windows for random coincidences rejections). The list of the most commonly used crystal

Crystal	I	$\lambda_p[nm]$	$\tau[ns]$	Z	$\rho[g/cm^3]$	$\epsilon E[\%]$	$1/\mu[mm]$
$NaI(Tl)$	100	410	230	51	3.7	10	29.4
BGO	15	480	300	75	7.1	10	11.2
GSO	30	430	65	59	6.7	8.5	15.0
LSO	75	420	40	66	7.4	10	12.3
LYSO	80	420	41	60	7.1	11	12.6
$LaBr_3$	146	358	21	47	5.1	3	21.3

Table 1.2: Principal crystals used in PET: I is the relative intensity of light yield, λ_p the peak wavelength, τ the time constant of the light emission process, Z the effective atomic number, ρ the crystal density, ϵ_E the energy resolution at $511\,keV$ and $1/\mu$ the attenuation length at $511\,keV$.

scintillators used is reported in table 1.2 together with their most salient characteristics. $NaI(Tl)$ is reported as a comparison but is not used anymore in PET, due to is very low stopping power at this energy. It is still widely used in gamma-cameras due to its low cost, high light output and high enough stopping power at those low energy.

For many years the scintillator of choice has been BGO (bismuth-germanate, $Bi_4Ge_3O_{12}$) due to its high stopping power. Recently a new crystal has become widespread available, Lutetium-Orthosilicate with cerium doping (LSO, $Lu_2SiO_5 : Ce$). Its density and effective Z, and therefore the stopping power, are comparable to BGO but with an higher light yield. The remarkable propriety of this material is a time constant that is a seventh of BGO. Unfortunately Lutetium is itself radioactive and this increases the level of random coincidences recorded. For production and commercial reasons a modified version of LSO has been developed: the cerium-doped lutetium-yttrium orthosilicate (LYSO, $Lu_{2(1-x)}Y_{2x}SiO_5 : Ce$). The resulting crystal maintains all of the proprieties of LSO with only a slightly longer

decay time. Its employment in PET scanners is interchangeable with LSO for all practical purposes. This crystals, with faster higher light output, allow much higher count rates, a welcomed feature in dynamic studies. This also makes possible the recording of Time-Of-Flight (TOF) information, which is the measurement of the difference in the time of arrival of the two photons, which can narrow the extent along the LOR of the position of the initial decay (see later Fig. 1.5) .

To accept an event two trigger conditions are required. The first condition is on the detected photon energy which must fall inside a predefined range. Usually the low energy threshold is between 365 and 425 keV. Higher energy threshold is not critical as there are very few potential sources of accidental counts in that energy range. It is generally set at 625 keV. The other trigger condition is on the timing coincidence. Generally with fast crystals the time windows is set to $4-6\,ns$. For comparisons if a photon has to travel 60 cm more than the other the arrival time difference is 2 ns. In slow crystals (like BGO) the time window is usually set to $9-12\,ns$.

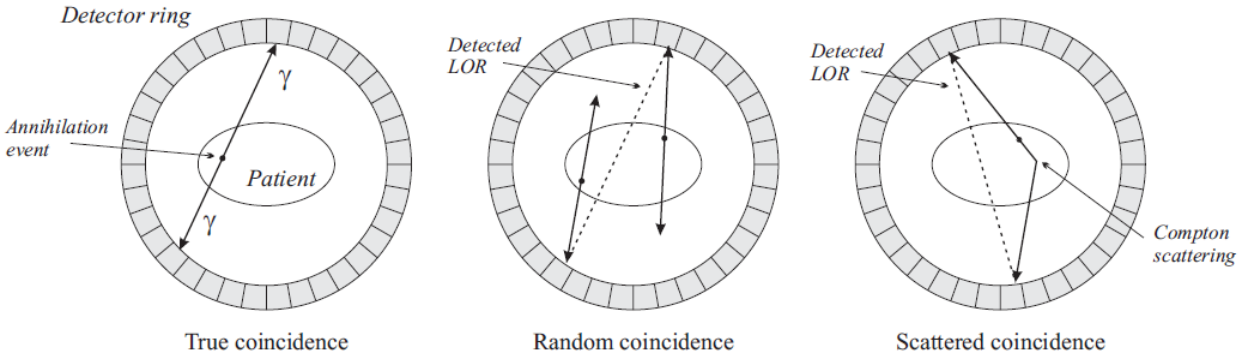

Figure 1.2: Types of coincidences detected by a PET tomograph.

Taken this into account it is possible to note that in a PET tomograph 3 types of coincidences can be recorded, as schematized in figure 1.2.

True coincidences True coincidences are the actual ones in which one is interested, with the two photons traveling along the Line Of Response and being detected correctly.

Random coincidences If a detector records events with a rate R_1 and it is put in coincidence with a second detector with an events rate R_2 a rate of random coincidences $R_r = R_1 R_2 \Delta\tau$ will be detected, with $\Delta\tau$ being the timing window used. In standard clinical PET acquisition this fraction of random coincidences can be of the same order of magnitude or even more than the rate of true coincidences. Two ways exist to deal with phenomenon: the delayed window method and the singles method. The first one records coincidence events in a delayed time window to the arrival of the first photon, much after the time resolution of the crystals. The rate of coincidences recorded will be then subtracted to the number of recorded counts. The problems associated with this method are the noisiness of the random counts estimate and the fact that the difference of two Poisson distributions is not anymore Poisson-distributed. Another strategy to correct for random coincidences is to measure

the single rate of each detector and then estimate the number of counts from the formula $R_r = R_1 R_2 \Delta\tau$ [2].

Scatter coincidences When a photon of $511\,keV$ travels in an organic tissue it has an high probability of undergoing compton scattering. Energy and momentum conservation impose that the outgoing photon has a lower energy with angular dependence:

$$E' = \frac{E}{1 + \frac{E}{m_e}(1 - cos\theta)}$$

Therefore a scattered photon has a lower energy. While photons being deflected for - let's say - 90° have half of the energy, and are easily rejected as they fall outside energy window, low angle scattered photons may fall inside the window. With a 10 % energy resolution photons of 10 % less energy con easily be accepted but, given the previous formula, a photon with a 10 % lower energy has been scattered at an angle of 25°. If the two photons are not back to back anymore the reconstructed line of response would not pass anymore by the point of the original annihilation, as shown in figure 1.2. The probability for a photon to be scattered at a specific angle is given by the notorious Klein-Nishina formula

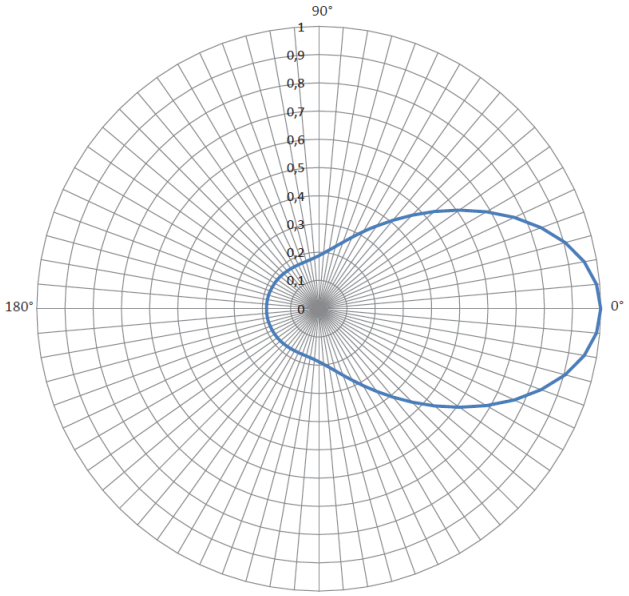

Figure 1.3: Plot of the Klein-Nishina distribution for an incident photon with energy of $511\,keV$

$$\frac{d\sigma}{d\Omega} = \frac{r_0^2}{2}\left(\frac{E'}{E}\right)^2\left(\frac{E'}{E} + \frac{E}{E'} - sin^2\theta\right)$$

It can be seen, also from its plot in figure 1.3, that the probability of scatter at low angles -the most problematic ones- is the highest.

In 2-dimensional acquisition modality the fraction of scattered events is generally low (less than 20%). In many cases of qualitative imaging often corrections were not applied for

this phenomenon. Simple correction models were effective when quantitative measurements were required. In 3-dimensional acquisition modality in the torso region the scatter fraction is as high as 50% or 60%, therefore corrections are always needed; they have to be also very accurate, if one event out of two has to be discarded.

The simplest correction techniques are "convolution-subtraction" techniques. These methods model the scatter distribution as a convolution of "unscattered" data with an empirically derived kernel function. Examples of such functions are a spatially invariant decreasing exponential $e^{-a|x-x_0|}$ [3] or a spatially variant modification $e^{-a(x)|x-x_0|}$ [4, 5]. Generally the parameters of these functions are fitted on the sinogram of the acquired data. More advanced techniques are the *Gaussian-fit* and the *model-based* technique. In particular, the first one models the scatter distribution as a gaussian function which is fitted on the tails of the sinogram data [6]. It works efficaciously if the object fills a small portion of the FOV and if the tails can be fitted robustly, i.e. the noise is low. For these reasons it is particularly suited for brain studies. The model based approach [7, 8, 9] uses the attenuation (obtained from a CT or from a transmission scan) and the emission map to calculate the percentage of scattered photons reaching each detector. Since the original emission map contains scatter the method has to be applied iteratively.

Attenuation Photons traveling trough a medium can be adsorbed by photoelectric effect. The probability for a photon to exit from all the material it is passing through is $P(x) = e^{-\int_a^x \mu(t)dt}$, with a being the distance of the emission point to the scanner center and $\mu(x)$ the attenuation coefficient at the point x. For a scanner of diameter r the probability that both photon reach their detectors is the product of the two probabilities, as the event are independent.

$$P_a = e^{-\int_a^x \mu(t)dt} e^{-\int_{-a}^x \mu(t)dt} = e^{-\int_{-r}^r \mu(t)dt}$$

Interestingly the result is independent from the emission point but depends only on the thickness (and the composition) of the medium that the LOR passes trough. This property is the basis of the attenuation correction: if the (integrated) attenuation coefficient of the medium is measured along each possible LOR, it is then possible to introduce a correction for the entire set of recorded data. To perform attenuation correction it is then just needed to have a map of $\mu(x)$. Traditionally transmissive scans were used. In those scans an external β^+ source, usually ^{68}Ge, was rotated in the air midway between the patient and the crystal blocks. The ration between an acquisition with and one without the patient in the middle allowed to measure directly $I/I_0 = e^{-\int \mu(t)dt}$. With the advent of combined PET/CT systems CT scans were available that were spatially registered to the PET scan. A CT scan already gives a map of μ in space, but for a different energy range. To make maps of attenuation at $511\,keV$ relations have been established that holds true for biological tissues (i.e.: low Z). An example is reported in figure 1.4.

Spatial resolution Many factors contribute to the spatial resolution of PET images. Following the whole physical process the first one encountered is the positron range. The space traveled by a positron in the matter depends on the energy of the decay and it has a non-gaussian shape with very long tails. Therefore high energy decays, like with ^{82}Rb, can

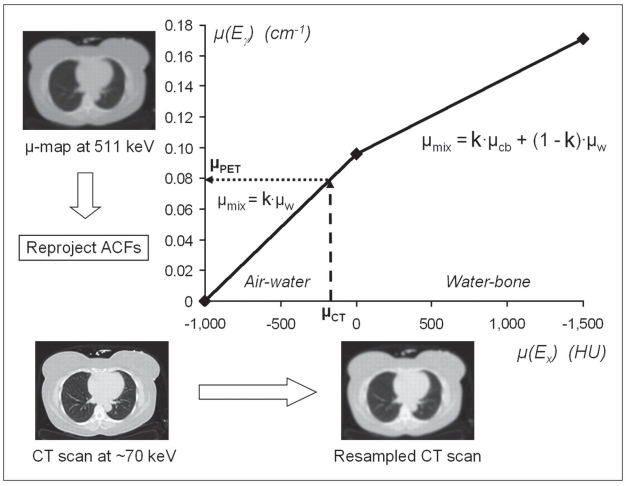

Figure 1.4: Example of conversion from Hounsfield units (HU) into attenuation coefficients at 511 keV energy

degrade spatial resolution down to $6\,mm$ before the whole chain of detection and reconstruction. Also positronium is not generally formed at rest and therefore the two γ are emitted with an average distribution of about 0.5° in the PET reference system, not perfectly back-to-back. On an $80\,cm$ diameter detector ring this means an uncertainty in the positioning of the event of about $2\,mm$. Finally the most important effect for human scanners is the finite dimension of the crystals, which defines the resolution of the LOR position. Generally with crystals of $4\,mm$ the resolution is limited to about $4\,mm$. Another $2\,mm$ are attributable to the crystal packing in a block of scintillators. This limits the resolution of an $80\,cm$ diameter scanner with $4\,mm$ crystals to about $5 - 6\,mm$.

Time of Flight information If the scintillators used are fast enough and if the readout electronics is capable of recording such fast signals maintaining the full temporal resolution it is then possible to measure the difference in the arrival time of the two photons. Numerically

$$\Delta t = \frac{1}{c}\left[(d+x) - (d-x)\right] = \frac{2x}{c}$$

Scintillators such as LSO and LYSO have a time resolution of about $700\,ps$ in the final assembled modules. Using error propagation it is possible to compute that with a coincidence timing resolution σ_t the distance x between the center of the LOR and the emission point can be calculated with a precision $\sigma_x = c\sigma_t/2$. With $700\,ps$ of time resolution a spatial localization of $10\,cm$ is possible. It is possible to exploit this information in the reconstruction process. This approach, called time of flight PET (TOF–PET), adds a further weight on each event: if in conventional PET every point of the detected LOR has the same probability of being the annihilation source, in TOF–PET it is possible to introduce a probability distribution along the LOR itself and restrict the uncertainty on the positioning of the event (see figure 1.5). This also helps in reducing both scatter and, in particular, random contributions, improving the image quality and the quantitative information [10, 11, 12, 13]. It has been shown that the improvement is the signal to noise ratio considering TOF information

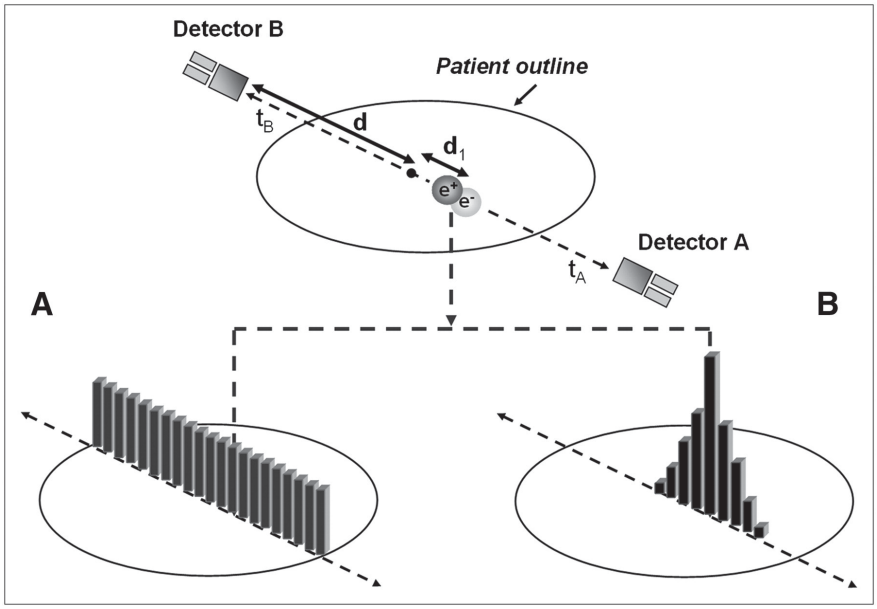

Figure 1.5: Simplified scheme of positron emission tomography, exemplifying also time-Of-Flight

in the image reconstruction is proportional to $\sqrt{\frac{D}{\sigma_x}}$, with D the diameter of the object, in a cylindrical approximation, and σ_x the spatial resolution along the LOR given by TOF.

1.2 Image reconstruction

For each recorded event a LOR is associated. They are arranged in *sinograms*, each of which represent the Radon transform of the activity concentration in a given transaxial plane of the Field Of View (FOV).

The information contained in a sinogram are sufficient to reconstruct the distribution of radioactivity in each slice. Two classes of algorithms exist to do this: analytic and statistical iterative procedures. Analytic algorithms are based on the computation of the inverse of the Radon-transform, adjusting the formulae to the discrete nature of the problem. The main advantages of these procedures are linearity, easy implementation and the speed of the computation. Nevertheless analytic reconstruction cannot take into account the physical proprieties of emission and detection processes and therefore give very noisy images as a result.

The statistical algorithms can instead consider both geometrical/physical information and the statistical proprieties of the collected data. They are intrinsically discrete and the model of the acquisition system can be inserted inside a system matrix. The Poisson nature of the noise in the acquired data can be included in the modeling, thus improving the signal-to-noise ratio (SNR) of the reconstructed images (Fig. 1.6).

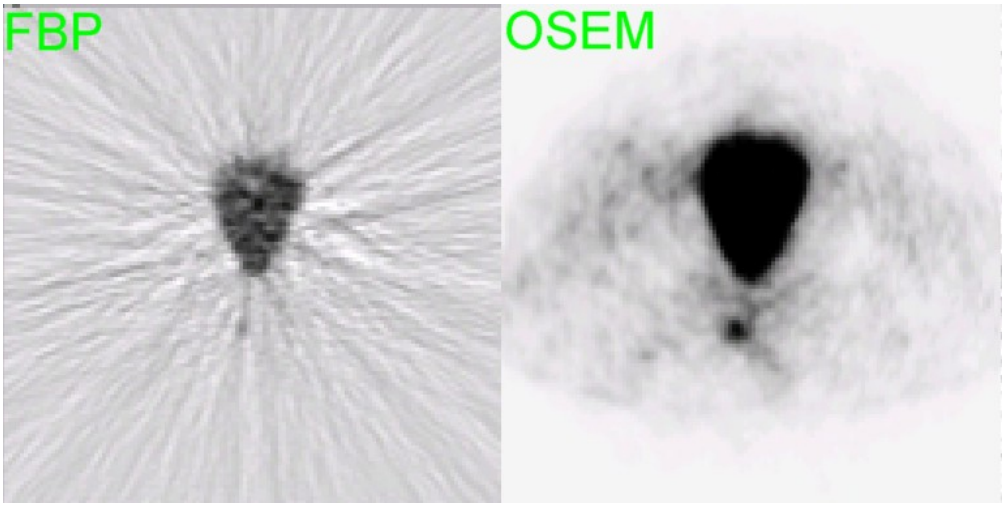

Figure 1.6: An analytic (left) and a statistical (right) reconstruction of the same raw data

1.2.1 Iterative reconstruction procedures

In the last years, there is an increasing interest in the development and application of iterative reconstruction algorithms for nuclear medicine. This success is motivated by the high quality of the images that such methods can produce. As stated above, the iterative approach of tomographic reconstruction consists in a discrete modeling of the imaging system; hence, the object function f(x, y) is modeled as a linear combination of basis functions:

$$f(x,y) = \sum_{i=1}^{P} f_i b_i(x,y)$$

where P is the number of voxels chosen to represent the object in the image plane, and $b_i(x,y)$ are the 2D unitary rectangular functions representing the i-st voxel in the $x-y$ plane. The coefficients f_i, for $i = 1, ..., P$, represent the intensity of the i-st voxel of the discretized object function. Given a system matrix A, the vector p containing the acquired data can be expressed as:

$$p_j = \sum_{i=1}^{P} A_{ij} f_i$$

In the previous equation, the elements p_j, for $j = 1, ..., M$, express the number of LORs recorded in the j-st detection tube. Each detection tube is in turn related to a given sinogram bin, thus the dimension M of the vector p is equal to the number of bins in the sinogram. The matrix element A_{ij} represents the probability that a photon pair emitted in the voxel i is recorded in the tube j. That probability is the product of many independent probabilities, taking into account the system geometry, the Poissonian nature of the radioactive decay, the attenuation encountered by each photon pair in a given detection tube, etc. Using this formalism, the image reconstruction consists in solving the previous equation with respect to f :

$$f_i = \sum_{i=1}^{M} A_{ij}^{-1} p_j$$

In all practical cases, the matrix A is not invertible analytically. This is due in part to the very large size of that matrix and partly to the bad conditioning of the problem. Hence, the solution of the inverse problem shall be computed iteratively by successive approximation. The most used algorithm for such purposes is the expectation maximization (EM) algorithm [14]

$$f_i^n = \frac{f_i^{n-1}}{\sum_{j'=1}^{M} A_{ij'} p_{j'}} \sum_{j=1}^{M} \frac{p_j A_{ij}}{\sum_{i'=1}^{p} f_{i'}^{n-1} A_{i'j}}$$

Usually, the reconstruction starts with $f_i^0 = 1$ for all i. The reconstruction based on the above formula can be computationally expensive. For this reason, a more efficient variant of the EM algorithm is used in practice. In this variant, the projection data is subdivided in ordered subsets, then the EM iteration is applied to each subset separately, the ordered subset EM algorithm (OS-EM) [15]. This converges faster to the solution, and this can be of practical advantage in the clinical setting. OSEM is a MLEM algorithm in which the entire set $\Omega = P(i)$, $i = 1 \dots nP$ of projections originating from detectors $p = 1 \dots M$ is divided into equipotent (and usually disjoint) *subsets* $S_k, k = 1 \dots K$

$$\Omega = \bigcup_{k=1}^{K} S_k$$

where K is a divisor of the number of angular projections M. Many different criteria for filling these subsets are present but the most used is to choose equispaced projections. Each MLEM iteration n on the entire set Ω is then divided into K sub–iterations (n, k) in which the approximation $f^{[n,k]}$— computed *using only the data in subset* S_k — is updated using the data in subset S_{k+1}. The resulting rule is consequently

$$f_i^{[n'+1]} = \frac{f_i^{n'}}{\sum_{d \epsilon S_k} A_{id} p_d} \sum_{d \epsilon S_k} \frac{p_d A_{id}}{\sum_{i'=1}^{p} f_{i'}^{n'} A_{i'd}}$$

where k' is a sub-iteration index defined as $n' = nK + k - 1$. It is possible to recognize the analogy to the MLEM case. It is important to note that a complete iteration $k \to k + 1$ in the OSEM algorithm corresponds to K effective iterations $n' \to n' + K$ while the time required for a sub-iteration is approximately $1/K$ due to reduced terms in the summations.

It is worth noting that the methodology described here for the 2D iterative reconstruction can be extended in the 3D case without changes in the formalism. In the 3D case, of course, the system matrix will be much larger than that used in the 2D case, and this will increase further the computational complexity of the reconstruction process.

1.3 Structure of the work

This works focuses on the application of PET in cardiac studies. The focus is primarily on the quantitative accuracy of the data extracted.

In this scope in Chapter 2 I started the thesis work with the characterization of a new tomograph that following was used for all the other experiments.

With chapter 3 starts the focus on cardiac images. In this chapter I performed a study with a static phantom to assess the accuracy of various reconstruction algorithms on that scanner to recover the correct value of the radioactivity concentration.

Following, chapter 4, a robotized phantom of the myocardial muscle is presented. This phantom was expressly designed and built for this thesis to assess the effects of cardiac motion on quantitative PET scans. A first experiment is performed and the results are reported

In Chapter 5 the most common solutions to the problems of motion are analyzed and the double gating technique is introduced. This technique is then applied to the phantom and to some patient studies. The results show a great improvement of spatial resolution but levels of noise too high for clinical applications.

In Chapter 6 two techniques are proposed to register images from different frames of a dual gated reconstruction in order to reduce the statistical noise and to make clinical use of double gating feasible in clinical routine. The techniques are then tested on patient data.

In Chapter 7 I analyzed the most common methods of quantifying myocardial perfusion using kinetic models of dynamic PET data. After a review of the techniques available a comparisons of the mathematical proprieties of two kinetic models of $^{13}NH_3$ is presented.

Finally in chapter 8 I analyzed, on actual patient data, the effect of the reconstruction algorithm on the quantification of myocardial blood flow using the De-Grado model of $^{13}NH_3$

Part I

Quantitative accuracy of PET data

Chapter 2

Characterization of a new PET tomograph

Quantitative studies in nuclear medicine are based on an interpretation of the radiotracer uptake, often as a function of time. The ideal tomograph to perform this kind of studies is able to record high count rates, specially in 3D-mode, and has an high sensitivity, to counterbalance the low statistics in short scan times. New scanners often incorporate Time of Flight (TOF) technology, that has been shown to reduce the noise in the images, providing an increased effective sensitivity. In our department, at the start of this thesis work, a state-of-the-art tomograph was acquired, the Discovery-690 (D-690, General Electric Medical Systems, GEMS, Milwaukee, WI) PET/CT system. The first work performed upon its arrival was a characterization of its performances, having in mind broad applications in oncology and neurology, on top of the specific applications in cardiology. This scanner was subsequently used for all the experiments and the acquisitions in this thesis.

2.1 Materials and Methods

2.1.1 Discovery-690 (D-690)

The D-690 system combines a LYSO block detector PET tomograph with a 64-slice CT scanner. The PET scanner has a multiring system design. The PET tomograph consists of 13'824 LYSO crystals with dimensions of $4.26 \times 6.3 \times 25\,mm^3$. The PET detection unit is a block of 54 (9×6) individual LYSO crystals coupled to a single squared photomultiplier tube with 4 anodes. The D-690 uses a low energy threshold of $425\,keV$ and a coincidence time window of $4.9\,ns$. The D-690 consists of 24 rings of detectors for an axial field of view (FOV) of $157\,mm$. The transaxial FOV is 70 cm. The D-690 operates only in 3-dimensional mode (3D) with an axial coincidence acceptance of ± 23 planes. A radioactive pin source of ^{68}Ge (18 MBq) is used for system calibration and daily quality control. The D-690 is equipped with a powerful modular array of cell processors (IBM Blade Centre) specifically designed to speed up image reconstruction and data processing. The D-690 system uses, as the standard PET reconstruction, a fully 3D ordered subset expectation maximization (3D-OSEM) [15] algorithm with all corrections (scatter, random, dead time,

attenuation and normalization) [16] incorporated into the iterative reconstruction scheme (GEMS name: VUE-point HD). Furthermore, new reconstruction algorithms are available on the D-690, which add to the standard VUEpoint HD configuration the time of flight information (GEMS name: VUE-point FX) and/or a 3D model of the D-690 PET point spread function (GEMS name: Sharp-IR) [17]. The PSF model implemented in the D-690 system is based on experimental measurements of a point source acquired in different positions within the 3D-PET FOV. The resulting spatially variant PSF was modeled and then coded in a system matrix, in the projection space, to be used in the reconstruction scheme of a 3D-OSEM algorithm. For the rest of the chapter, the different reconstruction algorithms will be identified as (i) HD for the standard configuration (3DOSEM, VUE-point HD), (ii) TOF for the VUE-point FX, (iii) PSF for the Sharp-IR, and (iv) TOFPSF when both TOF and PSF information are included in the reconstruction scheme. The CT system is the LightSpeed VCT with 64 slices. The detector matrix is characterized by 912 channels $\times$ 64 rows for a total of 58'368 solid state detector elements. The LightSpeed VCT allows full 360° rotational scans with a variable rotational time ranging from 0.35 to 2 s and slice thickness of $64 \times 0.625\,mm$, $32 \times 1.25\,mm$, $16 \times 2.5\,mm$ and $8 \times 5\,mm$. The physical performance of the D-690 (PET component) was assessed using GEMS proprietary software implemented on the D-690, according to the NEMA NU-2-2007 standard procedures [18], which account for the recommendations by Watson et al. [19] in the case of PET systems using crystal scintillators with intrinsic radioactivity (e.g., LYSO). In addition to the standard NEMA set of measurements, specific tests were performed (i) to measure the energy and coincidence timing resolution of the PET scanner and (ii) to assess image quality using phantoms representative of different clinical conditions (neurology and oncology). In such cases, the analysis of the data was performed using ad-hoc written software.

2.1.2 Energy and coincidence timing resolution

Phantom, isotope, and activity

In these tests, the pin radioactive source (^{68}Ge 18 MBq) of the system was used for the measures. The pin source (external diameter: 4 mm, length: 19 cm) was placed in the center of the scanner FOV and axially aligned with the Z axis of the tomograph. Two emission scans (5 min each, list mode acquisition) were performed to measure:

- energy resolution (ER);
- coincidence timing resolution (CTR).

Data were acquired using the detector calibration acquisition mode available on the scanner. In the calibration mode, the scanner acquires coincidence data with an open energy window and coincidence timing acceptance window of $611.5\,ns$. The scanner generates histograms of the energy deposited by the annihilation photons detected in each crystal and stores the histograms in a file. For each crystal, the scanner produces also a histogram of the difference between the detection times of the two coincidence annihilation photons. In particular, the time difference of a coincidence event is included in the histogram if one of the annihilation photons of the pair is detected in that crystal and both annihilation photons are within an

energy window of 425–650 keV. The scanner saves the resulting time difference histograms in a file. The files containing the timing difference and energy histograms were processed off-line to determine the full width at half the maximum (FWHM) of the timing and energy resolutions. To evaluate the uncertainty in the measures, both scans were repeated three more times. For each new measurement, the source was removed and then repositioned in the scanner FOV, to take into account also the error introduced by non perfect central positioning.

Data processing and data analysis

The ER and CTR were calculated, by linear interpolation between neighboring pixels, as the FWHM, for each of the 13'824 (crystals) spectra in the scanner. For the CTR, the spectra of coincidence events were corrected for random events before calculating the FWHM. The amplitude of randoms distribution was determined from the average counts in channels far from the true coincidences peak. The channel width used in the CTR analysis was 89 ps. In the calculation of the ER, the background depends in a complex way on the location of the crystal in the block and on the singles count rate in the detector. Because of this complicated dependence, background subtraction was not performed for the ER analysis; this may result in an overestimation of the ER. The channel width used for the energy resolution analysis was 2.5 keV. For each measure, ER and CTR were calculated as the mean over all the crystals in the PET scanner and then an average value was computed among the four results. Furthermore, the uncertainties of ER and CTR were calculated as the standard deviation (SD) among the values obtained in the four independent measurements.

2.1.3 Evaluation of the intrinsic radioactivity contribution from LYSO

The LYSO has an intrinsic component of natural radioactivity due to the presence of ^{176}Lu. This intrinsic radioactivity produces a background of coincidences (intrinsic trues and intrinsic randoms) that cannot be distinguished from coincidences due to an external radioactive source. To evaluate the amount of intrinsic radiation, a long (12 h) blank scan without objects or radioactive sources within the PET FOV was acquired. At the end of the scan, the total recorded events (prompts) were 49'765'779, while the estimated randoms were 49'718'396. This result implies that the intrinsic trues rate is 1 cps. Such low intrinsic trues rate can be considered negligible and was thus not accounted for in the analysis of the following NEMA measurements. The randoms rate, which was not negligible, was accounted for (subtracted) during the NEMA tests to avoid biased results.

2.2 PET NEMA NU 2-2007

2.2.1 Spatial resolution

Phantom, isotope, and activity. Three point sources with dimensions less than 1 mm were prepared inside three glass capillary tubes. The point sources were obtained from

a drop of 18F-FDG having a concentration of 370 MBq/ml. The activity in the FOV was such that the percent dead time losses were <5%

Experimental setup The point sources were positioned in the transverse FOV at the following (x,y) locations: (0,1), (0,10), (10,0) cm.

Data acquisition Two emission scans (1 min each) were performed: (i) in the center of the axial FOV (Z=0) and (ii) at one-fourth from the center of the axial FOV (Z=39.3 mm).

Data processing Reconstructions were performed using a 3D Reprojection algorithm53 (transaxial filter: ramp, FOV: 20 cm centered at x=5 cm and y=5 cm and matrix size:256 × 256).

Data analysis For each point source, the spatial resolution was calculated by linear interpolation between neighboring pixels, as FWHM and full width at a tenth of the maximum (FWTM) of the radial, tangential, and axial profiles. Corresponding radial, tangential, and axial resolution values (FWHM and FWTM) were then averaged for the two axial (Z=0 and Z=39.3 mm) positions.

2.2.2 Sensitivity

Phantom, isotope, and activity.

A phantom with 5 concentric aluminum sleeves (length: 70 cm), stacked one inside the other, was used (NEMA PET Sensitivity Phantom, Data Spectrum Corporation, Hillsborough, NC). The source to perform the test consists of a polyethylene tube (internal diameter: 2 mm, external diameter: 3.5 mm, length: 70 cm) filled with radioactivity. Before performing the NEMA sensitivity test, a dynamic study was acquired to determine the reference activity ($Sens\ a_{ref}$) at which the sensitivity test should be performed, as recommended by Watson et al. The polyethylene tube was filled with an activity of 23 MBq and this source was inserted in the smallest of the five aluminum tubes (to allow the full conversion of the positrons). The tube was positioned in the center of the transaxial FOV and aligned to the Z axis of the scanner. The acquisition protocol consisted of a dynamic scan of 29 frames (5 min each) with a delay of 20 min between consecutive frames. At the end of the scan, random coincidences were subtracted from prompt events to obtain $trues + scatter$ events. $Sens\ a_{ref}$ was thus determined by plotting the $randoms/(trues + scatter)$ ratio as a function of the activity in the source. As can be seen, the minimum ($Sens\ a_{ref}$) of this ratio was found at an activity of 4.8 MBq. The sensitivity test was then performed by filling the source (70 cm) with 4.9 MBq of $^{18}F - FDG$ in water. In such a condition, the count rate losses were <1%.

Experimental setup and data acquisition.

Five emission scans (1 min each) were performed, with the line source positioned in the center of the transaxial FOV (x$\frac{1}{4}$0, y$\frac{1}{4}$0) and aligned to the axis of the PET tomograph.

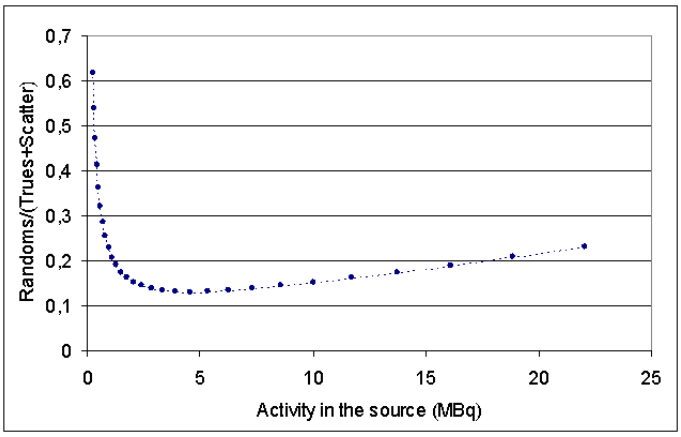

Figure 2.1: Randoms/(Trues+Scatter) Vs activity in the line source (length = 70 cm). The line source was inserted in the smallest aluminum tube of the NEMA sensitivity phantom.

The line source was surrounded by the first sleeve in the first emission scan. Larger sleeves were progressively added in each of the following scans. A second set of five emission scans was then performed with the line source positioned in the transverse plane at $x = 10\,cm$, $y = 10\,cm$ with respect to the center of the scanner FOV. The rate of randoms, estimated from the rate of singles, was recorded for each measure.

Data processing. Sinogram data were processed by a single-slice rebinning algorithm to produce 2D sinograms.

Data analysis. For each measurement, the trues rate was calculated by subtracting the randoms rate from the total prompts rate. The trues rate (R), for each measurement of the five sleeves (j), was corrected for isotope decay ($Rcorr, j$). The natural logarithm of $Rcorr_j$ was plotted, as a function of the sleeve thickness X_j and then fitted by a linear regression to obtain the extrapolated trues ($Rcorr, 0$) at X_0 when no attenuation is present in the FOV. The system sensitivity (S_{tot}) was then computed as $Rcorr, 0$ divided by the activity in the source. The axial sensitivity profile for each slice i was finally calculated as

$$S_i = \left(\frac{R_{corr,1,i}}{R_{corr,1}} \right) S_{tot}$$

where 1 represents the smallest tube. The same data analysis was repeated for the sensitivity measurement acquired at 10 cm radial offset from the tomograph center.

2.2.3 Scatter fraction, count losses and randoms measurement

Phantom, Isotope and Activity The phantom used for the test was the NEMA NU-2-2007 scatter phantom (NEMA Scatter Phantom SetTM – Data Spectrum Corporation, Hillsborough, NC). The phantom consists of a polyethylene cylinder (diameter 20 cm; length 70 cm) with a hole (at a radial distance of 4.5 cm) parallel to the central axis of the cylinder where a radioactive source can be inserted. The source consists of a polyethylene tube

(internal diameter 3.2 mm, external diameter 4.8 mm, length 70 cm) filled with a solution of 18F-FDG in water with a total activity of 1315 MBq.

Experimental Set-up The NEMA NU-2-2007 scatter phantom was positioned in the centre of the scanner FOV with the line source at x=0 cm and y= -4.5 cm (nearest to the patient bed).

Data Acquisition Thirty-eight emission frames were recorded to sample the response of the system at different count rates as the source decayed. Frames from 1 to 17 were acquired for 900 s, with no delay between consecutive frames, while the remaining 21 frames were acquired for 1500 s with a delay of 900 s between consecutive pairs of frames Randoms rate, estimated from singles rate, was recorded for each measure.

Data processing. Sinogram data were processed by a single-slice rebinning algorithm to produce 2D sinograms.

Data Analysis Data analysis was performed as described in the NEMA NU-2-2007. Each prompt and random sinogram i of each acquisition j was masked with a 12 cm region from the centre of the phantom. All the pixels outside the masked region were set to zero. Each projection of the prompt sinogram was shifted to align the pixel with the maximum value in the centre of the sinogram. The total events, $C_{TOT,i,j}$, and random events, $C_{r,i,j}$ were calculated as the sum of counts within the masked region. Random plus scatter events, $C_{r+s,i,j}$, were computed by estimating the events under a 40 mm wide strip centred on the peak and adding these events to counts outside this strip. The scatter fraction (SF) for each slice i of each acquisition j was then calculated as :

$$SF_{i,j} = \frac{C_{r+s,i,j} - C_{r,i,j}}{C_{TOT,i,j} - C_{r,i,j}}$$

The system scatter fraction, SF_j, was computed as the sum over all the slices i. For each slice i of each acquisition j the total events rate, $R_{TOT,i,j}$, the true events rate $R_{t,i,j}$, the random events rate, $R_{r,i,j}$, and the scatter events rate, $R_{s,i,j}$, were calculated dividing the corresponding recorded counts by the acquisition time of each frame j. The Noise Equivalent Count Rate, R_{NEC}, for each slice i and each acquisition j was then calculated as :

$$R_{NEC,i,j} = \frac{R_{t,i,j}^2}{R_{TOT,i,j} + R_{r,i,j}}$$

The second randoms term has been added because it is assumed that the randoms estimate is not smoothed (i.e. noisy). Finally, the system Noise Equivalent Count Rate for each acquisition j, $R_{NEC,j}$, was obtained as the sum over all the slices i.

2.2.4 Accuracy: correction for count losses and randoms

Accuracy of correction for dead time losses and random events was estimated by using the same data recorded during the scatter fraction and count rate test.

Data Processing Acquired data were corrected for random coincidences and dead time and then reconstructed using a 3D Reprojection algorithm (no transaxial filter, FOV: 18.0 cm centred in the scanner FOV and matrix size: 128×128). Even if the phantom is a 20 cm in diameter the reconstruction of the data on a 18 cm FOV does not affect the results of the test.

Data analysis Images were analyzed by drawing in each slice i of each acquisition j a circular region of interest, $ROI_{i,j}$ with a diameter of 180 mm, centred in the transverse FOV of the scanner. The trues rate, $R_{ROI,i,j}$, was calculated by dividing the true counts $C_{ROI,i,j}$ by the time of acquisition. The extrapolated true counting rate, $R_{Extr,i,j}$, was calculated from all acquisitions j with dead time losses $< 1\%$. Finally, the percent relative count rate error Δr was calculated for each slice i of each acquisition j as :

$$\Delta r_{i,j} = \left(\frac{R_{ROI,i,j}}{R_{Extr,i,j}} - 1 \right)$$

2.2.5 Image Quality, accuracy of attenuation and scatter corrections

Phantom, Isotope and Activity In this test both the NEMA IEC Body phantom and the NEMA scatter phantom were used (NEMA IEC Body Phantom SetTM and NEMA scatter phantom SetTM – Data Spectrum Corporation, Hillsborough, NC). The phantom ($24 \times 30 \times 24\, cm^3$) contains 6 coplanar spheres, equidistant from the centre of the phantom, with diameters of 10, 13, 17, 22 (simulating hot lesions) and 28, 37 mm (simulating cold lesions); a cylindrical insert simulating lungs (density $0.30 g/cm^3$, 5 cm diameter and as long as the phantom) positioned at the centre of the phantom. A solution of ^{18}F-FDG in water (activity concentration 5.3 kBq/ml) was used as a radioactive background, obtaining a lesion/background (L/B) ratio of 4:1. The line source of the scatter fraction phantom was filled with an activity of $105\, MBq$,. Such amount of activity should generate the same effective background concentration as in the background of the NEMA IEC body phantom.

Experimental setup The NEMA IEC Body phantom was centred in the transverse FOV of the scanner with the centre of the spheres coplanar to the centre of the axial FOV. The scatter phantom was placed just behind the NEMA IEC Body phantom to provide activity outside the axial FOV.

Data Acquisition A CT scan (140 kV, 90 mA) was performed (for attenuation correction) followed by three emission scans. The acquisition times for the three acquisitions were set, following the NEMA prescription, to 6 min 33 s, 6 min 50 s and 7 min 07 s, respectively. In particular the scan time was calculated as prescribed by the NEMA data collection which requires to simulate a total body scan of 100 cm in 60 min scan time. GEMS NEMA protocol requires to cover 100 cm with 9 beds positions. This results in a 6 min and 33s for bed position and to an overlap between adjacent scan position of 15 slices.

Data Reconstruction Image reconstruction was performed using the algorithms HD, TOF, PSF and TOFPSF. Common parameters for the different reconstruction algorithms were subsets = 18, iterations = 1, 2, 3, 5,10, 15 and 20, transaxial post-filter = Gaussian 2.0 mm FWHM, Z filter = Standard (average filter with weight coefficients of : 1-4-1), reconstructed FOV = 50 cm, image matrix = 256 x 256.

Data Analysis Circular ROIs, with a diameter equal to the physical size of each sphere, were drawn on the CT images and then copied onto the corresponding PET images. Twelve background ROIs (37 mm diameter) were drawn in the central slice and in slices at +/- 10 mm and +/- 20 mm from the central one. ROIs of a smaller size (10, 13, 17, 22, 28 mm) were drawn concentric to the 37 mm background ROIs. A ROI of 3 cm in diameter was drawn (in each slice of the phantom) in the central cylindrical insert. The percent hot contrast recovery coefficient ($HCRC$) for each hot sphere j was calculated as :

$$HCRC_j = \frac{C_{hot,j}/C_{bkg,j} - 1}{a_{hot}/a_{bkg} - 1} \tag{2.1}$$

where $C_{hot,j}$ is the average counts in the "hot" ROI and $C_{bkg,j}$ is the average of the background ROI counts for the sphere j, while, $a_{hot}/a_{bkg}$is the ratio of the true radioactivity concentration in the hot spheres and in the background. The percent cold contrast (CC) for each cold sphere j was calculated as :

$$CC = 1 - \frac{C_{cold,j}}{C_{bkg,j}} \tag{2.2}$$

where $C_{cold,j}$ is the average counts measured in the "cold" ROI for sphere j. The accuracy of attenuation and scatter correction (ΔC_{lung}) was estimated as the residual error in the lung region as:

$$\Delta C_{lung} = \frac{C_{lung}}{C_{bkg}}$$

where C_{lung} is the average counts in the lung insert ROI. The background variability (BV) for each sphere j was calculated as :

$$BV = \frac{SD_j}{C_{bkg,j}}$$

where SD is the standard deviation of the background ROI counts for each sphere j, calculated as :

$$SD_j = \sqrt{\frac{\sum_{k=1}^{k=60} \left(C_{bkg,j,k} - C_{bkg,j,k}\right)^2}{k-1}}$$

where k is the number of background ROIs.

2.2.6 Image quality in neurological studies: 3D Hoffman Brain phantom (3D-HBP)

Phantom, Isotope and Activity The 3D-HBP phantom (3D Hoffman Brain Phantom – Data Spectrum Corporation, Hillsborough, NC) consists of nineteen plexiglass plates

stacked into a cylindrical tank (diameter 18 cm, height 12 cm). Each plate simulates a cross section through the cranium. The 3D-HBP allows for a qualitative and a quantitative study of the 3D radioisotope distribution as it would appear in a 18F-FDG PET brain study. In particular, the 3D-HBP phantom simulates a 4:1 uptake ratio between gray and white matter. The 3D-HBP was filled with a radioactive solution of water and 18F-FDG.

Experimental set-up and Data Acquisition Once filled, the 3D-HBP phantom was positioned in the centre of the PET FOV. A CT scan (140 kV, 90 mA) was performed, followed by a 3D emission scan to record 200 Mcounts.

Data Reconstruction Four types of reconstructions (HD, TOF, PSF and TOFPSF) were performed. Parameters common to all the reconstruction algorithms were: Subsets = 18, Iterations = 1, 2, 3, 5,10, 15 and 20, transaxial post-filter = Gaussian 2.0 mm FWHM, Z filter = Standard (average filter with weight coefficients of: 1-4-1), reconstructed FOV = 30 cm, image matrix = 256 x 256.

Data Analysis Irregular ROIs were drawn, over gray and white matter, in five representative CT images. On each of the five slices 3 - 4 ROIs were drawn on gray and white matter. The ROIs were then transferred onto the corresponding PET images, and the average of the activity concentration in the gray and white matter was computed among the corresponding ROIs. Finally, the activity ratio between gray and white matter was calculated (expected true value 4:1).

2.2.7 Image quality in oncological studies: Big phantom

Phantom, Isotope and Activity. A big phantom made up of a plexiglass tank ($27 \times 39 \times 30 cm^3$) was used to simulate oncological studies. In our experience such a phantom simulates obese patients with a Body Mass Index between 30 to 35. The six spheres and the lung insert of the NEMA IEC Body phantom were used with this phantom to simulate hot and cold lesions. The phantom and the spheres were filled with a radioactive solution of water and ^{18}F-FDG to obtain a lesion-to-background activity ratio of L/B=8:1 and L/B=4:1, in two independent experiments. The radioactivity concentrations in the background were 2.87 kBq/ml (L/B=8:1) and 4.07 kBq/ml (L/B=4:1) respectively.

Experimental Set-up. The phantom was centred in the FOV of the scanner with the centres of the spheres coplanar to the centre of the axial FOV.

Data Acquisition A CT scan (140 kV, 400 mA) was performed followed by an emission scan acquired in list mode. Once acquired, the emission study (list file) was processed to generate two new sets of raw data corresponding to 50 and 200 Mcounts.

Data reconstruction Four types of reconstructions (HD, TOF, PSF and TOFPSF) were performed. Parameters common to all the reconstruction algorithms were: Subsets =

18, Iterations = 1, 2, 3, 5,10,15 and 20, transaxial post-filter = Gaussian 2.0 mm FWHM, Z filter = Standard (average filter with weight coefficients of : 1-4-1), reconstructed FOV = 50 cm, image matrix = 256 x 256.

Data Analysis The quantitative analysis was performed using three parameters: hot and cold contrast, as defined in formulae 2.1 and 2.2, and the coefficient of variation (COV) for the background. For each sphere in the phantom a volume of interest (VOI) was drawn (on the CT images) with the same diameter as the corresponding physical sphere. For the background, eleven circular ROIs (4 cm) were drawn in the central slice and in slices at +/- 10 from the central one. VOIs and ROIs were then transferred onto PET images to calculate HCRC, CC and COV.

2.3 Results

Figure 2.2 shows the representative energy and coincidence timing spectra. Average energy and coincidence timing resolution were found to be 12.4% (SD=0.02) and 544.3 ps ($SD = 1.5ps$) respectively.

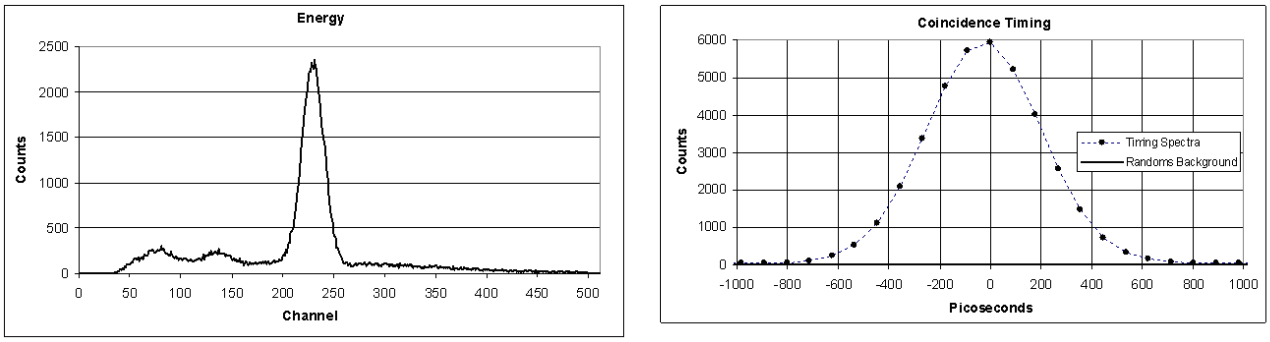

(a) Coincidence energy spectrum **(b)** Timing resolution spectrum

Figure 2.2: Energy and timing resolution spectra

Table2.1 reports the results of the NEMA NU-2-2007 measurements for: spatial resolution, sensitivity, scatter fraction and count rate tests. Plots of count rate (prompts, randoms, trues and NEC), randoms/trues and scatter fraction as a function of the activity concentration are shown in Fig. 2.3.

Figure 2.4, Table2.2 , and Fig. 2.5 show the results obtained for the NEMA image quality, accuracy of attenuation, and scatter corrections tests. Figure 2.4 shows the values for the hot and cold contrast; Table 2.2, the residual lung error and the background variability; Fig. 2.5, representative images of the NEMA IEC Body phantom obtained using different reconstruction algorithms (HD, TOF, PSF, TOFPSF) and number of iterations. As can be seen in Fig. 2.4, TOF shows better hot and cold contrast compared to HD over all the iterations. Furthermore, TOF, particularly for HCRC, reaches its best performance after few iterations (3–5). PSF has a lower HCRC than TOF at a low number of iterations but can

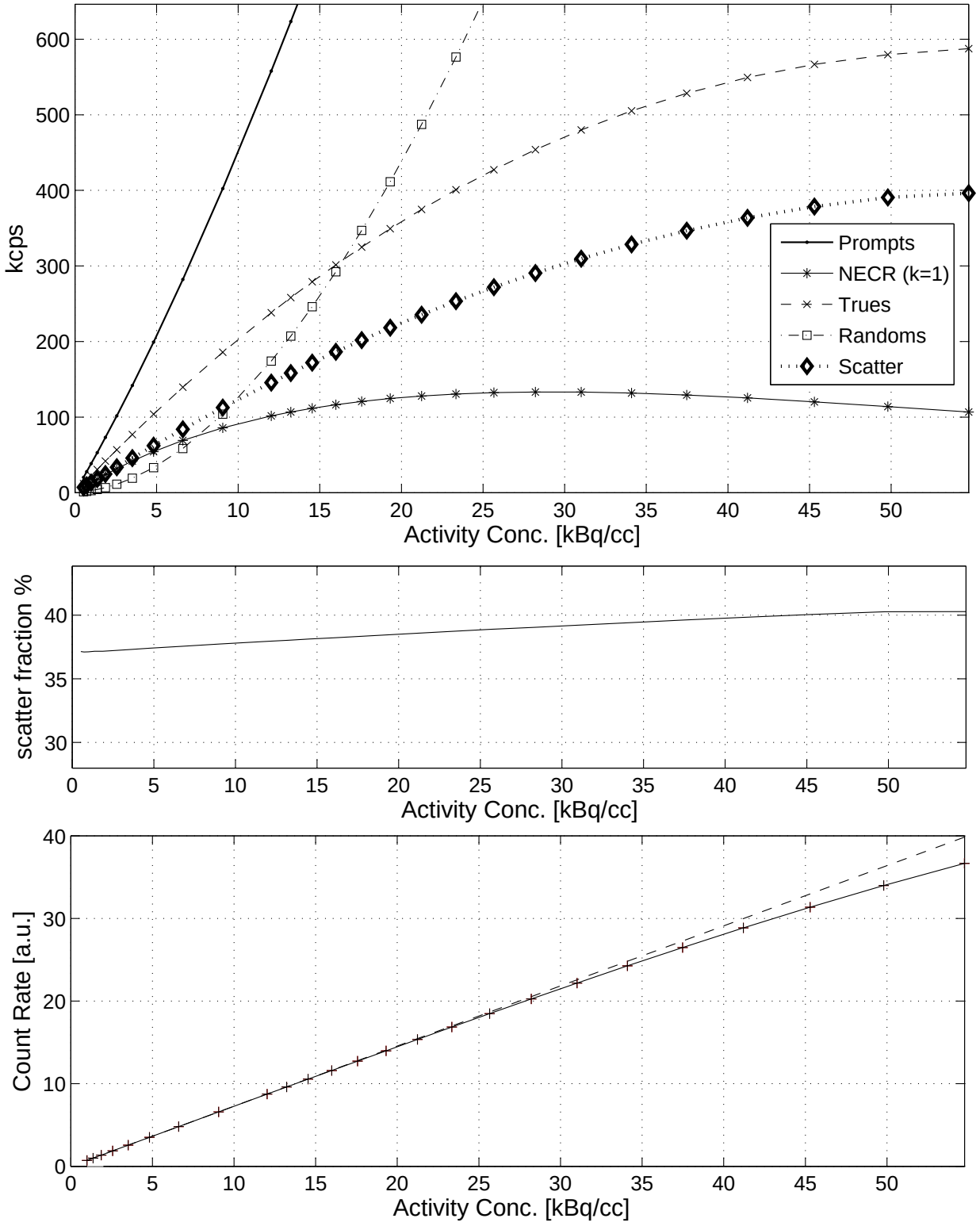

Figure 2.3: NEMA NU 2-2007 count rates vs activity concentration (top), randoms=trues vs activity concentration (middle), scatter fraction (%) vs activity concentration (bottom).

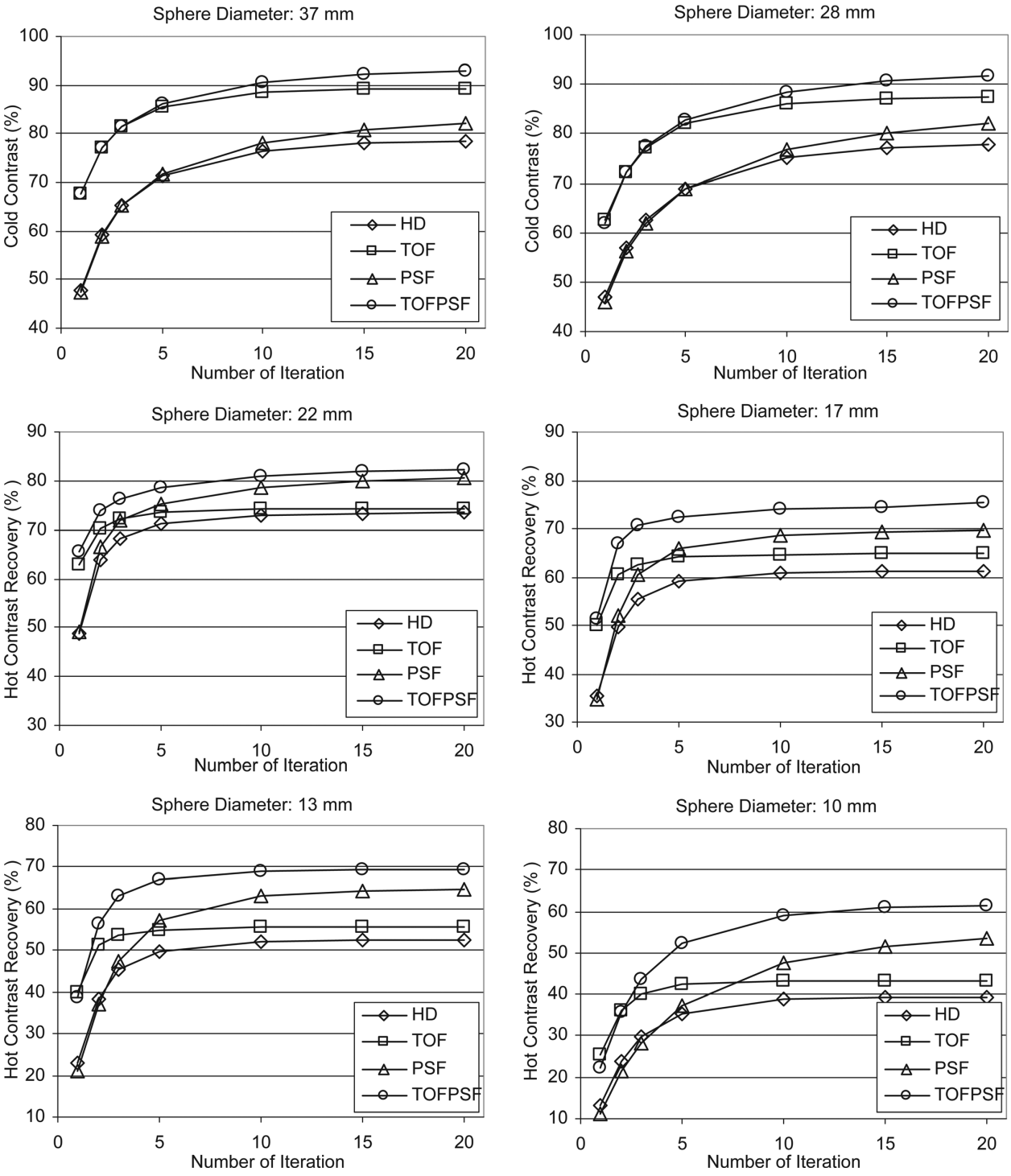

Figure 2.4: NEMA IEC Body phantom: Image quality test (L/B=4:1). Hot and cold contrast vs number of iterations (1, 2, 3, 5, 10, 15, and 20) for different reconstruction algorithms (HD, TOF, PSF, and TOFPSF).

Spatial Resolution(mm)	1 cm	FWHM	Radial and tangential average	4.70
			Axial	4.74
		FWTM	Radial and tangential average	8.83
			Axial	10.91
	10 cm	FWHM	Radial	5.34
			Tangential	4.79
			Axial	5.55
		FWTM	Radial	10.07
			Tangential	8.96
			Axial	11.14
Sensitivity (kcps/kBq)	0 cm			7.4
	10 cm			7.6
Scatter Fraction (%)				37
Maximum absolute error at NECR peak (%)				2.09
Peak NECR (kcps,kBq/cc)				139.1 | 29.0

Table 2.1: Nema-NU-2-2007 results

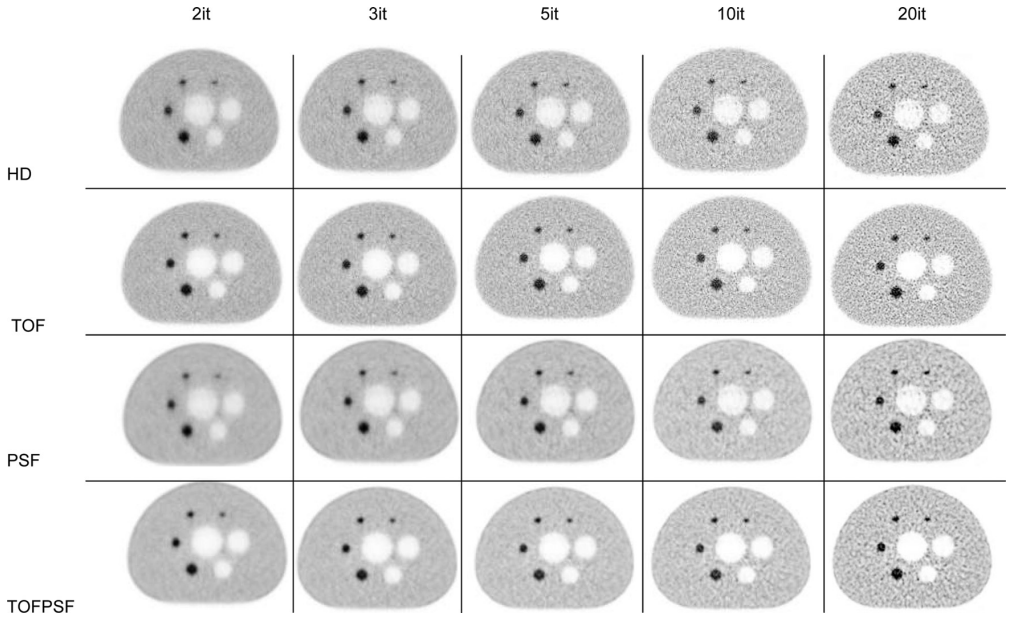

Figure 2.5: NEMA IEC body phantom: Image quality test (activity ratio L/B=4:1). Reconstructed images at: 2, 3, 5, 10, and 20 iterations (from left to right) obtained with different reconstruction algorithms: HD, TOF, PSF, TOFPSF (from top to bottom).

	Lung residual error for scatter and attenuation corrections																					
	HD					TOF					PSF					TOFPSF							
	2it	3 it	5 it	10 it	20 it	2 it	3 it	5 it	10 it	20 it	2 it	3 it	5 it	10 it	20 it	2 it	3 it	5 it	10 it	20 it			
Residual error (%)	29.9	24.1	18.6	14.3	13.4	18.0	9.8	6.5	3.6	1.0	43.4	31.2	25.2	19.7	13.0	18.5	10.1	6.7	3.6	0.4		
	Background Variability																					
	HD					TOF					PSF					TOFPSF						
Lesion diameter (mm)	2it	3 it	5 it	10 it	20 it	2 it	3 it	5 it	10 it	20 it	2 it	3 it	5 it	10 it	20 it	2 it	3 it	5 it	10 it	20 it		
10	4.5	5.5	6.9	8.9	10.3	4.7	5.6	6.7	7.7	8.1	3.8	4.7	6.3	9.0	11.0	4.1	5.0	6.4	8.4	10.5		
13	3.7	4.3	5.3	6.5	7.3	3.8	4.3	4.8	5.4	5.6	3.3	4.0	5.1	6.9	8.8	3.6	4.1	5.1	6.3	7.5		
17	3.1	3.5	4.1	4.8	5.1	3.1	3.4	3.7	3.9	4.0	2.9	3.4	4.2	5.4	6.6	3.0	3.4	4.0	4.8	5.5		
22	2.7	3.0	3.4	3.9	4.2	2.7	2.9	3.1	3.2	3.2	2.5	2.9	3.4	4.3	5.1	2.6	2.9	3.3	3.9	4.4		
28	2.3	2.5	2.7	2.9	3.1	2.2	2.3	2.4	2.4	2.4	2.3	2.5	2.9	3.4	3.9	2.3	2.4	2.7	3.1	3.3		
37	1.9	2.0	2.1	2.2	2.3	1.8	1.9	1.9	2.0	2.0	1.9	2.1	2.3	2.7	2.9	1.9	2.0	2.2	2.4	2.6		

Table 2.2: NEMA IEC Body phantom: Image quality test. Lung residual error and Background variability vs number of iterations (2, 3, 5, 10, and 20) as calculated for different reconstruction algorithms (HD, TOF, PSF, TOFPSF). The results here reported are the mean of three consecutive measurements as requested by the NEMA NU-2-2007 procedure.

achieve higher values as the number of iterations increases (>5), showing also a trend toward possible further HCRC improvement. Cold contrast is dominated by TOF, while HD and PSF have similar but worse performance (see also lung residual error in Table 2.2). Finally, the best results were obtained when both TOF and PSF were used together. In the case of CC, only a slight improvement was observed with TOFPSF compared to TOF alone, while for HCRC, the improvement was more relevant, at both low and high number of iterations. Quantitative results were confirmed by a qualitative evaluation of the corresponding PET images (Fig. 2.5).

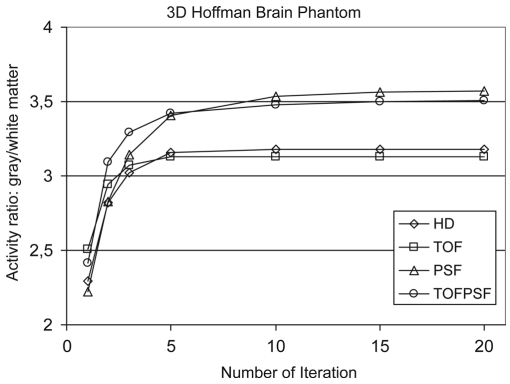

Figure 2.6: 3D Hoffman Brain Phantom. Activity ratio between gray and white matter (expected true value 4:1) vs number of iterations (1, 2, 3, 5, 10, 15, and 20) for different reconstruction algorithms (HD, TOF, PSF, and TOFPSF).

Figures 2.6, 2.7, 2.8, 2.9, 2.10, 2.11, 2.12 show the results obtained using the two phantoms simulating neurological and oncological studies. Figure 2.6 shows the activity ratio between gray and white matter,as calculated on the 3D-HBP, while in Fig. 2.7 representative images of the 3D-HBP reconstructed with different reconstruction algorithms and number of iterations are shown.As can be seen, HD and TOF have similar results (qualitatively and quantitatively) as well as PSF and TOFPSF. The improvement in spatial resolution, which can be seen in the PSF and TOFPSF images (Fig. 2.7, after 5 iterations) is mainly due to the action of PSF. Figures 2.8, 2.9, 2.10, 2.11 show the hot and cold contrast as a function of the coefficient of variation calculated on images of the big "oncological" phantom reconstructed with different algorithms. Figures 2.12, *a* and *b*, show corresponding representative reconstructed PET images for the 200 and 50 Mcounts and activity ratio of 8:1. These results confirm those obtained with the NEMA image quality test. In particular for the high statistic data (200 Mcounts, L/B=8:1 and 4:1, Figs. 2.8 and 2.9), TOF reaches the best results after few iterations (3–5), while more iterations were required (>10) for PSF to achieve similar (in the case of L/B=4:1) or even slightly higher HCRC values than TOF (in the case of L/B=8:1). A similar trend was observed at low statistics (50 Mcounts, L/B=8:1 and 4:1) as can be seen in Figs. 2.10 and 2.11. Similarly to the NEMA image quality test, the best results were obtained when TOF and PSF were used together. This was also confirmed by a qualitative evaluation of the corresponding reconstructed PET images (Figs. 2.12 *a* and *b*).

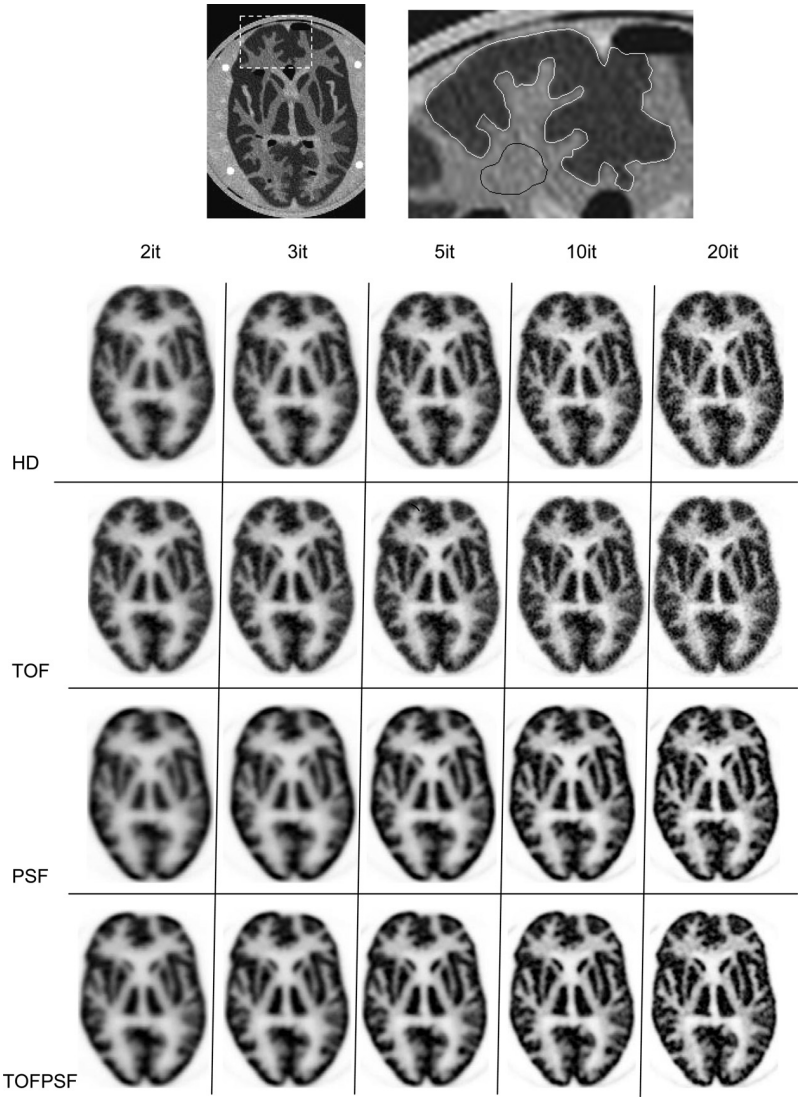

Figure 2.7: 3D Hoffman Brain Phantom. CT image (top) with a zoomed detail (rectangle region defined by the white dashed lines) showing two ROIs drawn on the gray (white ROI) and white (black ROI) matter. Reconstructed PET images at 2, 3, 5, 10, and 20 iterations (from left to right) obtained with different reconstruction algorithms: HD, TOF, PSF, TOFPSF (from top to bottom).

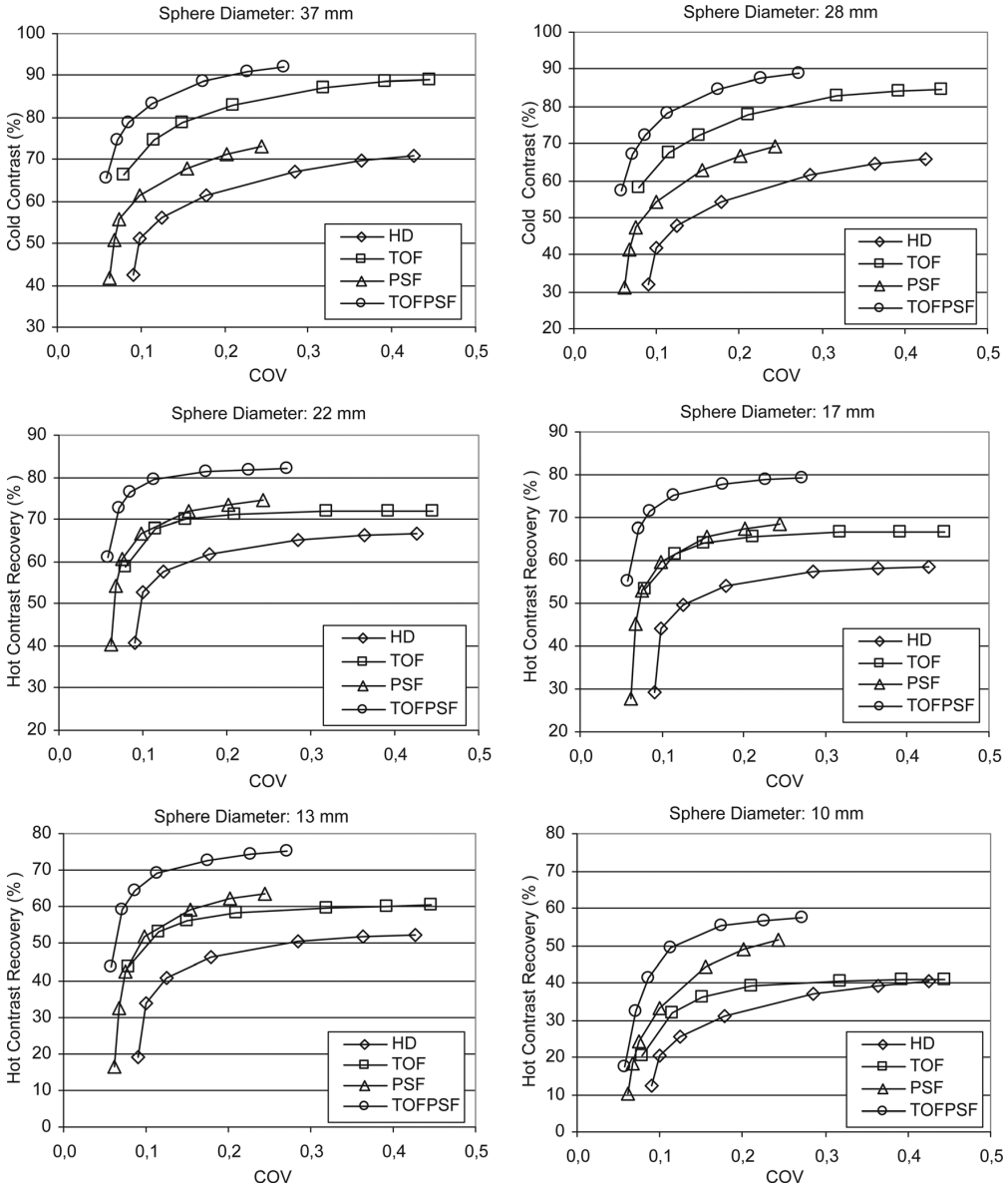

Figure 2.8: Big phantom. Cold and hot contrast (200 Mcounts, L/B=8:1) vs coefficient of variation (COV) for different reconstruction algorithms (HD, TOF, PSF, and TOFPSF) and number of iterations (points of each graph correspond to: 1, 2, 3, 5, 10, 15, and 20 iterations).

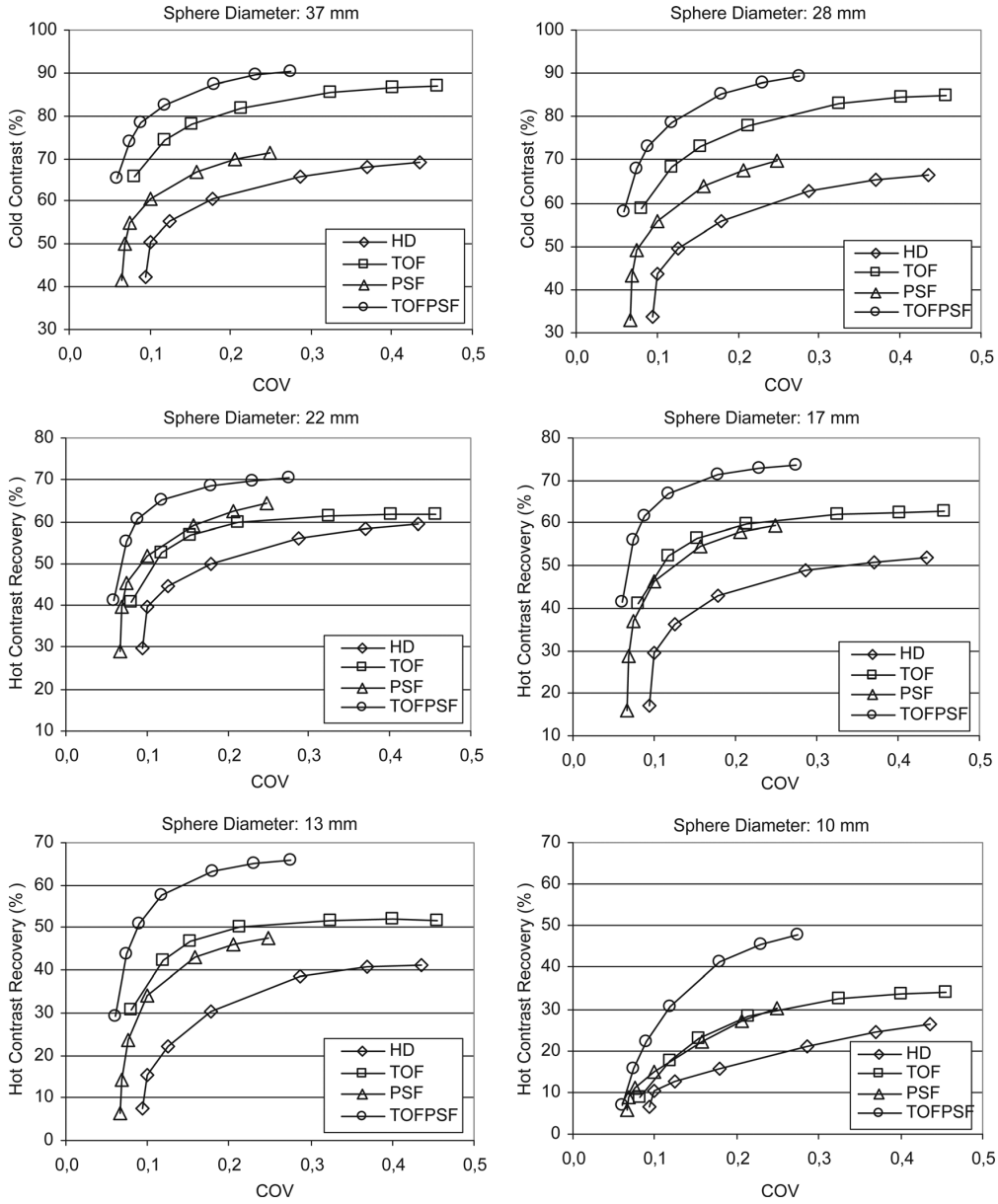

Figure 2.9: Big phantom. Cold and hot contrast (200 Mcounts, L/B=4:1) vs coefficient of variation (COV) for different reconstruction algorithms (HD, TOF, PSF, and TOFPSF) and number of iterations (points of each graph correspond to: 1, 2, 3, 5, 10, 15, and 20 iterations).

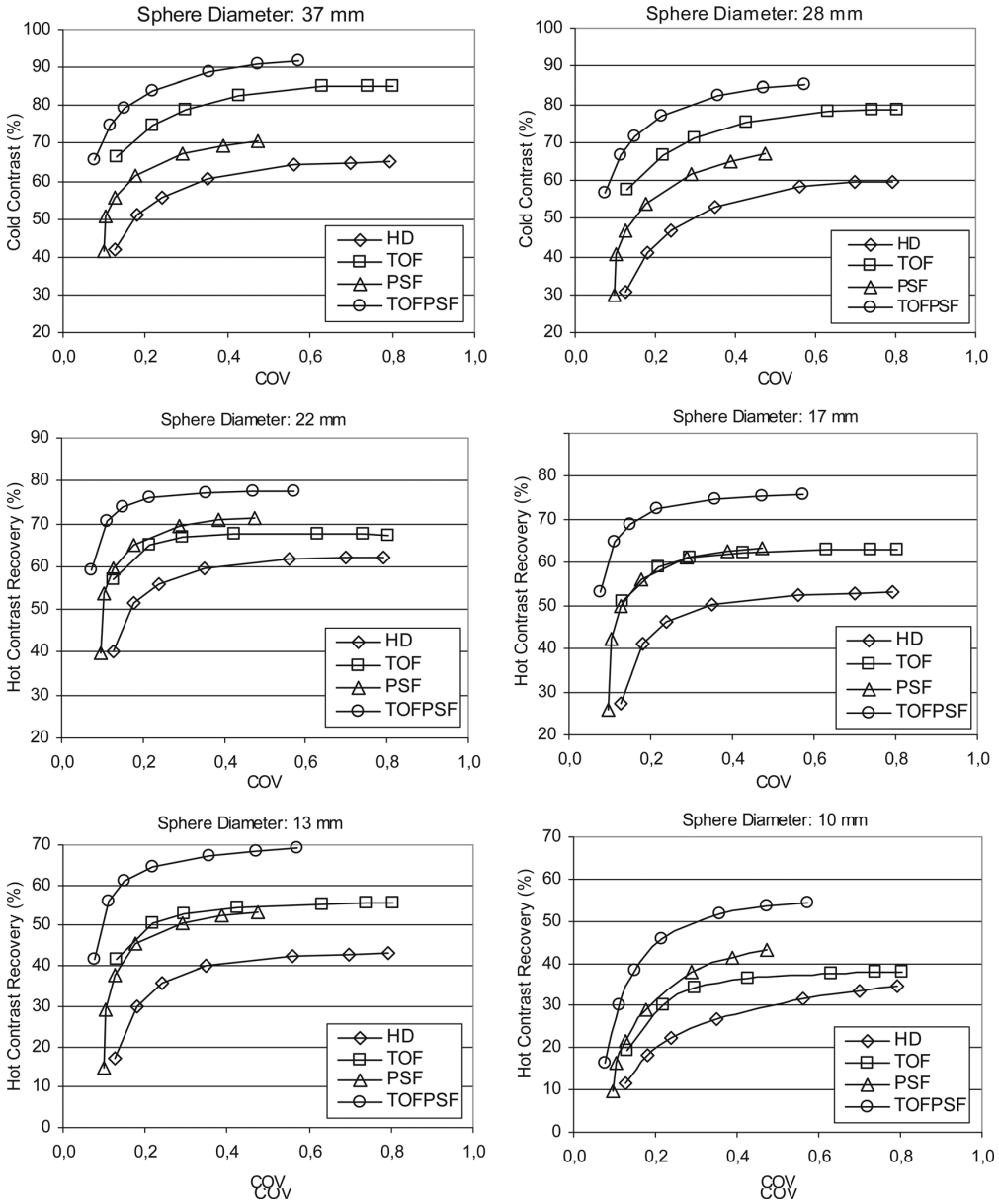

Figure 2.10: Big phantom. Cold and hot contrast (50 Mcounts, L/B=8:1) vs coefficient of variation (COV) for different reconstruction algorithms (HD, TOF, PSF, and TOFPSF) and number of iterations (points of each graph correspond to: 1, 2, 3, 5, 10, 15, and 20 iterations).

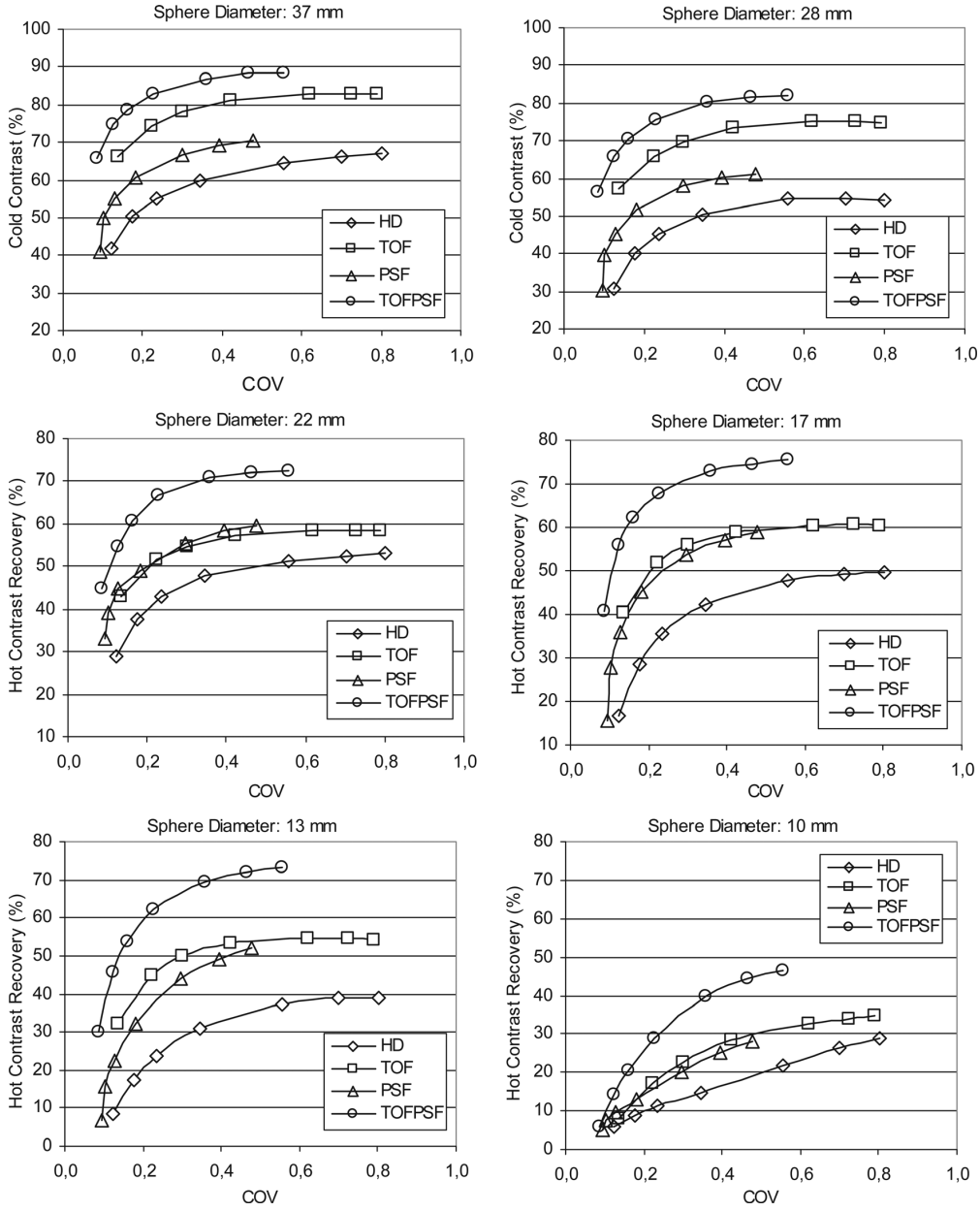

Figure 2.11: Big phantom. Cold and hot contrast (50 Mcounts, L/B=4:1) vs coefficient of variation (COV) for different reconstruction algorithms (HD, TOF, PSF, and TOFPSF) and number of iterations (points of each graph correspond to: 1, 2, 3, 5, 10, 15, and 20 iterations).

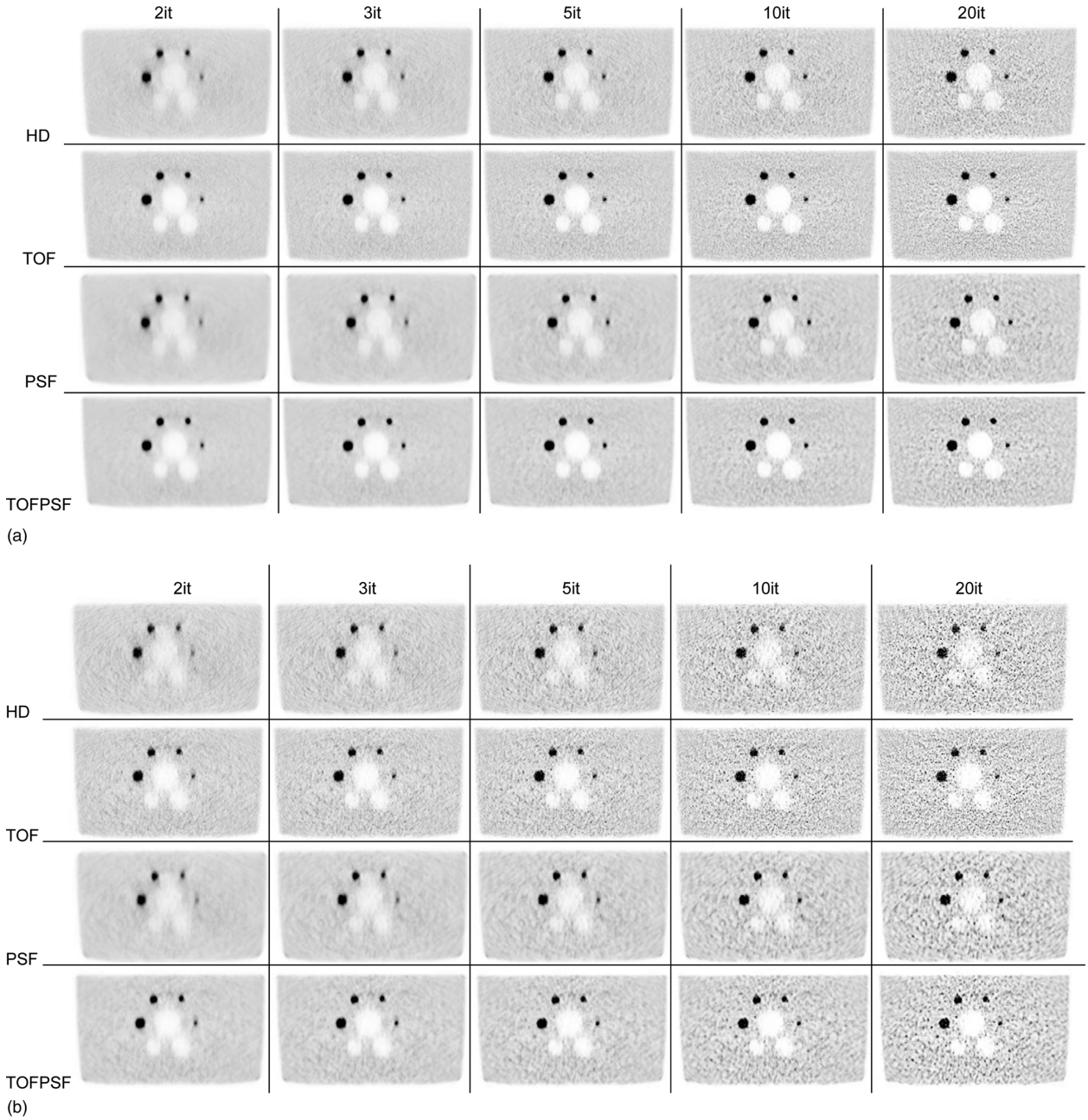

Figure 2.12: (a) Big Phantom (200 Mcounts, L/B=8:1). Reconstructed images at 2, 3, 5, 10, and 20 iterations (from left to right) obtained with different reconstruction algorithms: HD, TOF, PSF, TOFPSF (from top to bottom). (b) Big Phantom (50 Mcounts, L/B=8:1). Reconstructed images at 2, 3, 5, 10, and 20 iterations (from left to right) obtained with different reconstruction algorithms: HD, TOF, PSF, TOFPSF (from top to bottom).

2.4 Discussion

The D-690 scanner belongs to the latest generation of the Discovery PET/CT family (General Electric Medical Systems), which also includes the Discovery-LS, the Discovery-ST, the Discovery-STE, and the Discovery-600. The main difference of the D-690, compared to the other Discovery PET/CT systems, lies in the material used for the PET detectors. In fact, D-690 uses LYSO scintillators while the other Discovery PET systems are based on bismuth germanate (BGO) crystals. The best property of BGO is its higher stopping power (BGO density: $7.13\,g/cm^3$, effective atomic number: 74) compared to the other materials used in commercial PET scanners (e.g., GSO, LSO, and LYSO); however, BGO has a low light output (15%; reference 100% for the sodium iodide-NaI) and a slow decay constant (300 ns) [20]. Instead LYSO offers a good combination of the most important properties. It has high density and high atomic number (LYSO density: $7.1\,g/cm^3$, effective atomic number: 60) for good γ-ray detection efficiency, a high light output (80%, reference 100% for the NaI) for good energy resolution and signal discrimination, and a short decay constant (41 ns) for good coincidence timing resolution and high count rate performances. The drawback of LYSO is represented by its intrinsic component of natural radioactivity due to the presence of ^{176}Lu (with an abundance of 2.6% in natural lutetium), which results in a constant background counting rate. Fortunately, the level of intrinsic radioactivity is very low compared to the typical counting rates found in clinical studies; thus, it does not create any specific practical problem to the functionality of the PET system. D-690 operates only in 3D mode (as the Discovery- 600) as it was designed without inter-plane septa. Their removal allows the reduction of the detector ring diameter, from 88.6 cm (Discovery-ST and Discovery-STE) to 80.1 cm (Discovery-600 and Discovery-690). The reduction of the detector diameter geometrically increases the sensitivity of the PET scanner but, for the same reason, also slightly increases the scatter fraction. The crystal dimensions of the D-690 ($4.3 \times 6.3 \times 25\ mm^3$) are comparable to those of the Discovery-STE and Discovery-600 ($4.7 \times 6.3 \times 25\ mm^3$) thus the spatial resolution is similar (transverse [axial] resolution at 1 cm off axis, D-690: 4.70 [4.74] mm, D-600: 4.9 [5.6] mm, D-STE: 5.12 [5.18] mm) [21, 22, 23]. Sensitivity is lower than in BGO-based Discovery systems (D-690: 7.5 cps/kBq, D-600: 9.6 cps/kBq, D-STE: 8.8 cps/kBq, D-ST: 9.12 cps/kBq) [21, 22, 24] due to (i) lower intrinsic detection efficiency of LYSO compared to BGO and (ii) the shorter crystal (BGO: 30 mm, LYSO: 25 mm). The most relevant performance of the D-690, compared to the BGO-based Discovery systems, is its higher count rate performance (D-690: 139.3 kcps at 29 kBq/ml; D-600: 75.2 kcps at 12.9 kBq/ml, D-STE: 67.6 kcps at 12.1 kBq/ml, D-ST: 66 kcps at 14.8 kBq/ml) [21, 22, 24] which is due to the faster decay constant of LYSO compared to that of BGO. Furthermore, the coincidence timing resolution of the D-690 (544.3 ps) allows TOF information to be used in the reconstruction of PET data to improve the signal-to-noise ratio in the PET images, as it has already been shown in several other publications. Another important reconstruction improvement available with the D-690 and D-600 systems is represented by a 3D model (shift variant) of the point spread function of the PET tomograph. In fact, the PSF model can be used, during the reconstruction of the PET data, as an "inverse" effect to recover the degradation of the spatial resolution due the PET system.

In the D-690, both TOF and PSF can be taken into account in the reconstruction scheme

with the aim of improving the image quality and quantitative accuracy of the PET images, therefore we have extended the evaluation of image quality beyond the standard NEMA NU-2-2007 test (with the NEMA IEC Body phantom). Two other phantoms were used, representative of different clinical conditions (brain and whole body) in terms of radioactivity distribution and source dimensions. For each phantom, four different reconstruction algorithms (HD, TOF, PSF, and TOFPSF) were employed to evaluate the relative effect, particularly for TOF and PSF, when used independently or in combined action.

The analysis of the 3D-HBP reconstructed images (activity ratio between gray and white matter) shows that the main contribution to signal recovery came from PSF (fig 2.6,2.7). The PET images reconstructed with PSF showed a better definition of the "anatomical/functional" structures of the brain than those obtained without PSF modeling (at least for more than five iterations). The TOF impact on the 3DHBP images showed slightly better results in the first two/three iterations, but after that no further improvements were observed, not even compared to the standard HD. Similar considerations can be done for TOFPSF vs PSF reconstruction. These findings are explained by the relatively "small" dimension of the 3D-HBP (diameter 18 cm, height 12 cm) where the TOF action is not expected to have significant advantage over non-TOF reconstructions.

The results obtained by the analysis of the NEMA IEC Body phantom and the big "oncological" phantom show a general agreement even if a direct comparison is not possible. In fact, for the NEMA IEC Body phantom, 2D ROIs have been used to calculate the hot and cold contrast, while 3D VOIs have been used for the analysis of the big oncological phantom data. Nevertheless, in both cases, the results show that TOF clearly improves the performance of the reconstruction algorithm with respect to the conventional one (i.e., HD). Furthermore, few iterations (3–5) are needed with TOF to reach its nearly best performance, with a noise level comparable to HD. After that, only an increase of the noise with no further improvement of the signal was observed. These results are in agreement with those previously found by other authors [12]. Regarding the PSF reconstruction, it can improve signal recovery to a level similar to, or even better, than TOF, but this can be achieved only with more iterations (>5), particularly for small lesions and when the signal-to-background ratio is low (see Figs. 2.8,2.9,2.10 and 2.11 for the L/B=8:1 and 4:1). This is very important for the practical application of PSF because only few iterations (3) are often used in clinical situations to keep the reconstruction time compatible with the clinical context. In such conditions, the recovery effect of PSF would be modest, both qualitatively and quantitatively. For cold "signals" (cold sphere), TOF clearly has the best performance compared to HD and PSF, as can be seen in the reconstructed images (Figs. 2.5, and 2.8-2.11). On the other hand, the "convergence" of TOF for CC is slower than for HCRC (as expected) but comparable to that of non-TOF algorithms (e.g., HD).

Another difference we noted between TOF and PSF images was the noise appearance in the corresponding reconstructed images. In fact, TOF images show typical random noise, very similar to that of HD, while the noise in the PSF images has a more "correlated" appearance. This qualitative difference has a correspondence in the two parameters, BV and COV, each describing the noise characteristics in the reconstructed images. While BV does not really change very much for the different reconstruction methods (with worse results for the PSF), COV shows more difference among the reconstruction algorithms (with best results

for the PSF). This reflects the fact that BV tells more about local region-to-region variation (image uniformity) than noise dispersion, better represented by COV. These results are in agreement with those obtained by Tong et al. who, in particular, studied the noise properties in PSF based PET image reconstruction [25]. The difference in the noise characteristics could play an important role in terms of lesion detectability, particularly at high noise levels, and this would be worth further studies in the future.

Finally, the best results were always obtained when TOF and PSF were used at the same time. In fact, using TOF and PSF together allows them to take advantage of each other. Indeed, TOF improves the signal-to-noise ratio as a consequence of the more accurate events positioning, but it does not improve the spatial resolution, which is the main goal of PSF. Thus, if TOF acts as an "accelerator" for the convergence of the signal, PSF can recover a better signal at a lower number of iterations, introducing, at the same time, a "filtering" effect which contributes to reduce the noise in the reconstructed TOFPSF images.

2.5 Conclusion

The Discovery-690 shows very good PET physical performance for all the standard NEMA NU 2-2007 measurements. Furthermore, the new reconstruction algorithms available for PET data (TOF and PSF) allow further improvements of the D-690 image quality performance, both qualitatively and quantitatively.

Chapter 3

An anthropomorphic static phantom

After the characterization of the scanner and the analysis of its performances for neurological and oncological applications it followed an analysis focused on cardiac studies. The first step that faced was the analysis of the ability of the reconstruction algorithms to recover the true activity concentration in a realistic static phantom. Particular relevance was posed on the effect of TOF and PSF modeling. Few references exists on this topic, with a single paper addressing the effect of PSF modeling on the reconstruction for cardiac applications [26] and none, as of today to our knowledge, on TOF or combined TOF-PSF. No phantoms are assumed as the standard to assess PET or SPECT performances in cardiac applications. Starting from a commercial phantom, the RH-2 torso phantom (Kyoto Kagaku co. ltd), modifications were put in place to achieve a more realistic results. The original version features different compartments to model lungs, mediastinum, two ventricles and the left myocardial wall. Two improvements were added to the original design. In the original version the the lung compartments cannot simulate a radioactive uptake, which is often not negligible. The second limitation is the absence of a liver component, which, during a cardiac study, is the second most active organ in the FOV. A new compartment was added to simulate the liver, thus making this phantom more realistic.

3.1 Materials and Methods

3.1.1 Modification to the phantom

Lungs In the original version of the RH-2 phantom the lung inserts are filled with sawdust to achieve a density comparable to human lungs. The drawback of this material consists in the practical impossibility to simulate an uptake. The sawdust was removed to create a more flexible condition. The empty lung regions were then filled with spongy polymer inserts of the same shape. Before being used in the phantom these inserts can be immersed in a water solution, eventually containing a radiotracer. After being squeezed the "lungs" retained a part of water. The density of the squeezed "lungs" with a residual of water inside is such that its average CT number is about -830 HU (fig. 3.1). In case of a radioactive solution also the tracer is retained along with water thus simulating a physiological uptake.

Liver Another issue in cardiac studies is related to the presence of the liver in the same FOV. Usually the liver has an high activity, comparable to that of the heart itself. The original phantom did not include a liver insert therefore, in our modification, a second right lung insert was built; this time featuring an hole in the middle where a dedicated container, to simulate the liver, can be inserted. This container, volume 552 ml, can be filled with a radioactive solution to simulate liver activity. An image of the phantom with the introduced modifications is shown in figure 3.1.

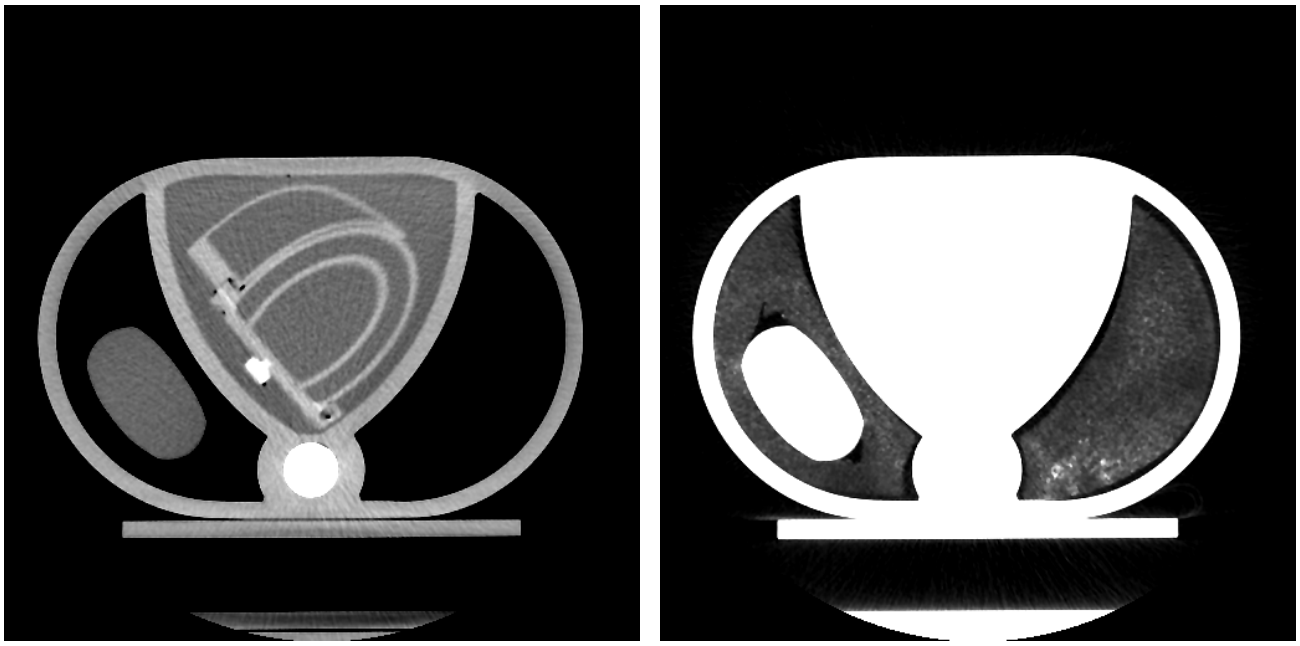

(a) CT W/L scale: 400/40 **(b)** CT W/L: 1000/-550

Figure 3.1: Modified heart phantom. In sub-figure a) the heart and the added liver can be appreciated and in sub-figure b) the lungs and the sub-structure of the polymer used are appreciable.

Heart defects To have regions of no uptake, simulating perfusion or metabolism defects, small parallelepipeds of silicon material which can be placed everywhere within the myocardium wall were built. The two sizes that we built were $40 \times 20 \times 10\,mm^3$ and $20 \times 20 \times 10\,mm^3$.

3.1.2 Phantom preparation

To evaluate the performance of this PET scanner for cardiac applications and of the new reconstruction algorithms different phantom configurations have been used in three experiments.

3.1.2.1 First experiment

The first experiment was devoted to the study of the capacity to PET tomograph to cope with very high count rates. (e.g. Those typically found in the bolus pass of $^{13}NH_3$ study). The main limitation is usually posed by the dead time of the detector, but also the fraction of random counts is specially high. The aim of this experiment was to check the accuracy of the corrections for these phenomena.

For this experiment the cardiac phantom was used in its original configuration. Instead of the heart insert a spherical container (volume $359\,ml$) was put in the mediastinum compartment . The phantom was positioned in the centre of the PET scanner FOV. The spherical container was filled with $18\,mCi$ (calibrated to the scan start) of $^{13}NH_3$ and quickly positioned in the phantom. A PET Emission scan (list mode) was immediately started to follow the decay of the tracer for 120 min (12 half-lives). At the end of the emission study a CT scan (140 kV, 90 mAs, 3.75 mm slice thickness, 3.27 mm slice spacing) was performed for attenuation correction.

With this amount of activity, all in the center of the scanner FOV, we achieved a peak count rate of $10\,MC/s$. This should be compared to the patient scans that never exceeds $4\,MC/s$, with our injection protocol of $10\,mCi$ of$^{13}NH_3$ (as defined in chapter 8). During patient studies the total activity is never concentrated in the center of the FOV, therefore the system response is tested on a wider range of activity concentration than it is found in clinical settings.

3.1.2.2 Second experiment

The second experiment was performed to simulate the distribution of the activity in the condition of the first pass of the tracer (bolus). The problem investigated here is the ability of the different algorithms to recover the cold contrast of the myocardium. Specifically, as in the previous chapter it was found that TOF increases very much the speed of convergence of cold objects and that PSF modeling is effective in reducing partial volume effect, we wanted to investigate the ability of each algorithm to recover the true activity concentration and to assess the optimal number of iteration to use. For this experiment the RH-2 phantom was used in the modified configuration but with no liver in place, (i.e. all of the left lung filled with the lung tissue). The phantom was filled with $^{18}F - FDG$. The two ventricles were filled with the same solution of $17.1\,kBq/ml$ while the mediastinum was filled with a solution of $9.95\,kBq/cc$. The myocardium was left cold. Lungs adsorbed a solution out of which they retained an average activity concentration of $4.9\,kBq/cc$. These ratios were chosen to be representative of a standard situation during the first frames of an $^{13}NH_3$ study. Once filled the phantom was positioned on the scanner bed and centered in the FOV. A CT scan (140 kV, 90 mAs, 3.75 mm slice thickness, 3.27 mm slice spacing) was performed followed by a PET scan (list mode) of 10 minutes. A total of 132 millions of prompt counts were collected
.

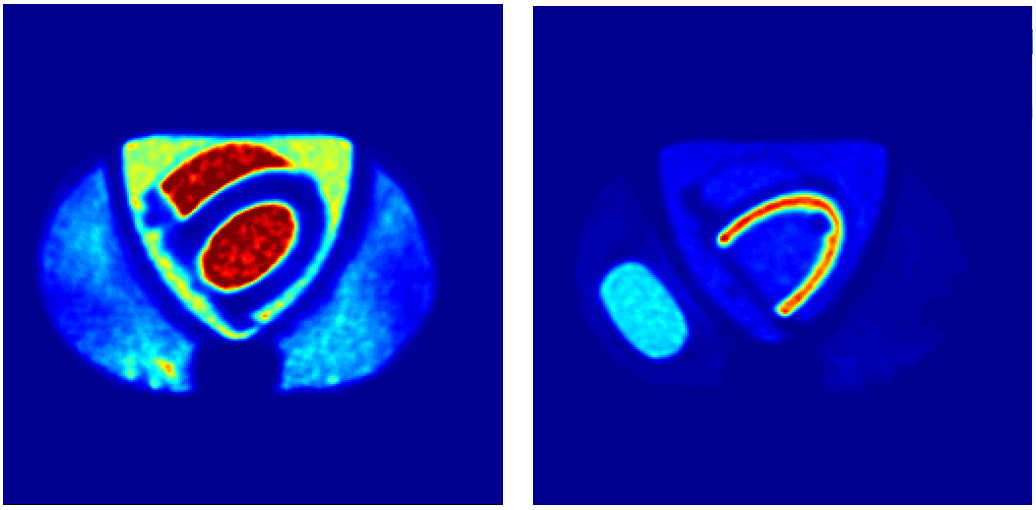

(a) Second experiment **(b)** Third experiment

Figure 3.2: A transaxial slice of the phantom in the second and in the third experiment.

3.1.2.3 Third experiment

The third experiment focuses on the opposite condition, the one representative of a steady state of $^{13}NH_3$ or $^{18}F-FDG$ studies. During this phase the healthy myocardium is the most active tissue in the PET FOV. In the previous chapter it was shown that usually hot objects converge differently from cold ones, therefore this experiment aims at optimizing the reconstruction protocol in this condition. It should also be noted that in the steady uptake phase the liver often has also an average activity quite close to the myocardium and falls inside the same FOV, potentially disturbing the reconstruction. This condition was replicated using the modified version of the RH-2 phantom with a 7 : 1 myocardium to mediastinum activity ratio and a 2 : 1 myocardium to liver activity ratio. To achieve this situation the myocardium was filled with a $54\,kBq/ml$ $^{18}F-FDG$ solution (activity calibrated at the time of the scan), the mediastinum with a $7.9\,kBq/ml$ solution and the liver with $26.8\,kBq/ml$. The lungs had an average activity of about $2.5\,kBq/cc$. These values are representative of those typically found in patients. Two cold defects (simulating infarcted regions) were put in place using the silicon parallelepipeds previously described. The first one ($40 \times 20 \times 10\,mm^3$) was located in the mid-anterior area while the other one ($20 \times 20 \times 10\,mm^3$) in the apical inferior area. Once filled the phantom was positioned on the scanner bed and centered in the FOV. A CT scan (140 kV, 90 mAs, 3.75 mm slice thickness, 3.27 mm slice spacing) was performed followed by a PET scan (list mode) of 15 minutes. A total of 262 millions of prompt counts were collected, an amount comparable to what is collected in the last 15 min of an $^{13}NH_3$ study.

3.1.3 Data processing of the acquired raw data

First experiment The list raw PET data was sorted in 25 dynamic frames with the following scheme:

- 10 frames 1 minute long, 2 minute inter-frame delay
- 12 frames 2 minutes long, 3 minutes inter-frame delay
- 3 frames 5 minutes long, 5 minutes inter-frame delay

Second experiment As the PET raw data have been acquired in list mode a second set of emission data corresponding to 4 millions of prompt counts were extracted. This low statistic data simulate a 10 s frames of a dynamic scan.

Third experiment From the 15 min PET raw data 8 independent new raw data scans were generated. Each new scan had about 35 million counts. Such statistics correspond to the amount of statistic collected in each frame of a gated study, with 12 cardiac gates. This strategy was implemented to have an estimate of the statistical error on the mean value of the radioactivity concentration measured in the different VOIs during data analysis.

3.1.4 Data reconstruction

Every set of data was reconstructed using a common procedure on the acquisition console, before being transferred to a computing workstation for further analysis. The common setting for all the reconstructions was:

- Reconstruction FOV: 35 cm diameter
- matrix size: 256x256 The voxel size was thus 1.37x1.37x3.27 mm3
- Number of subsets: 18
- Number of iterations: 1,2,3,5,10
- Transaxial post filter: Gaussian, 2 mm FWHM
- Axial post filter: average filter with weight coefficients [1,4,1]

For the first experiment only 3 reconstructions were performed, as the aim was only to check the corrections accuracy at high count rates and not the overall reconstruction performance. Dead time correction is applied on raw data. Randoms should be implemented in the same way in all the iterative algorithms, so it was decided to perform a reconstruction also with a reprojection algorithm. Scatter correction is implemented differently in TOF and non-TOF algorithms. In the end the algorithms used were HD (non-TOF) and TOF (introduced in chapter 2) with 3 iterations and 3D-reprojection (3D-RP) with an hanning filter of 4.3 mm (the smallest for this scanner given the Nyquist limit).

As before in the other cases the algorithms used were 4 : HD with and without PSF modeling and TOF with and without PSF modeling. In this chapter the four reconstruction will be referred to as HD, PSF, TOF and TOFPSF.

3.1.5 Analysis program and VOI definitions

After being transferred to the analysis workstation in DICOM format the images were analyzed using a software written ad-hoc in MATLAB.

First experiment A large VOI containing all of the volume 1 cm inside the borders of the hot area was used. The same VOI was transferred on all the frames of all the different reconstructions. The average value in the ROI was saved together with the mid-point of the scan to calculate the average activity present in the FOV in that frame.

Second and third experiment VOIs were defined for different types of regions that are commonly analyzed in cardiac studies. For each area the mean activity and its standard deviation were calculated. To avoid biases in positioning due to the low spatial resolution of PET images the VOIs were drawn on CT images and then transferred on the corresponding spatially coregistered PET images.

Mediastinum and Liver In the case of the mediastinum and the liver a single VOI was defined for each of the two districts. It was very large and positioned far from edges as well as from hot or cold objects to avoid as much as possible partial volume effect.

Right and left ventricles Two VOIs were positioned in the centres of the right and left ventricles and another one in the centre of the left ventricle, both over multiple slices.

Myocardium The analysis of the myocardium proceeded trough a VOI that was drawn on the CT image. This VOI comprehended the whole myocardium thickness, walls excluded. It also excluded the area of the two defects.

Lesions Two VOIs were drawn in correspondence of the two simulated lesions.

Figures of merit To assess the quality of the reconstructed images the following figures of merit were defined to be used.

- The ratio between the mean activity concentration in a VOI and the same quantity as calculated while filling the phantom (through activity measures in a well counter and volume measurements). Used to quantify the reconstruction precision.

$$A.R. = \frac{a_{meas}}{a_{true}}$$

- Coefficient of variation: Ration between the standard deviation between all the pixels in a VOI and the mean activity in the same VOI. Used to quantify image noise.

$$COV = \frac{sd(a_{VOI})}{mean(a_{VOI})}$$

- Cold contrast: ratio between the mean reconstructed activity in a VOI (put over a region where activity is not present) and the reconstructed activity in a VOI of a reference neighboring region.

$$CC = \frac{a_{Cold,meas}}{a_{hot,ref}}$$

3.2 Results

3.2.1 First experiment

This experiment showed that the D-690 is well suited for cardiac dynamic studies. With 15 mCi of activity in the middle of the FOV there is a quantification error of less than 10%. With the protocol in use (Chap. 8) the injection for our kinetic studies consists in 10 mCi of $^{13}NH_3$ over 20 s. Also they do not arrive at the same instant at the center of the FOV. Therefore we can guarantee a very limited error introduced by the high count rate in the first frames of the study. The activity measured in the HD reconstruction overlaps with the one measured in the 3D-RP; with TOF the trend is different. The expected trend of no deviation from the expected value is found with HD and 3D-RP while the activity in the FOV is limited ($< 5\,mCi$), followed by a decrease at higher concentrations. Results are reported

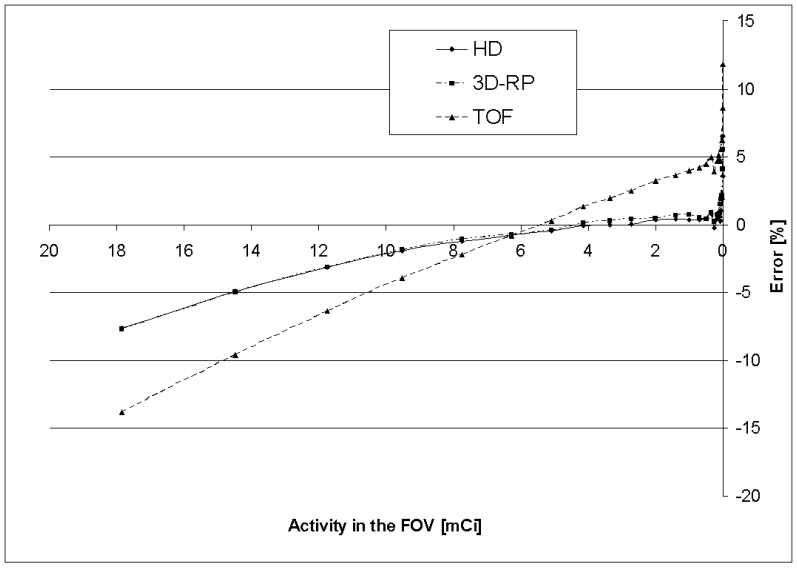

Figure 3.3: Ratio of measured activity over true activity at various concentrations in the FOV

in figure 3.3. It is possible to note that at extremely low concentration values ($< 0.05\,mCi$) the measured activity is overestimated (+3% for HD and FBP, +8% with TOF). It should be noted that in the range of activities encountered in a dynamic $^{13}NH_3$ study with our protocol the quantification errors introduced by imperfect corrections is limited to less than 5%.

3.2.2 Second experiment

Large structure, as the mediastinum, have very limited variations with differing number of iterations. In all the range of investigated iterations the *A.R.* remains limited between 90% and 98% for all the algorithms, with different trends. For the mediastinum all of the algorithms converge to comparable values. These trends are are shown in figure 3.4. In this

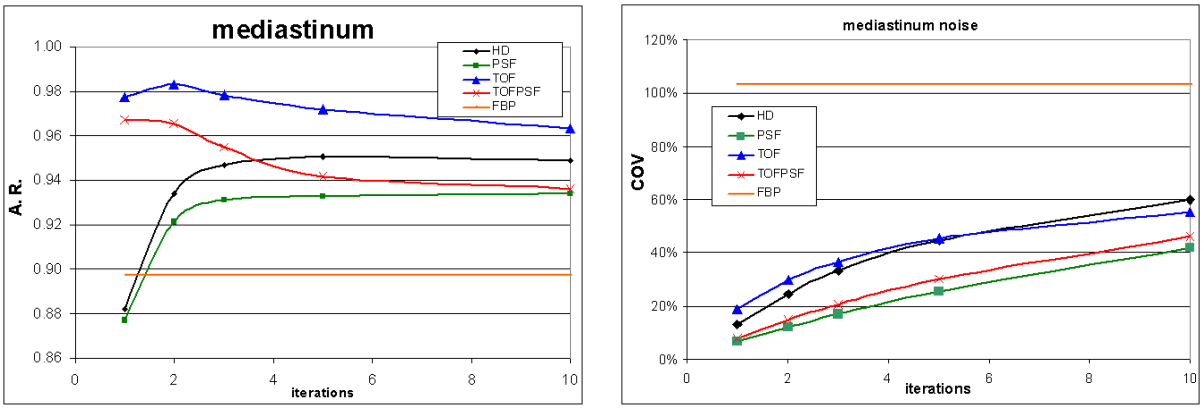

(a) Activity Ratio **(b)** Coefficient of Variation

Figure 3.4: Measured activity ratio (a) and noise (b), as COV, in the mediastinum.

figure also the noise, quantified as the COV, is reported.

The myocardium has more interesting proprieties, being small (compared to PET resolution). In this experiment it is cold, and this is known to lead to slower convergence with iterative algorithms (e.g. see Chap. 2). The results, at both statistics, are reported in figure 3.5. At a low number of iterations TOF markedly speeds the convergence, while PSF modifies the trends at higher number of iterations. Their combination provides the best result.

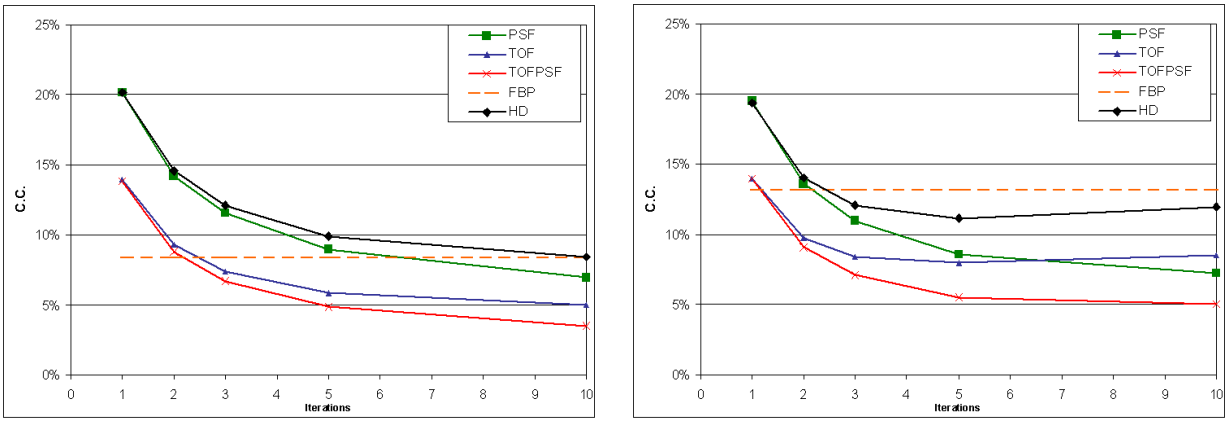

(a) Full statistic **(b)** Low statistic

Figure 3.5: Cold contrast of the myocardium, for full (a) and low (b) statistic.

An indication of noise can be found by the COV of large uniform regions against which the object of interest contrasts. In figure 3.4 the trend for the mediastinum is shown. The ventricles show similar trends. It is possible to note that 3D-RP has the highest noise. For iterative algorithms COV increases almost linearly with the number of iterations. The addition of PSF reduces the amount of noise, TOF and HD algorithms have almost the same noise level at every iteration.

3.2.3 Third experiment

In this experiment the same results are observed for the full statistic reconstruction and for the set reconstructed from a lower counts set. This probably indicates that at this level of counts no bias is introduced. Selected results are reported in figure 3.6.

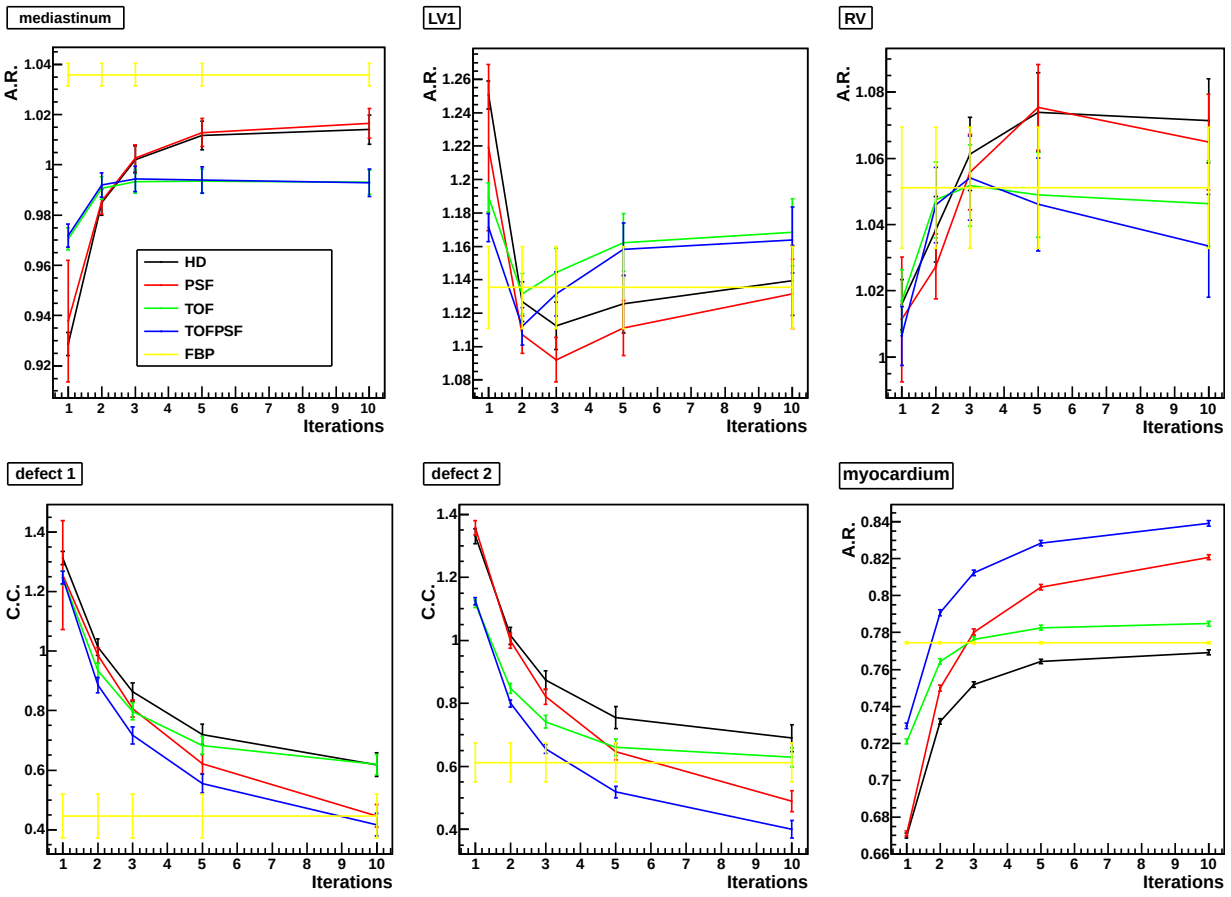

Figure 3.6: Activity Recovery or Cold Contrast (where appropriate) in the third experiment, when analyzing the reduced statistics set.

Large regions, as the mediastinum and the ventricles, keep similar values between all the algorithms and iterations number. In the mediastinum, as an example, $A.R.$ is comprised 92% and 102% in all of the cases.

Both the LB and the RV converge to values higher that the one measured in the well counter. The RV value is compatible, within the errors, on the activity concentration mea-

sured in the well counter. Instead the LV is significantly higher, also when compared to activity measured in the RV.

The analysis of the myocardium, the object of cardiac PET studies, shows the most interesting features: TOF increases the convergence speed of the algorithm (i.e.: for $N_{it} \leq 3$ algorithms with TOF have markedly higher $A.R.$) while PSF reduces spill-out at an high number of iterations (i.e.: for $N_{it} < 3$ the difference between algorithms with and without PSF is negligible, and increases with increasing iterations). At low iterations TOF and TOFPSF show similar trends, as HD and PSF do between them, while at an higher number of iterations HD approaches TOF values while PSF approaches TOFPSF.

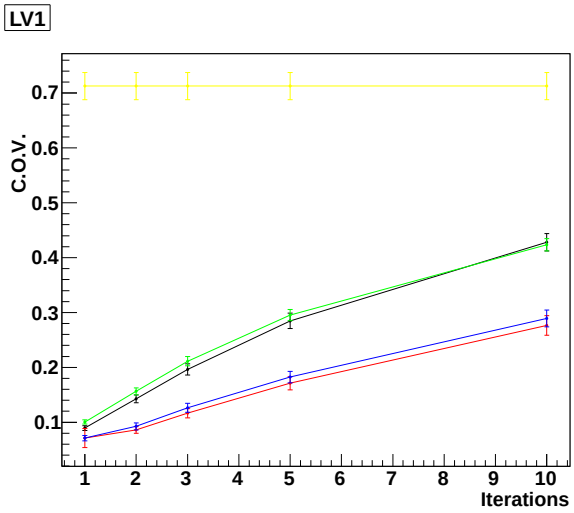

Figure 3.7: Noise (as COV) in the Left Ventricle.

In the two defects it appears that the relative important of TOF and PSF is variable, but in all of the cases their combination gives the best results. In this situation, dealing with smaller and cold objects, the convergence is slower.

For the noise we analyzed the COV inside the Left Ventricle (which has a similar behavior to the mediastinum, not reported), shown in Fig. 3.7. As in the second experiment iterative algorithms show an increase in noise that is almost linear with the iterations while 3D-RP has a markedly increased noise. Also here it can be noted that HD and TOF have similar noise levels, as PSF and TOFPSF but with at lower values.

3.3 Discussion

The first experiment shows that the PET scanner considered can behave well in the experimental situation of a dynamic scan, over a wide range of activity concentrations in the FOV and can cope with high count rates. The second experiment showed that the combination of TOF and PSF gives the best results, as TOF speeds up sensibly the convergence of the algorithms, particularly in cold regions, therefore the spill-in in the cold myocardium is minimized. It also appears that most of the signal is recovered in 5 iterations, increasing to an higher number of iteration would mainly increase the noise with only marginal gains in

terms of signal recovery. The analysis of the third experiment showed similar results: TOF increases the speed of convergence and PSF minimizes partial volume effect. Also in this case our optimal reconstruction algorithm appears to be TOFPSF at 5 iterations. This allows an almost complete recovery of the signal in the myocardium, a very good recovery of cold defects and a limited amount of noise.

Chapter 4

A dynamic myocardial phantom

While the results obtained with the previous phantom are useful for the optimization of the reconstruction protocol and for the assessment of the problems introduced by the limited spatial resolution of the PET technology they are not completely representative of PET cardiac imaging. It has been reported that respiratory motion can move the anterior wall of the heart up to $15\,mm$ while the beat itself moves the walls of the heart of more than $7\,mm$ [42]. These motions are bigger than the spatial resolution of the technique and they are also bigger or comparable to the thickness of the myocardial wall. Therefore, to assess the effect on the quality and on the quantitative accuracy of PET images a phantom capable to simulate these movements was needed. A number of phantoms specifically designed for cardiac applications have been proposed for CT [27, 28, 29], MRI [30] and PET/SPECT [31, 32, 33, 34, 35, 36, 37] studies. Most of them simulate the dynamic behavior of the heart beat, but very few are designed to account for both cardiac and respiratory motion [36, 37]. Taken this into account it was decided to design and build one specifically suited to our needs.

4.1 Mechanical Part

As the myocardial wall of the left ventricle is the target of the PET studies a phantom representative of this part of the heart was designed and build. In particular the LV model is composed by two compartments, separated by walls made of thin (˜1-2 mm) silicon gum. This material is very elastic and therefore suitable to build a volume that can be inflated and deflated many times while preserving its shape.

The inner cavity represent the blood pool of the left ventricle while the external one represents the myocardial wall. The shape chosen is that of half ellipsoid. The short axis for the inner cavity is 49 mm wide while the long axis is 82 mm long (Fig. 4.1). Therefore when not inflated the volume of our "left ventricle" is about 160 ml. The outer cavity replicates the same shape at 10 mm distance. The inner cavity is inflated by a pumping syste which in turn stretches also the outer one. The two cavities (internal and external) have they respective apical region connected by a small pin of the same material. This constraint allows the relative position of the two compartments during heart beating to be maintained. Two small tubes (inner diameter 3 mm) have been attached to the base of the LV to fill the

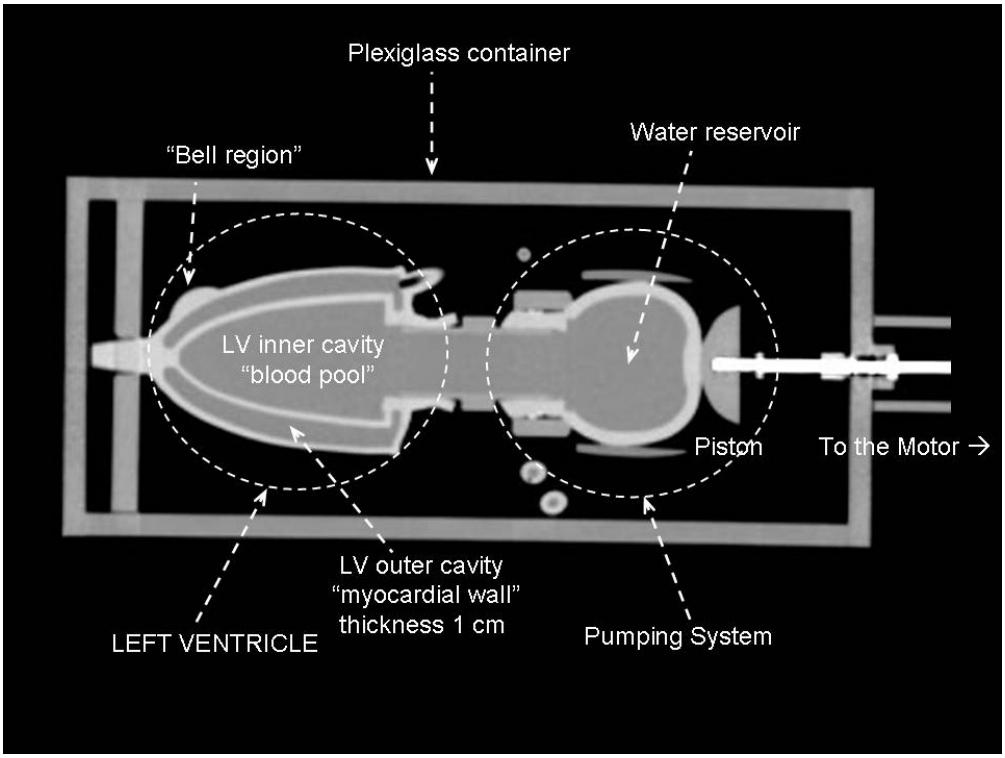

Figure 4.1: CT coronal slice of the dynamic heart phantom

myocardial wall (Fig. 4.2). The two tubes are located at the opposite sides of the phantom. In this way the lower tube can be used to inject "cold" or "hot" (radioactive) water while the upper one acts as a vent. This allows an easy filling of the cavity without the risk of leaving air bubbles inside.

A pumping system (Fig. 4.1) inflates the inner cavity; this in turn stretches the outer one changing both the volume of the LV as well as the thickness of the "myocardial wall", thus simulating the diastolic phase. Furthermore, to simulate myocardial defects, i.e. areas of reduced uptake, two "bell" regions have been created on the surface of the phantom. These "bell" regions can be independently inflated, by using a normal empty syringe attached to each "bell" (see Fig. 4.2) to produce a local pressure on the surface of the phantom. Depending on the pressure applied, the thickness of the myocardial wall can be compressed from a mild condition up to a full occlusion (Fig. 4.2). The two "bell" regions are positioned one in the basal infero-lateral area and the other one in the apical anterior area. The LV is enclosed in a waterproof container to prevent contamination in case of phantom breaking (Fig.4.3). The container can also be filled with liquid to simulate background uptake, photon attenuation and scatter around the myocardium. The inner dimension of the box is $320 \times 130 \times 150\, mm^3$.

4.1.1 Motor and pumping system

The part simulating the LV blood pool is connected with a pipe of 22 mm diameter to another a balloon used as a water reservoir. A piston pumps on this area and the water pumped out of this reservoir goes to inflate the heart simulating the systole/diastole sequence. The

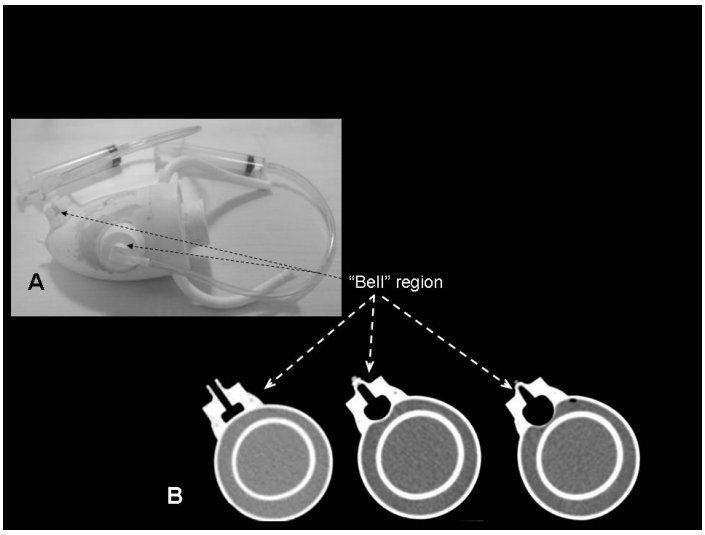

Figure 4.2: Details of the heart phantom. A) The silicon heart phantom. On the surface of the heart phantom the two "bell" regions (connected to the syringes used to inflate air) can be seen; B) CT transaxial section of the LV showing one of the two "bell" region. Note how different levels of inflated air can simulate different level of defects.

piston is attached to a gear-motor placed outside of the waterproof box (Fig. 4.1 and 4.3) . This connection is performed with a crank/handle system connected to a wheel attached to the motor. The crank can be attached at different radii of the wheel to achieve different pumping volumes.

4.1.1.1 Torque need estimation

A simple experiment was carried out to estimate the force needed to transfer all the liquid in the reservoir volume to the LV compartment, inflating the whole myocardium. Weights were added on top of this compartment until it was completely deflated. Three kg had to be added. Therefore the torque to be provided by the motorwould have to be at least of the order of magnitude of $\tau = F \times r$. As the outermost position to connect the crank to the wheel of our motor has a 2 cm radius, the requirement was set for a motor able to provide at least 60 Ncm of torque. To account for a safety factor and to allow the motor to work in a range far from its maximum performance a motors with a torque at least 4 times this value was searched.

Motor Given the previous technical considerations the motor was chosen to have the following characteristics:

- DC, low voltage power supply
- High torque (minimum: 240 N cm)
- Speed 60 rpm at least

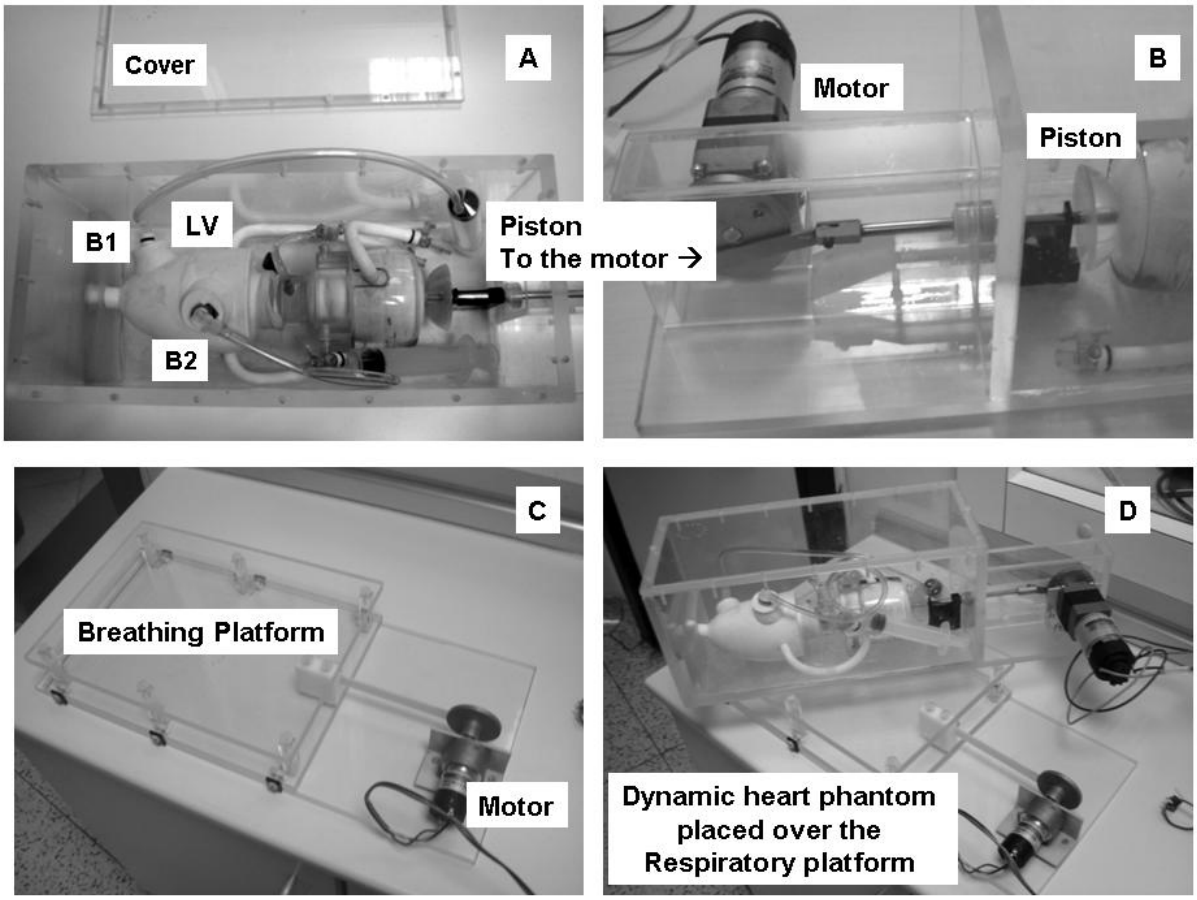

Figure 4.3: Images of the heart phantom. A) Frontal view of the heart phantom where it can be seen: the LV, the "bell" regions (B1 and B2), the pumping system, the piston connected to the motor, the container of the phantom and its cover; B) Detail of the motor and the piston; C) Breathing platform and its motor; D) Whole view of the heart phantom positioned over the breathing platform.

- Position encoder

The final choice was an epicycloidal gearmotor by Micromotors s.r.l., model : P205.39.24 It features a 350 Ncm torque, 24 V, 77 rpm at maximum torque, 105 rpm with no load, and a bipolar hall-effect encoder. The power rating for this motor is 51 W, 2.2A of current at 24 V.

4.1.2 Electronic circuit:

The electronic circuit has to perform two functions: provide a synchronized three-leads ECG signal and control the speed of the motor. This is needed from the PET point of view to simulate a gated acquisition, where the PET system infers the current phase of the cardiac cycle from an ECG signal. The circuit, that starts from a 24V stable power supply, can be seen as divided in four blocks:

1. Power distribution
2. Microcontroller (for speed control, position encoder reading and ECG synchronization)
3. ECG-signal generation
4. motor driver

The power distribution has a standard structure. It features high capacity capacitors to stabilize the different requirements of the motor during its cycle (in half of the cycle it has to pull with an increasing force, during the other half it is pushed) and smaller capacitors to filter faster spikes. The 24 V input is directly forwarded to the motor driver section and a 5V line is derived, using a 7805 IC rectifier, to feed the microcontroller and the logic units working at TTL levels.

Motor driving The most sensible way to instantaneously vary the power output of this kind of motors is to use Pulse Width Modulation (PWM). A convenient way to do this is to use an IC consisting of an H bridge. The choice fell on the National Semiconductor LMD 18200. It is rated for up to 3A continuous current (our motor has a nominal current absorption of 2.1A) and up to 55V of supply voltage. It features two power input pin and three command inputs (PWM, direction and brake).

Hall encoder reading An hall encoder varies its output voltage according to the magnetic field to which it is subject. To detect the speed of a motor a magnet is positioned on its shaft and two sensors placed 90° apart sense its field. It can be easily read using a TTL logic as shown in figure 4.4. From the sequence of the triggers it is possible to detect the direction of the motion while from the spacing between each trigger it is possible to detect the current speed of the motor.

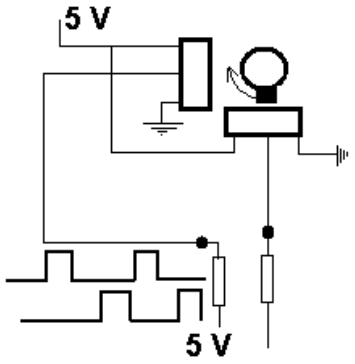

Figure 4.4: Scheme of the Hall-encoder and its TTL reading circuit.

ECG signal generation A typical ECG signal is about 2 mV wide and can be described as composed by a first large peak followed by an almost straight line with small variations occurring. A full and accurate simulation can be accomplished only by digitally sampling a realistic wave and playing it back, stretching and modifying it according to the current speed of the motor. This would have been extremely complex, technically. It should be noted that standard PET/SPECT gating ECGs uses the signal only to find the start of a new cardiac cycle, analyzing the peaks of the wave. Therefore I designed a circuit that produces a realistic enough signal with a lo-fi synthesis technique. The system used is schematized in figure 4.5. The synthesis is performed with a 3 bits resolution. In the DAC I did not use uniform resistor values but different ones, with the most significant bit producing a 3-fold voltage increase compared to the other bits. The DAC is followed by an RC low-pass filter, with extreme R and C values ($R = 4.7M\Omega,\ C = 0.47\mu F$). This produces a cutoff frequency of about $f_c \approx 2\,Hz$, much smaller than the frequency content of our signal (the complete signal is cyclic with ˜1 Hz frequency and the whole QRS complex lasts less than $100\,ms$). This allows

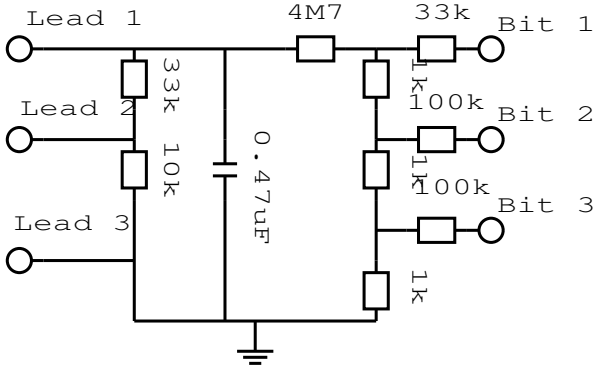

Figure 4.5: Schematics of the ECG signal synthesizer

to obtain a smooth signal from few square steps given in output from the microcontroller. The resistor values chosen in the DAC already reduce the voltage from 5V to about 150 mV. This filter additionally reduces the peak voltage to less than 2 mV, the same amplitude of

the ECG trace read in an actual patient. To generate a 3-leads signal the output ECG wave is replicated at a smaller amplitude, with a simple partitor, on lead 2. Lead 3 is grounded. In this way the trace reading L1-L2 of the ECG gives the highest signal.

The concept for the signal synchronization is to generate the QRS complex each time a cardiac cycle restarts, then producing the other traces of the ECG wave and finally setting to a baseline value while waiting for the cycle to end. This is similar to the human case where there is no electrical activity (and therefore no ECG signal) in the end-diastolic phase, before the polarization phase restarts, seen as the P-wave. To generate values inferior to this baseline this is set to the value corresponding to bit state 010; in this way negative peaks (like the Q or the S peak) can be generated with 000 (or 001). The typical output from the microcontroller therefore looks like in Fig. 4.6 (a), while the actual trace read from the ECG looks like in Fig. 4.6 (b). An actual ECG trace from a patient is shown, for comparison, in Fig. 4.6 (c).

Microcontroller: The requirements for the microcontroller were:

- A dedicated port with interrupt functionality to read the hall encoder signals
- Another port with 3 outputs for the ECG simulation
- A PWM generator to drive the motor
- At least two timers (on top of the one used for PWM generation) to control the speed of the motor and to time the ECG signal bits
- Two other bits to control the brake and direction inputs of the motor driver IC

The final choice was an 18 pin PIC, the 16F819, that features 4 I/O ports (of 4 bits each) 3 timers and a PWM generator (the PWM signal is generated by TMR2, therefore leaving only the two other timers free for other uses).

Microcontroller program description The program was designed giving priority to the reading of the motor encoder. I chose to use interrupts and to connect the two encoders to PORTB, where Interrupt On Change (IOC) can be enabled. In this way any state change on any of the two waves triggers an interrupt. The two other bits of the port were grounded to avoid any interrupt induced by electromagnetic interference. The main code was divided into two sections: parameters setup and steady functioning. At the beginning of the "steady functioning phase" a QRST ECG wave is produced and then the signal is set to a constant value. Here the program waits for the motor to end a complete turn. This is done reading a counter that is set during interrupt cycle. When a complete turn has been performed a P wave is generated on the ECG signal output and then the loop starts again with the QRST wave.

The interrupt section measures the time occurred from the previous interrupt, that should be constant in case of constant speed. This is compared to a prescribed value (that can be constant through the cycle or can be varied) and accordingly alters the PWM duty cycle to increase or decrease the motor power. This is fundamental since the motor needs much

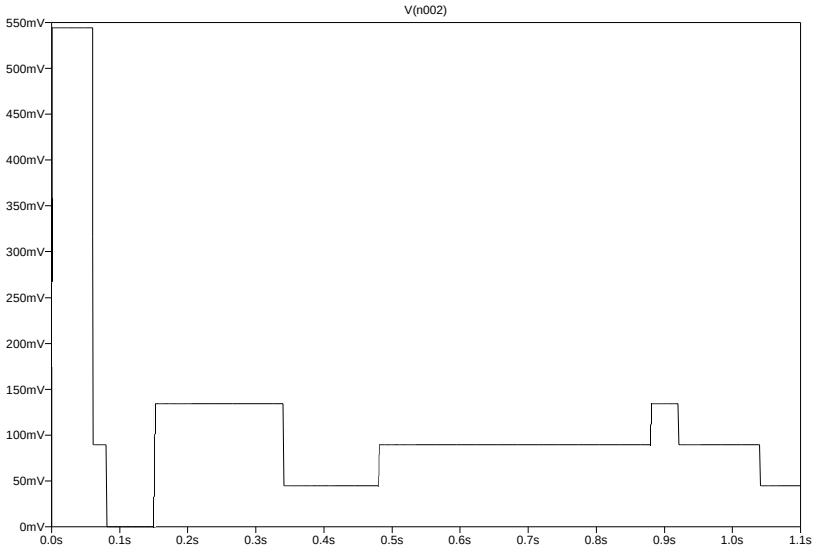

(a) Output from the DAC of the microcontroller

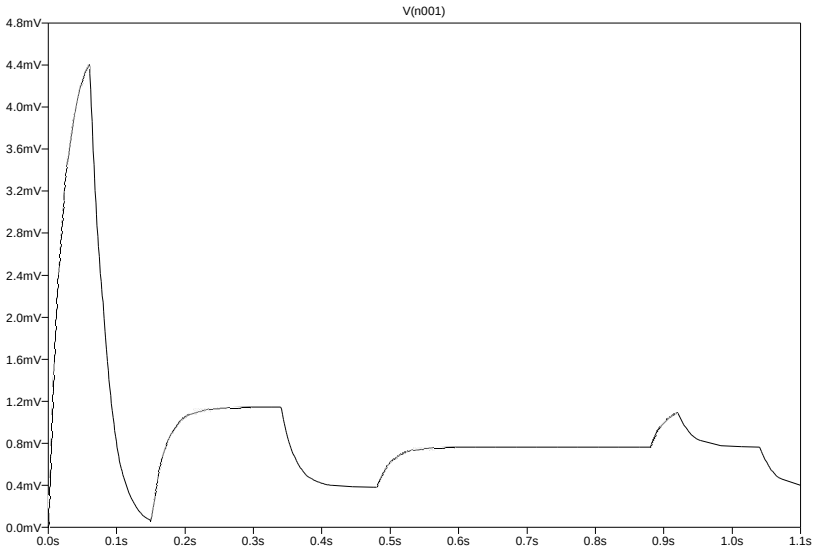

(b) ECG signal after the low pass filtering

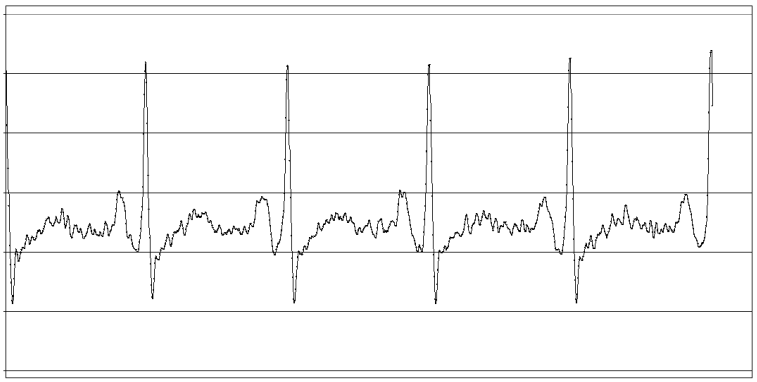

(c) Actual ECG trace from a patient, shown for comparison

Figure 4.6: ECG signal synthesis for the dynamic phantom

torque while inflating the LV and, conversely, is pushed in the deflating phase. Without this speed control the motor would be too fast in half of the cycle and too slow in the other half. The last part of the interrupt routine increase the counter of the acquired interrupts so that the main routine can know when a whole cycle has been completed.

4.2 Respiratory platform

To simulate the motion induced by breathing, a moving platform was designed and built. It is constituted by two Plexiglas planes: i) a bottom plane of $49 \times 22 \times 1\,cm^3$ and ii) an upper plane of $30 \times 22 \times 1\ cm^3$ (Fig. 4.3 c). The bottom plane lies on the scanner bed. The top one has a set of Delrin wheels that move inside tracks drilled in the bottom plane, to ensure repeatable movements. The top platform is connected to a gear-motor, trough a crank/handle mechanism (Fig. 4.3 d) that can be attached to the wheel of the motor at 3 different radii to simulate movements of 10, 15 and 20 mm. The motor is a MicroMotors RH 158.12.200, with 33 rpm max speed with no-load, 23 rpm at max-load. For this motor no electronic speed control was implemented. Varying the voltage of the power supply is sufficient to achieve any breathing periods between 10 and 2 seconds.

To simulate the respiratory motion on the heart phantom this can be simply positioned on the upper plane of the respiratory platform (as in Fig. 4.3 d) resulting in a solidale "respiratory" motion.

Chapter 5

Gating techniques

To obtain images free from motion artifacts the most used technique is "gating". The basic assumption for this technique is that the motion under investigation is cyclical. If a signal that indicates the current "*phase*" of one of these "*cycle*" can be found than all of the emission events that happened in the same phase interval, in many different cycles, can be grouped to form a common "gate", as schematized in figure 5.1. The first application to achieve widespread clinical use is cardiac gating, which is the simplest to implement and which provides cardiac motility information. These techniques were implemented as early as 1975 [38, 39].

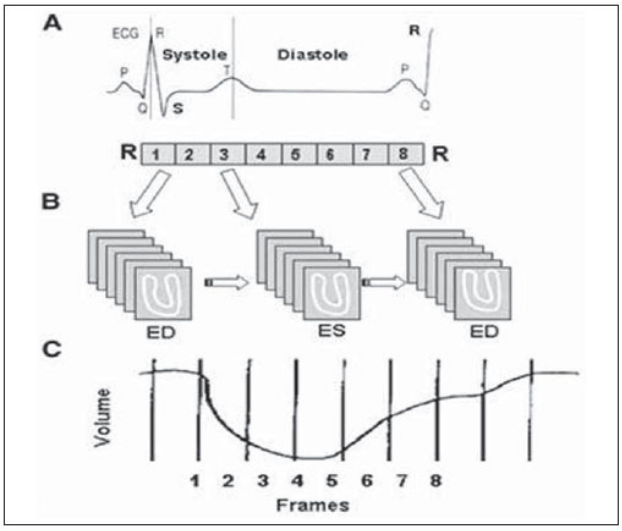

Figure 5.1: General concept of cardiac gating

While the influence of respiratory motion was also inferred quite early, as reported in 1982 [40], respiratory gating techniques were not proposed until much later, one of the first feasibility studies being published in 2004 [41]. The combination of cardiac and respiratory gating, even if suggested by the aforementioned 1982 study [40], was not implemented until the year 2000 [42] and that still today is not mature for routine clinical application.

5.1 Motion in imaging studies

In fast imaging modalities, like X-RAY planar imaging or CT-scans, it is common to ask the patient to hold his breath. for the time of the study. This is done with the aim to avoid respiratory motion artifacts and image quality degradation. Most of the patients can hold their breath comfortably for at least 30 seconds, enough for a complete thorax-abdomen CT scan. Cardiac motion is more difficult to address. The average heartbeat for a resting patient while lying is about 60 *bpm* therefore, to achieve a motion free image, one should acquire the full image in less than $\sim 250\,ms$ (i.e.:1/4 of the cardiac cycle, exploiting the staticity of the heart in the diastolic phase).

In emission tomography current technology does not allow the acquisition of an high enough level of counts in so short amount of time. Future scanners with increased sensitivity and coincidence timing resolution of $\sim 300\,ps$ should allow the acquisition of a diagnostic grade image in $\sim 40\,s$ and therefore should allow the acquisition of images during breath-hold, resolving breathing related motion problems.

With current and past technologies to achieve motion-free images, in nuclear medicine, a different strategy has to be used. The current one is based on gating. This is based on the assumption of a cyclic periodic motion of the process under analysis. Under this hypothesis an indicator of the "phase" of the cycle should be found and then it is assumed that at the same "phase" the organs being imaged are back at the same position.

Prospective or retrospective gating Two gating modalities are possible: prospective and retrospective. Both are driven by some kind of "monitor" which tracks the phase of the motion under analysis.

In prospective gating, multiple fixed partitions covering the whole breathing/cardiac cycle or a single specific partition (eg, end of the expiration, end of the diastolic phase) are set before starting data acquisition. Data acquisition is then triggered by the acquired signal. Nowadays prospective gating with a single partition is the acquisition technique most commonly used to obtain motion-free images representative of a specific moment of the physiologic process. Conversely, in retrospective gating, data are collected during the whole breathing/ cardiac cycle and only subsequently sorted into the established number of partitions, according to the recorded signal.

In transmission imaging modalities (like CT) the situation is different. Acquiring data continously implies irradiating the patient when the information might not be needed. New technological developments made it possible to use high intensity short current bursts, in the x-ray tube. This has the great advantage of avoiding the irradiation of the patient when the information acquired is not required. This allows a mean dose reduction of 69%, from 11 mSv to 3.5 mSv [44].

5.2 Cardiac gating

Gating was first applied to cardiac motion [39, 40]. On top of providing very useful information for the clinician, e.g. cardiac motility, it could be implemented with few technical difficulties. The physiological signal which can be exploited is the natural electrical activity

of the heart. The monitoring of cardiac movement is well established and codified. The cardiac electric activity, which is itself responsible of the heart beating, is the ideal signal to monitor and track heart contraction and motion. When the sinus-atrial node fires, the electrical impulse that moves towards the atria causing their contraction, is recorded as a 'P' wave on the electrocardiogram (ECG). The electrical impulse then moves to the atrio-ventricular node and afterward crosses the ventricles, causing their contraction. The 'PR' interval and the 'QRS' complex are therefore recorded on the ECG. The final return of the ventricles to the rest condition generates the 'ST' segment and the 'T' wave. All of this phases are schematized in the "Wigger diagram" shown in figure 5.2. When interfaced to the

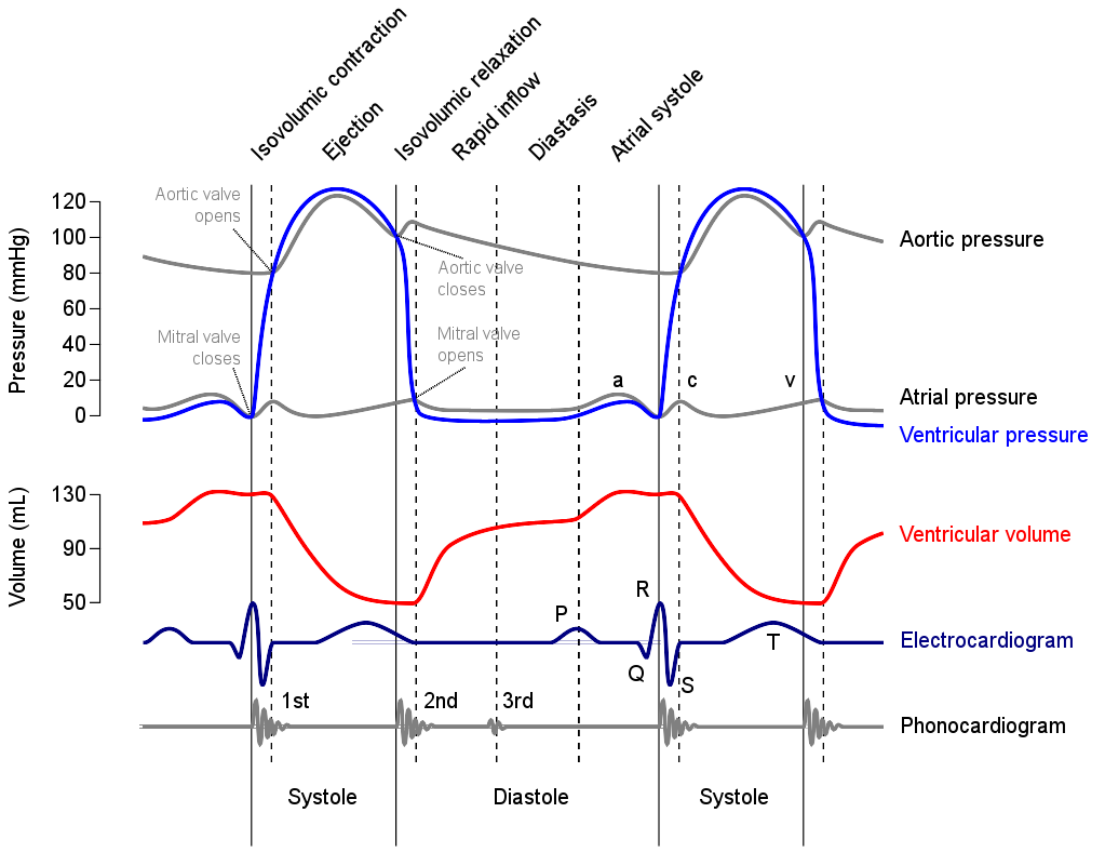

Figure 5.2: "Wigger diagram", showing the relation, in a normal heart, between ECG signal, electrical activity, cardiac volume and physiological states

PET or CT imaging system, the electrocardiograph provides trigger signals to synchronize the data acquisition to the cardiac cycle, as shown previously in figure 5.1. In particular, trigger pulses are usually generated in correspondence of the R peaks. When cardiac gating is performed in prospective mode, data acquisition starts after a specific delay following the R-wave (usually after the QRS complex) and then lasts for a defined percentage of the cardiac cycle (e.g., 80%). When instead gating is performed in retrospective mode, data are collected over the whole cardiac cycle and successively sorted. In order to obtain 4D cardiac images free from artifacts, a regular and low cardiac frequency is required. Usually

auto-feedback and/or breath hold manoeuvres can help the patient in reducing his heart frequency. Otherwise, pharmacological regularizators (e.g. beta blockers) must be used.

5.3 Respiratory gating

Breathing is not associated with a well codified physical effect that can be easily detected from outside the patient therefore, to assess the phase of this cycle, several Motion Tracking Systems (MTSs) have been designed. Differences essentially concern the kind of physiological signal monitored (e.g. air flux, lung volume, abdominal displacement) and the signal processing method. From this perspective two families of signal interpretation has been developed: phase or amplitude divisions. In phase-based gating, each cycle is divided in a defined number of partitions (phases) by considering only the temporal information associated to the signal, independently from its amplitude. This type of data processing has been demonstrated to work well for patients with regular respiratory cycle but results in motion artifacts with patients having irregular patterns [45, 46]. On the contrary, amplitude-based gating techniques divide the total respiration amplitude into different gates (bins) independently on the time information associated to the signal. It has been shown that amplitude gating techniques are more robust than phase gating techniques, thus allowing for a better suppression of motion artifacts [45, 46].

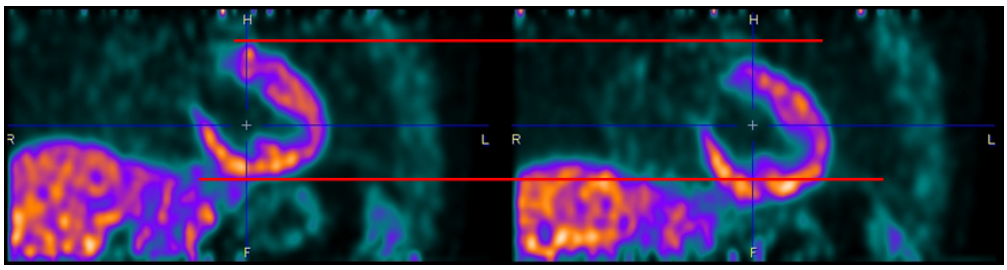

Figure 5.3: Example of the effect of respiratory motion in a cardiac PET study

Alternatively to gating, breath hold (BH) methods have been recently proposed for oncologic applications, in which the patient is asked to hold his breath with the aim to achieve organ immobilization:

- at a specific moment of the breathing cycle (e.g., end inspiration, end expiration etc. . .)
- for a predefined time duration (e.g., 10 s, 20 s, as long as possible, etc..) [47, 48].

5.3.1 Breathing motion

Breathing is an active process requiring the contraction of skeletal muscles. Muscles mainly involved in respiration are the external intercostal muscles and the diaphragm. During inspiration such muscles contract inducing a raising of ribs and sternum and a drawdown of diaphragm, corresponding respectively to a front-to-back and vertical increase of the thoracic cavity dimension. The consequent reduction of the air pressure in the lungs determines the

entry of the outside air. During expiration muscles relax, diaphragm, ribs and sternum return to the rest position, thus restoring the thoracic cavity to the pre-inspiratory volume. The consequent air pressure increase in the lungs forces air emission. The design of a Respiratory MTS (RMTS) can rely on monitoring the physiologic signal associated to the internal changes of the lungs volume or to the external changes in the shape of the thoracic or abdominal region [49, 50]. While the first solution is directly associated to the physiologic process of respiration, the second one detects only a surrogate of the true respiratory signal. A critical issue for RMTSs is the assumption that the detected signal correlates well with the true motion of the organ under investigation [51, 52, 53], therefore the choice of the signal to be monitored must be carefully accomplished. Other aspects which must be taken into account in the design of a RMTS are: (i) invasivity, (ii) patient comfort, (iii) adaptability, (iv) ease of setting and handling both for the patient and for the technicians [54, 55]. Furthermore, the system should be highly reliable (hardware and software), accurate and reproducible in all the different possible working conditions. In particular, the sensor used to monitor and track the target signal should: (i) respond fast to the variations of the signal, (ii) not introduce drifts in the signal baseline, (iii) have an high signal to noise ratio and (iv) not produce artifacts on the acquired images [54, 55].

5.3.2 Respiratory tracking system devices

One of the first RMS was the spirometer. This device measures volume and rate of the air flow inspired and expired by the lungs and so is, theoretically, the ideal RMTS [54, 55, 56, 57]. Nonetheless the spirometer has some drawbacks that prevented it from becoming a routine technique. The first one consists in the signal baseline drift, which particularly affects long run sessions and which can be due to different causes depending on the specific spirometer model (e.g., flow sensitivity calibration error, imperfect zero-flow adjustment, non linear response to different flow rates, etc.) Another drawback regards the relative discomfort of the spirometer, which forces the patient to breath only with the mouth for a relatively long period of time. Currently, to our knowledge, no commercial devices based on a spirometer are interfaced to any PET or PET/CT system.

Commercial devices Another approach is based on the detection of a surrogate signal related to the breathing process. The only commercial devices to perform respiratory gating are based on such signals and achieved widespread success. These systems are generally easy to use and well tolerated by the patient. Most of the commercial devices were originally developed for RT systems and only recently have been interfaced to PET and PET/CT systems [49, 50]. They are usually based on tracking the external motion of the thorax or of the abdomen and analyzing this signal as an index of the phase of the respiratory cycle. Three popular devices emerged on the market based on this principle. The most used, that was used in this thesis, is the Real Time Position Management System (RPM). It is described in more detail in section 5.3.2.1. Another system is the Anzai (AZ-773V), by Anzai Medical, Tokyo [68, 67]. It consists of a pressure transducer fasted with a belt on the chest/abdomen of the patient. The expansion of the thorax due to the respiration stretches the belt. This in turn changes the pressure applied to the transducer and results in a surrogate signal of

the respiratory cycle. The other system is the Respiratory Bellow System (RBS, Medspira, Minneapolis, Minnesota) [69, 70, 71], which, similarly to the Anzai, is constituted by a belt fastened around the patient chest/abdomen. The stretch of the bell induces changes of pressure in the bellow which is sensed and digitally transmitted to the gating software.

5.3.2.1 The Real Time Position Management System (RPM)

The Real Time Position Management system (RPM, Varian Medical Systems, Palo alto, CA, USA) is the most used, evaluated and compared RMTS for both clinical and research applications [72, 50, 73, 74, 75, 76, 77, 67, 68]. RPM is a non-invasive, optoelectronic system based on a charge coupled device (CCD) sensible to infrared (IR) and visible light, whose lens are surrounded by a matrix of infrared light-emitting diodes (LEDs). The camera, firmly attached to the patient table, illuminates a marker block, which is usually positioned on the patient abdomen near the point of maximum excursion. On the surface of the marker block, facing the video camera, there are two passive reflective markers (circular dots of 5 mm in diameter, 3 cm distance between the two dots). The upper marker is used to track the respiratory motion, while the lower one is used to calibrate the system. When the patient breaths, the block follows the motion of the abdomen and the system, by the simultaneous tracking of the light reflected by the two markers, detects the vertical component of the motion and maintains the calibration. In this way a mono-dimensional signal surrogate of the patient's respiratory signal is generated (Fig. 5.4). The RPM sampling frequency is 25-30 Hz. The recorded signal is processed and presented (in real time) as a waveform on the display of a personal computer. Recently, a new version of RPM which uses six passive markers has been made commercially available allowing for a finer tracking (in 3D) of the patient breathing. The RPM system can perform both prospective or retrospective, phase or amplitude gating depending by the third-party imaging system's characteristics (hardware and software). When set for prospective gating, RPM establishes synchronization by controlling the image acquisition process. In particular it outputs a trigger pulse whenever the phase or amplitude of the respiration signal crosses a user-specified level. The imaging device responds to the trigger and starts or stops the image acquisition. When set for retrospective gating, RPM and the imaging device exchange pulses that are recorded by either or both systems as synchronization tags. Once image acquisition is finished the synchronization tags can be used to correlate the acquired images/data with the phase or amplitude of the breathing signal recorded by RPM. In case of phase-mode analysis, values originally established in real time during acquisition can be recomputed at the end of the study, thus allowing a data sorting better correlated with the respiratory phases. More in general, all the information recorded by RPM during a study as well as the input–output synchronization signals are stored in a file, which can be edited and used for data post-processing.

5.3.3 Attenuation correction for organs in motion

A separate topic that must be dealt with when analyzing moving organs is the correct strategy to achieve the attenuation map used for attenuation correction (AC). When transmissive scans were the only technical possibility this scan, lasting many breathing cycles ($\sim 10\,min$) naturally averaged the motion of the targets over a large period of time. With the advent of

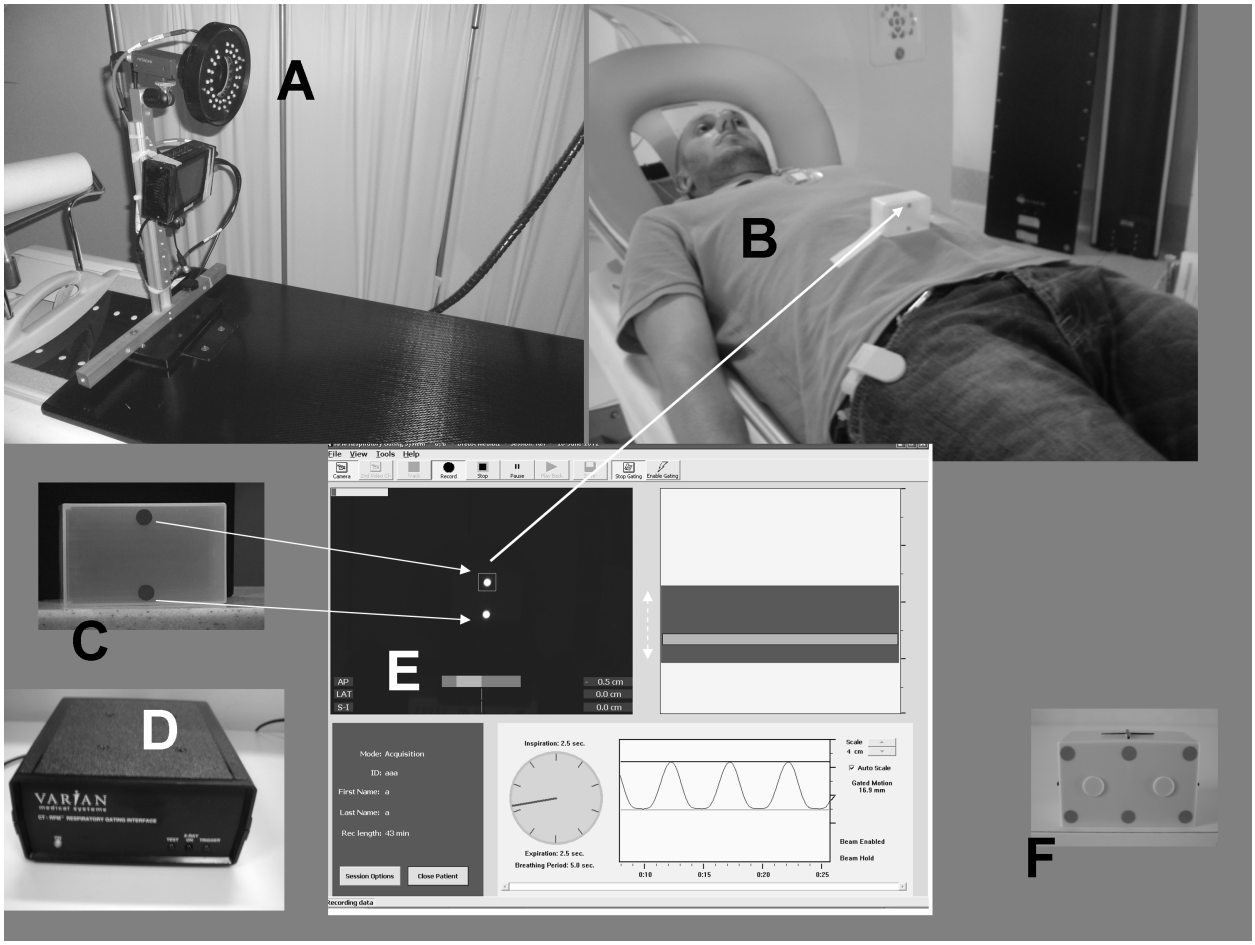

Figure 5.4: Setup of the RPM signal: (A)scanner table with CCD camera and LED illuminators complex. (B) patient and tracker device. (C) 2 markers tracker. (D) processor box. (E) software interface, showing the respiratory cycle and the tracker image. (F) the 6 marker tracker

integrated PET/CT scanner attenuation correction maps are generated from a non-contrast-enhanced low-dose helical CT scans. In this way, with a modern MSCT, the attenuation map of the thorax and of the abdomen is achieved in few seconds. This randomly selects a specific phase of the respiratory cycle, if the patient is breathing freely. Diagnostic CT scans are performed in breath-hold and, usually, in deep inspiration. This could result in misalignments between CT and PET scans of more than 2 cm. To overcome this problem various solutions have been proposed. One uses a conventional helical scan with the slowest possible rotation time and slowest possible pitch, to achieve the same "averaging" effect of a transmission scan. Other options involve the use of CINE-CT scan [80, 79]. This is an axial acquisition modality, with an acquisition lasting many turns for each z-position, with a duration to be set as long as the respiratory cycle. After this kind of CT scan has been performed two strategies can be used to calculate the attenuation map. The first one creates an average image from the sum of all the images acquired, therefore mimicking the averaging effect of old transmission scans. The second strategy, that can be used only in respiratory gating, is to divide the acquired image in respiratory gates, one for each PET gate, and then reconstruct each gate using, for AC purposes, its matched CT scan. On the negative side it should be noted that this modality increases the dose given to the patient, as the exposition time is increased depending on the patient breathing cycle. To reduce at the minimal terms this problem a strategy is to use lowest possible tube current that provides accurate AC results, independently from the image quality of the CT images.

In this thesis we always used CINE-CT scans for the attenuation correction and respiratory gated reconstructions with phase-matched attenuation correction.

5.3.3.1 Effects of ICD and pacemaker on the attenuation correction.

An important application of cardiac PET is for patients with Implantable-Cardioverter-Defibrillators (ICD) or pacemakers (PM), since they cannot undergo Magnetic Resonance Imaging. Unfortunately these devices give artifacts in the CT image and therefore it is important to assess their influence on the final PET image, due to the eventually incorrect attenuation correction.

Both PM and ICD consist, nowadays, in small metallic objects implanted generally near the shoulder and electrodes that are placed near the myocardium (i.e. in the right atrium and right ventricle, with contacts near the wall of the left atrium and left ventricle). This has the effect of having a metallic wire all around the myocardium and bigger metallic terminals in specific positions, to deliver electrical pulses (PM) or electrical shocks (ICD). This materials are extremely attenuating for photons of the X-ray energy (i.e.: $\sim 40keV$) used for the CTAC. On the other side their attenuation is limited at γ rays of β^+ annihilations. Therefore these situation need to be addressed properly in the generation of the attenuation map. PM electrodes are of limited dimension and consequently their attenuation is modest, in case of ICDs, which need to deliver high-current discharges to the myocardium, the electrodes are bigger and made of platinated platinum, a metal with almost the same Z of lead and more than twice its density. In this cases often, even at very high tube currents, photon depletion happens and extremely noisy and artefactual CT-images are obtained, as can be observed in figure 5.5. Studies reported in literature suggest that the effect of PM electrodes are indeed negligible [81, 82], and that also ICD electrodes, while they might give limited differences in

the image quality, do not influence clinical results [82].

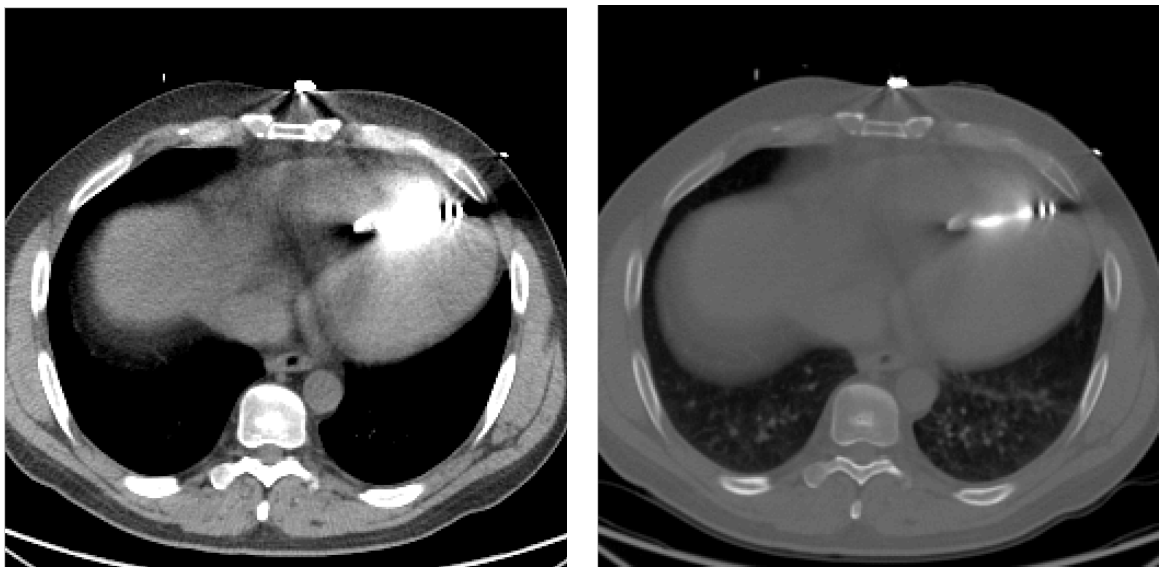

(a) W/L:400/40 **(b)** W/L:1100/300

Figure 5.5: CT scan of a patient with an ICD coil, shown with two different window/level settings. In the one with the usual W/L huge streak artifacts can be seen and also photon depletion. With wider windows the structure of the catheter can be observed.

5.4 Double gating

A natural extensions of the gating techniques previously described to recover myocardial motion is the application of double gating. This procedure consists in the subdivision of the acquired data in frames according to two physiological signals (respiratory and cardiac). In this way one obtains a large number of frames each corresponding to a specific phase of the respiratory cycle and a specific phase of the cardiac cycle. Given a subdivision of the respiratory cycle in n frames and of the cardiac cycle in m frames $n \times m$ total double gating frames are obtained. A feasibility study [42] was performed in 2008. Differently from the strategies used in cardiac and respiratory gating (uniform subdivision of each cycle in equal duration frames) here some strategies have been proposed to achieve the smallest possible number of frames [83]. In this thesis we used a research software written by a collaborating partner to perform double gating: the RGToolbox (Respiratory Gating Toolbox) from General Electrics.

These images can be used also to study the coronary arteries where an high spatial resolution is mandatory due to the small dimension of the target. To this respect, one of the most challenging projects is the one aiming at detecting coronary plaques prone to rupture [84, 85, 86, 87, 88]. Vulnerable plaques are inflamed and therefore have an high concentration of activated macrophage foam cells around the thin fibrous cap. Angiography is the gold standard for the detection of coronary artery stenosis, but it does not provide information

about vessel wall and plaque composition. MRI and CT conversely provide information about the plaque structure but they are not specific enough for plaque vulnerability assessment. $^{18}F - FDG$ PET has instead shown to be able to characterize coronary plaques [85]. The intensity of $^{18}F - FDG$ uptake has shown to correlate with macrophage density and plaque inflammatory state. Furthermore, recent data suggest that the biological composition and the inflammatory state of an atherosclerotic plaque may be the principal determinants for acute clinical events, more than the degree of stenosis or the plaque size. Therefore gated PET/CT appears as the combined functional and structural imaging system with good potentialities for the visualization and the characterization of coronary atherosclerosis and plaque inflammation [86, 87, 88].

5.5 Test of the effectiveness of gating

In this section the effects of motion in cardiac PET studies are investigated. At first the amount of underestimation introduced by the different motion was investigated using the phantom built in chapter 4. Following gated reconstructions of patient studies were performed.

5.5.1 Test on the dynamic phantom

To assess the effects of motion on a cardiac PET image experiments were performed using the phantom described in chapter 4. This experiment was conducted on the PET/CT scanner GE Discovery-690, described in chapter 2. For this test 20 MBq of ^{18}F were injected in the myocardial wall, while the LV was filled with "cold" water. The container of the phantom (simulating the background) was filled with air. One of the two defects was inflated to simulate an infarct. Four different acquisitions were performed sequentially:

1. No motion (heart stopped in the systolic phase)
2. Dual motion (Cardiac: 58 bpm and breathing: 4 s period, 10 mm displacement, motion direction: 45° respect to the scanner axis)
3. Only breathing (respiratory parameters as before, heart stopped in systolic phase)
4. Only heartbeat (58 bpm). Each acquisition consisted of a PET and of a CT scan, used for attenuation correction (AC).

Scan 1 and 4 underwent a helical CT scan (120 kV, 45 mAs), while scan 2 and 3, to account for the respiratory motion, underwent a CINE-CT scan (120 kV, 90 mA, rotation time: 0.5s, cine duration: 5s). The CINE-CT was used to generate an average CT to account for the respiratory motion [80, 79]. PET image reconstructions were performed with the following settings: FOV 30 cm, matrix size: 256x256, transaxial post-filter: 2 mm, axial filter: light (average filter with coefficients [1-6-1]), reconstruction algorithm: 3D-OSEM with PSF modeling [17, 25], 18 subsets, 10 iterations. Static images (no motion compensation) were reconstructed for all the scans. In addition, gated reconstructions were performed for scans 2, 3, 4. Scan 2 was reconstructed with respiratory gating with 6 phases, a cardiac gating with

12 phases, and a double gating reconstruction (4 respiratory phases and 9 cardiac phases, 36 total phases). For scan 3 I performed a respiratory gated reconstruction with 6 frames and for scan 4 a cardiac gated reconstruction with 12 phases.

5.5.1.1 Analysis

PET images were evaluated by using the CARIMAS software (version 2.4, Turku PET Centre, http://www.turkupetcentre.fi/carimas), which allows an automatic analysis of the heart following the standard AHA 17-segments representation. Scan 1 (no motion) was used as the reference to assess the activity underestimation introduced by motion and the quality of the gated reconstructions.

5.5.1.2 Results

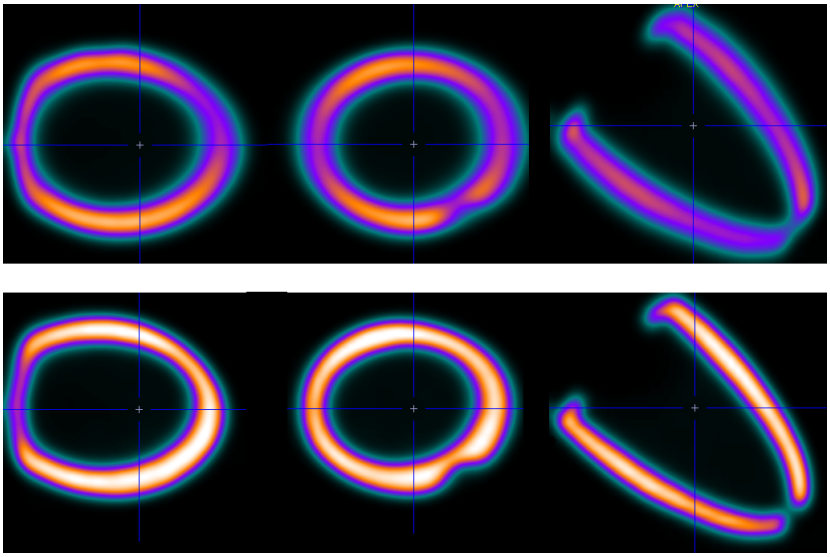

Figure 5.6: Upper row: static reconstruction of scan 2, with both motions. Lower row: scan 1, without any motions. Same color levels used for both images.

Figure 5.6 shows the static reconstructions of acquisition 1 and acquisition 2. A lower level of measured activity can be clearly observed. The borders of the defect can be seen as more sharp. In acquisition 2 the uptake is not uniform and the walls parallel to the direction of respiratory motion show an increasingly underestimated uptake.

Static reconstructions All the static reconstruction of the scans subject to motion showed an underestimation of activity concentration with respect with scan 1. The complete results are reported in figure 5.7. Specifically it was found a reduction of

- 26% for scan 2 (both motion)
- 10% for scan 3 (only respiratory motion)
- 15% for scan 4 (only cardiac motion)

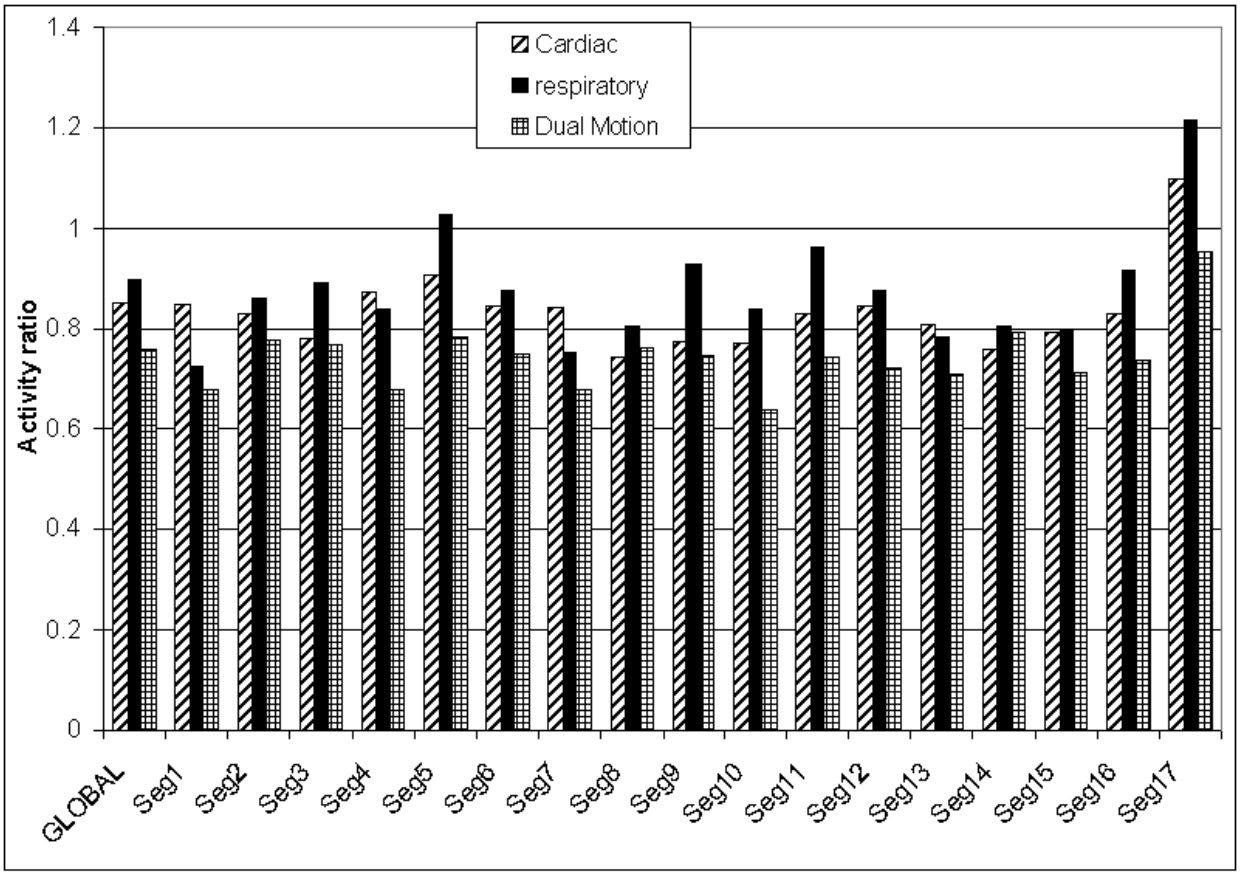

Figure 5.7: Ratio of activity measured in the static reconstruction with different motions activated, compared to the acquisition without motion.

Effects of respiratory gating Processing for respiratory motion was applied on scan 2 and scan 3.

In scan 2 only a modest improvement was observed, and the average underestimation of radioactivity concentration was 21%.

With scan 3, that was subject only to respiratory motion, the respiratory gated reconstruction provided full recovery of activity (measured activity concentration ratio: 95%)

Effects of cardiac gating Cardiac gating was performed on scan 2 and scan 4.

Analyzing a systolic gate of scan 2 a slight improvement was observed compared to the static reconstruction, with an 15% reduction in the measured activity.

On scan 4 cardiac gating was able to recover the full activity concentration (measured ratio 100%). It is possible to note an higher measured activity in the systolic gate compared to the diastolic gate. This is due to the different amount of partial volume effect suffered by the myocardial wall in the different cardiac phases, where the wall thickness vary.

Effects of double gating In the last test scan2 was processed by using a double gating technique Also in this case in the systolic gates full recovery was achieved (average activity ratio: 102%). A qualitative image of the double gated reconstruction is shown in figure 5.8.

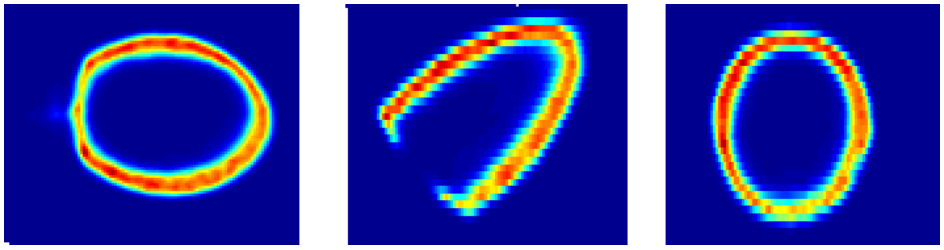

Figure 5.8: Image of a double gated reconstruction of the phantom.

5.5.2 Test on patients

The next step involved applying gating techniques to patient studies. The images analyzed came from data acquired in studies coming from either $^{13}NH_3$ studies or $^{18}F-FDG$. $^{13}NH_3$ scan were originally performed for perfusion quantification, see Chap. 7, and were performed with an injection of $10\,mCi$ of $^{13}NH_3$ and $20\,min$ of acquisition. For $^{13}NH_3$ studies the first $5\,min$ of acquisition were discarded as the uptake in the myocardial tissue is not enough. In these $15\,min$ the average prompt counts (total coincidences, including random and scatter ones) acquired were of the order of $500\,M$. In $^{18}F-FDG$ studies the acquisitions were performed $1\,h$ after the injection of $10\,mCi$ of tracer and counts were collected for $20\,min$. On average up to $600\,M$ prompt counts were collected for each patient.

As for patient studies there is no motion free reference to compare to qualitative evaluations of the resulting images were performed. Aquantitative analysis with CARIMAS in the same fashion of the phantom was performed, taking as the reference the activity measured in a double gated gate, assuming it to be the correct one.

Respiratory gating Respiratory gating was performed dividing the respiratory cycle in 6 uniform phase gates. The reconstructions were performed with each gate coupled to a corresponding CT phase for attenuation correction. A qualitative analysis clearly showed that the heart was subject to motion in all of the patient, with different excursion amplitudes.

Cardiac gating Cardiac gating of the PET scan is commonly used to quantify cardiac function, diastolic and systolic volume and ejection fraction. In all of the scans 12 phases gating was performed. These reconstructions were then used to perform the aforementioned volumes estimation.

Double gating Finally double gating reconstructions were performed in a number of cases. The chosen setting was 4 respiratory and 7 cardiac gates, for a total of 28 gates.

Analysis To perform a comparison similar to the one performed with the phantom it was assumed that the double gated reconstruction is free from motion artifacts and the activity measured in various situations was compared with the activity measured in a systolic gate of the double gated reconstruction.

5.5.2.1 Results

Quantitative analysis The quantitative results are reported in figure 5.9. The activity measured in the static reconstruction is 30.5% compared to a systolic phase of the double gated reconstruction. This compares well to the 26% reduction seen with the phantom. Similarly to the phantom almost no improvements were found using respiratory gating on the scan with both movements: the measured activity concentration ratio is 29.6% less than the reference (much similar to the static reconstruction). More effective is the cardiac gating. Comparing a systolic phase with the corresponding dual gated phase the observed activity is only 9% (compared to 15% for the phantom).

Qualitative analysis An example of qualitative results is shown in figure 5.10. The myocardial wall looks much thinner on the double-gated image. Another feature is the inferior and the superior wall. On the static reconstruction the wall looks less intense and more blurred, compatibly with the effect of respiratory motion that acts in this direction.

Another example is presented in figure 5.11. Here the walls look thicker, as expected during the contraction.

A third example is shown in figure 5.12. Also here, as in the previous case, in the static image a thinning in the superior and inferior wall, seen in the coronal image, appears in the static reconstruction and seems to disappear in the double gated reconstructions.

The last example reported is that of a dilative cardiomyopathy patient in a $^{18}F - FDG$ study, in figure 5.13.

A common feature of all these images are the extreme levels of noise in the double gated reconstruction. With such high levels of noise it is not possible for a physician to perform a diagnosis, as exemplified by fig. 5.13, where the reduction of activity in the lateral wall

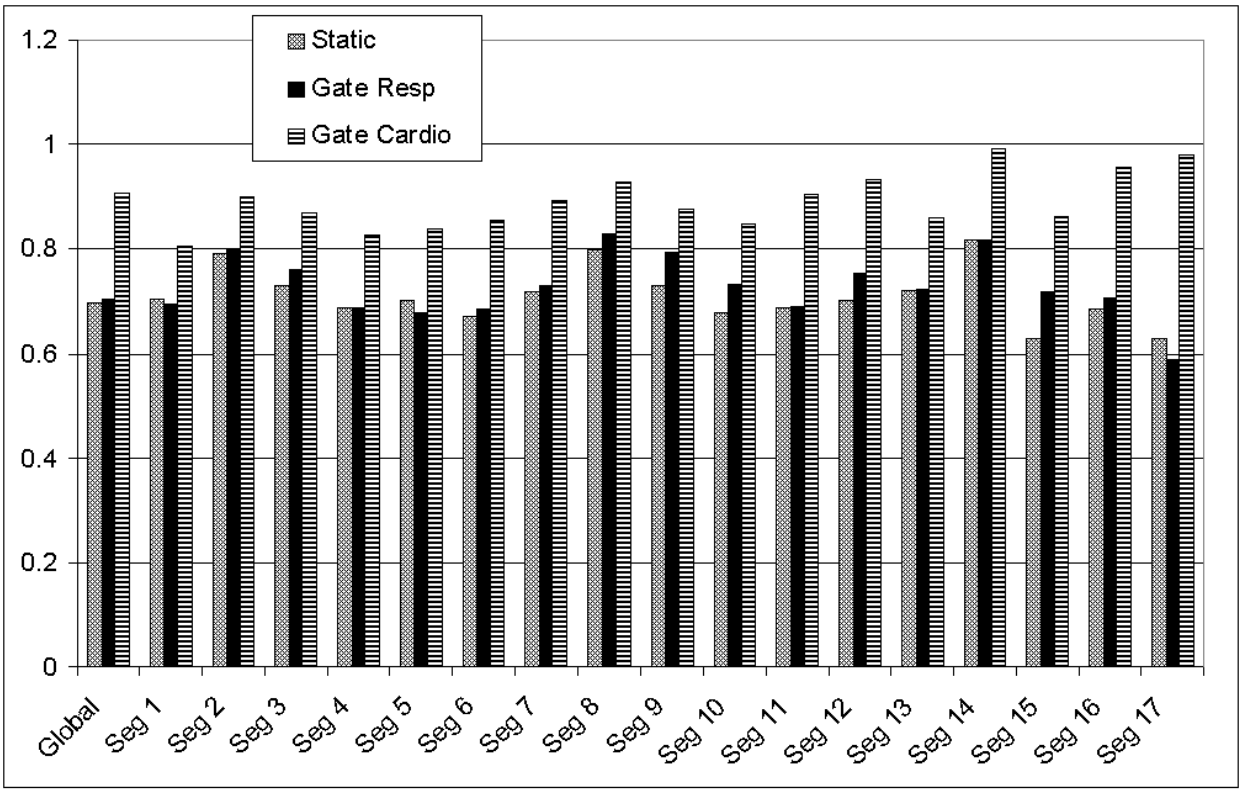

Figure 5.9: Ratio of the activity measured in the various segments of a patient with reference to a systolic frame of the double gated reconstruction.

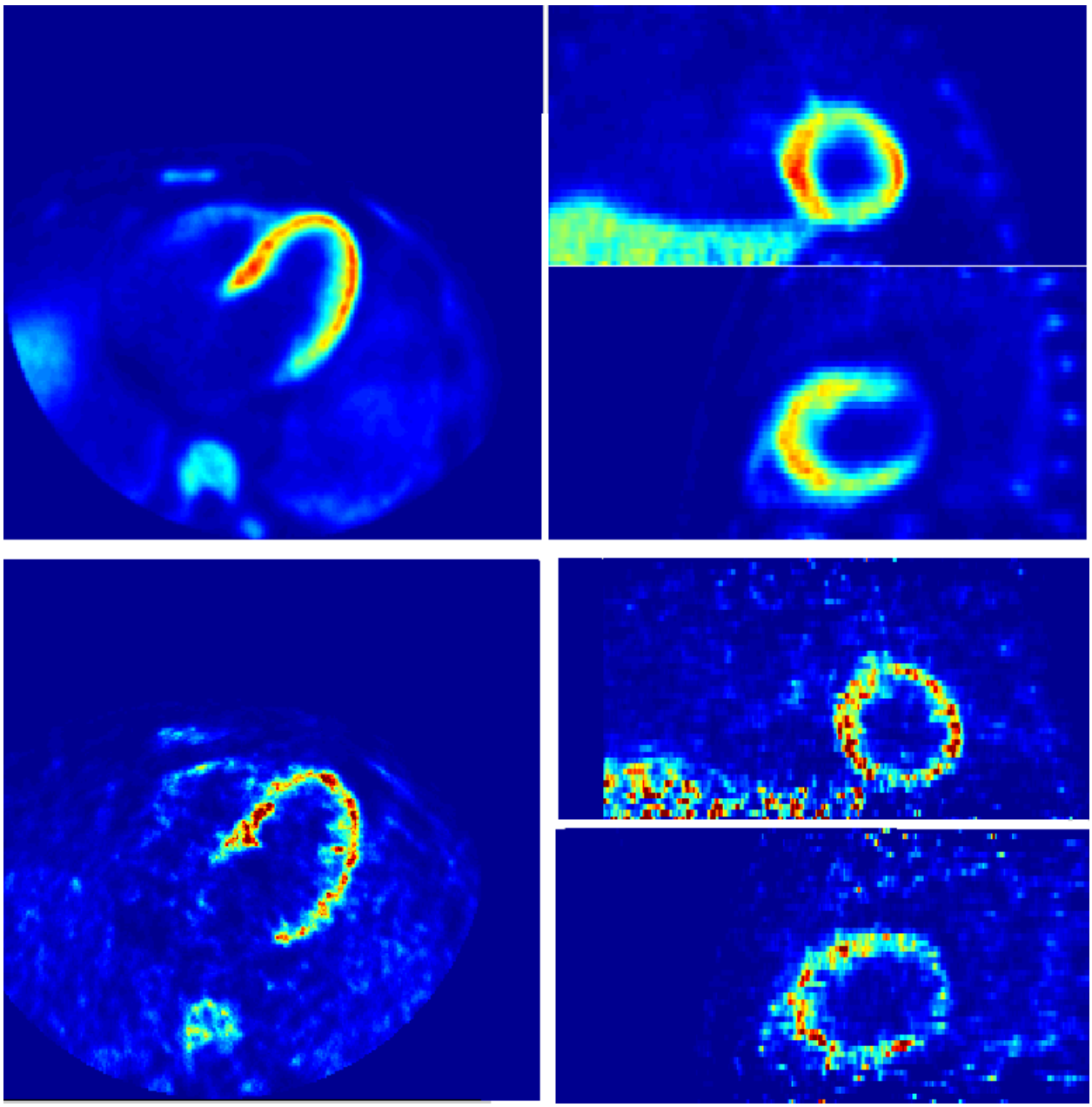

Figure 5.10: A comparison of the static reconstruction and of a diastolic frame of a double gated reconstruction for an $^{13}NH_3$ study

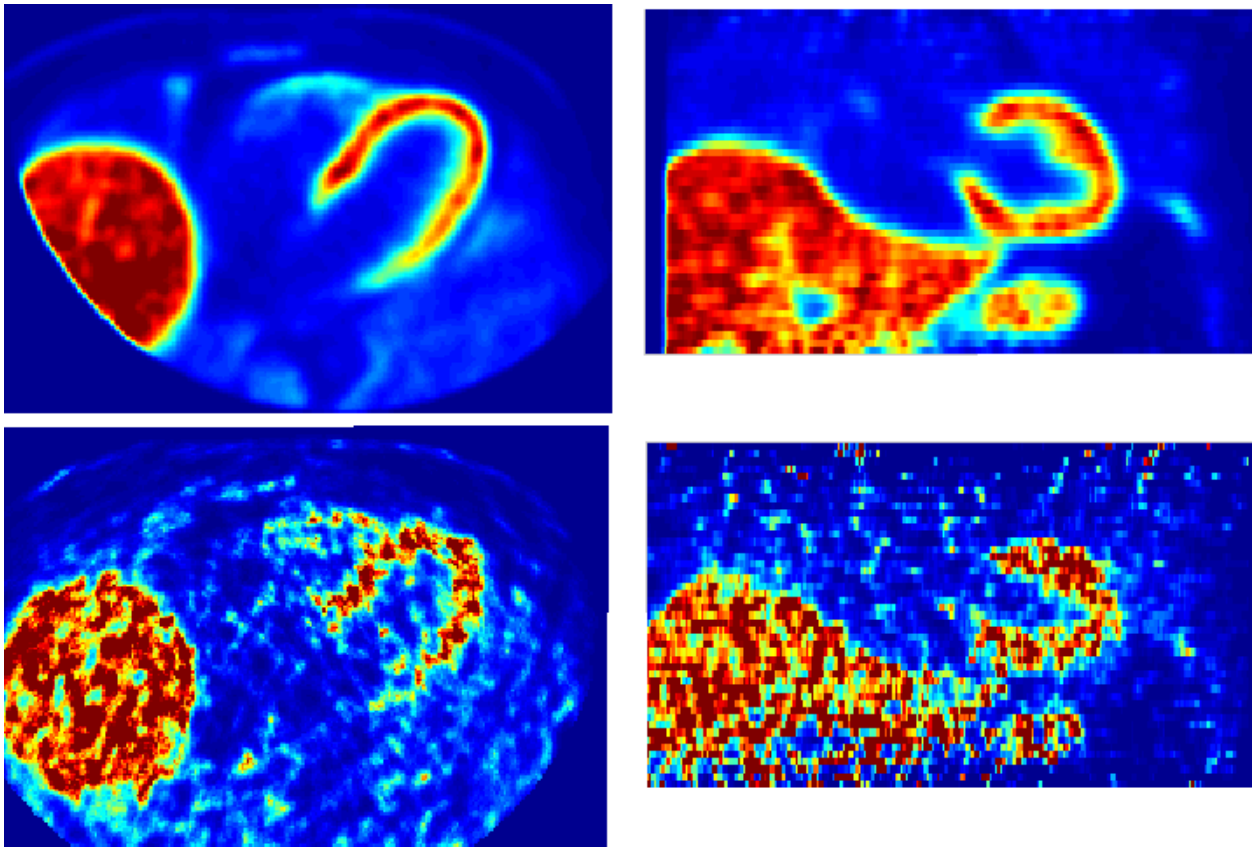

Figure 5.11: A systolic double gated frame of a $^{13}NH_3$ study compared to the static reconstruction.

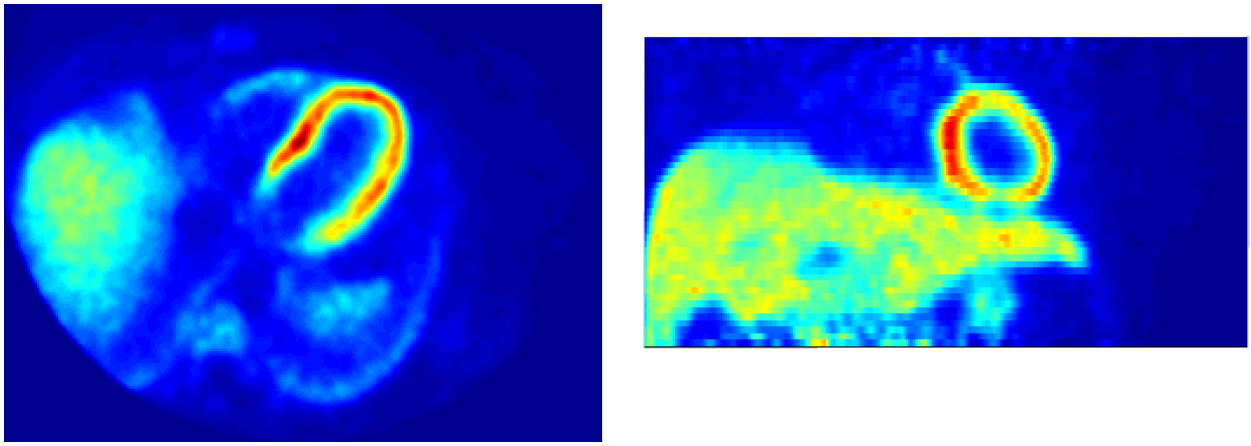

(a) The static reconstruction

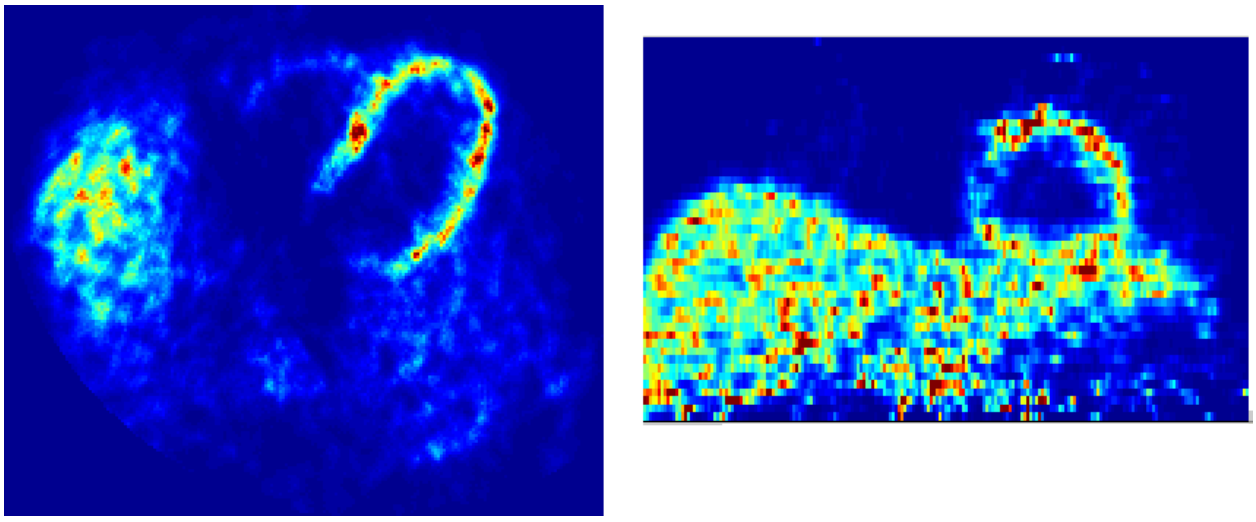

(b) A diastolic frame of the double-gated reconstruction

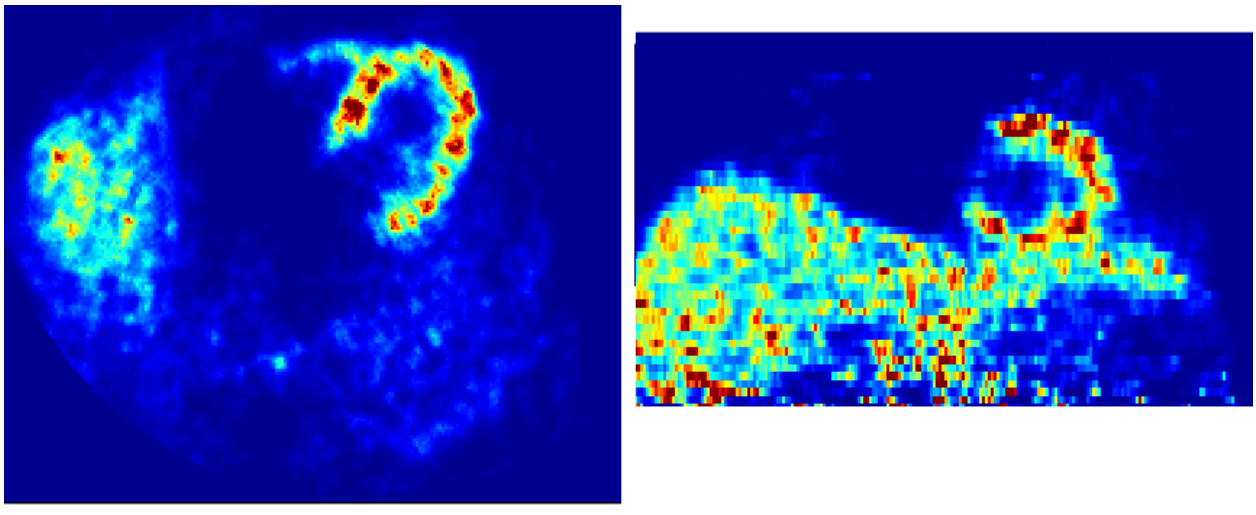

(c) A systolic frame of the double-gated reconstruction

Figure 5.12: The static reconstruction and two different phases of a double gated reconstruction of a $^{13}NH_3$ study.

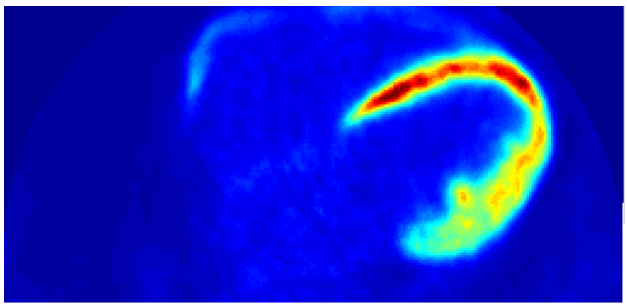

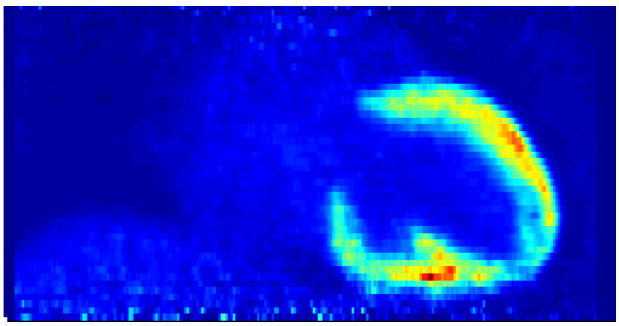

(a) The static reconstruction

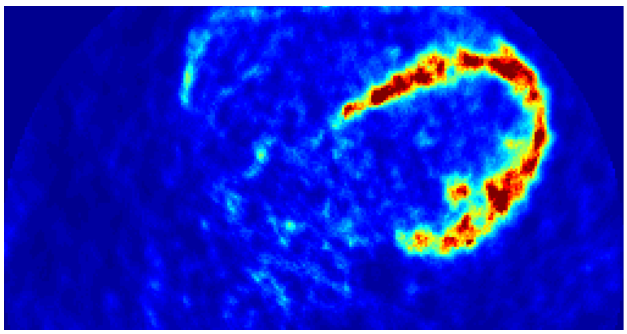

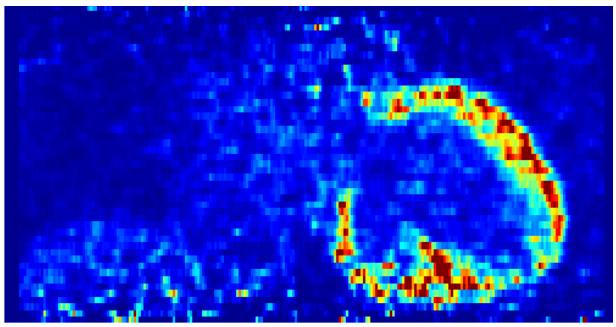

(b) A diastolic frame of a double gated reconstruction

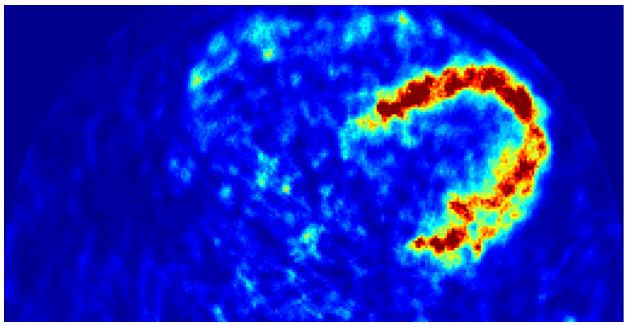

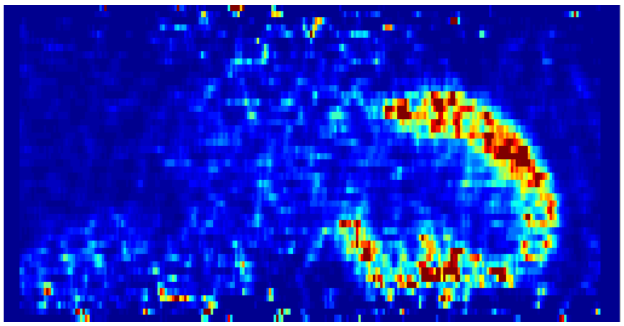

(c) A systolic phase of a double gated reconstruction

Figure 5.13: Double gated an static reconstruction of an $^{18}F - FDG$ study in a dilative cardiomyopathy patient.

is evident in the static reconstruction but it is very difficult to spot it in the double gated reconstructions.

Chapter 6

Segmentation and morphing

Introduction Results from the previous chapter showed a very high noise in the reconstructed double gated images. The origin of this noise is the partition of the data in an high number of subdivisions (~ 30). Once excluded the possibility to acquire 30 times more counts, as the amount of injected activity cannot be increased much more and the scan times are already long, the only possibility to preserve motion-free images with low levels of noise lies in registration of the different reconstructed gates.

As stated a number of times in this thesis the motion of the heart is the sum of the respiration and the cardiac beating. Breathing motion is of "large scale" and mainly of translatory nature (see sec. 5.3.1), therefore it is possible to think to correct for it using registration techniques based on "simple" mathematical models. On the other side cardiac beating is complex, also involving changes in the thickness of the myocardial wall. Therefore I propose two different algorithms to register the different gates. The first one involves the registration of all the different gates in the same cardiac frame with an almost rigid (affine) registration. The other algorithm aims at registering all of the gates, using an elastic registration.

6.1 Affine registration of respiratory gates

Concept The motion of the heart due to patient breathing is of large scale and a "regular" structure (see sec. 5.3.1). Breathing deforms the lungs, inflating them like balloons. Therefore at the apex the motion is quite small while near the diaphragm this motion is more pronounced. The amount of displacement depends also on the breathing pattern. The motion is mostly a translation in the cranio-caudal direction but, as the lungs expand, they also move outward. On a nearby organ this can induce small rotations on top of translations. The heart, specifically, can feel more the pressure from the lungs on its anterior wall, in contact with the lung, than on the inferior wall, in contact with organs that are not subject to breathing motion [42]. With this in mind I propose a technique to register cardiac PET images coming from different respiratory phases (i.e.: different respiratory phases of the same cardiac gate in a double gated study but also single gated respiratory gated cardiac images).

The concept underlying the technique is to parametrize the motion of the heart alone (not of all the organs falling in the PET FOV) with an affine registration. This choice can

be viewed as approximating the the breathing motion locally as a rototranslation but also accounting for small deformations (trough the scale and shear parameters).

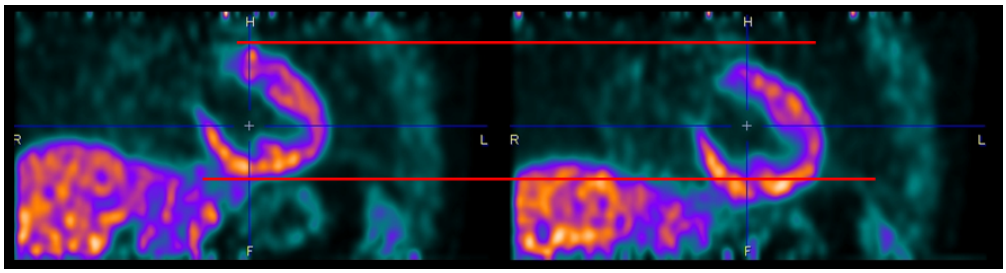

Figure 6.1: Example of two respiratory phases seen during a cardiac PET scan

6.1.1 Software implementation

A software package was developed to perform this almost-rigid realignment. It features two steps from the user point of view. In the first step the user selects the volume of the PET image in which the heart is present in all the gates, and then this volume is isolated. The second step is the registration of each gate with the corresponding reference respiratory gate.

6.1.1.1 Heart extraction

The first operation performed is the extraction of the heart. This is needed for two reason. As the affine transformation is valid only locally including other structures in the FOV would give erroneous results. The second reason is of computational nature. To find the transformation parameter an objective function is calculated between the target and the reference image. Each evaluation requires the computation of the transformed image. Typically more than 100 evaluations are performed for each registration. Reducing the number of the voxel that needs to be transformed reduces computation times. Given the common heart size one can reduce the data matrix size from $256 \times 256 \times 47$ to about $100 \times 100 \times 35$, reducing the computational burden of a factor ˜9, in normal sized hearts.

The user is presented with two Most-Intense-Pixel (MIP) projections, one in the latero-lateral direction and the other one in the anterior-posterior direction. On each projection a draggable ellipse is present. The user moves the ellipses until they are centered around the LV and changes their size until they include the whole myocardium. The first ellipse has center x, z and axes length r_x, r_z while the second one, conversely, y, z and r_y, r_z. The volume cut out is defined by the ellipsoid with center x, y, z with radii r_x, r_y, r_z. Therefore an automation has been implemented for which, when the user moves each of the ellipses, the z and r_z of the other ellipse are changed. The dialog box in which the user crops the heart is shown in figure 6.2.

To ensure the best possible definition by the user of the correct volume the MIP projections are performed with a weighting technique. Usual techniques involves a linear function decreasing with the depth from the front to the back of the volume, according to the angle along which the projection is performed. In this case a linear weighting is performed but it

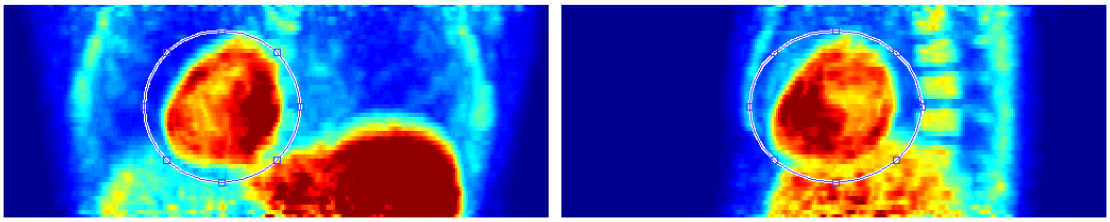

Figure 6.2: Interface presented to the user for heart cropping

decreases from the current center of the ellipses towards both extremities. In this way the heart becomes more prominent to the background as the user adjusts the selection.

After the selection of the myocardial volume the data are saved in a structure with DICOM headers and then written in a MATLAB file.

6.1.1.2 Registration procedure

The registration phase interface features three sections. In the upper sections the two images are shown overlaid. In the lower section buttons to save the results and to start the registration of that gate are present. On the right there is a panel with the registration parameters currently found by the fitting procedure. They can also be freely set and/or modified by the user (if he wants to try the effect of a specific parameter or in the case of macroscopic failures of the minimization). The interface is shown in figure 6.3.

Display section In the display section the usual three orthogonal views are shown (axial, coronal and sagittal). To allow the user to check the quality of the registration the target and the reference image must be superimposed. Many techniques are available to fuse the images, but all of them have some failures when it comes to superimpose two noisy images with poorly defined borders. In the final version the program sends the first volume on the red channel and the second volume on the green channel, with a linear mapping. When the two images are perfectly superimposed their superimposition is yellow, as can be appreciated in figure 6.3 (a) and (b) .

Objective function and Interpolation technique As we are analyzing two images coming from the same modality the algorithm of choice was the "sum of the squared differences" (SSD), defined as

$$SSD = \sum_{i=1}^{N} (I_1(i) - I_2(i))^2$$

It is a measure of the difference of pixel values between two images. There are a number of subtleties to be implemented correctly for this minimization to provide meaningful results. The first one is about the voxels included in the sum. In the previous section the extraction of the heart was discussed as the affine approximation is valid only locally. Therefore in the sum only the pixel falling inside the mask previously defined should be included. Nonetheless, as the registration moves one of the two images, pixels that were originally outside of the

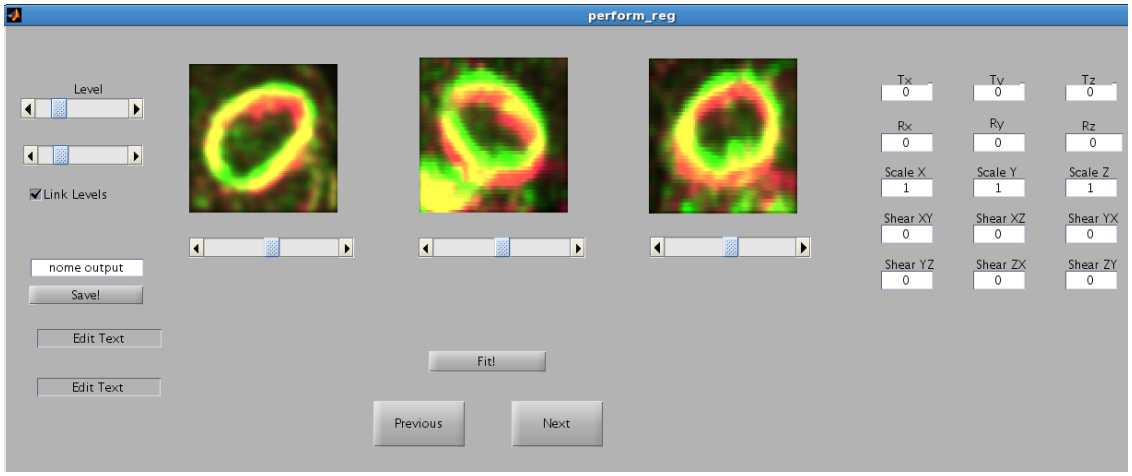

(a) Software interface showing an image to undergo transformation

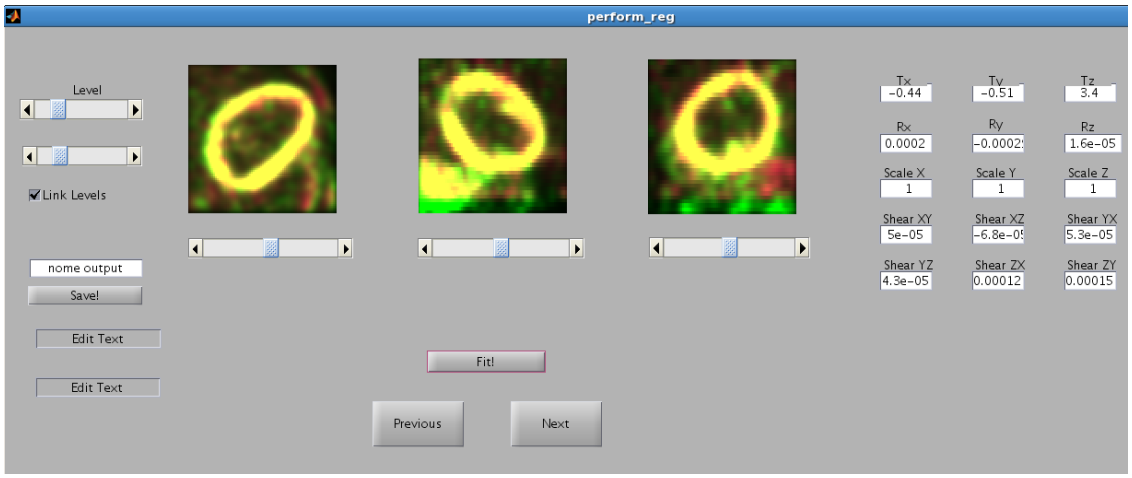

(b) The same, after registration

Figure 6.3: The registration software in its final implementation. On the right the transformation parameters are shown.

mask must be dealt with. Setting their value to zero would obviously introduce a bias. A first solution would be to analyze only in the region where the original and the translated mask superimpose and divide the SSD by the number of overlapping voxel. However this would introduce a non-continuity in the objective function, as shown in figure 6.4. The final solution used is to save also a padding region of voxels outside of the mask, that, with the translation, fall inside of the mask.

The second problem was the choice of the interpolation technique. A linear one is extremely simple and computationally light but it suffers from "bad" mathematical proprieties (e.g.: discontinuous derivative). To overcome this problem a cubic or spline interpolation technique would be better, but this require a computational time that is not acceptable (˜10 times more while starting from a technique that already takes more than a minute for each registration). The final solution used linear interpolation but smoothed heavily the image beforehand. This does not change the position of the minimum and it also has the favorable propriety of avoiding the influence of noise in registration. It should also be kept in mind that, as our double gating reconstruction are not post-filtered beforehand, they could be non-bandwidth-limited.

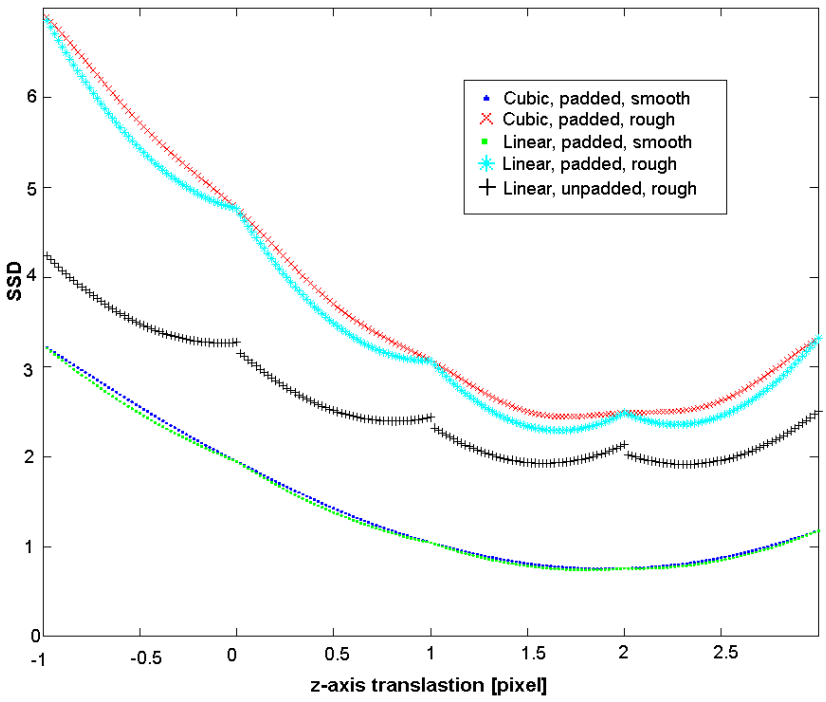

Figure 6.4: Trend of the SSD vs. the $z-$axis translation, with different interpolation, masking and smoothing techniques

To illustrate the problems described in figure 6.4 the trend of the SSD as a function of the $z-$translation for two images from a patient study (we chose the $z-$axis as it is the one along which the most important changes happen). It can be seen that without smoothing both the cubic interpolation and the linear interpolation have much higher values, due to the influence

of noise. Also, for the cubic interpolation, the minimum is very broad, almost splitting in two local minima. Without smoothing linear interpolation has local minima, each shifting toward lower values the objective function near half a pixel translation. This happens because the linear interpolation has a smoothing effect far from integer values of translation. It can also be seen that without the proper padding outside of the mask the function not only has local minima but also wide discontinuities. Finally it can be appreciated that when smoothing is applied the cubic and the linear interpolation behave in an almost superimposible manner with a single well-defined minimum.

The minimization algorithm of choice is one present by default in MATLAB, the Broyden–Fletcher–Goldfarb–Shanno (BFGS) method, which is appropriate for a continuous function with 12 free parameters.

6.1.2 Results obtained with this procedure

Visual assessment of the performances were performed on various double gating patient studies, acquired both at rest and during stress in $^{13}NH_3$ studies or only in resting conditions in $^{18}F-FDG$ vitality studies. These studies have been performed in all of the cardiac gates, therefore with different image proprieties. A results is reported in figure 6.5. It can be noted

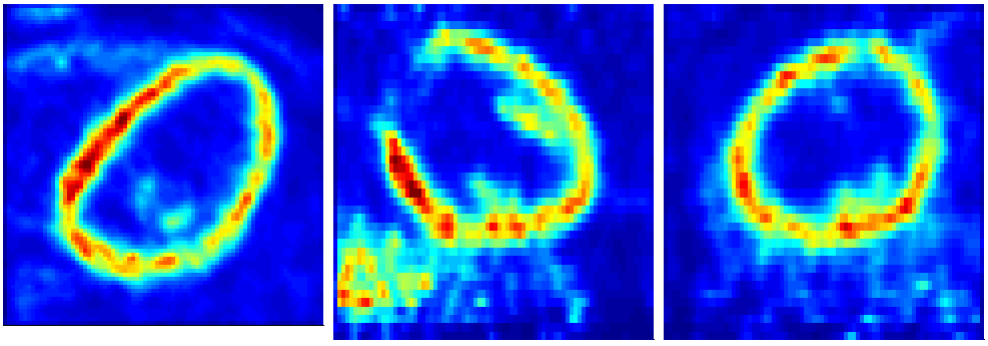

(a) Affine registration

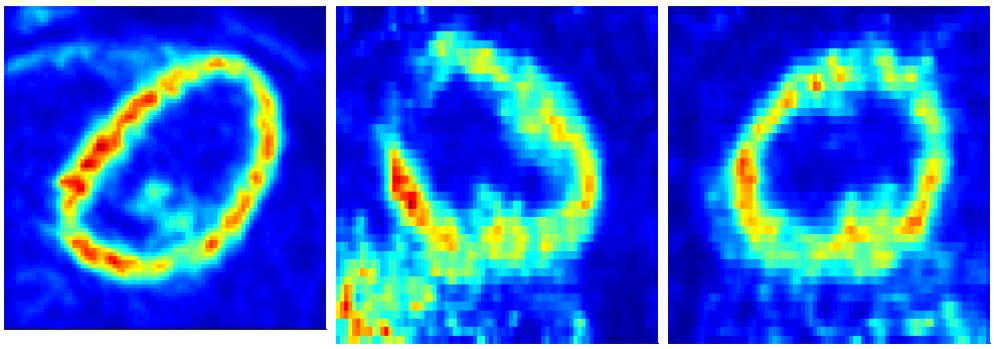

(b) Cardiac gating

Figure 6.5: Result of an affine registration of a diastolic gate. It can be noted that the measured activity concentration increases while the motion blurring effect disappear, as both papillary muscles becomes clearly distinguishable.

that the level of noise starts to be acceptable. Two other features clearly appear. The first one is an increase in the activity seen in the myocardial wall, that can be attributed to less motion-induced partial volume effect. The second is the clear delineation of the papillary muscles, that is a sign of reduced motion blur.

6.2 Elastic registration of the myocardial wall in different cardiac phases

While the respiratory motion can be described by a translation an small linear deformations the cardiac beat is more complex. Therefore, in order to register images coming from different cardiac phases, a purely elastic technique should be used. The algorithm proposed in this section to register this kind of images is based on the creation of a map of points describing the left ventricle surface which are then used to build a thin-plate-spline (TPS) deformation field. Similar approaches were already suggested by Kovalski in 2008 [89] and by Slomka in 2004 [90]. These studies were focused on SPECT images, that intrinsically have much lower resolution, and differed in how they extracted the surface to define the deformation field.

6.2.1 Thin Plate Spline Deformations

An elastic deformation is a generic $R^3 \rightarrow R^3$ mapping. What is looked for is to build a field $J(x, y, z)$ from an original image $I(x, y, z)$ after a free deformation of the coordinates such that our registered image J is defined, in term of the original I image as $J(x, y, z) = I(x', y', z')$ with $x' = x + t_x(x, y, z)$ (and similar equations for the other two coordinates). Many ways exists to define the so called "deformation field" t. We chose to use the "thin plate spline" approach to build this field. It has been suggested in 1989 by Bookstein [91] and was widely adopted after in the more disparate fields of image processing.

Thin plate splines (TPS) take their name from the physical phenomenon out of which they were modeled. If one takes an ideal thin plate of metal and bends it in N points the resulting surface displacement would be described by

$$z(x, y) = \sum_{k=1}^{N} \phi_k U\left(|(x, y) - D_k|\right)$$

with $U(r) = r^2 \ln r$, D_k the x, y coordinate of the $k-$th vertex and ϕ_k is related to the displacement at the vertex k. This solution, which is structured as a *linear* combination of *radial basis functions,* has the propriety of being the *unique* minimum of the "bending energy" E, defined as

$$E(f_{x,y}) = \iint_{R^2} \left(\frac{\partial^2 f}{\partial x^2}\right)^2 + 2\left(\frac{\partial^2 f}{\partial x \partial y}\right)^2 + \left(\frac{\partial^2 f}{\partial y^2}\right)^2 \mathrm{d}x\mathrm{d}y$$

In analogy with this phenomenon it is possible to define a mapping operator $x_i' = x_i + t_i(\bar{x})$ with $t_i(\bar{x})$ as the "bending" of our mapping in the $i-$th direction in the $\bar{x}$ point. To describe

the $t_i(\bar{x})$ is possible to use solutions of the bending energy (expressed in 3D this time, for volumetric images). The difference with the bent metal sheets is that this time the bending is in the same direction we are analyzing and not perpendicular to the plane. Defining our mapping using the three $t_i(x, y, z)$ each one as a linear combination of U_j such that they pass trough the "control points" it has been proven [91] that the final mapping will have the following proprieties:

1. This interpolator passes exactly trough the control points
2. The t_i functions are the unique minima of the 3D bending energy
3. The t_i are continuously differentiable everywhere in the image
4. If there are no fold (as in physical situations) the transformation behaves as a diffeomorphism

These t_i are then called "Thin Plate Spline" (TPS) of the transformation and work as an interpolator, passing exactly by the control points that we imposed.

6.2.2 Segmentation of the heart

Concept

The proposed technique extracts the control points to build the TPS field segmenting the myocardial wall.

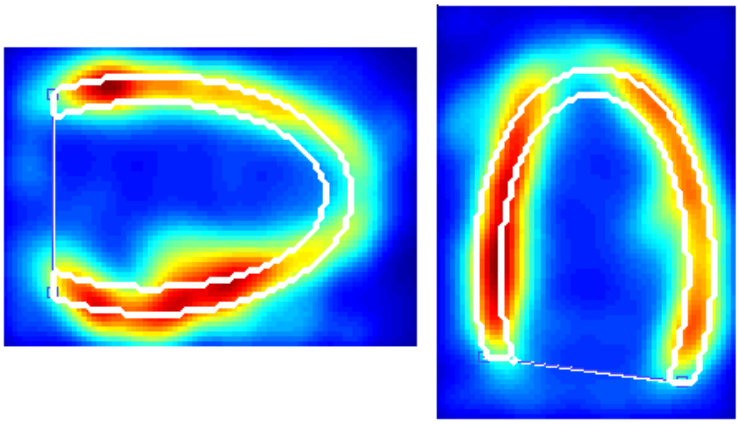

Figure 6.6: Myocardial muscle in two long-axis view with an ellipse superimposed. It can be easily noticed how well this structure can be described by an ellipsoidal function.

The segmentation algorithm used describes the shape of the left ventricle as an almost elliptical object. This is justified by what can be seen in figure 6.6. Then the myocardial wall itself, along this ellipsoidal structure, is described with a gaussian profile, as shown in figure 6.7.

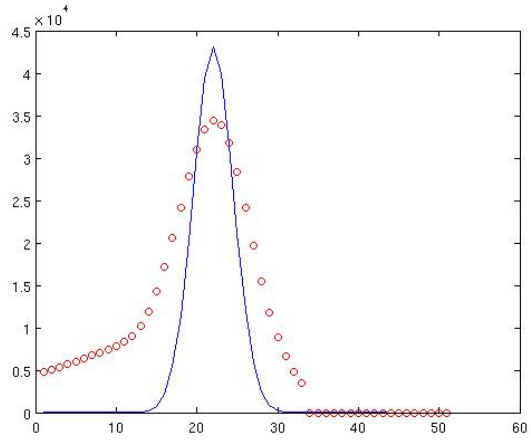

Figure 6.7: A profile of the myocardial muscle with a gaussian (not fitted) superimposed.

Software developed

To perform all these operation a software program was necessary where the user can do easily all the operations needed sequentially. The ideal steps in which the whole operation can be schematized are:

- Reorientation of the heart to its axes
- Initialization of the parameters of the segmentation
- Fine segmentation of the whole surface

Extraction and reorientation of the heart

Dealing only with the surface of the left ventricle it is not needed to save and process the whole FOV of the PET. This also reduces the computational burden and avoids the influence of extraneous structures. The natural orientation of the left ventricle is not parallel to the axes of the PET scanner therefore a re-orientation of the image is usually performed [92]. For this reason the PET image is usually reoriented along its main axes. The implemented approach is based on having the user defining the euler angles. The procedure and the various steps are shown in figure 6.8. In the first panel the user is asked to draw a line in a transaxial plane, from the base to the apex along the direction of the long axis. This defines the first euler angle. Then the program shows an image along a plane defined by the line just drawn and the z axis. Here the user again draws a line parallel to the long axis. This defines the second euler angle. The third one is obtained by showing the user a plane perpendicular to the long axes. The user here draws a line which defines the rotation along the long axis, the last free parameter to determine a 3D-rotation. The length of the lines drawn by the user is used to define the sampling range of the re-oriented image. The new image is interpolated from the original one with an isotropic pixel spacing of $1.5\,mm$. Starting from an original PET image with a size of $256 \times 256 \times 47$ the final image has an average size of about $60 \times 60 \times 90$, depending on the heart size, a reduction of about a factor 10 of the amount of data to be handled.

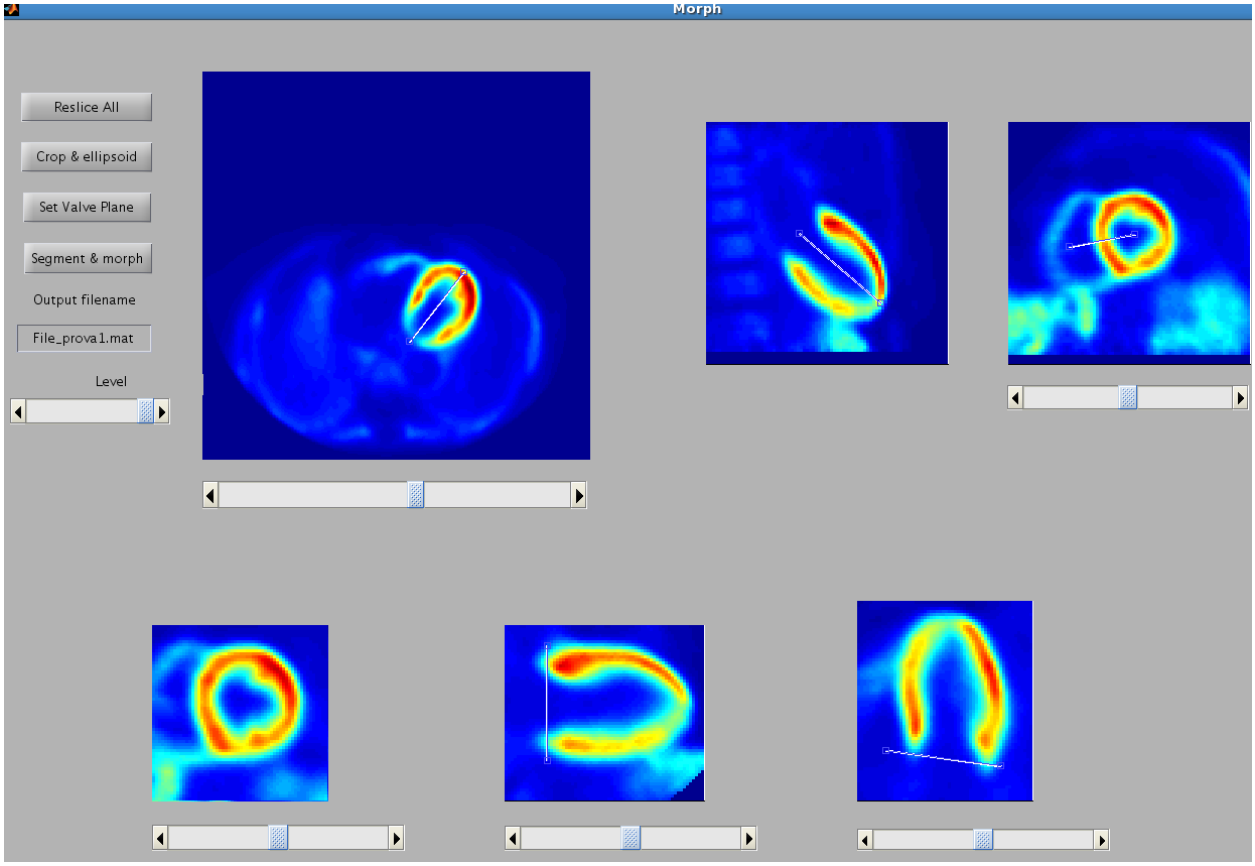

Figure 6.8: GUI of the morphing software. The upper left image is a transaxial plane, on which the user draw the first euler angle of the long axes and defines its length. Upper center shows a vertical plane passing trough the line previously drawn. Here the user defines the second Euler angle of the heart. In the third image the user is shown a short axis view of the heart where he defines the third Euler angle. In the bottom row the three reoriented images, in their reduced field of view, are shown.

Coarse segmentation of the heart

A first guess of the heart shape is obtained approximating the heart with an ellipse. The original idea was to approximate the myocardial wall with a gaussian profile along an elliptical centerline. Therefore our approximated image would be

$$I(x, y, z) = bkg + c \times \exp\left(-\frac{r^2}{2\sigma^2}\right)$$

with bkg being the average activity in the background, c the peak activity concentration of the myocardial wall, σ parametrizing the wall thickness of the heart and r the distance from the "center" of the heart as in

$$r = \sqrt{\frac{(x - x_c)^2}{a^2} + \frac{(y - y_c)^2}{a^2} + \frac{(z - z_c)^2}{b^2}}$$

with a being the short axis length and b the long axis length. To find the optimal parameters the minimum of the sum of the squared differences between the parametrization and the original image is searched, using the BFGS algorithm. The parameters to be found are 9: bkg, c, σ, x_c, y_c, z_c, a, b. The objective function is:

$$F = \sum_{x,y,z=0}^{N} \left(PET_{x,y,z} - I\left(bkg,\, c,\, \sigma,\, x_c,\, y_c,\, z_c,\, a,\, b\right)_{x,y,z}\right)^2$$

Unfortunately this algorithm can seldom be applied "as is" on a frame of a double gated image as the minimization usually fails or encours in a local minimum. Therefore several strategies were implemented to guarantee the finding of the optimal solution.

Smoothing of the image Double gated image are too noisy, therefore the software applies a 3D-gaussian filter with a FWHM of 12 mm. Such an heavy smoothing virtually eliminates any noise. It does not impact the segmentation accuracy as a linear smoothing does not shift the position of the maximum of the myocardial wall.

Reduction of the number of free parameters. While the addition of a free parameters allows to describe better the original image it also increases the risk of finding a local minimum and enlarges the confidence interval for each parameter. Fixing some parameters allows for a more reliable solution. To this regard a two step minimization was implemented. In the first one the parameter σ is fixed to the equivalent of $10\,mm$ FWHM, and the fit is conducted on a summed image of all the gates. The results of this fit are used to fix the bkg parameter afterward, which is not expected to vary along different gates. The other parameters are used as starting point for the next fits, since incorrect initial guess can induce the minimization in errors. Following single gates are fitted with both σ and bkg fix. Effectively we are fitting only the position of the center and the length of the short and long axes.

Imposing penalties on unfavored solutions To avoid non-physical solution the imposition of allowed ranges would be helpful. Nonetheless this has disadvantages because this might end in the parameter being stuck at the range borders, something which would be nonetheless a non-physical solution. A more elegant mathematical approach is to impose penalties in the objective function. In this case we added penalty terms on the variables themselves, emulating an allowed range. Fourth orders polynomials, which are well behaved C^∞ functions. This simulates a step-wise behavior, giving very small values inside the "range" and very sharply increasing values outside. Specifically the penalty terms, imposed on each parameter, were

$$P_t = \lambda \left(\frac{t - t_0}{R} \right)^4$$

with R representing the allowed range, t_0 the initial guess and λ the penalty strength.

Scaling of the parameters The BFGS minimization algorithm should theoretically be independent on parameters values, as the size of the steps performed depend on the Hessian. Nonetheless, to reduce the computation time, its implementation during the first steps moves with uniform steps along the direction of the gradient. That poses problems when the values are of different orders of magnitude, as in this case where activity values are of the order of 10^4, since they are expressed in $^{Bq}/_{cc}$, while typical values of the axes length are of the order of 10. To give all the parameters equal weight during the minimization they are scaled according to their expected order of magnitude.

Making a correct initial guess Minimizing algorithm are all very sensible to local minima. Therefore providing the best initial guess is crucial to obtain accurate results. For the first fit, the one of the summed image, the initial guess is x_c, y_c as the middle values of the x and y axis. The length of the short axis is initialized to $^1/_3$ of the dimension of the image (this is because the dimension of the image was chosen based on what the user indicated as the length of the short axis). Since the left ventricle is best approximated by half an ellipse the center location is initialized on the z-axis at $^1/_3$ of the dimension of the image and the z-axis length to $^2/_3$. The peak activity is initialized to 0.9 the maximum value of the smoothed and summed image and the bkg parameter to 0.7 the mean value of the activity in the image.

For the other fits, those on single gates, the program initializes the first frame fit to the results of the fit of the summed image and the following frames to the results of the previous one, as variations are supposed to be limited between a frame and the following one.

Improving minimization speed The BFGS proceeds basing the next step on the gradient of the objective function. The default implementation in MATLAB computes the gradient using finite differences. If it is possible to provide analytical expression for the gradient, calculations are sped up by a factor equal to the number of variables. Therefore I computed explicitly the gradient of the solution.

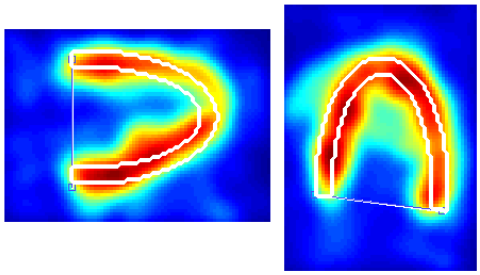

Figure 6.9: An ellipsoid fitted to a systolic gate

6.2.3 Fine segmentation of the heart

The strategy used for the segmentation of the heart is based on that proposed by Kovalsky [93]. In short this strategy defines a "center" of the heart and then, at regular angular intervals, finds the distance of the center of the myocardium, which profile is described by a gaussian shape. The simplest implementation would be to resample the image in spherical coordinate, starting from the center of the image, and fit a gaussian function along each profile. However this approach has a drawback in that several ($\sim 1'000$) fits are performed independently, and each one can fail. Regions with low activity (i.e.: defects or the apex) can lead to imprecise or wrong fits. Another drawback is that in this way the full amount of information present is not exploited . The first knowledge that can be added is that the heart is quite big and continuous, therefore the radius of the heart should be slowly varying from one sampling direction to the closest ones.

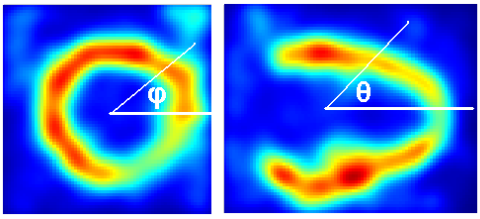

Figure 6.10: Definition of the spherical coordinate angles

Final implementation of the segmentation technique The implementation of the algorithm is based on the idea of fitting together all the different radial profiles. This would not give different results from fitting all the radii independently, since the minimum of the sum of positive functions is equivalent to the sum of the minima. However it is possible to implement in the objective function some constraints and penalties to take advantage of the nature of the problem. The coarse segmentation previously performed provides a good initial guess and also finds the point most suited to be used as the center of the radial segmentation. After the image $I(x, y, z)$ has been resampled to spherical coordinates $I(r, \theta, \phi)$ one can imagine our segmentation technique as a series of fit along each θ and ϕ coordinate. For each θ, ϕ radius the sum of the squared differences (SSD) between the radial

profile of the image and the parametrization function

$$F_{\theta,\phi} = bkg(\theta,\phi) + a(\theta,\phi) \times exp\left(-\frac{(r - r_{max}(\theta,\phi))^2}{2\sigma^2}\right)$$

is computed. In this segmentation model $a(\theta,\phi)$ represents the activity concentration in the sector of the heart in the θ,ϕ direction of the heart, $r_{max}(\theta,\phi)$, when converted back to cartesian coordinates, represent the position of the center of the myocardial wall in that point and $\sigma(\theta,\phi)$ parametrizes the wall thickness. In this model the epicardial and endocardial walls of the heart are defined by the mesh of points at the coordinates $r(\theta,\phi) \pm \sigma(\theta,\phi)$. The myocardial wall is divided in 31 steps along the θ and ϕ dimension, while the radial dimension it is sampled 51 times. The complete procedure goes as follow:

- Resampling of the original image in spherical coordinates (the center used for each gate is the one found in the coarse segmentation)
- Definition of two logical masks in spherical space
  - The first mask is used to exclude the voxels in the spherical space outside the volume of the image in the cartesian space
  - The second mask discards directions where the myocardial wall is not present (i.e.: more basal than the septal plane)
- Initialization of the variables:
  - r is initialized to $r_{i,j} = a\cos^2\phi + b\sin^2\phi$
  - $a_{\theta,\phi}$ is initialized to the maximum value along each radius. Then this matrix is smoothed with a median filter to remove potential outliers.
  - σ is uniformly initialized to the equivalent of $10\,mm$
  - bkg is set to the value previously found in the coarse segmentation.
- A first fit is performed to determine the values of a and r vectors. Here we fix bkg to 0 and σ is fixed to the equivalent of $10\,mm$ FWHM. A roughness penalty, explained later, is imposed on each parameter.
- A second fit is performed fixing a to the values previously found (subtracting bkg) and fitting σ together with r. (This is needed to allow finer adjustments of r when the wall thickness is modified). Also here a roughness penalty is applied on each parameter.

In figure 6.11 we show, as an example, an iteration of the first step of the fit, showing the original image, in spherical coordinates, and the simulated image being fitted (The two main differences that can be noted are the profile having a constant width, due to the fixed σ, and the null background).

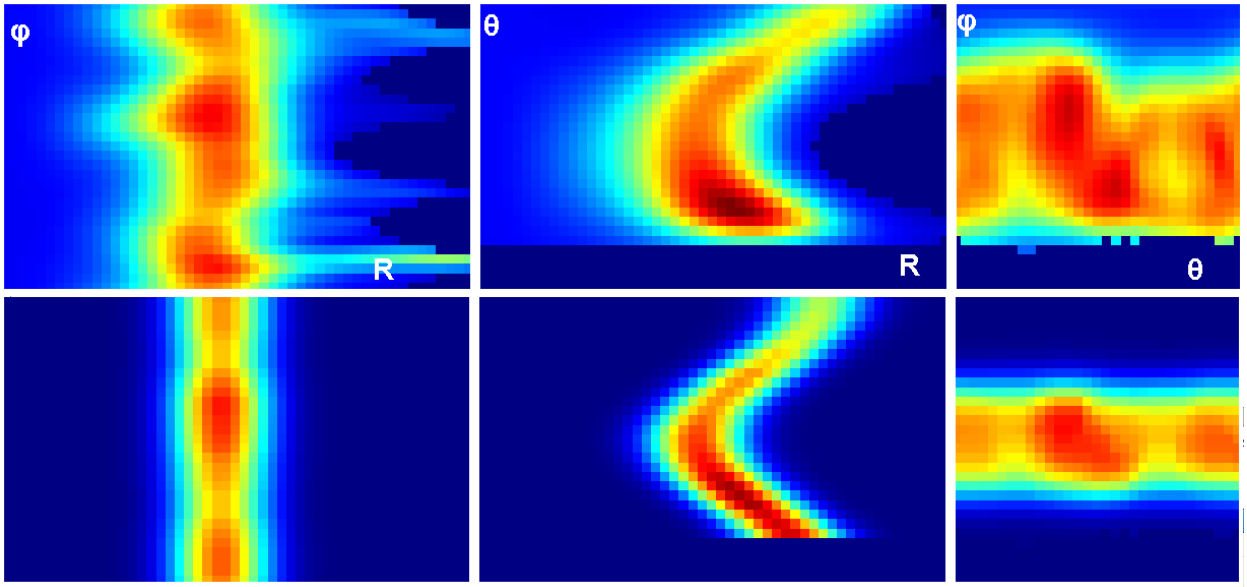

Figure 6.11: Upper row: orthogonal view of the myocardial image resampled in polar coordinates. Lower row: the image being fitted. It can be seed how the position of the peak activity is almost independent on the ϕ direction and how it varies smoothly along θ. It can be seen how the position of the peak increases with θ.

6.2.3.1 Roughness penalty

A piece of information that can be exploited to improve segmentation quality is the fact that the shape of the heart is regular. Therefore in the fit it can be imposed a penalty on the roughness of the parameters matrices. The penalty looked for avoids sharp variations of any parameter from one point to the other. Therefore I defined the roughness of a matrix of parameters as the sum of squared differences between a matrix and a smoothed version of itself. If the vector is already smooth the difference will be minimal or none, while if sharp variations are present this quantity would be larger. Given V as the matrix of parameters and V_{sm} the smoothed matrix of V, with an appropriate kernel, the roughness is then defined as

$$R_V = \sum_{\theta} \sum_{\phi} \left(V(\theta, \phi) - V_{sm}(\theta, \phi) \right)^2$$

Kernel and convolution

In this implementation the myocardial wall is resampled each 12° along the ϕ direction and each 6° in the θ direction. The condition imposed is that variations in the geometry of the heart are of a scale larger than these constants. Given the average radius of the heart in the diastolic phase ($\sim 25\,mm$) this mean that a measure is taken about each $5\,mm$. It is imposed that the of changes in the geometry of the heart happens on a larger scale, therefore the smoothed reference is obtained fwith a gaussian kernel with an half pixel σ, which corresponds to 1.17 pixel FWHM (e.g. variations of the shape of the heart on a scale larger than $11\,mm$). A kernel of 5×5 dimension was used. The reason for this assumption

is evident for the σ and a parameters, because modifications of the average wall thickness on such small scales (σ) are not known and because anyway in PET uptake defects (reductions of a) on scales smaller than $\sim 10\,mm$ cannot be seen. For the r parameter this requires an ad-hoc assumption. It is known that, being the figure closer to an ellipsoid than to a circle, r increases with increasing θ. Nonetheless we hypothesize, and this is empirically justified, that the LV is indeed similar to an ellipsoid, therefore with r varying smoothly with θ and that eventual changes from the circular geometry in each short-axis plane ($\theta = const$) are not isolated bumps but "big" structures that should occupy many ϕ samples and be replicated in more than one plane. Figure 6.12 shows the value of the r parameter for all the θ, ϕ pairs for a converged fit accurately defining a myocardial wall. A clear pattern of values justifying the roughness penalty can be appreciated.

The discrete convolution is, of course, ill-defined at the borders of a matrix. To overcome this problem the matrices of the parameters are padded at the borders to allow an accurate computation in the original range. Along the ϕ direction it is possible to exploit the circular symmetry of the variable, i.e. $M(\phi + 2\pi, \theta) = M(\phi, \theta)$. Therefore the pad of the matrix along the ϕ dimension takes values from the elements at the other side using the previously written relation. Each side is padded with 2 elements, as the kernel dimension is 5×5. For what concerns the θ variable is not periodical and is limited between $[0, \pi]$. As can be seen

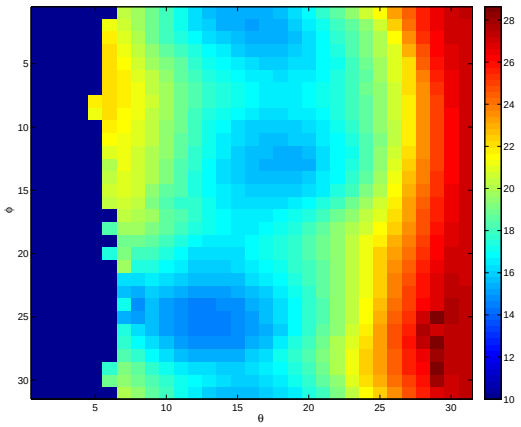

Figure 6.12: Map of the r parameter. The pixel in dark blue at the left are those corresponding to directions upper than the septal plane. The units of the $z-$axis are in pixel.

from figure 6.12 approaching π converges all of the elements to the same value, as all of the ϕ radii approach to the same point. A natural padding for this dimension is a reflection (i.e.: ...N-2,N-1,N;N-1,N-2 etc...) that can be thought as returning back, after having arrived to a pole of the sphere. So a reflection of two pixels is performed at this border. On the other side the myocardium "finishes", the septal plane does not starts at $\theta = 0$. To account for this a mask is present on the parameter maps, as shown in figure 6.12. Nonetheless a pad with zeros along that direction before performing the convolution would introduce an unphysical bias in that direction. To cope with this a pad along each $\phi = const$ line is done with the value of the last unmasked element, in the assumption that is value is already the best estimate, resulting in no introduced bias.

6.2.4 Visualization of the segmentation results.

After the segmentation has been performed it is necessary to visualize it, to evaluate the result. To do this I implemented a program in MATLAB that shows three orthogonal slices of the myocardial PET (short axis, horizontal long axis and vertical long axis). Since this segmentation procedure does not give in output a binary logical mask an ad-hoc strategy must be adopted. The visualization technique chosen is to superimpose on the three orthogonal slices the contours of the mesh of points obtained. To generate the contour an approximated segmentation mask was used. This mask was generated in the following way:

- A mask is set to true in the pixels corresponding to points given in the surface meshes.
- This is done for all the three mesh, endo, mid and epi surface
- A closure operation is performed (dilation followed by erosion, with a cubic square element of 10 voxel side, 15 mm)

The result of this operation is shown in figure 6.13. This produces a segmentation mask with

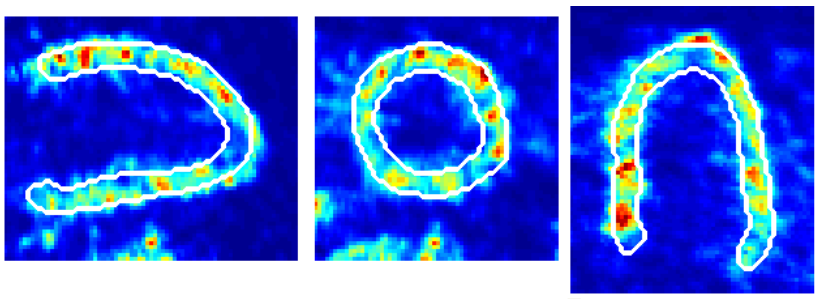

Figure 6.13: Visualization of the segmentation results

a good approximation. Drawing the contour of this matrix overlapped on the PET image allows to check qualitatively the segmentation accuracy.

6.2.5 Coupling of the control points for the spline generation

This segmentation technique produces in output a set of points which describe the surface of the myocardium wall. To morph the different gates it is necessary to generate a deformation field which brings the points associated with the same "bit" of the heart to the same position. Therefore it is necessary to describe a rule for the 1-to-1 correspondence between each of the points found in the target gate and the points found in the gate that needs to be morphed. The fundamental hypothesis used is that the heart does not twist much while contracting. This can be translated with the fact that the ϕ coordinate for each bit of tissue does not change between the different gates. On the θ axis it is not possible to make similar assumptions as the tissue-bits will indeed move. Also the range of θ value will restrict during contraction. Nonetheless it is possible to make an easier to justify assumption saying that the relative position along the θ axis will not change, as bit of muscles do not jump over themselves. The most basal bit remains the most basal one and the apical one remains the apical, with all those in the middle moving accordingly, as schematized in figure 6.14.

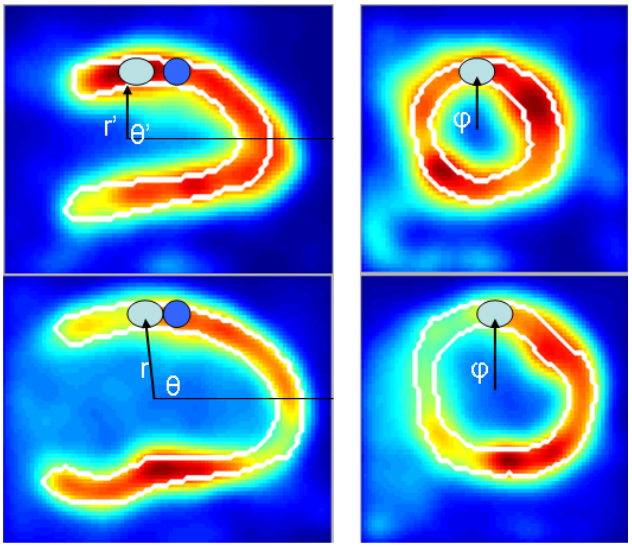

Figure 6.14: Concept of the morphing procedure. A selected "bit of tissue" (represented as the greenish oval) during contraction will change its distance from the heart center from r to r', Its θ coordinate will also change to θ', both because the long axis reduces its length and because the definition of the "center" along this direction is not unique. Nonetheless the order of the points along the θ axis must remain the same as a "bit of tissue" cannot jump over its neighbors (represented as the blue circle). The other assumption made is that the myocardium does not twist much during contraction, therefore the ϕ that identifies a "bit of tissue" remains constant. Control points of the TPS are then coupled using this principle (same ϕ and same order along θ)

This assumption can be translated in a simple criterion if the mesh of points coming from the segmentation procedure have the same number of points and are ordered according to θ and ϕ. In this case the coupling is naturally defined by linking points that occupy the same position in the vector. The actual situation is a more complicated as the number of points along θ is different in each gate. To overcome this the method makes use of the mask defined in section 6.2.3. The second mask describes the sampling radii that are associated with the myocardium. It should be noted that, due to the inclination of the septal plane, the number of valid θ samplings is generally different along each ϕ direction. The strategy implemented is interpolating the number of θ elements along each ϕ direction to the number of elements in the in the target gate. In this way for both the target image and the original image there are matrices of points describing the myocardial surface with the same number of elements and in the same order. In this way the algorithms couples, back in cartesian coordinates, the elements according to their order in the matrix. Afterward the TPS field, described in subsection 6.2.1, is built using this control points. The deformation is then applied on the original images and each gate is stored. In this way the user can observe the quality of the morphing procedure on each gate, before averaging them.

6.3 Evaluation of the performance of the morphing procedure

6.3.1 Phantom test

The first test of the procedure was performed on our phantom, with the data acquired and reported in section 5.5.1. The first evaluation performed was a qualitative evaluation. The morphed image of the double gated reconstruction and the static images are shown in figure 6.15. A number of improvements can be appreciated. After the application of morphing the activity concentration becomes uniform along the wall, whereas in the static reconstruction the activity along the inferior and superior walls is underestimated. On top of this the measured activity concentration is higher. Finally, the defect in the inferior-later is sharp, with the thin wall maintaining almost the full activity and the defect region showing almost no uptake. This is like in the acquisition without motion and differently from the static reconstruction of the acquisition with motion, where a single area of reduced uptake can be seen.

A more quantitative test performed was the calculation of a similarity function between the reference image and the target image. Again the sum of squared differences (SSD) was used. In figure 6.16 the trend of the SSD between different respiratory gates at a fixed cardiac gate is shown, before and after morphing. It can be noted that with distant respiratory gates the SSD increases markedly. With the application of morphing all the gates lower the SSD down to a similar very low value. A similar result is seen when analyzing the SSD as a function of the cardiac gate at a fixed respiratory gate, figure 6.17. It can be noted that the SSD increases drastically when the systolic phase approaches (n=4) and decreases back to almost zero when going back to the diastole. With morphing it can be noted that the SSD is reduced markedly for each gate, but the residual value still shows an increased value for

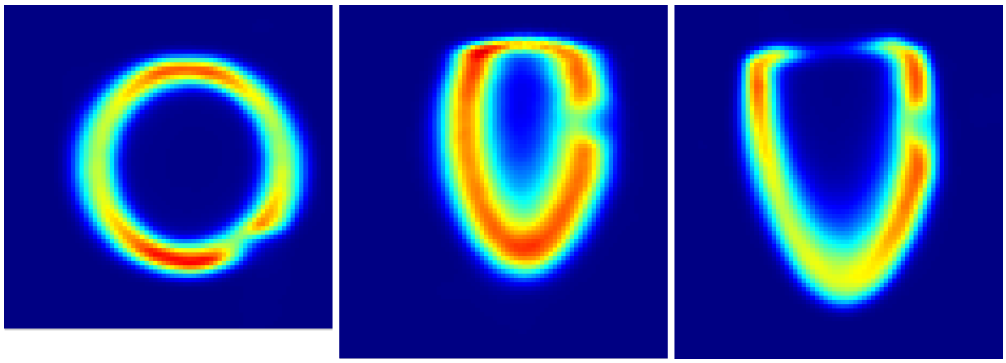

(a) Static reconstruction

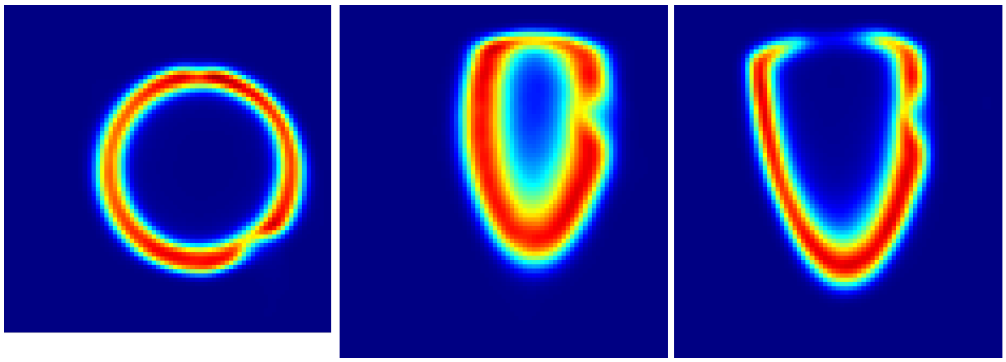

(b) Results of morphing

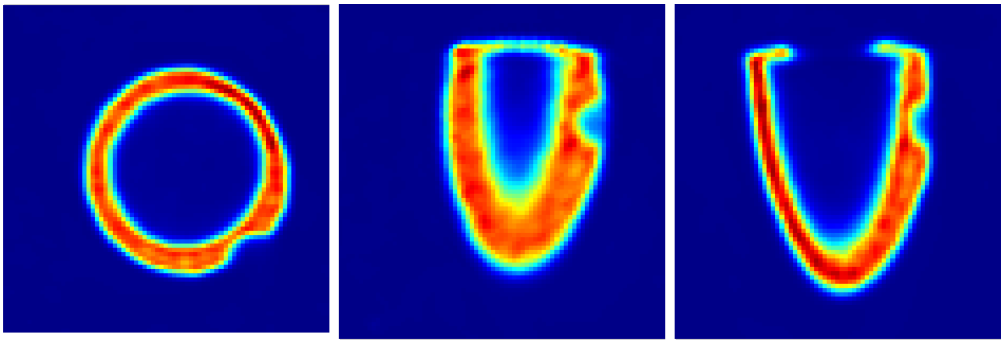

(c) The static acquisition.

Figure 6.15: Visual comparison of the images obtained applying the morphing procedure to our dynamic phantom, compared to the image affected by motion and to the images obtained in the motion-free acquisition. The color level used are the same.

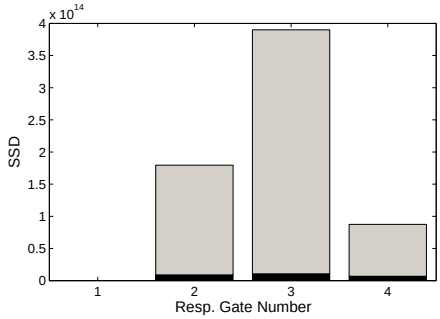

Figure 6.16: Sum of the squared differences between the four respiratory gates at a fixed cardiac gate. In gray are reported the original values and in black those after the application of morphing. (For gate 1 the SSD is zero as it is the reference gate)

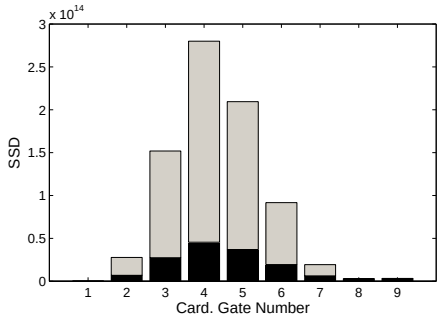

Figure 6.17: Sum of the squared differences between the 9 respiratory gates at a fixed respiratory gate. In gray are reported the original values and in black those after the application of morphing. (For gate 1 the SSD is zero as it is the reference gate)

the most "distant" cardiac phases.

6.3.2 Application to patient data

Afterward the procedure has been applied to double gated reconstructions of patient data that underwent either $^{18}F - FDG$ or $^{13}NH_3$ scans. In case of ammonia studies both rest and stress scan were processed. There is no ground truth so the only possibility is to spot qualitative differences, evident artifacts or visibly incorrect segmentation results. I tried the morphing procedure on a total of 15 studies and it visibly failed only two times.

Problems encountered The results involved artefactual images that were due to wrong segmentation results. In both cases the reason for the failure was a peculiar LV anatomy. The first case involved a patient with a very active liver in contact with the inferior wall, shown in figure 6.18. In this case the segmentation failed (but for such extreme cases the information about the wall position is absent, therefore any algorithm based on PET data will probably fail). The second case involved a patient with hypertrophic cardiomyopathy

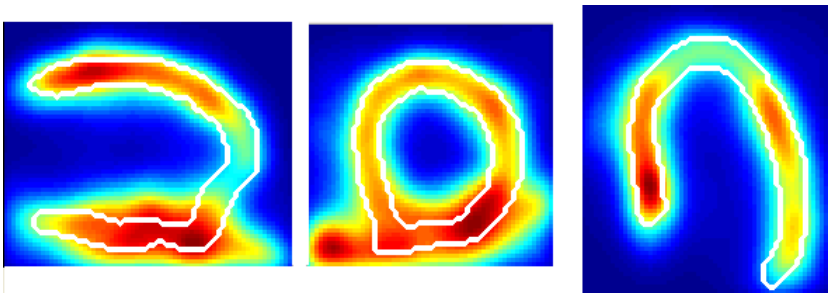

(a) A diastolic gate

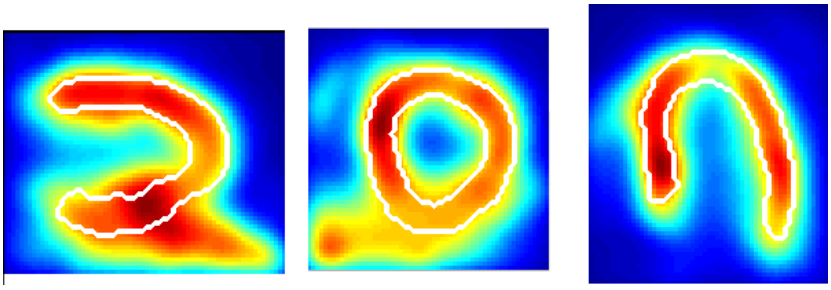

(b) A systolic gate

Figure 6.18: A patient on which the algorithm failed. As can be seen the activity in the liver is so high that the segmentation algorithm can not distinguish the two structures.

of the apex. In the stress exam this area suffered from hyschemia that results in a reduced uptake. For this reason in the diastolic phase the algorithm correctly found the myocardial wall along the apical region, while in the systolic phases it passed trough a different place as a more basal area of continuous uptake appeared, shown in figure 6.19. Therefore the coupling of the point was erroneous, as it referred to different structures, and consequently gave artifacted results.

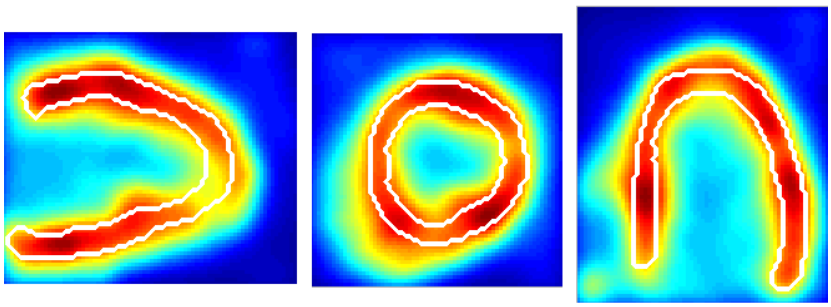

(a) The diastolic gate

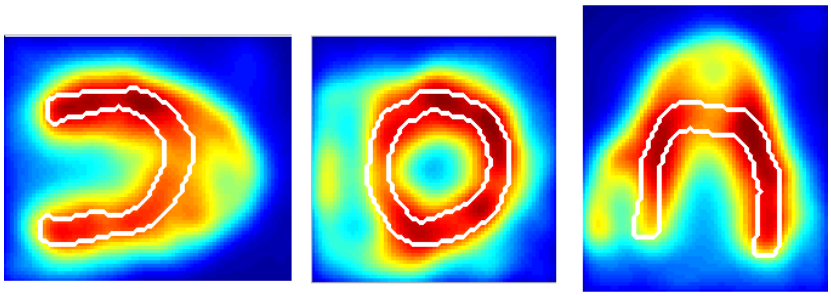

(b) A systolic gate

Figure 6.19: Another patient on which the algorithm failed. The structure of the hyschemia in the apex of this patient is so peculiar that the algorithm identifies as the apex, in the systolic gate, only a part of the myocardial wall.

Successful outcomes For all of the other 13 studies on which the morphing procedure was tried the segmentation looked correct in all of the phases and, as a consequence, the results of the morphing procedure looked natural and free from artifact.

A complete sequence is shown here for a successfully working patient. In figure 6.20 two frames from a double gated study are shown. The first one is the diastolic gate used as a reference and the second one is a systolic frame, the most distant condition. It can be seen that the amount of stretching to be performed is considerable. The segmentation procedure gave the results shown in figure 6.21, on smoothed images for more clarity. It can be noted that the estimated contour is quite regular and replicates well the appearance of the myocardial wall. Following the different gates were morphed according to this segmentation. Two single gates are shown in figure 6.22. The first shown is a diastolic gate, a different one from the reference. It can be noted how the image looks natural, as most of the transformation consists in a translation and a very limited stretching. Instead the systolic gate shows how much it has been stretched. Still no artifacts appeared and its shape is effectively the one of the reference image.

Finally all the morphed frames are averaged, with the results being shown in figure 6.23. The level of noise this time is acceptable for diagnostic purposes, especially considering that these images are not post-filtered. Many other differences can be appreciated between the static reconstruction and the morphed double gated image. The myocardial wall is thinner in the morphed image. It also has a less blurred appearance. The ventricle as a whole appears bigger, as all has been restored to the diastolic phase, and the activity distribution looks

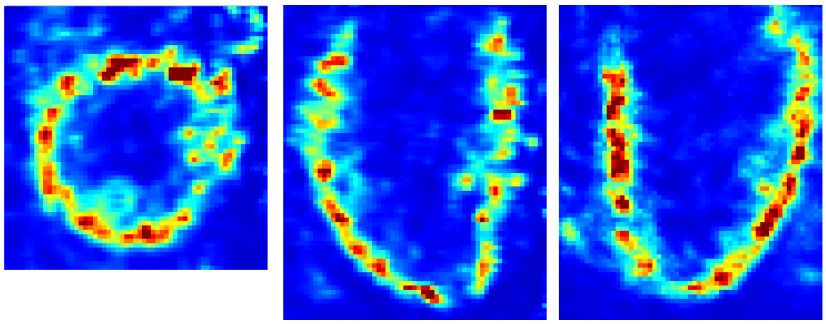

(a) the diastolic reference frame

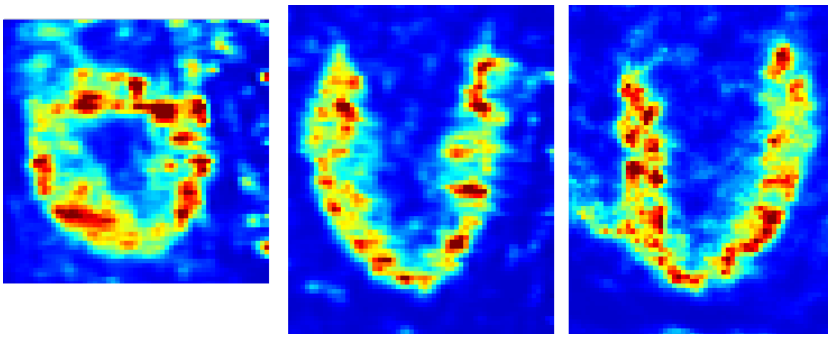

(b) systolic frame

Figure 6.20: The diastolic reference (a) and a systolic frame (b) of a double gated cardiac study

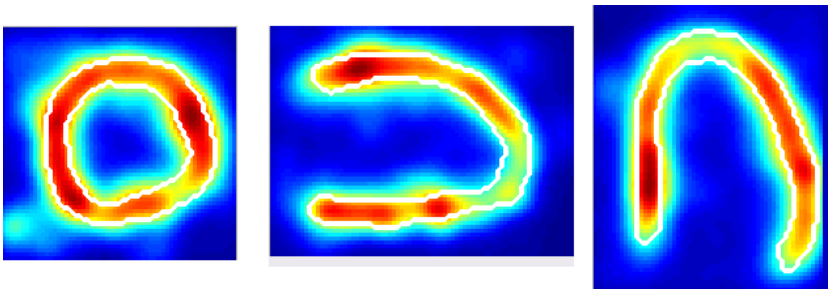

(a) A diastolic gate

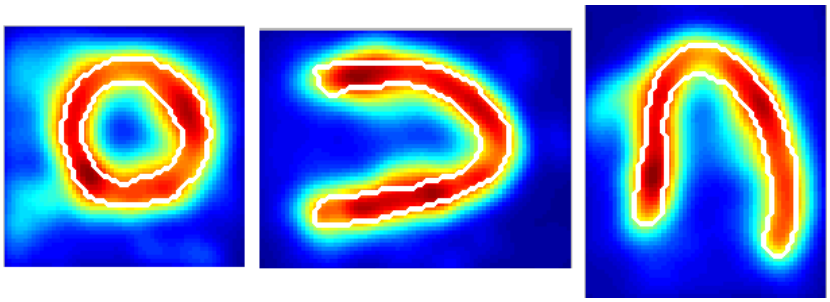

(b) A systolic gate

Figure 6.21: Results of the segmentation in two different cardiac phases

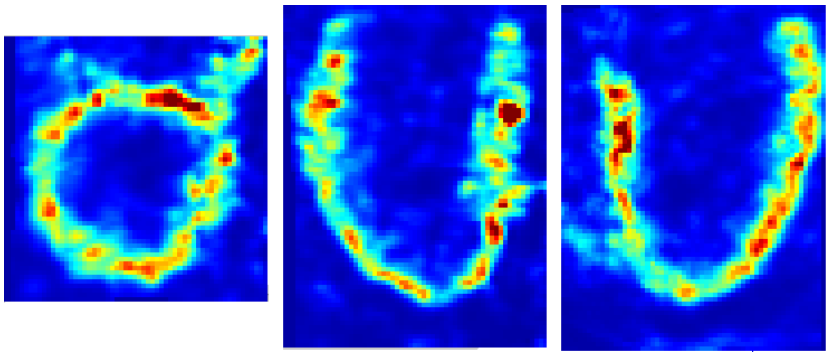

(a) A diastolic gate

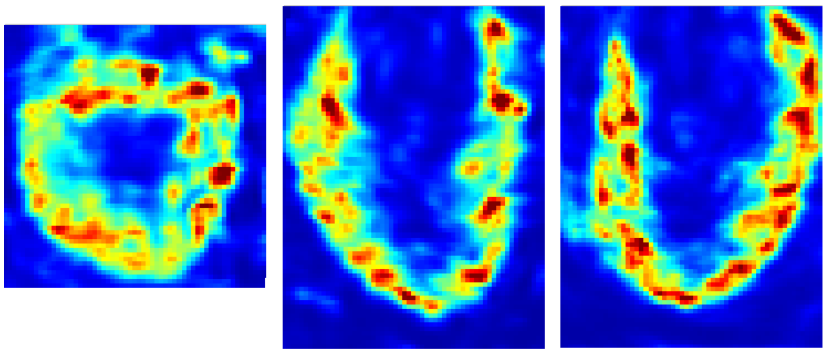

(b) A systolic gate

Figure 6.22: Single gates morphed

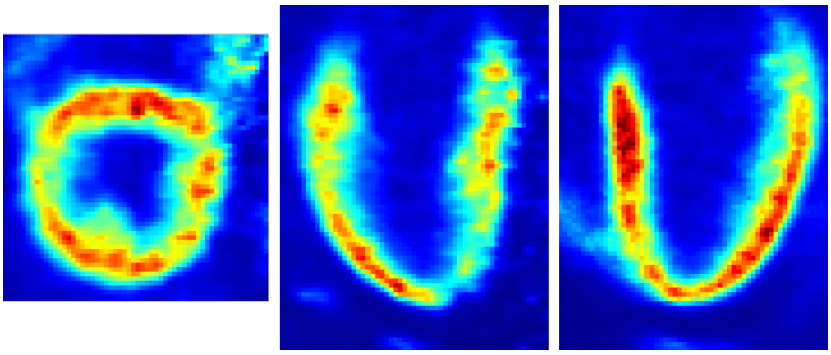

(a) Static reconstruction

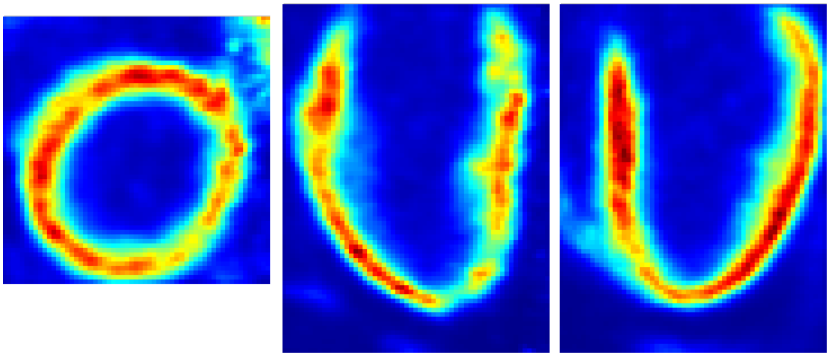

(b) Morphed image

Figure 6.23: Results of the morphing procedure compared to the static reconstruction, the same color scale is used for the two images

more homogenous. This can be noted particularly in the basal-anterior and in the basal-later sections.

Another case is reported in figure 6.24, and is relative to an $^{18}F-FDG$ study of a patient suffering from dilative cardiomyopathy, that shows a defect in the anterior wall The defect in

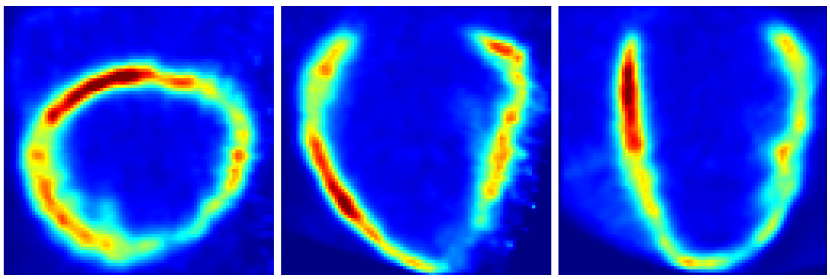

(a) The morphed image

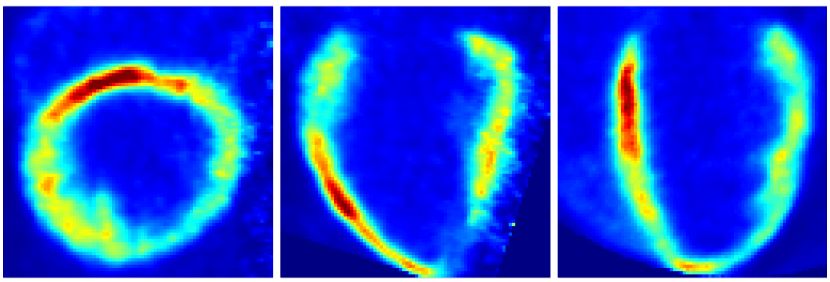

(b) Original image

Figure 6.24: The comparison of the morphed double gated reconstruction and of the static reconstruction of an $^{18}F-FDG$ study.

the anterior wall (horizontal long axis view) is more defined and many of the wall segments are less blurred, as the antero-lateral wall in the short axis view or the inferior wall in the horizontal long axis view.

The last case presented is those coming from a stress $^{13}NH_3$ study of an hypertrophic patient with a relatively small heart and with an inducible hyschemia in the basal-anterior wall, in the hypertrophic segment, Fig. 6.25. Many features already seen in the phantom and in the other patients can be appreciated here. The uptake in the healthy regions becomes more uniform, as can be seen a bit in the inferior wall (horizontal long axis view) and much more in the lateral wall (vertical long axis view); these walls appear also as less blurred. No differences can be noted in the defect, this is probably due to the large size of this structure in an hypertrophic patient.

6.4 Conclusion

Two different algorithms to register images myocardial PET images have been proposed. The first one aims at registering different respiratory phases of a study. It can not recover the whole statistic of a double gated study but it should be particularly reliable and exempt from artefacts.

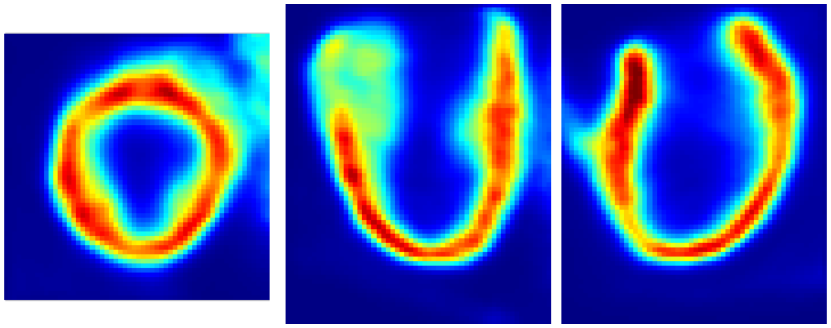

(a) Morphism

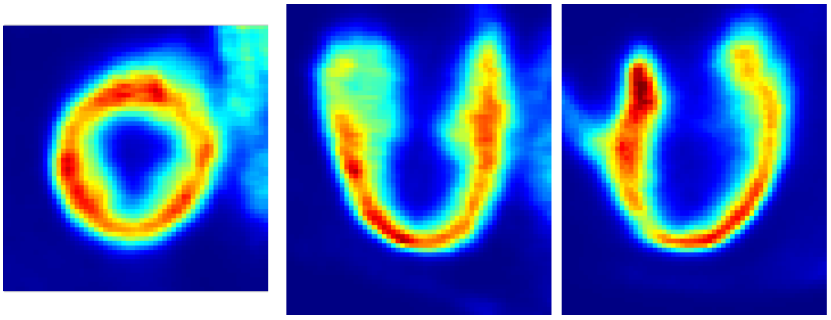

(b) Static reconstruction

Figure 6.25: An hypertrophic hyschemic patient in a stress $^{13}NH_3$ study, comparing the morphed double gated reconstruction and the static reconstruction

The second algorithm proposed aims at registering all of the phases of a double gated study. This would allow to recover the full statistic acquired in a study and, therefore, to achieve the best signal to noise ratio, providing therefore an improved diagnostic confidence. Of all the studies on which the procedure were tried it failed in only two times, both due to peculiar reasons specific to the patient. In all of the other cases no evident artefacts were seen and the final result was an improvement in the image quality due to better structure definition of the static reconstruction and noise levels comparable to that, recovering from the unfavourable appearences of the double gated images.

Part II

Kinetic modeling to assess myocardial perfusion

Chapter 7

Kinetic modeling for myocardial perfusion assessment

In the previous chapters several techniques to improve the quality of the image of a PET scan were studied. Nonetheless a unique feature of PET is the ability to provide quantitative information regarding physiological processes. This is achieved analyzing the change of the tracer concentration in a volume over time. This is referred to as "kinetic modeling" as it models the kinetics of a drug. One of the basic biologic functionality is blood perfusion (i.e.: the amount of blood flowing in a unit time in a unit of tissue). In the case of the two most important organs of the human body, the heart and the brain, perfusion is of particular clinical significance. The potentials of PET technology to investigate perfusion has been addressed already in the same days when the first PET tomographs were being built. In 1971 the use of ammonia marked with ^{13}N was proposed [94], in 1972 the possibility to image the myocardium was studied [95] and in 1979 the use of this tracer to assess quantitatively myocardial perfusion was investigated in depth by Schelbert, Phelps et. al [96]. Another nuclide of particular interest is ^{15}O. The possibilities of using elements so common in biology was looked with particular interest by the nuclear medicine community but, due to their short life, only a limited number of compounds proved feasible to be synthesized. Still a number of compounds of interest have been achieved. One, of evident biological significance, is $^{15}O - H_2O$, but also CO, CO_2 and O_2. An useful feature of $^{15}O - CO$ is that is tags hemoglobin *in-vivo* therefore allowing the imaging of blood vessels. The feasibility of perfusion studies with $H_2{}^{15}O$ also dates back to the '70s, with a first paper from Ter-Pogossian dating back to 1969 [97]. Following cardiac perfusion was widely studied in the research setting but lacked a definite role in clinical practice. Recently the interest in quantification in cardiac perfusion studies revamped as a number of studies showed the importance of added information of the myocardial blood flow, both as a diagnostic factor [98, 99] and as a prognostic factor [100]. In this scope in this chapter I perform a brief review of the existing techniques, than I perform an evaluation of the mathematical proprieties of the most common analysis strategies. Following, in the next chapter, I report a study about the effect of image reconstruction techniques on quantified myocardial blood flow with $^{13}NH_3$ PET.

7.1 Kinetic modeling

A peculiarity of PET imaging is that it is possible to record the activity concentration in each part of the body in a dynamic fashion. Typical framing schemes encompass frame durations as short as 5 seconds, with this limitation being imposed only by the amount of counts recorded. In this way it is possible to follow the changes of the distribution of a pharmacon in a tissue over time. If this kinetic can be described by a simple mathematical model it is possible to compare the activity variation over time to this model and extract parameters of clinical interest. This process is usually referred to as "kinetic modeling".

The concept underlying kinetic modeling is that of "compartments", that has been borrowed from biochemistry. Following a drug inside the human body it is said to be in a new "compartment" each time it enters a new biological structure or each time it changes its molecular structure due to an interaction [101]. An example of biological structure change is the movement from the blood to the extra vascular space, from there to inside a cell and so on. Example of molecular changes include the interaction with an enzyme, the binding with a receptor, the different steps of a methabolization cycle in a mitochondria etc... It can be see that generally the number of compartments for a drug can be very high (i.e. : > 100)

With this in mind in nuclear medicine a mathematical multi-compartmental model was proposed to described tracer dynamics [102]. Here a compartment is defined as an homogenous entity within which the entities being modeled are equivalent. In practice, for nuclear medicine, this means that inside a specific tissue volume, assumed to be homogeneous, there are a number of compartments describing the changes to which the drug undergoes. In each compartment C_i the rate of change of tracer concentration is described with a set of linear differential equations. In its most general definition a system with n compartments is described by the set of ordinary differential equations $\dot{q} = Kq + u$ with

$$K = \begin{matrix} k_{11} & k_{12} & \cdots & k_{1n} \\ k_{21} & k_{22} & \cdots & \vdots \\ \vdots & \vdots & \ddots & \vdots \\ k_{n1} & k_{n2} & \cdots & k_{nn} \end{matrix}$$

being the matrix that parametrizes the exchang between all the compartments in the two directions (k_{12} describes the amount of tracer going from compartment 1 to compartment 2 and k_{21} the opposite.) This matrix is not symmetrical. q is the vector of the tracer concentration in each compartment and u is the vector of the stimula applied to each compartment. In nuclear medicine study there is (usually) only one external stimulus, which is the concentration of the injected drug in the arterial blood (i.e.: what has been injected). This stimulus interacts only with the first compartment, which represent, generally, the extravascular space or a related entity. In nuclear medicine the most complex models are limited to three compartments and interactions are allowed only between contigouus compartments (i.e.: the matrix K is a very sparse matrix, often a band matrix of bandwidth not more than 3). A general kinetic model for a brain receptor and the kinetic model for $^{18}F - FDG$ are shown in figure 7.1 as examples.

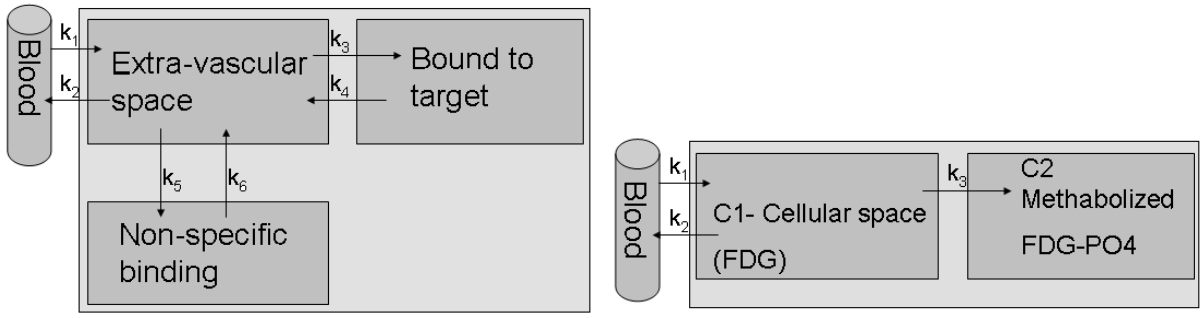

(a) A general kinetic model **(b)** $^{18}F - FDG$ kinetic model

Figure 7.1: Two sample kinetic models. In subfigure (a) a general model for, let's say, a cerebral receptor, which also models non-specific binding. In subfigure (b) a simpler model, which describes the most widely used PET tracer, $^{18}F - FDG$, which features irreversible tracer uptake. This tracer enters the cellular space and then it enters the mythocondria as the normal glucose. Differently from glucose when it undergoes phosporillation it cannot undergo glycolysis becaus it misses the hydroxyl group. Therefore the tracer in this molecular state is trapped and cannot be released back to the blood or undergo any further transformation. All the various compartments are enclosed in a single box to underline that with a nuclear medicine study it is not possible to distinguish the amount of tracer in the various compartments as they all contribute to the activity measured in that volume

7.1.1 Fitting, Time Activity Curves, Input function and metabolites

With the equations previosly stated it is possible to compute, knowing the various k_i the concentration of tracer over time for the various compartments. Conversely, fitting the time variation of the tracer contentration in the various compartment over time, it is possible to determine the values of the various k_i. As these parameters characterize metabolical processes some or all of these k are of clinical interest. PET can determine only the total activity concentration in a volume, there is no way to distinguish the various contribution of each compartment. Therefore it is not possible to measure C_i for each compartment i but instead only a quantity referred to as C_{Tissue}, wich is the sum of the concentration of all the compartments present in that volume. On top of this, as blood perfuse each tissue up to a microscopical level, a fraction of the volume analyzed will be necessarily occupated by blood. Therefore the final measured activity concentration C_{PET} will be $C_{PET} = v_b C_{blood} + (1 - v_B) \times \sum C_i$, with C_i the activity concentration in each compartment present in the tissue imaged in the PET voxel analyzed, C_{blood} the activity concentration of the blood and v_b the, dimensionless, fraction of the volume under analysis occupied by the blood.

When analyzing a dynamic PET scan, usually one would define a Volume Of Interest (VOI) and replicate it over all the dynamic frames. The average activity in the VOI in each frame would then be associated to the time stamp of that frame and a Time-Activity-Curve (TAC) of C_{PET} would be built. To estimate the parameters of the kinetic model a minimization is performed, usually of the χ^2 of the predicted response compared to the measured C_{PET}.

There are two main strategies to acquire this input function (IF), which is the concentration of the injected tracer in the arterial blood. The first strategy is to perform an arterial blood sampling. Its advantages is that it can be extremely precise if continous radioactivity samplers are used and that, once the patient is connected, arterial blood samples can be acquired at any time. Its disadvantages are that it is invasive, that requires a good cross-calibration with the PET scanner and that, mostly in cardiac studies, there can be problems of time synchronization between the arrival of the tracer to the organ and to the sampling access. This is problematic only in a limited number of cases, where fast dynamics are studied and fast bolus injections are used. The other option is to measure the radiaoctivity concentration of the blood on the PET images themselves. Given the poor spatial resolution of PET this is possible only where large (i.e. $> 1\,cm$ in diameter) blood pools are present. This is often the case in cardiac studies where the ventricles and the aorta are clearly visibile and separeted from other organs. The advantage of this methodology is that it is very easy to use and does not require any bothersome treatment to the patient. In cardiac studies the time syncronization of the tracer concentration with the heart itself is of course good. On the negative side this strategy is affected by all the known PET quantification problems and also by patient motion.

A problem associated with input function, independently on how they are measured, is the presence in the blood of the so called "metabolites". These are different molecules from the injected ones that are tagged with the same nuclide. They form by the interaction of the original tracer molecule in other organs and/or with different pathways compared to the one under study. The problem with them is that their activity is indistinguishable to that of the actual tracer, but they behave with different kinetics. Therefore their contribution to the activity of the inpuct function must be estimated and then dealt with.

If the new compound(s) is such that it does not interact with the organ under study it is possible just to subtract the activity of the metabolite from the input function activity to achieve a correct fit. If the metabolites also interact with the tissue under study, on top of measuring the metabolites fraction in the blood over time like before, ad-hoc procedures must be developed to address the situation.

7.2 Quantitative Cardiac perfusion measurments

Cardiac perfusion is defined as the volume of blood entering an amount of myocardial tissue in a time unit. The unit usually chosen to measure this quantity are $ml\,mg^{-1}min^{-1}$; with this units the normal values of flow range from 0.5, in a resting setting, up to 4, in the most extreme hyperaemic condition [103]. Perfusion would show up as the k_1 of any tracer which has the proprierty of being fully extracted from the capillary bed during the blood passagge. This fraction of tracer that gets extracted in a single passagge is called "extraction fraction", and depends on the flow itself. A limited number of compunds actually satisfy this request of extraction fraction close to 1 in the flow regions of interest. The "Renkin-Krone model" relates the amount of molecule extracted by the capillary bed in a single passagge to the flow with the formula

$$E = 1 - e^{-\frac{PS}{F}}$$

where E is the extraction fraction, F is the flow and PS is the Permeability-Surface product. The permeability is different for each molecule and depends also on the organ studied (i.e. in the brain, due to the blood-brain barrier, many compounds have reduced or no permeability). This model has been proposed and takes its name from two different scientist that studied this effect while modeling pharmaco-kinetics, not related to PET imaging [104, 105].The effect of the extraction fraction for the most common PET MBF tracers is shown in figure 7.2.

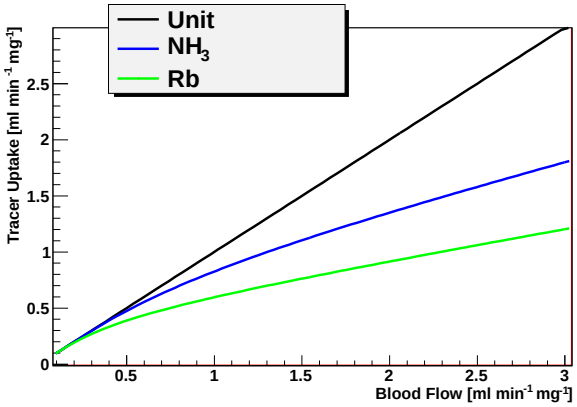

Figure 7.2: Tracer uptake for NH_3 and Rb [106]. Unity line has been superimposed. H_2O extraction fraction has been measured to be close to 1 in all flow range investigated [106]. Studies on $^{18}F-$Fluripidaz found an extraction fraction greater than 90% in all the range investigated [108, 109].

Since k_1 is measured in units of $[T^{-1}]$ to obtain the myocardial blood flow in the requested units it is necessary to divide it by the myocardium density, which has been measured to be $1.04 g/cm^3$.

The most widely used tracer to quantify blood perfusion are ^{15}O-water and ^{13}N-ammonia. Some models have also been proposed to quantify perfusion using ^{82}Rb but they did not gain widespread use, since it suffers from a very low extraction fraction, which must be corrected for, thus amplyfying the error [107]. Recently a new tracer marked with ^{18}F has been proposed and has finished phase 2 clinical trials. A summon of the most salient proprieties of the tracer in question is reported in table 7.1.

7.2.1 Water

An important tracer to study myocardial perfusion is water. ^{15}O is obtained by the reaction $^{14}N(d,n) \rightarrow^{15} O$. It has the advantage of having an extremely simple kinetic, since water is the main constituent of the blood. Its main disadvantages are its short half life, $t_{1/2} = 2\,min$, and a medium positron range. As the kinetics of water does not allow its trapping inside the myocardium it is difficult to visualize it. Its short half life does not allow to accumulate an high counting statistics, therefore contributing to the poor image quality. To generate an image where the myocardium is visible with an high enough contrast the technique usually used is to subtract the sum of those dynamic frames where all the activity is concentrated

Tracer	^{82}Rb	$^{13}NH_3$	$H_2\,^{15}O$	$^{18}F - Fluripidaz$
$t_{1/2}$	$76\,s$	$9\,min\,58\,s$	$122\,s$	$109\,min$
Positron mean range	$5.9\,mm$	$1.5\,mm$	$2.5\,mm$	$0.6\,mm$
Positron max range	$17\,mm$	$5.1\,mm$	$8.0\,mm$	$2.4\,mm$
Positron Max energy	$3.3\,MeV$	$1.2\,MeV$	$1.7\,MeV$	$0.635\,MeV$
Dose for a Rest/Stress study with current protocols	$5\,mSv$	$1.6\,mSv$	$1\,mSv$	$6\,mSv$
Kinetic	Uptake	Uptake	Clearence	Uptake
Notes	Low quality images, problematic quantification		Only quantitative studies possible	

Table 7.1: Proprieties of the PET MBF tracers currently used in clinics or under experimental investigation

inside the blood pool to the sum of those frame where the activity is mostly concentrated inside the myocardium. This allows to recognize the structures clearly enough to position the ROIs. The water data are analyzed with a 1-compartment reversible model. A peculiarity of water is that, as it completely mixes with blood, it is possible to impose a constrain on the relation between k_1 and k_2. As blood does not accumulate inside tissue, the inflow of blood entering a volume of tissue equals the outflow. This kind of model is called a "freely diffusible model", as the tracer is diffusing freely in the tissue and does not interact inside it. Therefore in a $^{15}O - H_2O$ study the MBF can be calculated from the k_2 of the model, instead that from the k_1. This has great advantages. k_2 regulates an exponential decay, which is self-similar. This allow the extraction of the k_2 value only from the trend of the function and not from its absolute values. Therefore it is less influenced by inaccurate quantification due to PET limited resolution. There is also another advantage, as this system allows the differentiation between two different origin of undeperfusion. In presence of necrotic tissue, but with correctly working coronary arteries, the k_1 would be limited, as only a fraction of the cells is perfused. In this case k_2 would retain its full value, as the cells that are still alive have full flow. On the contrary, in case of reduced flow and healthy tissue, k_1 and k_2 would retain have the same value. To account for this phenomenon a parameter, called "Tissue Fraction", T.F., is introduced. It represents the fraction of tissue perfused in the volume analyzed. The kinetic model has as a solution

$$C_{myo}(t) = T.F. \times MBFe^{-MBF \times t} \otimes C_b(t)$$

In this way it is possible not only to measure accurately MBF but also to distinguish impairment due to necrotic tissue from those due to coronary disease. The mean dosimetry

for a study with current protocols is very limited, less than $2\,mSv$ for a complete rest-stress study.

7.2.2 Rubidium

A nuclide commonly used to assess miocardial perfusion is ^{82}Rb. Its main advantage is that can be provided by a generator, the exploits the $^{82}Sr \rightarrow^{82} Rb$ electron capture. ^{82}Sr half life is of $25.5\,d$, allowing a very easy shipping and handling. ^{82}Rb has, instead, an half life of $75\,s$. The q-value of the β^+ decay is $3.3\,MeV$, which is unfavourable as it gives an average positron range of $2.8\,mm$. This contribution to the PSF of the PET scan should be compared to 1.1 mm of range for water, 0.4 mm for ammonia and negligible for fluorated compunds. The activity injected is usually very high ($\sim 800\,MBq$) to achieve sufficient count statistics. Given the very high positron energy, even if the half life is very short, the mean dose given to the patient for a complete examination is $3 - 6\ mSv$. As shown previously in figure 7.2, its extraction fraction saturates fastly for MBF over $1\,ml\,mg^{-1}\,min^{-1}$. Quantification is possible, with an ad hoc kinetic model but, given the low extraction factor at high MBF, large corrections are needed and these amplyfies the noise to unacceptable levels [107].

7.2.3 Fluripidaz

Recently a new tracer has been proposed, which has been called Fluripidaz [108], and is marked with ^{18}F. Exploiting the same logistics used for $^{18}F - FDG$, on-site cyclotron would not be required to use this radiopharmaceutical. This tracer has an high extraction fraction, 0.94, almost independent of MBF [108, 109]. This tracer is retained in the myocardial wall, therefore allowing qualitative images. Given the high half life of this tracer long scans can be performed after the uptake phase and, consequently, high quality static images can be observed. MBF quantification is possible with dynamic acquisitions and the first trials performed appear very promising [109]. Given its very low energy positron, counterbalanced by its relatively long half life, the dosimetry for a single day rest/stress study with the proposed injected activities should be limited to about $5\,mSv$.

7.2.4 Ammonia

A popular tracer for MBF perfusion studies is ammonia tagged with ^{13}N. This nuclied is produced in a cyclotron with the reaction $p+^{16}O \rightarrow^{13} N + \alpha$ on a water target. When a ^{13}N nucleus has been produced it reacts the water solution and it forms $^{13}N - NH_3$, therefore no chemical synthesis is needed after the target irradiation has finished. ^{13}N half life is 9.98 min, therefore allowing an easier manipulation of the compound and the accumulation of an higher counting statistic, compared to $^{15}O - H_2O$. Ammonia has an almost unit extraction fraction, up to high flow values [110]. Contrary to water after ammonia enters a cell it might encounter methabolic trapping, in the form of glutammine. This trapping is irreversible, at least to the time scales comparable to the tracer half-life. Ammonia forms a metabolite in the blood, which must be accounted for. The dosimetry for this tracer is quite favourable, like for water. Lower doses are injected and the positron energy is less, but the half life is longer, therefore the dosimetry for a complet rest-stress study amounts to $1.5 - 3\,mSv$

7.2.4.1 Ammonia kinetics

The possibility to use ammonia as a myocardial perfusion tracer were analyzed in deep by Schelbert et. al in 1981 [110], after the same group proposed the use of this tracer in 1979 [111]. They also fully described its kinetic proprieties. In the blood NH_3 is in equilibrium with NH_4^+. Both of them pass from the capillaries to the extra-vascular space with equal rates, and also in this compartment, the two are in equilibrium. Following they enter the metabolic compartment, from which they can escape in this form, or they can undergo a conversion in $^{13}N-$glutamine, with two possible paths. Once converted into glutammine there is no backward transformation and ^{13}N is trapped inside the cell. The complete path is schematized in figure 7.3 Four different kinetic models have been proposed

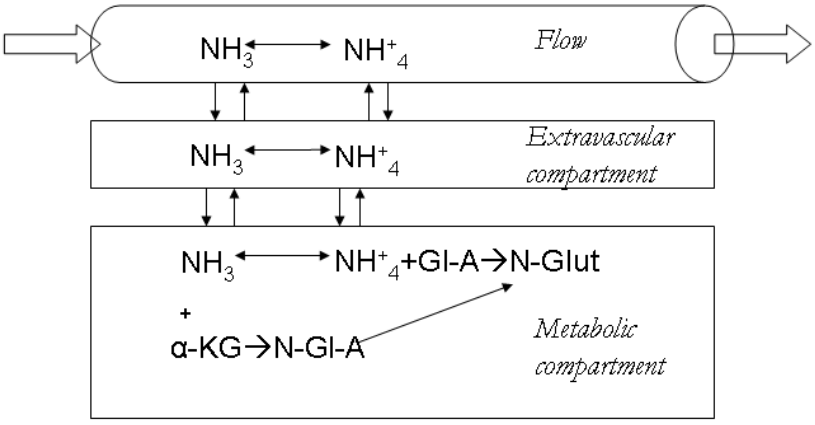

Figure 7.3: Scheme of the path followed by ammonia in the myocardium. Gl-A stands for glutamic acid; glut for glutamine, α-KG for α-ketoglutarate. The conversion from NH_4^+ and glutamic acid to glutamin is operated by the enzime "glutamine synthetase".

to analyze dynamic PET data; some attempt to parameterize the whole process while others are proposed only as effective models for greater semplicity or stability.

7.2.4.2 The Hutchins model

In 1990 Hutchins proposed a model [112] describing a kinetic model for ammonia that modeled schematically all of the processes described in the previous section and detailed in figure 7.3. The model has 2 compartments with irreversible trapping and therefore 3 rate constants. It is schematized in figure 7.4, where the equivalency with the full kinetic description can be easilly observed.

While this model should be able to describe the uptake of ammonia for an indefinite duration the fit is usually limited 10 minutes. The main reason lies in the metabolites correction. Usually they are not directly measured and their fraction goes to about 50% of the blood activity during the first 4 minutes and saturates to unity later. The differential equations describing this model are

$$\begin{cases} \frac{\mathrm{d}C_1}{\mathrm{d}t} = k_1 IF(t) - (k_2 + k_3)C_1(t) \\ \frac{\mathrm{d}C_2}{\mathrm{d}t} = k_3 C_1(t) \end{cases}$$

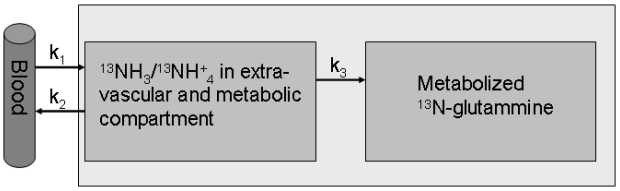

Figure 7.4: Scheme of the Hutchins model

and the solution of this model for C_{tissue} is

$$C_{tissue} = \left(\frac{k_1 k_2}{k_2 + k_3} e^{-(k_2+k_3)t} + \frac{k_1 k_3}{k_2 + k_3} \right) \otimes IF(t)$$

7.2.4.3 The De-Grado model

DeGrado proposed a different model to describe the ammonia uptake, that deliberately neglects the glutammine trapping of ammonia in the metabolic compartment. Omitting this compartment had already been proposed by Hutchins but fitting 10 minutes of data with in this way gave very biased results. DeGrado suggested stopping the fit at 4 minutes and compared it to the fitting 10 minutes and to the model proposed by Hutchins [113]. The results was that a single compartment model was not accurate when fitting 10 minutes of data while it is as accurate as the one proposed by Hutchins when limited to 4 minutes but it is more stable, especially at low MBF.

There is only one differential equation to describe this kinetic model

$$\frac{\mathrm{d}C_1}{\mathrm{d}t} = k_1 IF(t) - (k_2) C_1(t)$$

which solution for C_{tissue} (equal to C_1 in this case) is

$$C_{tissue} = k_1 e^{-k_2 t} \otimes IF(t)$$

7.2.4.4 Other kinetic models

In 1990 Bellina et. al. [114] proposed an extremely simplified method to asses NH_3 myocardial perfusion. It is based on the measurment of the retention fraction of the tracer shortly after the injection. Numerically

$$MBF = \frac{C_{myo}(T)}{\int_0^T IF(t)dt}$$

This model is equivalent to the Hutchins model with $k_2 = k_3 = 0$. This approximation holds only for very short time scans and therefore T is generally set to $120\,s$. This model generally underestimates MBF, specially in hyperaemic conditions where k_2 is greater.

Another method not applied anymore, to our knowledge, is the one proposed by the UCLA team in 1989 [115]. It consisted of a freely diffusible model coupled with a reversible compartment, as shown in figure 7.5.

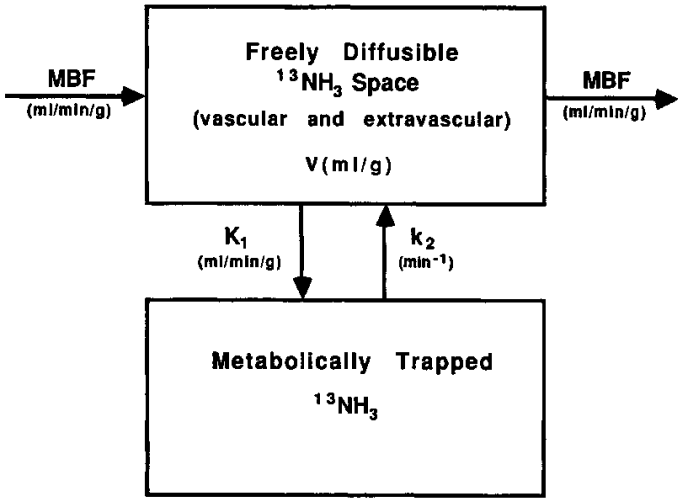

Figure 7.5: Scheme of the UCLA model for ammonia MBF

7.2.4.5 Metabolite correction techniques

In MBF studies the parameter of interest is k_1. With fast injections this parameter describes the trend and the height of the curve in the first minute. In such a short time the metabolite buildup is small. Some authors suggested ignoring the methabolite buildup alltoghether [112]. This is feasible since the activity in the blood after the first pass of the bolus is negligible, compared to the one measured during the bolus pass. Correction to a quantity that is already small are, in a first approximation, negligible themselves. This holds especially when short scan duration are considered. To improve the precision of the results two corrections have been proposed, one for the De-Grado model and one for the Hutchins model. For the De-Grado model, limited to 4 minutes, a linear correction has been proposed:

$$C_{NH_3} = C_{blood}\,(1 - m_{corr} \times t)$$

with m_{corr} experimentally determined to be $0.077 min^{-1}$ in humans [113], therefore at the 4^{th} minute the metabolite buildup is about 30%. The linear correction obviously fails for duration of more than 13 minutes where it would be more than 1. For the hutchins model a different correction has been developed, that is valid for longer time intervals. The correction proposed [116] is a delayed exponential growth.

$$\begin{cases} C_{NH_3} = C_{blood} & t \leq t_0 \\ C_{NH_3} = C_{blood}\left(1 - e^{\frac{t-t_0}{\tau}}\right) & t > t_0 \end{cases}$$

with the two parameters experimentally determined to be $t_0 = 0.48\,min$ and $\tau = 9.65\,min$. The two correction strategies overlap well until 5 minutes after the injection.

7.2.4.6 Spillover correction technique

As the myocardial wall is quite thin compared to the PET scanner resolution strategies are necessary to correct for the partial volume effect. Older techniques to account for it required

the estimation, trough simulations or experiments, of some recovery coefficients. These strategies were of course prone to severe errors ad unreliability. A very sagacious strategy that can be applied for the special case of the myocardium was proposed by Hutchins [117].

This strategy is based on the parameter used to account for the fraction of the tissue occupied by blood, previously introduced in section 7.1.1. The concept underlying this strategy is that the myocardial muscle is filled with blood therefore all of the movements (cardiac and respiratory) and also the limited resolution of PET has the effect of giving a map of activity values which is the sum of blood activity and actual myoardial activity. The method proposed by Hutchins is to let this parameter to be fitted along with the kinetic model parameters. In its paper Hutchins demonstrated the efficacy of this method on animal experiments and with montecarlo simulations.

The theoretical correctness of this approach is evident for what concernes motion modeling and actual blood fraction. A separate discussion must be performed for the partial volume effect. In a filtered backprojection reconstruction this parameterization is correct, given the linearity of this reconstruction and of the filters involved. For OSEM this might not be the case, especially considering that during the first pass of the radioactive bolus typical activity contrast are about $1:10$ while during the steady uptake phase they reverse to as much as $10:1$. OSEM algorithms are known to converge at different speeds depending on the contrast involved. Nonetheless it is possible to accept this approximation, specially with a good resolution scanner (where the effect to correct for is inerently small), and also taking into account that this is only one of the three contributions to the value of this parameters.

7.3 Analysis of the proprieties of the ammonia models

7.3.1 Fitting of the Huthcins model

At resting conditions the values of k_2 are generally small. A simple analysis of 22 consecutive patients coming to our center shows an average k_2 of $0.18 \pm 0.5\ min^{-1}$. Statistically speaking that means that roughly some more of 15% of the people have k_2 basal values of less than $0.13\, min^{-1}$. The hutchins model describes the PET measured uptake with the formula

$$C_{PET}(t) = \left(\frac{K_1 k_2}{k_2 + k_3} e^{-(k_2+k_3)t} + \frac{K_1 k_3}{k_2 + k_3} \right) \otimes C_{blood}(t)$$

If one expands to the first order in t the impulse response part of the formula the result is

$$C_{PET}(t) \approx \frac{K_1}{k_2 + k_3} \left(k_2 - k_2 \left(k_2 + k_3\right) + k_3\right) \otimes C_{blood}(t)$$

$$C_{PET}(t) \approx K_1(1 - k_2) \otimes C_{blood}(t)$$

that can be again expressed in terms of an exponential form as

$$C_{PET}(t) \approx K_1 e^{-k_2 t} \otimes C_{blood}(t) \tag{7.1}$$

This equation, incidentally, is the one of the De-Grado Model. Therefore it can be already suspected that, at least where $(k_2 + k_3)\, t \ll 1$, k_3 should be difficult to be determined

experimentally, as the differences introduced by k_3 are negligible. An in-depth analysis of the behaviour of the χ^2 can be useful. Given

$$\chi^2 = \sum_{i=1}^{N} \left(f(k_1, k_2, k_3, t_i) - C_{PET}(t_i)\right)^2$$

one can compute the derivatives to see how much the χ^2 is influenced by each parameter at the various time istants.

$$\frac{\mathrm{d}\chi^2}{dk_j} = \sum_{i=1}^{N} 2\left(f(k_1, k_2, k_3, t_i) - C_{PET}(t_i)\right) \frac{\mathrm{d}f(k_1, k_2, k_3, t_i)}{dk_j}$$

Therefore at each time sample t_i the χ^2 depends on each k_j by a factor depending on the difference between the fitting function and the experimental data and on the derivative of the KM. function, with respect to the analyzed k_j. At this point it is possible to compare the relative strenght of these derivatives at various time istants. Assuming as our f the impulse response with adequate calculations it turns out that

$$\frac{\mathrm{d}f}{\mathrm{d}k_1} = \frac{k_2 e^{-(k_2+k_3)t} + k_3}{k_2 + k_3}$$

$$\frac{\mathrm{d}f}{\mathrm{d}k_2} = \frac{k_1}{k_2 + k_3}\left\{e^{-(k_2+k_3)t}\left[1 - k_2 t\right] - \frac{1}{k_2 + k_3}\left[k_3 + k_2 e^{-(k_2+k_3)t}\right]\right\}$$

$$\frac{\mathrm{d}f}{\mathrm{d}k_3} = \frac{k_1}{k_2 + k_3}\left\{1 - k_2 t\, e^{-(k_2+k_3)t} - \frac{1}{k_2 + k_3}\left[k_3 + k_2 e^{-(k_2+k_3)t}\right]\right\}$$

It is already possible to see that the influence of k_2 and k_3 on the χ^2 depends linearly on k_1. It is also possible to note the the derivative with respect to k_1 has a maximum for $t = 0$ and then decreases. On the other side both the other derivatives start from 0 and then increase their magnitude. To get the idea in figure 7.6 the three derivatives in four different conditions are plotted superimposed. The first two plots are for resting MBF with small and average k_2, while the other two plots are for high MBF with small and average k_2, taking into account that k_2 usually doubles at stress. It can be noted that for low values of k_2 and k_1 k_3 has a little impact on the functions, also at time points distant from the start of the scan. This does not hold true anymore for large values of k_2 and k_1. As stated at the beginning of this subsection more than 15% of the patients naturally have a k_2 values of less than $0.13\,min^{-1}$ in basal conditions. For them a failure of the fit of this model is justified, by the small influence of k_3 on the χ^2.

A toy simulation To assess the behaviour of the two models in an ideal situation I performed a toy-montecarlo simulation. Specifically an error-free TAC was simulated corresponding to $k_1 = 0.8\,min^{-1}$, $k_2 = 0.1\,min^{-1}$ and $k_3 = 0.1\,min^{-1}$. Afterwards time-framed curves were generated with a framing scheme of $8 \times 5\,s$, $7 \times 10\,s$, $8 \times 15\,s$, $12 \times 30\,s$. Following noise was added to the TAC, and the χ^2 was calculated between the noisy TAC and a theoretical curve over a grid of parameters. The χ^2 distribution was obtained for both the

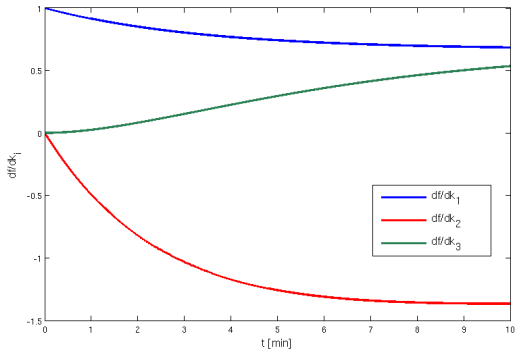

(a) $k_1 = 0.6min^{-1}$, $k_2 = 0.1min^{-1}$, $k_3 = 0.2min^{-1}$

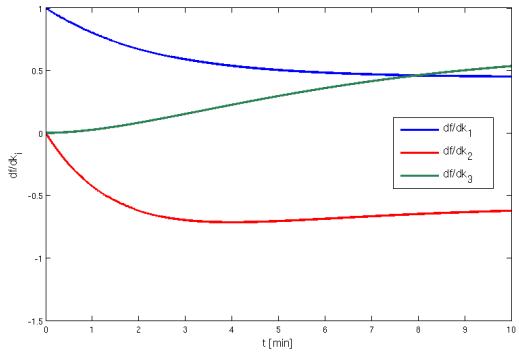

(b) $k_1 = 0.6min^{-1}$, $k_2 = 0.25min^{-1}$, $k_3 = 0.2min^{-1}$

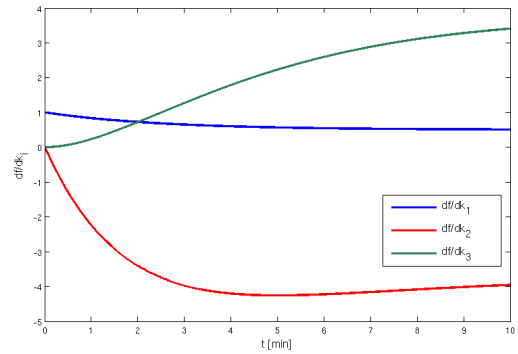

(c) $k_1 = 3min^{-1}$, $k_2 = 0.2min^{-1}$, $k_3 = 0.2min^{-1}$

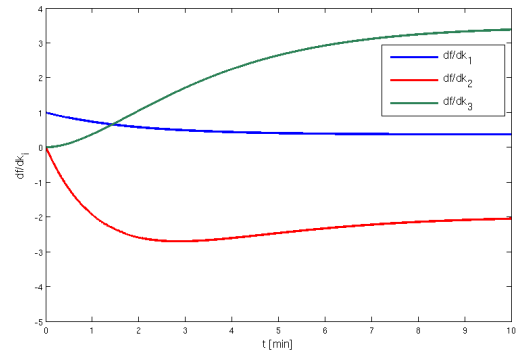

(d) $k_1 = 3min^{-1}$, $k_2 = 0.35min^{-1}$, $k_3 = 0.2min^{-1}$

Figure 7.6: Derivatives of the impulse response function at different values of k_j. In blue $^{df}/_{dk_1}$,in red $^{df}/_{dk_2}$, in green $^{df}/_{dk_3}$.Upper row: $k_1 = 0.6min^{-1}$, representative resting conditions. Lower row: $k_1 = 3min^{-1}$, representing hyperaemic conditions.

Hutchins model and the De-Grado model. For the Hutchins model 256 noise realizations were performed while for the De-Grado model 2048 realization were possible. The noise added was a gaussian with a modulus of 12% of the activity plus a constant term, to simulate noise in frames without activity. The χ^2 was calculated on only 4 minutes of data for the De-Grado model and on 10 minutes of data for the Hutchins model, as prescribed by the authors.

The results are reported in figure 7.7 and 7.8. The $1-\sigma$ confidence range for the

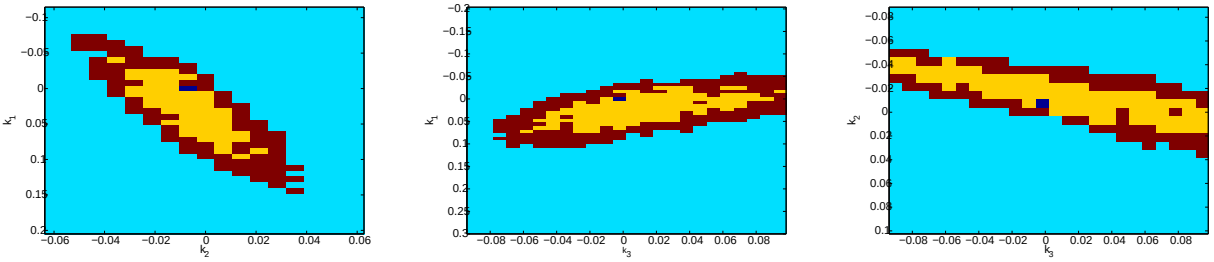

(a) View of the $k_1 - k_2$ distribution

(b) View of the $k_1 - k_3$ distribution

(c) View of the $k_2 - k_3$ distribution

Figure 7.7: χ^2 distribution of the Hutchins model. In yellowish it is reported the 70% confidence level and in red the 95% confidence level. The blue point is the true value.

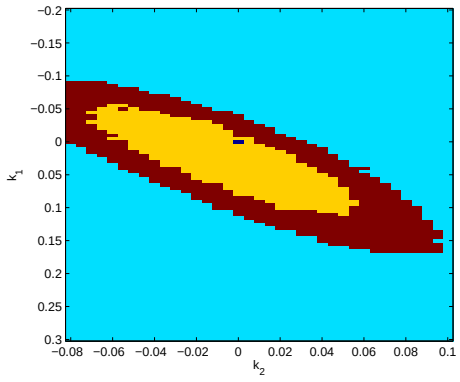

Figure 7.8: χ^2 distribution of the De-Grado model. In yellowish it is reported the 70% confidence level and in red the 95% confidence level. The blue point is the true value.

De-Grado model for k_1 is $\pm 0.07\, min^{-1}$ wide while for the Hutchins model it is $\pm 0.09\, min^{-1}$ wide. On top of this increase in the confidence range the Hutchins model has an extremely wide minima in the $k_2 - k_3$ plane, therefore leaving the minimization procedure prone to errors.

A similar simulation was conducted at higher flow rates, with higher k_2 also (as usually the increase in k_1 is similar to the one in k_2). The simulated values were $k_1 = 2.5\, min^{-1}$, $k_2 = 0.4\, min^{-1}$ and $k_3 = 0.2\, min^{-1}$. With faster time constants the minima should be more narrow, fitting the same time range. The error applied to the TAC was the same as before.

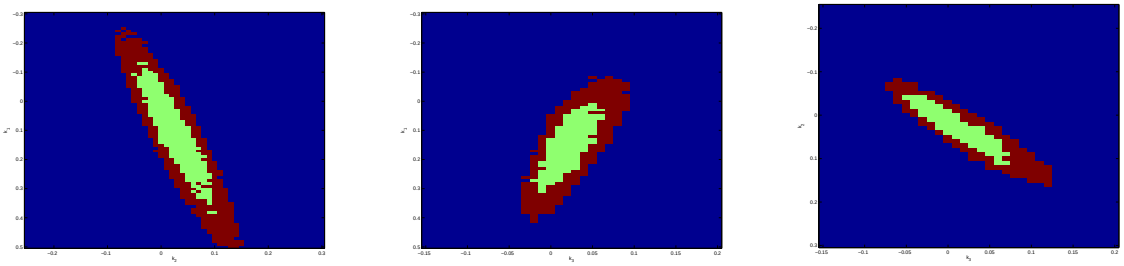

(a) $k_1 - k_2$ plane **(b)** $k_1 - k_3$ plane **(c)** $k_2 - k_3$ plane

Figure 7.9: Slices of the χ^2 distribution around the minimum for the Hutchins model at high flow. The regions represented are the 1 and 2 σ confidence level.

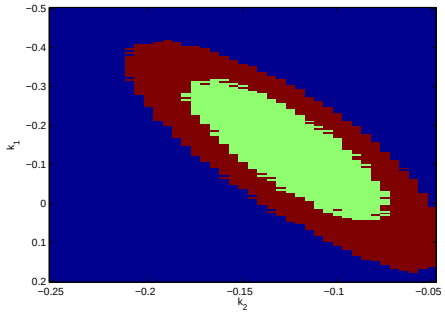

Figure 7.10: Distribution of the χ^2 of the De-Grado model around its minimum. Represented are the 1 and 2 σ confidence level

Results are shown in figure 7.10 and in figure 7.9. With the DeGrado model the minimum found was at $k_1 = 2.4\,min^{-1}$ and the confidence range was $\pm 0.18\,min^{-1}$, (about the double than with low flow ranges, meaning a decrease of the relative error). With the Hutchins model the minimum found was at $k_1 = 2.66\,min^{-1}$ and the $1-\sigma$ range is $\pm 0.22\,min^{-1}$ wide. Watching the $k_2 - k_3$ plane does not show a broad minimum as at rest, but a correlation between the two parameteres remain.

A note on the error weighting in the χ^2 minimization To perform a proper fit of the kinetic model to the experimental curve obtained one should compute the χ^2 as

$$\chi^2 = \sum_{i=1}^{N} \frac{\left(y_i - f\left(i, k_1, k_2 ....\right)\right)^2}{\sigma_i^2}$$

with σ_i being the error associated with the $i-th$ point. If each σ_i is the same for each point i this parameter can be eliminated from the calculations since it will affect only the absolute value of the χ^2 and not its position. In a PET dynamic scan indeed the relative error on each measurement point cannot be tougth to be constant. Theoretically a direct estimation of the pixel noise would be possible with FBP images, given the number of acquired counts, where an analytical expression is present. From this the estimation of the error on a sampled region is straightforward. Anyway the minimum of the χ^2 is independent for a common factor multiplication of σ. On the other side, when using iterative reconstruction algorithms, the error estimation is not directly possible and, specially in low statistic regions, the errors distribution is not gaussian but heavilly right-tailed. Therefore in the program used to assess MBF in the clinical case we decided to use some fitting weights σ_i that simulate a constant relative error behaviour.

7.3.2 Behaviour of the De-Grado Model at various flow conditions

In the previous section the reasons for which the Hutchins models is more subject to problems in resting conditions was analyzed. It is possible to say that using this model one is trying to overfit the data. It was shown, in equation 7.1, that the first order approximation in t of the Hutchins model is the De-Grado model. Since in the previous section it was stated that this approximation is reasonable and better behaved that the full equation in a number of cases in this section its validity is investigated. Intuitively it can be seen, from section 7.3.1, that the De-Grado model should be effective for $(k_2 + k_3)\,t \ll 1$. Given the average values of the k found in patients the approximation should hold at least for $t < 3\,min$, counting from the peak activity in the myocardial blood, which happens about $50\,s$ after the injection. In reality the tracer injection is not a δ impulse, but rather a bolus that is infused in some seconds followed by a recirculation of the tracer. Therefore when this model to be valid for longer scan durations.

7.3.2.1 Simulation of the De-Grado Model

To assess the error introduced in fitting the experimental data with the De-Grado model a MonteCarlo approach was used. A realistic input function was produced and used to

calculate the true tissue TAC with different values of ks. Then the data were resampled to reasonable framing schemes and subsequently these activities were fitted using the De-Grado model.

Input function A typical input function is a narrow peak of concentrated activity, rapidly decaying to smaller concentrations. Then this decrease becomes much slower because of tracer recirculation. Still in some minutes its concentration drops to nearly zero, and most of the activity found in the blood is due to radioactive metabolites of the original tracer. This function was parameterized using a sharp gaussian followed by an exponential decay. The gaussian has a peak activity of 100 (a.u.) and a FWHM of $14\,s$. Its peak is located $19\,s$ after the start of the simulation. At $30\,s$ it is substituted, continously, by an exponential decay with a time constant of $100\,s$. The IF is generated with a time resolution of $10\,ms$.

Tissue TAC generation The true tissue TAC has been generated from the previous input function trough numerical approximation of the differential equations, using very fine time steps ($10\,ms$) and a midpoint Euler method. The TAC were simulated to respond to the Hutchins model. The parameters were simulated in the range:

- $0.4\,min^{-1} < k_1 < 3.3\,min^{-1}$, in 0.1 steps
- $0.1\,min^{-1} < k_2 < 0.8\,min^{-1}$,in 0.05 steps
- $0.05\,min^{-1} < k_3 < 0.45\,min^{-1}$, in 0.05 steps

To simulate the results of a PET acquisition, which measures the average activity in a voxel, discrete TAC were generated averaging the activity values in a time-step of a pre-defined framing scheming. In this simulation we used a framing scheme of $5 \times 10\,s, 4 \times 20\,s, 4 \times 30\,s$. This reframing was applied to the IF and to the TAC. Following this data were fitted with the De-Grado model and k_1 and k_2 values compared to the true values.

Results As expected this model has an increasing bias of the MBF with increasing value of k_2 or k_3. In these cases k_1 is underestimated by the De-Grado model. This bias is found to be independent of k_1. In this simulations in the most extreme case, with $k_2 = 0.8\,min^{-1}$ and $k_3 = 0.45\,min^{-1}$, k_1 has a reduction of 19%, independent of k_1. A linear description of the error introduced by the De-Grado approximation, extracted from this simulation, gives that, in this range of k_1, k_2 and k_3, the bias of the De-Grado model is

$$\frac{\Delta k_1}{k_1} = -10\%\,min \times k_2 - 13\%\,min \times k_3$$

As in most patient in hyperaemic studies k_2 is limited to $0.25\,min^{-1}$ and k_3 to $0.2\,min^{-1}$, the error introduced by the De-Grado approximation results therefore to be limited to 5%. For what concerns k_2 we find that the value fitted by the De-Grado model decreases strongly with k_3 and very mildly with k_2 itself (no dependence is found on k_1). For $k_3 = 0.45\,min^{-1}$ a reduction of k_2 of 61% is observed. An effective parametrization is

$$\frac{\Delta k_2}{k_2} = -12\%\,min \times k_2 - 125\%\,min \times k_3$$

This results, schematized in figure 7.11, reflect the fact that the De-Grado model responds

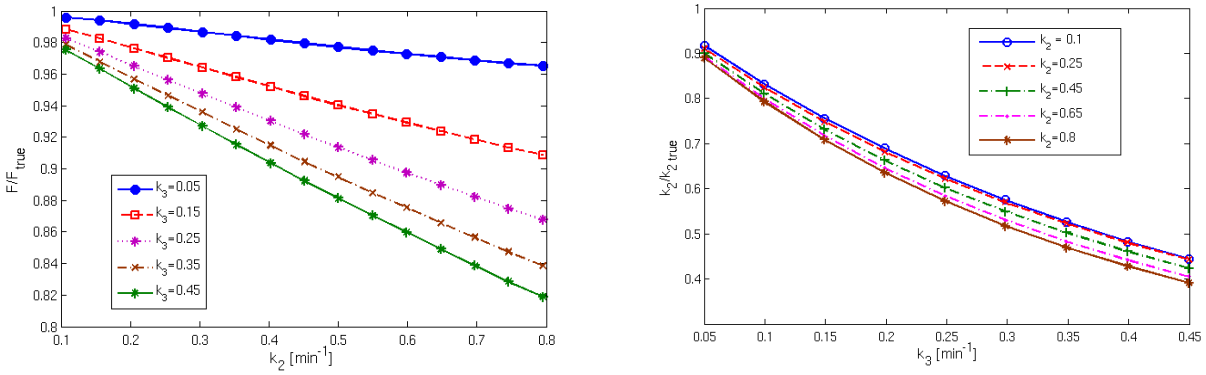

(a) MBF vs. k_2 at various k_3.

(b) Measured k_2 vs. k_3 at different k_2

Figure 7.11: Most significative results of the montecarlo simulation of the accuracy of the De-Grado model. It can be noted *(a)* that the estimation of the MBF depends both on k_2 and k_3. The measured k_2 *(b)* instead has a slight dependence on k_2 itself and a very strong one on k_3

to an increased retention of ammonia (higher k_3) decreasing the washout parameter (lower k_2). Therefore using this model an acceptable precision is achieved on the determination of k_1, the parameter of clinical interest, at the cost of a bias in the determination of k_2, which is not used for diagnosis or analyzed anyotherway, at least now.

7.3.3 Assesment of the influence of the approximate metabolite corrections

Anoter topic analyzed is the effects of an approximate metabolite correction. Their influence can be expected to be small, specially on the De-Grado model, because the fitted time range is short and because their buildup reaches a non-negligible fraction only when C_{blood} is small. A correction to the input function, when this is already small, is expected to have a small impact.

To check the impact of an imprecise metabolite correction another toy simulation was performed. A TAC was calculated, with different k_1 and k_2, as the exact response to an input function, assuming the De-Grado model as exact. The same IF of the previous section was used. Following a metabolite buildup was simulated and a C_{blood} curve computed. The buildup simulated was such that

$$IF\,(t) = C_{blood}\,(t) - m_{true} \times t$$

This is the model generally used to account for metabolite buildup in the DeGrado model, with $m = 0.077\,min^{-1}$ [113]. Then the TAC was fitted, using the DeGrado model and a "measured" input function $IF_{meas}\,(t) = C_{blood}\,(t) - 0.077 min^{-1} \times t$ to assess the changes in the fitted k_1 and k_2 parameters using an input function corrected with an m parameter different from the actual one. The fit was limited to 4 minutes.

The simulated values of k_1, k_2 and m_{true} were

- $0.5min^{-1} < k_1 < 3.5min^{-1}$, in 0.1 steps
- $0.05min^{-1} < k_2 < 0.49min^{-1}$, in 0.02 steps
- $0.01min^{-1} < m_{true} < 0.2min^{-1}$, in 0.005 steps.

Therefore the range of values tested range from about $1/7$ to 2.5 times the average value found in actual human measurments.

The results of this simulation is that $k_1$is almost not influenced by the metabolite correction. In this wide range the maximum relative difference between the true and the fitted k_1 is $+2.5\% \setminus -2\%$. The most extreme variations ($\Delta k_1 > 1\%$) happen in the small region defined by $m_{true} > 0.16min^{-1}$ and $k_2 > 0.43min^{-1}$. On the negative side variations of $\Delta k_1 < -1\%$ happen only in the, very few, points with $m_{true} < 0.015min^{-1}$and $k_2 > 0.4min^{-1}$.

The same cannot be said for k_2. In particular it is possible to note that for values of m_{true} lower than the applied correction k_2 increases while it decreases for higher values. The absolute variations are $\sim +0.05\, min^{-1}$(in a first approximation independent of k_2) for $m_{true} = 0.01$ and $\sim +0.1\, min^{-1}$ for $m_{true} = 0.2$. Depending on the k_2 value this differences can be higher than the value of k_2 itself.

Concluding it can be said that the parameter of clinical interest, k_1 is extremely stable over a very wide range of metabolite build-up speeds. This happens thanks to the modification of k_2. It is possible to interpret intuitively the variation of k_2 as a response to the different input in late frames. With a smaller-than-due metabolites correction in late frames an higher amount of tracer is seen enterering C_1(with k_1 fixed). Therefore, to keep the value of C_1 fixed, the kinetic models responds increasing the amount of tracer that is let out of the compartment (increasing k_2).

7.4 Conclusions

In this chapter the proprieties of the kinetic models proposed to analyze $^{13}NH_3$ studies have been analyzed. It was found that the model proposed by DeGrado provides a parameter estimation with less statistical uncertainty, as only two parameters have to be fitted instead of three, at the cost of a small negative bias in hyperaemic studies (quantified to be limited to 5% in most cases). On top of this it also avoids the risk of fitting instabilities in resting studies, where the χ^2 map has an extremely wide valley in the $k_2 - k_3$ plane. It has halso been shown that the approximate metabolite correction affects in an extremely limited way the DeGrado model, as only a 1% bias was introduced by a twofold error on this parameter. It turned out that this stability to the parameter of clinical interest, k_1 happens at the price of k_2. This parameters is strongly influenced by an imperfect metabolite correction and its estimation is strongly biased in the DeGrado model, depending on the value of the neglected k_3. As this parameter is not of clinical interest we can use the DeGrado model with great confidence to perform perfusion studies.

Chapter 8

Influence of the reconstruction algorithm on the MBF quantification

As reported in chapter 3 reconstruction algorithms influence the quantification of the activity in PET images, therefore the extraction of Time Activity Curves (TAC) and Image-Derived-Input-Functions (*IDIF* or, for extension, *IF*) can be expected to be reconstruction dependent. Conversely the quantification procedure, that fits this data, could result biased. In this chapter four reconstruction procedures were chosen and the differences in the quantified parameters were assessed.

The first analysis performed assessed the differences in the TAC and in the IF. Following quantification was performed and the results were compared. This comparison did not involve only the MBF but all of the parameters of the kinetic model. Following the results obtained by two different analysis software programs were compared, to assess the difference induced in the results by the different image sampling strategy. Finally also the variabilities between the various techniques were assessed.

8.1 MATERIALS AND METHODS

8.1.1 Patient population

Twenty-two consecutive patients (8 females; mean age: 55.5 years, age range: 30-76) were retrospectively analyzed in this study. The patients were referred to our centre for a myocardial perfusion study with $^{13}NH_3$ between October 2011 and February 2012. The referral diagnosis were: Hypertrophic cardiomyopathy (n=7), Coronary Artery Disease (n=5), Microvascular dysfunction (n=6), Dilatative cardiomyopathy (n=1), Systemic hypertension (n=3). Written informed consent was obtained from each patient to perform the $^{13}NH_3$ study and for anonymous publication of disease-related information.

8.1.2 Experimental Setup

8.1.2.1 PET Scanner

The studies were performed on a Discovery 690 (D-690, General Electric Medical Systems - GEMS, Milwaukee, USA) PET/CT system, previously described (chapter 2) . This scanner operates only in 3-dimensional mode (3D). The available reconstruction algorithms include analytical (3D Re-projection, 3D-RP) and iterative (3D ordered subsets expectation maximization, 3D-OSEM) methods.

8.1.2.2 Patient preparation and PET Acquisition Protocol

All the patients were instructed to fast for 6 hours and to avoid any caffeine intake for 12 hours before the study. The patient was positioned on the scanner bed with the arms raised over his/her head. A dedicated armrest was used to improve patient comfort. This reduced the probability of patient motion since many patients found it difficult to maintain this position for more than 20 minutes without an adequate support. An ECG trace was acquired and the arterial pressure was measured before the rest injection. After the CT scout view, a low dose cine-CT scan was acquired for attenuation correction (axial cine-CT, slice thickness: 5 mm, 100-120 kVp, mA: 15-20 mA both according to patient size, cine duration: based on the patient respiratory period). The 3D-PET scan in list mode started simultaneously with the injection of 370 MBq of $^{13}NH_3$ in 8 ml over 20 sec followed by a saline flush. Scan duration was 20 minutes. Patient respiratory period was measured with RPM, as described in section 5.3.2.1. Before removing the patient from the scanner, the internal laser beams of the scanner were projected and marked, with a pencil, on the patient's skin, in order to reproduce the same position in the hyperaemic study. The patient was allowed to relax off the scanner for 30 minutes. Then he was repositioned using the previously drawn markers. A second scout view was performed to check the FOV limits. Following dipyridamole ($0.56\,mg/kg$) was infused intravenously for 4 minutes. Three minutes after the end of the infusion, a second injection of 370 MBq of $^{13}NH_3$ was administered. The PET acquisition was repeated as above. Finally a second low dose cine-CT scan was performed for the attenuation correction of the stress study. Blood pressure, heart rate and ECG signals were recorded every minute from the start of Dipyridamole infusion and constantly monitored.

8.1.2.3 Data Processing

The list mode PET raw data were processed to generate a dynamic set of data with the following framing scheme: 9x10s, 6x15s,3x20s,2x30s,1x900s. Cine-CT images were also processed to generate an average image (AVE-CT) to be used for attenuation correction of PET data, as previously described.

8.1.2.4 Image Reconstruction

Image reconstruction for both dynamic rest and stress data was performed as follows, with this common settings: Image Matrix: 256, FOV: 30 cm.

1. 3D-RP: 3D-Reprojection, post filter 3D-Hanning: cut-off 4.3 mm FWHM (which corresponds to the Nyquist frequency in the image space for this scanner).
2. 3D-OSEM3: 3D-OSEM, subsets:18, iterations: 3, 3D-Hanning post filter: 4.3 mm FWHM.
3. 3D-OSEM5: same as above, iterations: 5
4. 3D-TOFPSF: 3D-OSEM with TOF and PSF modeling, subsets:18, iterations: 5, 2D-Gaussian transaxial post filter: 2 mm FWHM, axial filter: light (weighted average with coefficients $[1 - 6 - 1]$).

The rationale for choosing these reconstructions comes from the analysis of chapter 4, 3D-RP with the smallest possible filter was used as the standard reference reconstruction, which is known to be quantitatively accurate even if very noisy and of low quality. The two OSEM algorithms were used to simulate a typically used algorithm in clinical situations (with few iterations) and another one that should be more quantitatively accurate (with more iterations). Then we used an algorithm encompassing both TOF and PSF modeling at an high enough number of iteration to obtain almost full recovery, still with limited noise, according to what we saw in the phantom we performed. For all the reconstructions the attenuation correction was performed using the AVE-CT image set. An example of the different images obtained with the different algorithms (at rest) is shown in Figure 8.1 .

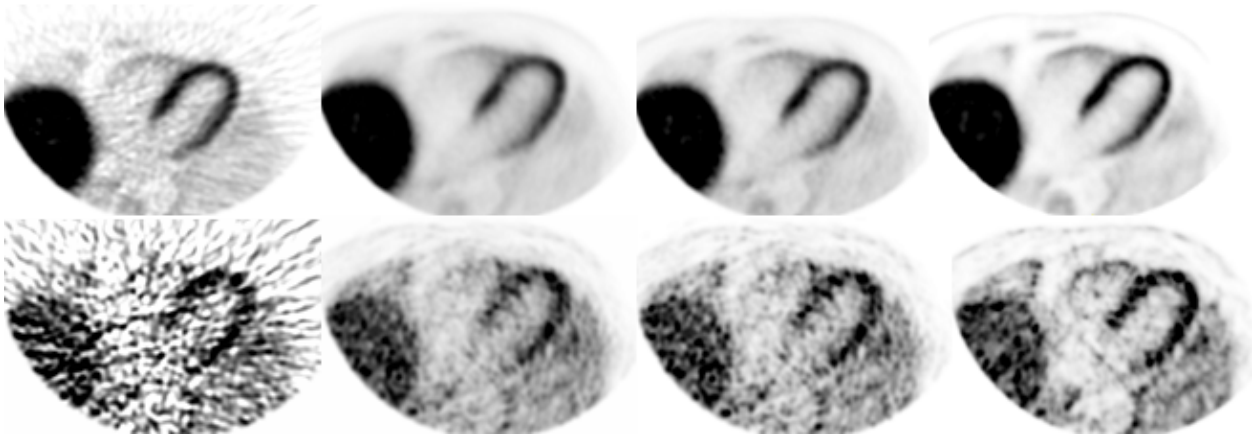

Figure 8.1: A representative transaxial slice of an $^{13}NH_3$ PET study for two different count statistics (Upper row: last 15 minutes of the study, Lower row: a 20" frame, from 3'40" to 4') and for different reconstructions (From left to right: 3D-RP, 3D-OSEM3, 3D-OSEM5, 3D-TOFPSF). The color scale is the same for each images in the same row.

They come from a high count statistics frame (900 s) and from a short dynamic frame (20 s). A profile was drawn from the base to the apex on the four images and they are shown in Figure 8.2 . A higher level of noise can be clearly seen in 3D-RP images, especially in the short frame, where the borders of the myocardium are poorly identified. A better structure definition and higher contrast can be noted in 3D-TOFPSF images, where the right ventricular (RV) wall is visible even in the low statistic frame.

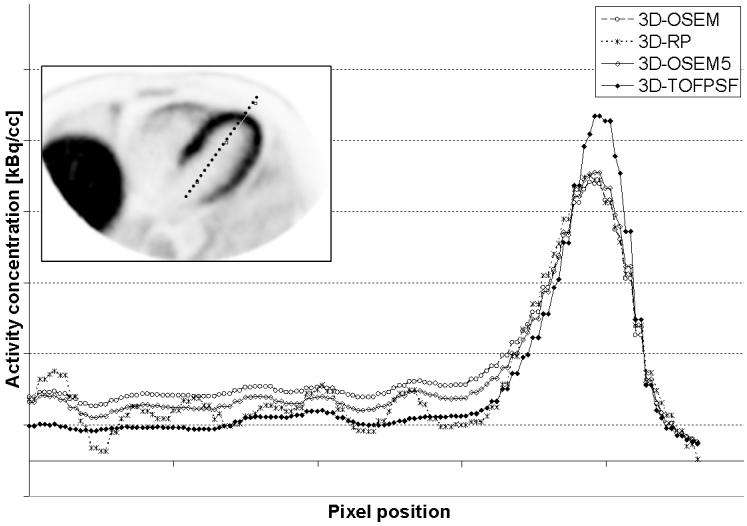

Figure 8.2: Radioactivity profiles sampled trough the LV and the apex of the heart (see the position of the profile in the image in the upper left corner of the heart) on images obtained with different reconstructions.

8.1.2.5 Quality control check

Once reconstructed, the last frame (900 s) of the PET dynamic image set (rest and stress) was fused with the corresponding AVE-CT images to verify for possible spatial mismatch between CT and PET images. In no case, PET and CT images were found misaligned. Patient movements between frames were qualitatively evaluated on each dynamic image by superimposing the myocardial centreline, defined by PMOD during the Volume-Of-Interest (VOI) definition. In all patient studies, the first 4 minutes frames were free from misalignment.

8.1.3 DATA ANALYSIS

8.1.3.1 PMOD software

PMOD © v 3.1 (PMOD Technologies, Zurich) is an image analysis software, featuring a dedicated cardiac module to automatically extract Time Activity Curves (TAC) and to fit them to a $^{13}NH_3$ myocardial perfusion kinetic model, for the quantification of MBF. By using PMOD the steps we followed to perform the analysis of the data were:

1) Generation of blood pool and myocardium images

- Blood Pool: average of frames from 0 to 50 s
- Myocardium: average of frames from 2 min to 4 min.

Both images were smoothed with a Gaussian filter of 5.5 mm (FWHM) in the case of the 3D-RP reconstruction, while a 4 mm (FWHM) filter was used on the 3D-OSEM3, 3D-OSEM5 and 3D-TOFPSF reconstructed images; this resulted in a noise level comparable among all the different reconstructed image sets. The smoothing operation

was performed only on the image used for VOIs definition, TAC are generated on the original images and therefore are not affected by this operation. Furthermore, to enhance contrast, a fraction of the blood pool image (10% in this study) was subtracted from the myocardium image.

2) Re-orientation of the heart in the short axis view

Images were re-oriented manually. For each study the re-orientation parameters were saved to reproduce the same set-up in subsequent analyses.

3) Definition of the volume of interest (VOI)

Three VOIs (LV cavity, RV cavity, and myocardium) were defined. The operator always started the automatic VOI definition and, once defined, manually adjusted them. The LV VOI was a cube of 1 cm side. The RV VOI, with an irregular shape, was generated as an isocontour on blood pool images. Finally, the myocardium VOI was defined using a centreline running along the myocardial wall, which was used as a guide for a subsequent sampling algorithm. To comply with the American Heart Association (AHA) prescription [92] we defined as the most basal slice the last one showing the myocardium as a full ring. Myocardial TACs were thus obtained from the previously defined centreline extracting the maximum values along the radii perpendicular to it in a defined spatial range of $\pm 5\,mm$. This method allows the sampling of the activity in the point least affected by heart motion and spillover. Furthermore, to reduce statistical noise, two neighboring voxels in the radial direction and two in the tangential direction were averaged for each point. The global myocardium TAC, used to fit the MBF, was calculated by averaging all the myocardial sampled points.

4) Reslicing and TAC generation

The transaxial myocardial images were resliced, so that the full myocardium, from the most basal slice to the most apical point, occupies 20 slices, resulting in an average slice thickness of 4.2 mm, depending on the heart size. The voxel size in the short axis plane was the same as in the transaxial plane before reorientation (1.17 mm in our case). An example of VOI definition and positioning is shown in Figure 8.3 .

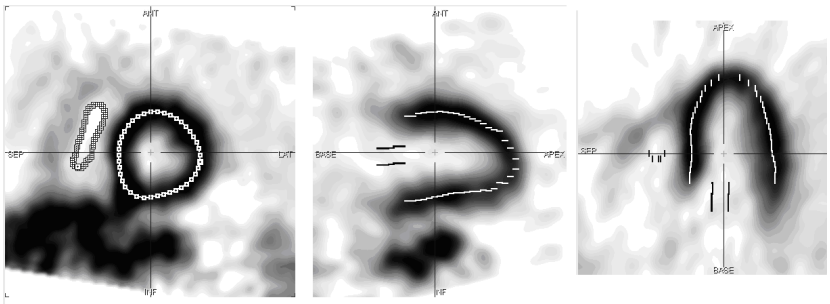

Figure 8.3: Example of VOI positioning in PMOD

5) Kinetic model fitting

Myocardium TAC was fitted to the kinetic model for the quantification of MBF. The quality of the fit was visually assessed by the operator in particular by inspecting the residuals distribution. In this way macroscopic failures could be avoided. TACs and the parameters fitted by the kinetic model were finally saved and exported in text format.

8.1.3.2 CARIMAS

CARIMAS, (CARdiac Image AnalysiS, v2.4, Turku PET Centre, Suomi, Finland), is a research software, freely available for the scientific community, (http://www.turkupetcentre.fi/carimas) developed at the Turku PET centre. As PMOD, CARIMAS is highly automated and thus it usually requires very little user intervention. By using CARIMAS the analysis steps to perform MBF quantification were performed as follows:

1) Myocardium image generation

The myocardium image was generated by summing selected frames (from 2' to 4') from the dynamic study. Differently from PMOD, CARIMAS does not allow any smoothing on the resulting images

2) Re-orientation of the heart in the short axis view

Reslicing of the images to the standard short axis views was obtained by manually drawing the axis of the heart in different views and dynamically adjusting them, until satisfaction.

3) Definition of the Volume Of Interest (VOI)

Three VOIs (LV cavity, RV cavity, and myocardium) were automatically defined by a segmentation algorithm implemented in CARIMAS. In particular, the LV VOI consisted in a cylinder defined from the basal up to the mid plane of the heart, the RV VOI was an arc of an ellipsoidal annulus and the myocardium VOI included all the myocardium wall. Once defined the VOIs could be modified by the user, if needed, using some predefined "global action" buttons. This procedure of VOI manipulation allows only to move coarsely large sections of the VOI. Furthermore, the LV VOI, cannot be moved, but only shrunk or enlarged. Nonetheless, only in few cases some modifications were needed and they were accomplished with the tools provided in CARIMAS.

4) Reslicing and TAC generation

Following VOIs definition, the global myocardium TAC was calculated as the average activity over the whole myocardium. An example of VOI definition and positioning is shown in Figure .

5) Kinetic model fitting.

Myocardium TACs were then fitted to the kinetic model for the quantification of MBF.

By using PMOD and CARIMAS software, data analysis was performed on both rest and stress study.

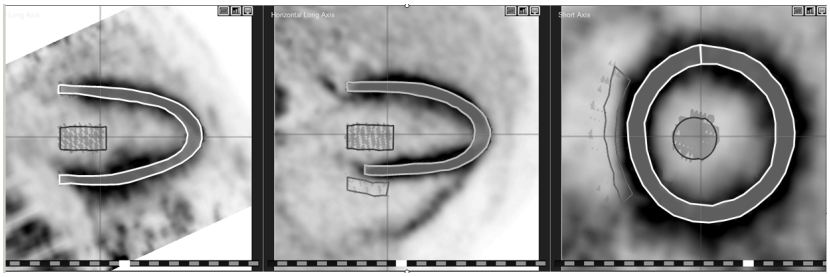

Figure 8.4: Example of VOI definitions in CARIMAS

8.1.4 Kinetic model

In both programs the software the TAC were fitted to the De-Grado model, thoroughly described in section 7.2.4.3. The three parameters that are fitted in this implementation are

- MBF (k_1 divided by the tissue density of the myocardial muscle)
- k_2, the washout parameter
- vLv, the fractional blood volume, as described in section 7.2.4.6.

8.1.5 Data comparison

8.1.5.1 Different Reconstruction algorithms - same VOIs

This analysis was performed to assess how the reconstruction algorithm affects quantification, independently of VOIs definition (i.e. assuming well defined and positioned VOIs). The analysis was performed by an expert operator using PMOD. 3D-RP images were first analyzed. Re-orientation parameters and VOIs were saved to be subsequently applied to images reconstructed by the other algorithms. For all images, the operator always verified whether the VOIs were properly positioned to prevent macroscopic misalignments. In no cases VOIs were found incorrectly positioned. For each patient study (rest and stress) and for each reconstruction algorithm, the following data were saved:

1. Input function TAC
2. Total myocardium TAC
3. Results of the kinetic model fitting

These data were then exported, in text format, to another workstation where they were automatically analyzed with ROOT (website: http://root.cern.ch) for statistical testing. The following data were compared (3D-OSEM3, 3D-OSEM5, 3D-TOFPSF vs 3D-RP):

- input function TAC in late frames (1 min 50 s – 4 min) (to evaluate whether some of the algorithms had higher values, as an effect of higher spillover from neighboring myocardial walls)

- total myocardium TAC in late frames (1 min 50 s– 4 min) (to evaluate whether some of the algorithms had on average higher or lower values with respect to 3D-RP)

- fitted kinetic model parameters (to evaluate the dependence of MBF and the other kinetic model parameters on the reconstruction protocols)

8.1.5.2 Different reconstruction algorithms - different VOIs

This analysis was carried in order to assess whether the use of different reconstruction algorithms cause the operators to position VOIs differently, thus leading to different final results (MBF, kinetic model parameters). The analysis was then carried out as described above, with the following differences:

- TACs were not saved and not analyzed;

- VOIs were defined independently, and blindly from one reconstruction algorithm to the other.

MBF values and kinetic parameters were compared (3D-OSEM3, 3D-OSEM5, 3D-TOFPSF vs 3D-RP). Data were analyzed by PMOD. For 3D-TOFPSF the analysis was also performed with CARIMAS.

8.1.5.3 PMOD - CARIMAS

The performances of the two analysis software were compared on images reconstructed by 3D-RP and 3D-TOFPSF. For PMOD, the results saved in the previous analysis on 3D-RP reconstructed data were used. In CARIMAS, the same operator analyzed the images blindly with respect to the analyses previously performed. The results of the kinetic modeling were then saved in text format, transferred to a computing workstation, and automatically analyzed in ROOT for statistical testing.

8.1.6 Statistical Analysis

Since the different analysis of the same sample can be modeled as a repeated test we used paired t-tests. The null-hypothesis, against which all the p-values were calculated, is that of no variation of each estimated parameter between the two algorithms compared. The various reconstruction algorithms were compared against 3D-RP. To compare the variations in the TACs (input functions, whole myocardium) we analyzed the mean relative variation, as we did the MBF values. For k_2 and vLv we analyzed the mean absolute variation. Relative differences for MBF values were compared also with Bland-Altman plots [118]. Finally, we evaluated the variability of MBF values with different reconstruction algorithms and with different processing software (PMOD, CARIMAS), as the root mean square of the relative differences.

8.2 Results

8.2.1 Different reconstructions – Same VOIs

Table 8.1-8.5 report the comparison of TACs (input function and myocardial TAC) and kinetic parameters (global MBF, vLv, k_2) obtained by PMOD software using the same VOIs on 3D-OSEM3, 3D-OSEM5, 3D-TOFPSF vs 3D-RP reconstructed images (rest and stress).

Algorithm	Rest variation	p-value	Stress variation	p-value
3D-OSEM3	+14%	$2\,10^{-4}$	+20%	$2\,10^{-4}$
3D-OSEM5	+6%	0.05	+11%	0.02
3D-TOFPSF	-20%	$< 1\,10^{-4}$	-18%	$5\,10^{-4}$

Table 8.1: Difference in the input function values in late frames with different reconstruction algorithms compared to 3D-RP

Input function (Table 8.1). In the late frames, 3D-OSEM3 and 3D-OSEM5 algorithms displayed a statistically significant increase in the mean value of the input function compared to 3D-RP, both in rest and stress conditions. 3D-TOFPSF exhibited a marked decrease (statistically significant). A representative input function is presented in figure 8.5.

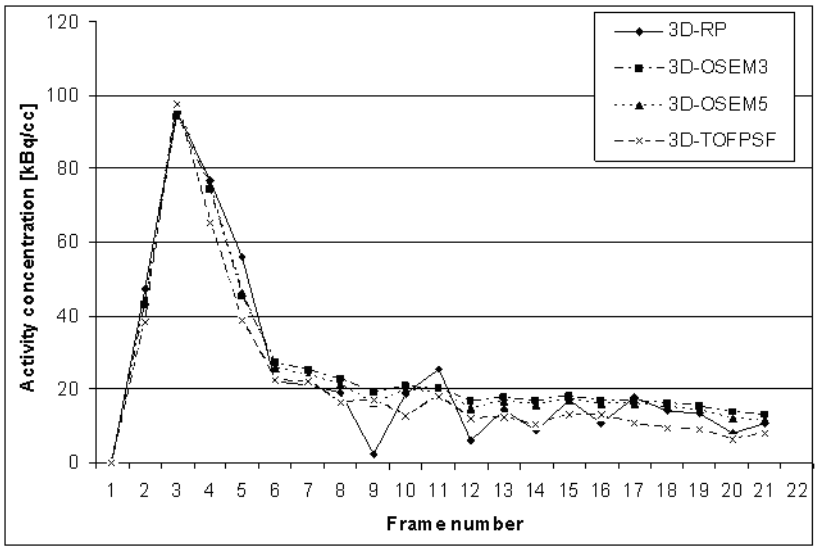

Figure 8.5: TAC of the input function for a selected patient obtained with different reconstruction. The rise of the input function looks perfectly overlapped for all the reconstruction. In late frames 3D-TOFPSF shows lower values of compared to the other reconstructions. Also 3D-RP is on average lower than the two 3D-OSEM reconstructions. It can also be noted that the 3D-RP curve shows higher variability in late frames

Total myocardium TAC (Table 8.2). Minimal differences were observed ($< 5\%$, both in rest and stress studies). Nonetheless, 3D-OSEM3 has a statistically significant decrease vs 3D-RP, 3D-OSEM5 reported no significant difference, while a statistically significant increase was seen for 3D-TOFPSF. Data in Table 8.2 are consistent with the profiles drawn on the

Algorithm	Rest variation	p-value	Stress variation	p-value
3D-OSEM3	-5%	$< 1\,10^{-4}$	-3%	$1\,10^{-4}$
3D-OSEM5	0.1%	0.99	0.8%	0.25
3D-TOFPSF	+3.7%%	$< 1\,10^{-4}$	+5%	$1\,10^{-4}$

Table 8.2: Difference in Global Myocardium TAC at late frames with different reconstructions, compared with 3D-RP.

myocardial wall shown in figure 8.2. A representative total myocardium TAC is shown in figure 8.6.

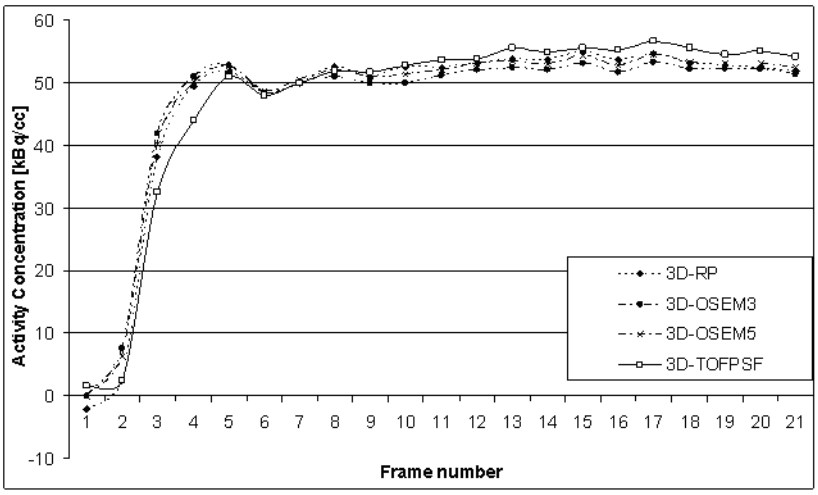

Figure 8.6: Global myocardium TAC for the different reconstructions for a selected patient. It should be noted that in late frames 3D-TOFPSF is the highest curve. During the first frames (from 2 to 4, when the activity in the blood pool is the highest due to the bolus pass) 3D-TOFPSF has markedly less activity, sign of less spillover from the ventricles.

MBF (Table 8.3). The comparisons of 3D-OSEM3, 3D-OSEM5 vs 3D-RP did not highlight any MBF significant differences, both in rest and stress conditions. 3D-TOFPSF yielded higher MBF values, on average. The increase was small but statistically significant. Variability of the differences across patient studies were higher for 3D-TOFPSF than for the other algorithms. Figure 8.7, 8.8 and 8.9 show a scatter plot and a Bland-Altman plot for each comparison, respectively. Note that the bias in the Bland-Altman plots, where rest and stress studies were analyzed altogether, is comparable to that obtained for the separate analyses (see Table 8.3).

Blood fraction vLv (Table 8.4). The variation of vLv in the rest studies manifested a marked increase for 3D-OSEM3 compared to 3D-RP; while in stress conditions the increase was smaller. For 3D-OSEM5 the increase at rest was modest but statistically significant; at stress there was no variation. 3D-TOFPSF exhibited a significant decrease both in rest and stress conditions. Furthermore it can be noted that the mean value of vLv increased during stress, as expected.

Algorithm	Rest variation	Variability	p-value	Stress variation	Variability	p-values
3D-OSEM3	-1.8%	4.5%	0.08	2.1%	6.5%	0.17
3D-OSEM5	-0.5%	4.2%	0.62	1.4%	6.1%	0.33
3D-TOFPSF	+5.2%	5.5%	$2\,10^{-4}$	8.3%	9.2%	$1\,10^{-3}$

Table 8.3: Variation in MBF quantification with different reconstruction algorithms compared to 3D-RP using the same VOIs.

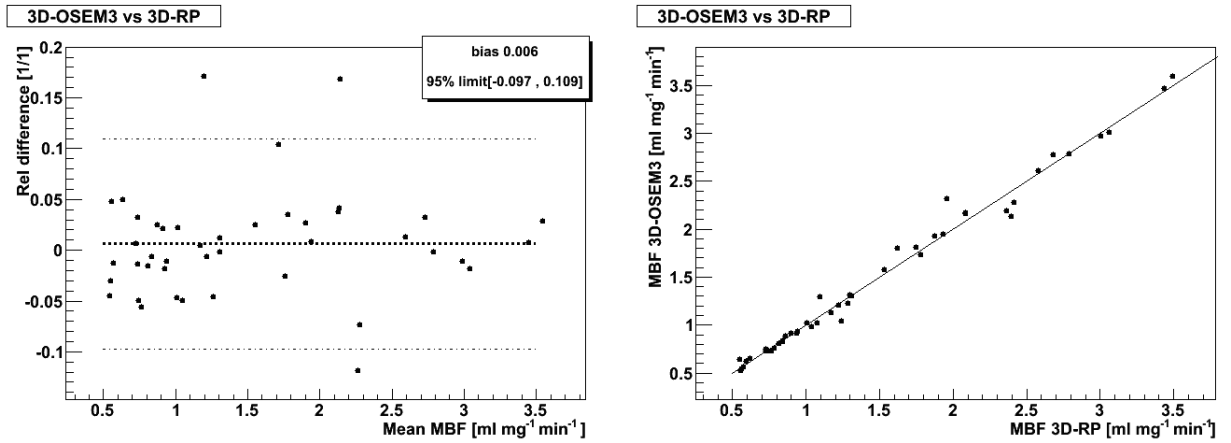

(a) Bland-Altman Plot

(b) Scatter plot, with line of identity superimposed

Figure 8.7: Scatter plot and Bland-Altman plot comparing results with 3D-OSEM3 and 3D-RP

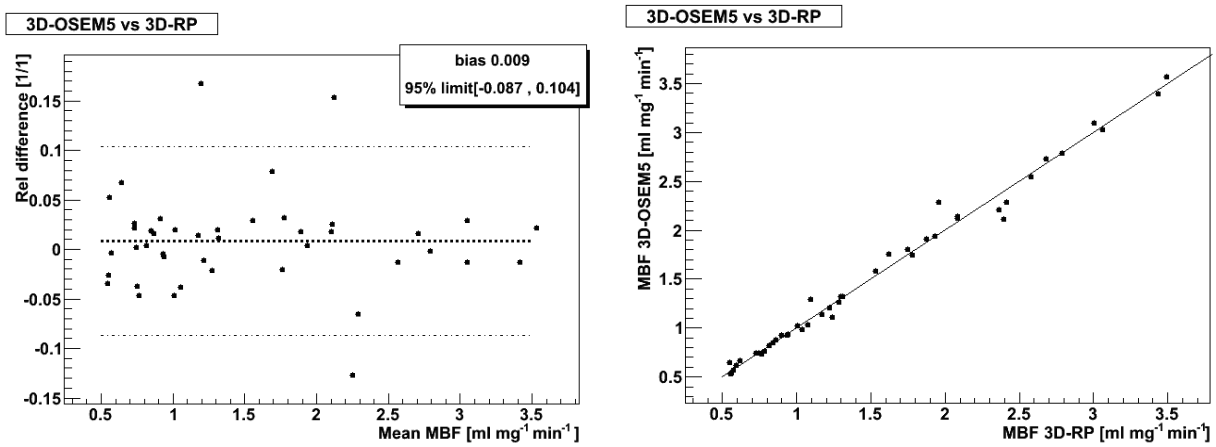

(a) Bland-Altman Plot

(b) Scatter Plot, with line of identity superimposed

Figure 8.8: Scatter plot and Bland-Altman plot comparing 3D-OSEM5 and 3D-RP

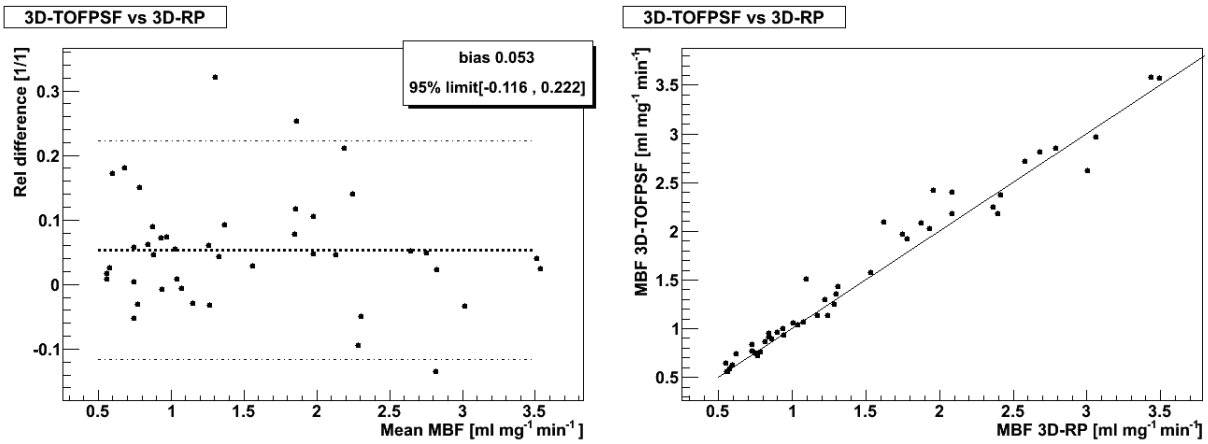

(a) Bland-Altman Plot **(b)** Scatter plot, line of identity superimposed

Figure 8.9: Scatter plot and Bland-Altman plot comparing 3D-TOFPSF to 3D-RP

Algorithm	Rest mean	p-value	Stress mean	p-value
3D-RP	0.197		0.227	
3D-OSEM3	0.228 (+17%)	$1\,10^{-4}$	0.242 (+6.6%)	$5\,10^{-3}$
3D-OSEM5	0.206 (+7%)	$7\,10^{-3}$	0.227 (0)	1
3D-TOFPSF	0.156 (-18%)	$1\,10^{-4}$	0.197 (-13%)	$1\,10^{-4}$

Table 8.4: Comparison of the vLv parameter fitted from different reconstructions, comparing to 3D-RP when using the same VOIs

k_2 value (Table 8.5). At rest, 3D-OSEM3 displayed an increase in the k_2 value, present

Algorithm	Rest mean	p-value	Stress mean	p-value
3D-RP	0.181		0.345	
3D-OSEM3	0.203 (+14%)	$1\,10^{-3}$	0.415 (+6.6%)	$< 1\,10^{-4}$
3D-OSEM5	0.189 (+8%)	0.07	0.385 (0)	$< 1\,10^{-3}$
3D-TOFPSF	0.145 (-18%)	$< 1\,10^{-4}$	0.300 (-13%)	$< 1\,10^{-3}$

Table 8.5: Comparison of the k_2 value with different reconstruction algorithms, when copying the same VOIs, comparing with 3D-RP.

also at stress more pronounced. At rest 3D-OSEM5 had a modest (8%) increase in k_2, with borderline statistical significance, at stress this increase was more pronounced. 3D-TOFPSF presented a significant decrease in k_2 both at rest and stress. Beside the variation of k_2 it can be seen that its mean value approximately doubled at stress. This is in agreement with the known increase of the ammonia washout from the myocardial tissue during hyperaemia.

8.2.2 Different reconstruction algorithms - Different VOIs

Table 6-8 summarize the comparison of the kinetic parameters (global MBF, vLv, k_2) when VOIs were redrawn independently on each reconstruction.

Global MBF (Table 8.6). The trend observed in the "Different algorithm – Same VOIs"

Algorithm	Rest variation	Variability	p-value	Stress variation	Variability	p-values
3D-OSEM3	-3.5%	8.2%	0.05	+2.9%	6.3%	0.06
3D-OSEM5	-4.6%	7.1%	0.007	+0.6%	7.7%	0.7
3D-TOFPSF	+2.2%	7%	$< 1\,10^{-3}$	+8.5%	9.1%	$< 1\,10^{-3}$
3D-TOFPSF (CARIMAS)	+4.5%	7.2%	$< 1\,10^{-3}$	+7.3%	8.3%	$< 1\,10^{-3}$

Table 8.6: Variation in MBF quantification with different reconstruction algorithms compared to 3D-RP using the same VOIs.

analysis was confirmed: similar MBF values in 3D-OSEM3 and 3D-OSEM5 images with respect to 3D-RP and an increase in 3DTOFPSF images (both by PMOD and CARIMAS). In the rest study the 3D-TOFPSF increase with PMOD was not significant. The variability

at rest was consistently higher than in the "Different algorithm – same VOIs", as expected. At stress, variability did not change between the two analyses.

Blood fraction (Table 8.7). All results were in good agreement with those obtained in

Algorithm	Rest mean	p-value	Stress mean	p-value
3D-OSEM3	+12%	$< 1\,10^{-3}$	+6.6%	< 0.05
3D-OSEM5	0	1	0.1%	0.52
3D-TOFPSF	-24%	$< 1\,10^{-4}$	-9%	< 0.05

Table 8.7: Comparison of the vLv parameter fitted from different reconstructions, comparing to 3D-RP when using the same VOIs

the "Different algorithm – same VOIs" analysis. In particular the variation of 3D-OSEM5 at rest is not statistically significant in this analysis. Nonetheless this result is in agreement with the "Same VOI analysis" within the experimental error (p=0.09)

k_2 value (Table 8.8) . The results were in agreement with those obtained in the "Different

Algorithm	Rest mean	p-value	Stress mean	p-value
3D-OSEM3	+7.7%	0.09	+14%	$< 1\,10^{-4}$
3D-OSEM5	0	1	+2.6%	0.39
3D-TOFPSF	-24%	$< 1\,10^{-4}$	-16%	$< 1\,10^{-4}$

Table 8.8: Comparison of the k2 value with different reconstruction algorithms, when copying the same VOIs, comparing with 3D-RP.

reconstruction algorithms - Same VOIs" analysis. With 3D-OSEM5 k_2 had little or no increase compared to 3D-RP, even so these results were compatible with the "same VOI" analysis (p=0.18 at rest, p = 0.33 at stress).

8.2.3 PMOD vs. CARIMAS comparison

The differences in the estimated parameters between PMOD and CARIMAS, both using 3D-RP and 3D-TOFPSF, are presented in Table 8.9. The difference was calculated such that a negative bias means that in CARIMAS the parameter has a lower value. The Bland-Altman plot and a scatter plot are shown in Figure 8.10 .

CARIMAS provided on average a lower MBF than PMOD, both analyzing 3D-RP and 3D-TOFPSF images. With 3D-TOFPSF at rest and stress there was a marked decrease in the inter-software variability(-30%, p<0.0001 in both cases). Also, CARIMAS had a higher vLv (+20% at rest and +15% at stress with 3DRP, +35% at rest and +20% at stress with 3D-TOFPSF).

Parameter	Rest			Stress		
	Variation	Variability	p	Variation	Variability	p
3D-RP (MBF)	-3.9%	6.4%	< 0.01	-4.8%	13.4%	0.15
3D-TOFPSF (MBF)	-4.6%	4.6%	< 0.001	-5.8%	9.2%	0.01
3D-RP (vLv)	+0.047	0.038	$< 1\,10^{-4}$	+0.033	0.048	$< 1\,10^{-3}$
3D-TOFPSF (vLv)	+0.050	0.023	$< 1\,10^{-4}$	+0.042	0.035	$< 1\,10^{-4}$
3D-RP k_2	+0.019	0.036	< 0.05	+0.021	0.069	0.2
3D-TOFPSF k_2	+0.024	0.029	$< 1\,10^{-3}$	+0.027	0.035	$< 1\,10^{-3}$

Table 8.9: Variation observed between and CARIMAS in the kinetic model parameters using 3D-RP and 3D-TOFPSF

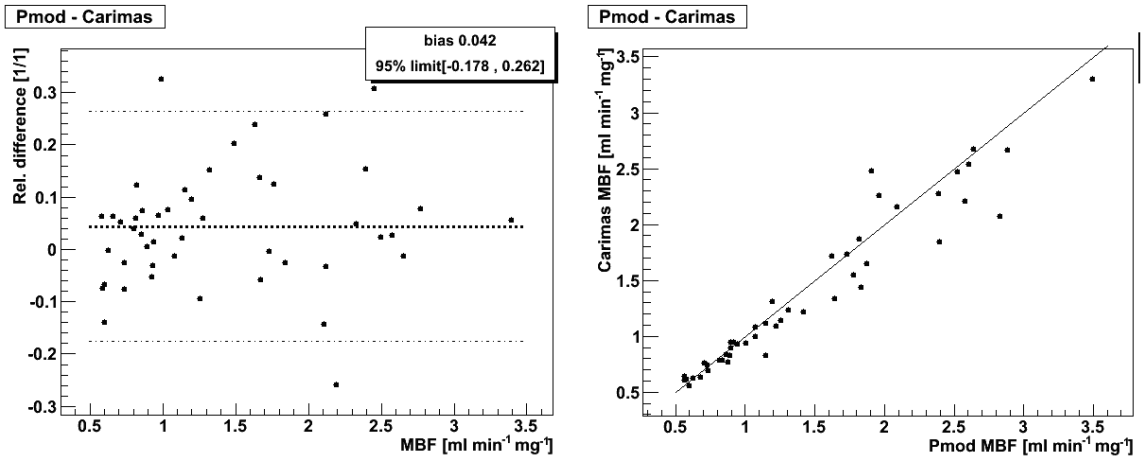

(a) Bland-Altman Plot **(b)** Scatter plot

Figure 8.10: Scatter plot and Bland-Altman plot of the MBF measured between PMOD and CARIMAS

8.3 Results

In this chapter we performed a comprehensive analysis of the difference induced by the reconstruction algorithms and the analysis software programs on the Myocardial Blood Flow quantified with the De-Grado model.

The analysis of the input function highlighted a higher activity in the blood pool with 3D-OSEM3 and 3D-OSEM5, compared to 3D-RP, while 3D-TOFPSF had lower values. This can be attributed to different spill-in from the myocardium. The differences in the global myocardium TAC were limited but highly statistically significant. The differences behave correspondingly to the input function analysis: lowest value (highest spill-out) with 3D-OSEM3 and highest (better contrast recovery) with 3D-TOFPSF.

The comparison of the MBF with the 4 different algorithms showed comparable values; 3D-RP, 3D-OSEM3 and 3D-OSEM5 did not display any appreciable mean difference while 3D-TOFPSF had a small positive bias compared to 3D-RP(+4% at rest, +5% at stress).

The stability of the MBF quantification, despite different image proprieties and amounts of partial volume effect, lays in the modification of the other parameters of the kinetic model. The vLv parameter, representative of the amount of PVE, resulted highest with 3D-OSEM3 and lowest with 3D-TOFPSF (30% difference at rest between these two, 20% at stress). This is in agreement with the results of the TAC and Input Function analysis (fig.8.1 and fig.8.2). 3D-RP at the Nyquist limit has a lower partial volume effect compared to 3D-OSEM at few iterations (i.e. 3), while the combination of TOF information and PSF modeling are effective in reducing partial volume effect.

For what concerns k_2, as it is related to a biological process, the expectation would be of no mean variation across different image reconstruction algorithms. Nonetheless our findings showed marked mean differences. In the DeGrado model the metabolic trapping of ammonia in glutamine is neglected and therefore the k_2 is only an imperfect approximation of the actual washout from the extra-vascular compartment. A possible explanation of these results lays in the modification of the values of the input functions in the late frames of the acquisition. The model probably responds to increasing values of measured activity in the blood by increasing the tracer washout from extra-vascular compartment. This would be similar to what was observed in section 7.3.3.

The comparison of PMOD and CARIMAS showed a small negative bias of the MBF in the latter. This can be attributed to the different sampling strategies, that give rise to different amounts of partial volume effect. Strictly related was the strong increase of the vLv parameter (˜+20%). PMOD samples the voxels of maximum uptake (centreline of the myocardial wall) where the partial volume effect is supposed to be minimum. On the contrary CARIMAS uses a more conventional method of sampling which include the whole thickness of the myocardial wall. In this way voxels with higher spillover from the blood pool are included. This in turn increases the spillover correction. In fact, sampling the whole myocardial wall includes both voxels with higher spillover from the left ventricle, effectively parameterized by the vLv parameter, but also epicardial voxels that have a spillout towards other organs, which is not accounted for. This was effectively seen with simulations [117]. It should also be noted that the inter-program variability between PMOD and CARIMAS significantly decreased when comparing 3D-TOFPSF images with respect to 3D-RP images.

This can be explained by the reduced noise and better structure definition of the 3D-TOFPSF images compared to 3D-RP; this allowed both the operator and the segmentation algorithms to define with more confidence the VOIs.

8.4 Conclusion

Absolute quantification of MBF with 3D-PET, $^{13}NH_3$, and DeGrado modelization was consistently stable across different reconstruction methods and analysis software like PMOD or CARIMAS.

The most innovative reconstruction algorithm, including Time-Of-Flight information and 3D-PET Point-Spread-Function, showed a small positive bias in the MBF as well as the need for significantly less spillover correction when compared to the other reconstruction algorithms considered in the work (3D-RP and 3D-OSEM).

Chapter 9

Conclusion

In this thesis many aspects of cardiac PET imaging have been analyzed. Chapter 2 dealt with the characterization of a new tomograph with fast scintillators (LYSO) and TOF recording capabilities. It was found that the General Electrics Discovery-690 is suited to perform dynamic studies thanks to its very high NECR and high count rate capabilities. The effect of reconstruction algorithms for oncologic and neurologic settings were studied and it was found that reconstruction algorithms encompassing TOF and PSF modeling are effective in providing a better reconstruction, quantitatively and qualitatively.

Chapter 3 dealt with studies performed with an anthropomorphic static phantom to assess the most suited reconstruction procedure to process cardiac data. It turned out that also in this case the combination of TOF and PSF modeling give the best results, with TOF increasing the convergence speed of the iterative algorithms, specially in cold regions, and PSF modeling decreasing spillover effect. The accuracy of the corrections for dead time were tested up to high count rates and it was found that they do not introduce bias up to regions of count rate much higher than those found in clinical studies.

Chapter 4 described the design of a dynamic phantom used to assess the effect of cardiac motion in cardiac PET studies. This phantom simulates, separately, both cardiac and respiratory motion. This phantom was later used in this thesis to assess the quantitative effects of motion and to test the efficacy of motion compensation algorithms.

Following chapter 5 introduces gating techniques, used to compensate for motion. It was found, analyzing the data acquired using our phantom, that motion, on top of blurring the image, reduced the measured activity concentration by 26%, averaged over the whole volume. It was found that respiratory or cardiac gating alone are not effective in recovering the true activity concentration while double gating is. Similar reductions in measured activity were found in patients comparing the activity measured in a double gated reconstruction to those of standard reconstructions. Qualitative analysis suggested better structure definition in double gated images, that, nonetheless, suffered from a very high level of noise.

To compensate for this high statistical noise in chapter 6 I proposed two different algorithms to register images coming from different gates. The first method registers only the respiratory motion at a fixed cardiac phase. While this method is robust and mimics realistically the actual biologic process this method is not able to recover the full information contained in the scan. For this reason also an elastic registration technique was introduced.

Both techniques were tested on our phantom and, following, were applied to patient data. The qualitative results were that of an improvement in structure definition, compared to static reconstructions, and a level of noise comparable to static reconstructions.

Following the focus was shifted to kinetic modeling for myocardial perfusion. In chapter 7, after a review of the available techniques, I analyzed the mathematical proprieties of the models describing $^{13}NH_3$ uptake. It was found that the model proposed by DeGrado, while being less realistic than the model proposed by Hutchins, provides more accurate results for the parameter of clinical interest. This is specially true at resting conditions where the Hucthins model might fall inside wide minima. It has been found that the accuracy of the estimated Myocardial Blood Flow (MBF) comes at the cost of a bias in the washout parameter (k_2) which is not of clinical interest. Also the effect of imperfect corrections of metabolites in the input function were studied and it was found that the MBF is not influenced by it while instead k_2 varies much.

Finally, in chapter 8, the influence of the reconstruction algorithm on quantification performed with the DeGrado model was studied. The results where that the MBF is quite stable to different reconstruction techniques. This happens at a cost of variation in the k_2 parameter and in the parameter that models the spillout from the left ventricle to the myocardium (vLv). It also turned out that this parameter is minimized by the reconstruction algorithm encompassing TOF and PSF modeling, compatibly with the results observed in chapter 4 that indicated this algorithms as the most precise.

Future work

Starting from these results many lines of research can be pursued. An interesting one would be the quantification of the improvement of diagnostic confidence in cardiac studies provided by double gating followed by registration procedure. Another research could analyze the possibility to correct for motion inside the reconstruction algorithm to achieve more accurate images. Finally, for what concerns kinetic modeling for myocardial perfusion, lines of research could concern strategies to reduce the noise in the MBF data, in strategies to achieve parametric images with a low enough level of noise to be of diagnostic quality and in simultaneous reconstruction and quantification.

Bibliography

[1] G. Muehllehner and J. S. Karp. Positron emission tomography. Phys. Med. Biol., 51:R117–R137, 2006.

[2] C. Stearns, D. McDaniel, S. Kohlmyer, P. Arul, B. Geiser, and V. Shanmugam, "Random coincidence estimation from single event rates on the Discovery ST PET-CT scanner." in IEEE Nuclear Science Symposium Conference Record (Portland, Oregon, 2003), Vol. 5, pp. 3067–3069.

[3] D. L. Bailey and S. R. Meikle. A convolution–subtraction scatter correction method for 3D PET. Phys. Med. Biol., 39:411–424, 1994

[4] M. Bentourkia, P. Msaki, J. Cadorette, and R. Lecompte. Assessment of scatter components in high-resolution PET: Correction by nonstationary convolution subtraction. J. Nucl. Med., 36:121–130, 1995.

[5] M. Lubberink, T. Kosugi, H. Schneider, H. Ohba, and M. Bergstrom. Non stationary convolution subtraction scatter correction with a dual–exponential scatter kernel for the Hamamatsu SHR–7700 animal PET scanner. Phys. Med. Biol., 49:833–842, 2004.

[6] C. W. Stearns. Scatter correction method for 3D PET using 2D fitted gaussian functions. J. Nucl. Med., 36:105P, 1995

[7] M. Iatrou, R. Manjeshwar, S. Ross, K. Thielemans, and C. Stearns. 3D implementation of scatter estimation in 3D PET. In Nuclear Science Symposium Conference Record, pages 2142–2145. IEEE, 2006

[8] J. M. Ollinger. Model-based scatter correction for fully 3D PET. Phys. Med. Biol., 41:153–176, 1996.

[9] M. Iatrou, R. Manjeshwar, S. Ross, K. Thielemans, and C. Stearns, "3D implementation of scatter estimation in 3D PET," in IEEE Nuclear Science Symposium Conference Record (San Diego, CA, 2006), pp. 2142–2145.

[10] N. Cao, R. H. Huesman, W. W. Moses, and J. Qi. Detection performance analysis for time-of-flight PET. Phys. Med. Biol., 55:6931–6950, 2010.

[11] M. Conti. State of the art and challenges of time-of-flight PET. Physica Medica, 25:1–11, 2009

[12] M. Conti. Why is TOF PET reconstruction a more robust method in presence of inconsistent data? Phys. Med. Biol., 56:155–168, 2011

[13] C. Lois, B. W. Jakoby, M. J. Long, K. F. Hubner, D. W. Barker, M. E. Casey, M. Conti, V. Y. Panin, D. J. Kadrmas, and D. W. Townsend. An assessment of the impact of incorporating time-of-flight information into clinical PET/CT imaging. J. Nucl. Med., 51:237–245, 2010

[14] L. A. Shepp, Y. Vardi, Maximum likelihood reconstruction for emission tomography, IEEE Trans. Med. Im. 1 (2) 1982, 113-122

[15] Hudson, H.M., Larkin, R.S. (1994) "Accelerated image reconstruction using ordered subsets of projection data", IEEE Trans. Medical Imaging, 13 (4), 601–609 doi:10.1109/42.363108

[16] M. Iatrou, S. G. Ross, R. M. Manjeshwar, and C. W. Stearns, "A fully 3D iterative image reconstruction algorithm incorporating data corrections," in IEEE Nuclear Science Symposium Conference Record (Rome, Italy, 2004), Vol. 4, pp. 2493–2497.

[17] A. M. Alessio, C. W. Stearns, S. Tong, S. G. Ross, S. Kohlmyer, A. Ganin, and P. E. Kinahan, "Application and evaluation of a measured spatially variant system model for PET image reconstruction," IEEE Trans. Med. Imaging 29, 938–949 (2010).

[18] National Electrical Manufacturers Association, NEMA NU-2 Standards Publication NU-2-2007: Performance Measurements of Positron Emission Tomography (National Electrical Manufacturers Association, Rosslyn, VA, 2007).

[19] C. C. Watson, M. E. Casey, L. Eriksson, T. Mulnix, D. Adams, and B. Bendriem, "NEMA NU 2 performance tests for scanners with intrinsic radioactivity," J. Nucl. Med. 45, 822–826 (2004).

[20] T. K. Lewellen, "The challenge of detector designs for PET," AJR, Am. J. Roentgenol. 195, 301–309 (2010).

[21] M. Teras, T. Tolvanen, J. J. Johansson, J. J. Williams, and J. Knuuti, "Performance of the new generation of whole-body PET=CT scanners: Discovery STE and Discovery VCT," Eur. J. Nucl. Med. Mol. Imaging 34, 1683–1692 (2007)

[22] S. D. Sharma, R. Prasad, B. Shetye, V. Rangarajan, D. Deshpande, S. K. Shrivastava, and K. A. Dinshaw, "Whole-body PET acceptance test in 2D and 3D using NEMA NU 2-2001 protocol," J. Med. Phys. 32, 150–155 (2007).

[23] E. De Ponti, S. Morzenti, L. Guerra, C. Pasquali, M. Arosio, V. Bettinardi, A. Crespi, M. C. Gilardi, and C. Messa, "Performance measurements for the PET/CT Discovery-600 using NEMA NU 2-2007 standards," Med. Phys. 38, 968–974 (2011).

[24] V. Bettinardi, M. Danna, A. Savi, M. Lecchi, I. Castiglioni, M. C. Gilardi, H. Bammer, G. Lucignani, and F. Fazio, "Performance evaluation of the new whole-body PET/CT scanner: Discovery ST," Eur. J. Nucl. Med. Mol. Imaging 31, 867–881 (2004).

[25] S. Tong, A. M. Alessio, and P. E. Kinahan, "Noise and signal properties in PSF-based fully 3D PET image reconstruction: An experimental evaluation," Phys. Med. Biol. 55, 1453–1473 (2010).

[26] Le Meunier L et. al. Enhanced definition PET for cardiac imaging. J Nucl Cardiol. 2010 Jun;17(3):414-26

[27] Begemann PG, van Stevendaal U, Manzke R, Stork A, Weiss F, Nolte-Ernsting C, Grass M, Adam G. Evaluation of spatial and temporal resolution for ECG-gated 16-row multidetector CT using a dynamic cardiac phantom. Eur Radiol.15, 1015-26 (2005).

[28] Begemann PG, van Stevendaal U, Koester R, Mahnken AH, Koops A, Adam G, Grass M, Nolte-Ernsting C. Evaluation of the influence of acquisition and reconstruction parameters for 16-row multidetector CT on coronary calcium scoring using a stationary and dynamic cardiac phantom. Eur Radiol. 17,1985-94 (2007).

[29] Boll DT, Merkle EM, Paulson EK, Mirza RA, Fleiter TR. Calcified vascular plaque specimens: assessment with cardiac dual-energy multidetector CT in anthropomorphically moving heart phantom. Radiology. 249, 119-26 (2008).

[30] Swailes NE, MacDonald ME, Frayne R. Dynamic phantom with heart, lung, and blood motion for initial validation of MRI techniques. J Magn Reson Imaging. 34, 941-6 (2011).

[31] De Bondt P, Claessens T, Rys B, De Winter O, Vandenberghe S, Segers P, Verdonck P, Dierckx RA. Accuracy of 4 different algorithms for the analysis of tomographic radionuclide ventriculography using a physical, dynamic 4-chamber cardiac phantom. J Nucl Med. 46, 165-71 (2005).

[32] .Ceriani L, Ruberto T, Delaloye AB, Prior JO, Giovanella L. Three-dimensional ordered-subset expectation maximization iterative protocol for evaluation of left ventricular volumes and function by quantitative gated SPECT: a dynamic phantom study. J Nucl Med Technol. 38, 18-23 (2010)

[33] Sloboda RS, Hardie DI, Schmid M, Morris PB, Hughes J, Malik MH. A dynamic quality control phantom for radionuclide cardiology. Med Phys. 13, 90-2 (1986).

[34] Nickles RJ. A dynamic phantom for radionuclide cardiology. J Nucl Med. 20, 547-9 (1979).

[35] Debrun D, Thérain F, Nguyen LD, Léger CP, Visser JJ, Busemann-Sokole E. Volume measurements in nuclear medicine gated SPECT and 4D echocardiography: validation using a dynamic cardiac phantom. Int J Cardiovasc Imaging. 21, 239-47; discussion 249-51 (2005)

[36] King M, Rodgers Z, Giger ML, Bardo DM, Patel AR. Computerized method for evaluating diagnostic image quality of calcified plaque images in cardiac CT: validation on a physical dynamic cardiac phantom. Med Phys. 37, 5777-86 (2010)

[37] Kokki T, Sipilä HT, Teräs M, Noponen T, Durand-Schaefer N, Klén R, Knuuti J. Dual gated PET/CT imaging of small targets of the heart: method description and testing with a dynamic heart phantom. J Nucl Cardiol. 17, 71-84 (2010).

[38] Green MV, Ostrow HG, Douglas MA et. al: High temporal resolution ECG-gated scintigraphic angiography. J. Nucl. Med. 16:95-98, 1975

[39] Berman DS, Salel AF, DeNardo GL et al. : Clinical assessment of left ventricular regional contraction patterns and ejection fraction by high-resolution gated scintigraphy. J Nucl Med 16: 865-874, 1975

[40] Ter-Pogossian MM, Bergmann SR, Sobel BE. Influence of cardiac and respiratory motion on tomographic reconstructions of the heart: implications for quantitative nuclear cardiology. J Comput Assist Tomogr. 1982;6:1148-55.

[41] Boucher L, Rodrigue S, Lecomte R, et al.: Respiratory gating for 3-dimensional PET of the thorax: feasibility and initial results. J Nucl Med 2004;45:214-19.

[42] Teräs M, Kokki T, Durand-Schaefer N, Noponen T, Pietilä M, Kiss J, Hoppela E, Sipilä HT, Knuuti J. Dual-gated cardiac PET-clinical feasibility study. Eur J Nucl Med Mol Imaging. 2010 Mar;37(3):505-16. Epub 2009 Sep 30

[43] Hsieh J, Londt J, Vass M, Li J, Tang X, Okerlund D. Step-and-shoot data acquisition and reconstruction for cardiac x-ray computed tomography. Med Phys 2006; 33: 4236–4248

[44] Hausleiter J et. al. Image quality and radiation exposure with prospectively ECG-triggered axial scanning for coronary CT angiography: the multicenter, multivendor, randomized PROTECTION-III study. JACC Cardiovasc Imaging. 2012 May;5(5):484-93.

[45] Lu W, Parikh PJ, Hubenschmidt JP, et al. A comparison between amplitude sorting and phase-angle sorting using external respiratory measurement for 4D CT. Med Phys 2006;33:2964-74.

[46] Dawood M, Büther F, Lang N, et al. Respiratory gating in positron emission tomography: a quantitative comparison of different gating schemes. Med Phys 2007;34:3067-76.

[47] Nehmeh SA, Erdi YE, Meirelles GS, et al. Deep-inspiration breath-hold PET/CT of the thorax. J Nucl Med 2007;48: 22-6.

[48] Fin L, Daouk J, Morvan J, et al. Initial clinical results for breath-hold CT-based processing of respiratory-gated PET acquisitions. Eur J Nucl Med Mol 2008;35:1971-80.

[49] Nehmeh SA, Erdi YE. Respiratory motion in positron emission tomography/computed tomography: a review. Semin Nucl Med. 2008;38:167-76.

[50] Moorees J, Bezak E. Four dimensional CT imaging: a review of current technologies and modalities. Australas Phys Eng Sci Med. 2012;35:9-23.

[51] Gierga DP, Brewer J, Sharp GC, et al.The correlation between internal and external markers for abdominal tumors: implications for respiratory gating. Int J Radiat Oncol Biol Phys 2005;61:1551-8.

[52] Ionascu D, Jiang SB, Nishioka S, et al. Internal-external correlation investigations of respiratory induced motion of lung tumors. Med Phys 2007;34:3893-903.

[53] Beddar AS, Kainz K, Briere TM, et al. Correlation between internal fiducial tumor motion and external marker motion for liver tumors imaged with 4D-CT. Int J Radiat Oncol Biol Phys 2007;67:630-8.

[54] Kubo HD, Hill BC. Respiration gated radiotherapy treatment: a technical study. Phys Med Biol 1996;41:83-91.

[55] Riedel M. Respiratory Motion Estimation: Tests and Comparison of Different Sensors. IDP - Interdisciplinary Project (Physics). Technische Universitat Munchen. Fakultat fur Informatik 2006.

[56] Zhang T, Keller H, O'Brien MJ, et al. Application of the spyrometer in respiratory gated radiotherapy. Med Phys 2003;30:3165-71.

[57] 27. D'Souza WD, Kwok Y, Deyoung C, et al. Gated CT imaging using a free-breathing respiration signal from flow-volume spirometry. Med Phys 2005;32:3641-9.

[58] Garcia R, Oozeer R, Le Thanh H, et al. Radiotherapy of lung cancer: the inspiration breath hold with spirometric monitoring. Cancer Radiother. 2002;6(1):30-8.

[59] Wong JW, Sharpe MB, Jaffray DA, et al. The use of active breathing control (ABC) to reduce margin for breathing motion. Int J Radiat Oncol Biol Phys 1999;44:911–19.

[60] Ozhasoglu C, Murphy MJ. Issues in respiratory motion compensation during external-beam radiotherapy. Int J Radiat Oncol Biol Phys 2002;52:1389-99.

[61] Dawson LA, Brock KK, Kazanjian S, et al. The reproducibility of organ position using active breathing control (ABC) during liver radiotherapy. Int J Radiat Oncol Biol Phys 2001;51:1410-21.

[62] Remouchamps VM, Letts N, Vicini FA, et al. Initial clinical experience with moderate deep-inspiration breath hold using an active breathing control device in the treatment of patients with left sided breast cancer using external beam radiation therapy. Int J Radiat Oncol Biol Phys 2003;56:704–15.

[63] Kimura T, Hirokawa Y, Murakami Y, et al. Reproducibility of organ position using voluntary breath-hold method with spyrometer for extracranial stereotactic radiotherapy. Int J Radiat Oncol Biol Phys 2004;60:1307-13

[64] Ha J, Perlow D, Yi BY, et al. On the sources of drift in a turbine-based spirometer. Phys Med Biol 2008;53:4269–83.

[65] Möller AM, Bundschuh R, Riedel M, et al. Comparison of respiratory sensors and its compliance for respiratory gating in emission tomography. J Nucl Med. 2007;48 (Supplement 2):426P

[66] Kokki T, Lepomaki V, Kajander S, et al. Spirometry based respiratory gating method for cardiac PET and MRI imaging. Nuclear Science Symposium Conference Record, 2008. NSS '08. IEEE pages: 4832 – 34.

[67] Li XA, Stepaniak C, Gore E. Technical and dosimetric aspects of respiratory gating using a pressure-sensor motion monitoring system. Med Phys 2006;33:145-54.

[68] Otani Y, Fukuda I, Tsukamoto N, et al. A comparison of the respiratory signals acquired by different respiratory monitoring systems used in respiratory gated radiotherapy. Med Phys 2010;37:6178-86.

[69] Carlson SK, Felmlee JP, Bender CE, et al. Intermittent-mode CT fluoroscopy-guided biopsy of the lung or upper abdomen with breath-hold monitoring and feedback: system development and feasibility. Radiology 2003;229:906-12.

[70] Carlson SK, Felmlee JP, Bender CE, et al. CT fluoroscopy-guided biopsy of the lung or upper abdomen with a breath-hold monitoring and feedback system: a prospective randomized controlled clinical trial. Radiology 2005 Nov;237(2):701-8.

[71] Shyn PB, Tatli S, Sainani NI et al. Minimizing image misregistration during PET/CT-guided percutaneous interventions with monitored breath-hold PET and CT acquisitions. J Vasc Interv Radiol 2011;22:1287-92.

[72] Nehmeh SA, Erdi YE. Respiratory motion in positron emission tomography/computed tomography: a review. Semin Nucl Med. 2008;38:167-76.

[73] Vedam SS, Keall PJ, Kini VR, et al. Acquiring a four-dimensional computed tomography dataset using an external respiratory signal. Phys Med Biol 2003;48:45-62.

[74] Brandner ED, Wu A, Chen H, et al. Abdominal organ motion measured using 4D CT. Int J Radiat Oncol Biol Phys. 2006;65:554-60.

[75] Chang Z, Liu T, Cai J, et al. Evaluation of integrated respiratory gating systems on a Novalis Tx system. J Appl Clin Med Phys 2011;12:71-9.

[76] Kauweloa KI, Ruan D, Park JC, et al. GateCTTM surface tracking system for respiratory signal reconstruction in 4DCT imaging. Med Phys 2012;39:492-502.

[77] Dunn L, Kron T, Johnston PN, et al. A programmable motion phantom for quality assurance of motion management in radiotherapy. Australas Phys Eng Sci Med 2012;35:93-100.

[78] Chi PC, Balter P, Luo D, et al. Relation of external surface to internal tumor motion studied with cine CT. Med Phys 2006;33:3116-23.

[79] Vedam SS, Keall PJ, Kini VR, et al. Acquiring a four-dimensional computed tomography dataset using an external respiratory signal. Phys Med Biol. 2003;48:45-62.

[80] Alessio AM, Kohlmyer S, Branch K, Chen G, Caldwell J, Kinahan P. Cine CT for Attenuation Correction in Cardiac PET/CT. J Nucl Med. 2007 May;48(5):794-801

[81] DiFilippo FP, Brunken RC. Do implanted pacemaker leads and ICD leads cause metal-related artifact in cardiac PET/CT J Nucl Med. 2005 Mar;46(3):436-43.

[82] Ghafarian P, Aghamiri SM, Ay MR, Rahmim A, Schindler TH, Ratib O, Zaidi H. Is metal artefact reduction mandatory in cardiac PET/CT imaging in the presence of pacemaker and implantable cardioverter defibrillator leads? Eur J Nucl Med Mol Imaging. 2011 Feb;38(2):252-62

[83] Kokki T, Sipilä HT, Teräs M, Noponen T, Durand-Schaefer N, Klén R, Knuuti J. Dual gated PET/CT imaging of small targets of the heart: method description and testing with a dynamic heart phantom. J Nucl Cardiol. 2010 Jan-Feb;17(1):71-84.

[84] Virmani R, Allen BP, Farb A, et al. Pathology of the vulnerable plaque. J Am Coll Cardiol 2006;47:13–8.

[85] Chen W, Dilsizian V. (18)F-fluorodeoxyglucose PET imaging of coronary atherosclerosis and plaque inflammation. Curr Cardiol Rep 2010;12:179-84.

[86] Pugliese F, Gaemperli O, Kinderlerer AR, et al. Imaging of vascular inflammation with [11C]-PK11195 and positron emission tomography/computed tomography angiography. J Am Coll Cardiol 2010;56:653-61.

[87] Joshi F, Rosenbaum D, Bordes S, et al. Vascular imaging with positron emission tomography. J Intern Med 2011;270:99-109.

[88] Matter CM, Stuber M, Nahrendorf M. Imaging of the unstable plaque: how far have we got?. Eur Heart J 2009;30:2566–74.

[89] Kovalski G, Keidar Z, Frenkel A, Sachs J, Attia S, Azhari H. Dual "motion-frozen heart" combining respiration and contraction compensation in clinical myocardial perfusion SPECT imaging. J Nucl Cardiol. 2009 May-Jun;16(3):396-404.

[90] Slomka PJ, Nishina H, Berman DS, Kang X, Akincioglu C, Friedman JD, Hayes SW, Aladl UE, Germano G. "Motion-frozen" display and quantification of myocardial perfusion. J Nucl Med. 2004 Jul;45(7):1128-34.

[91] F. L. Bookstein, "Principal warps: Thin-plate splines and the decomposition of deformations" IEEE Trans. Pattern Anal. Machine. Intell., vol. 11, pp. 567–585, June 1989.

[92] Cerqueira,M.D. et al, Standardized Myocardial Segmentation and Nomenclature for Tomographic Imaging of the Heart, Circulation 2002; 105:593-542

[93] Myometrix White Paper, GE Healthcare, 2006.

[94] Hunter WW Jr, Monahan WG: 13N-ammonia: a new physiologic radiotracer for molecular medicine. (abstr) J Nucl Med 12: 368, 1971

[95] Harper PV, Lathrop KA, Krizek H, Lembares N, Stark V, Hoffer PB: Clinical feasibility of myocardial imaging with 13NH3. J Nucl Med 13: 278, 1972

[96] Schelbert HR, Phelps ME, Hoffman EJ, Huang S, Selin CE, Kuhl DE: Regional myocardial perfusion assessed with N-13 labeled ammonia and positron emission computerized axial tomography. Am J Cardiol 43: 209, 1979

[97] Ter-Pogossian MM, Eichling JO, Davis DO, Welch MJ, Metzger JM: The determination of regional cerebral blood flow by means of water labeled with radioactive oxygen 15. Radiology 93: 31-40, 1969

[98] Michael Fiechter et. al. "Diagnostic Value of 13N-Ammonia Myocardial Perfusion PET Added Value of Myocardial Flow Reserve" J Nucl Med. 2012 Aug;53(8):1230-4

[99] Camici PG, Crea F. Coronary microvascular dysfunction. N Engl J Med. 2007 Feb 22;356(8):830-40

[100] Herzog BA, Husmann L, Valenta I, Gaemperli O, Siegrist PT, Tay FM, Burkhard N, Wyss CA, Kaufmann PA. Long-term prognostic value of 13N-ammonia myocardial perfusion positron emission tomography added value of coronary flow reserve. J Am Coll Cardiol. 2009 Jul 7;54(2):150-6

[101] Lassen, N. and Perl, W. (1979). Tracer kinetic methods in medical physiology. Raven Press, New York.

[102] Godfrey, K., Compartmental Models and Their Application, Academic Press, 1983

[103] Rimoldi OE, Camici PG. Positron emission tomography for quantitation of myocardial perfusion. J Nucl Cardiol. 2004 Jul-Aug;11(4):482-90.

[104] Crone, C. (1963). The permeability of capillaries in various organs as determined by use of the indicator diusion method. Acta Physiol Scand, 58:292-305.

[105] Renkin, E. (1959). Transport of potassium-42 from blood to tissue in isolated mammalian skeletal muscles. American Journal of Physiology, 197(6):1205-1210.

[106] Phelps M. Molecular Imaging and Its Biological Applications. pgg 397

[107] Lautamaki R, George RT, Kitagawa K, et al. 82Rb PET-CT for quantitative assessment of myocardial blood flow: validation in a canine model of coronary artery stenosis. Eur J Nucl Med Mol Imaging. 2009;36:576–586.

[108] Yalamanchili P, Wexler E, Hayes M, et al. Mechanism of uptake and retention of 18F BMS747158-02 in cardiomyocytes: a novel PET myocardial imaging agent. J Nucl Cardiol. 2007;14:782–788.

[109] Sherif HM, Nekolla SG, Saraste A, Reder S, Yu M, Robinson S, Schwaiger M. Simplified quantification of myocardial flow reserve with flurpiridaz F 18: validation with microspheres in a pig model. J Nucl Med. 2011 Apr;52(4):617-24.

[110] H R Schelbert, M E Phelps, S C Huang, N S MacDonald, H Hansen, C Selin and D E Kuhl N-13 ammonia as an indicator of myocardial blood flow. Circulation. 1981;63:1259-1272

[111] Schelbert HR, Phelps ME, Hoffman EJ, Huang SC, Selin CE, Kuhl DE. Regional myocardial perfusion assessed with N-13 labeled ammonia and positron emission computerized axial tomography. Am J Cardiol. 1979 Feb;43(2):209-18.

[112] Hutchins GD, Schwaiger M, Rosenspire KC, Krivokapich J, Schelbert H, Kuhl DE. Noninvasive quantification of regional blood flow in the human heart using N-13 ammonia and dynamic positron emission tomographic imaging. J Am Coll Cardiol. 1990 Apr;15(5):1032-42.

[113] DeGrado TR, Hanson MW, Turkington TG, Delong DM, Brezinski DA, Vallée JP, Hedlund LW, Zhang J, Cobb F, Sullivan MJ, Coleman RE. Estimation of myocardial blood flow for longitudinal studies with 13N-labeled ammonia and positron emission tomography. J Nucl Cardiol. 1996 Nov-Dec;3(6 Pt 1):494-507.

[114] C. R. Bellina, O. Parodi, P. Camici, P. A. Salvadori, L. Taddei, L. Fusani, R. Guzzardi, G. A. Klassen, A. L. L'Abbate, L. Donato, Simultaneous in vitro and in vivo validation of nitrogen-13-ammonia for the assessment of regional myocardial blood flow, J. Nucl. Med. 31 (8) 1990, 1335-1343

[115] Krivokapich J, Smith G, Huang S, et al. 13N-ammonia myocardial imaging at rest and with exercise in normal volunteers. Circulation 1989;80:1328-37.

[116] van den Hoff J, Burchert W, Borner AR, Fricke H, Kuhnel G, Meyer GJ, Otto D, Weckesser E, Wolpers HG, Knapp WH. [1-(11)C]Acetate as a quantitative perfusion tracer in myocardial PET. J Nucl Med. 2001;42(8):1174-82

[117] Hutchins GD, Caraher JM, Raylman RR. A region of interest strategy for minimizing resolution distortions in quantitative myocardial PET studies. J Nucl Med. 1992 Jun;33(6):1243-50.

[118] Altman DG, Bland JM (1983). "Measurement in medicine: the analysis of method comparison studies". Statistician 32: 307–317